Biosensor development using organic electrochemical transistors (OECTs) fabricated via printing techniques

by

Jiaxin Fan

A thesis submitted in partial fulfillment of the requirements for the degree of

Doctor of Philosophy

in

Microsystems and Nanodevices

Department of Electrical and Computer Engineering
University of Alberta

Abstract

Continuous health monitoring and integrated diagnostic devices are revolutionizing the modern healthcare system. Biosensors serve as an essential tool in detecting and monitoring a wide range of medical conditions from diabetes to cancer for precision healthcare. The global biosensor market value was 22.4 billion USD in 2020 and is expected to reach 41.8 billion USD by 2028. In 2020, the medical segment accounted for 66.6% of the biosensor market revenue [1]. The invention of conducting polymer, which has excellent properties, paved the path for creating inexpensive organic electronics for biosensing. Organic electrochemical transistors (OECTs) have emerged as a versatile biosensing platform due to their low operation voltages, compatibility with aqueous environments, and intrinsic signal amplification. Owing to the simple device structure, OECTs are compatible with 3D printing technology that enables rapid customization of biosensing platforms to meet specific requirements.

In this work, OECTs are fabricated and optimized using two different 3D printing systems. The influence of geometric parameters on the performance of the printed OECTs is first studied. The geometric optimization study is important for achieving the desired sensitivity and detection limit. Ions and certain molecules can be directly sensed by OECT due to the intrinsic ion sensitivity of channel materials and electrochemical properties of the molecules. Interaction with most analytes and selectivity of biosensors rely on functionalizing the devices with bioreceptors that only respond to the target analyte. Two functionalization approaches, physisorption and chemisorption, are taken to modify the printed OECTs for different sensing applications.

The unfunctionalized printed OECTs are capable of sensing ions and Δ^9-THC

concentrations in synthetic saliva buffer. These results indicate that 3D printing techniques are suitable for fabricating high-performance OECTs that have sufficient precision for biosensing applications.

Functionalization of aerosol jet printed OECTs with glucose oxidase (GOx) via physisorption for glucose sensing is thoroughly studied. The effects of functionalization sites and nanomaterials are investigated by comparing four configurations: unfunctionalized OECT with floating GOx, GOx functionalized channel, GOx functionalized printed Pt gate, and GOx functionalized sputtered Pt gate. The printed OECT with GOx functionalized printed Pt gate shows the best performance with a detection range between 100 nM to 50 mM and two sensitivities of 0.022NR/dec for 100 nM to 250 μM and 0.255NR/dec for 250 μM to 50 mM. The performance of this sensor is then evaluated in artificial sweat with a detection range of 0.1 to 10 mM, which is well within the human sweat glucose concentration range.

N-heterocyclic carbene (NHC) ligands form extremely stable bonds with metals and have great potential in conjugating organic molecules to metal surfaces. Printed Au electrodes are functionalized with alkyne-modified NHC ligands. The biotin molecules are tethered to the Au electrodes by copper-catalyzed alkyne-azide click chemistry. These modified electrodes are used as gate electrodes for printed OECTs, and streptavidin binding is detected. As the gate functionalization is completely isolated from the device, a variety of processes can be used without damaging the OECT device performance.

Lastly, a point-of-care (POC) COVID-19 diagnostic device is developed. The POC COVID-19 diagnostic device consists of a single-use disposable OECT based biosensor and a custom designed signal processing circuit. Anti-SARS-CoV-2 antibodies are conjugated onto the in-plane gate electrode of the printed OECT. The OECT based biosensor shows selectivity towards SARS-CoV-2 spike proteins with a limit of detection of 1 fg/mL and detects virus-like particles (VLPs) with a sensitivity of -45.7 $\pm$ 13.0 mV/dec. The POC diagnostic device is used to test clinical nasopharyngeal

samples with an overall accuracy of 87.5%. This is a label-free technique that takes less than 10 minutes to test each sample. This rapid POC diagnostic system could be easily translated to real-world on-site or at home detection device and modified for other applications.

In summary, 3D printing techniques have been employed for fabricating high-performance OECTs that are functionalized using different strategies for the detection of glucose, streptavidin, and SARS-CoV-2. These 3D printed OECTs are suitable for different biosensing applications and capable of detecting the analyte in various electrolytes including saliva, sweat, and nasopharyngeal samples. Therefore, this work has demonstrated that there is a bright future for 3D printed OECT based biosensors which will make a significant contribution towards the advancement of precision health.

Preface

The work presented in this thesis was carried out in the Department of Electrical and Computer Engineering at the University of Alberta between September 2016 and July 2021. Dr. Manisha Gupta conceptualized the research and initial methodology. All the fabrication, characterization, analysis, and review and editing of the manuscript were carried out by Jiaxin Fan unless specified.

In chapter 3, the material printing parameter optimization using both nScrypt 3D printing system and aerosol jet 5X system, the material characterization, and data analysis were performed by Jiaxin Fan.

Chapter 4 of this thesis has been published as Jiaxin Fan, Carlo Montemagno, and Manisha Gupta "3D printed high transconductance organic electrochemical transistors on flexible substrates", Organic Electronics, vol. 73, 122-129. Jiaxin Fan conducted all the experiments and data analysis and wrote the original draft. Dr. Carlo Montemagno contributed to manuscript editing. Dr. Manisha Gupta helped with data analysis and review and editing of the manuscript.

Chapter 5 presents the device optimization for aerosol jet printed OECTs. All the OECT fabrication, device characterization, and data analysis were carried out by Jiaxin Fan.

The work presented in chapter 6 is part of the disposable Δ^9-THC biosensor project. Jiaxin Fan contributed to the fabrication of devices used for Δ^9-THC sensing, investigated sensing of Δ^9-THC in synthetic saliva buffer using aerosol jet printed OECTs, and analyzed the data.

Chapter 7 describes glucose sensing using OECTs with different functionalization

configurations. Jiaxin Fan conducted all the device fabrication, characterization, glucose sensing experiments, and data analysis. The AFM images presented in Appendix A were collected by Andres Alejandro Forero Pico and analyzed by Jiaxin Fan. The original draft of the manuscript was written by Jiaxin Fan. Dr. Manisha Gupta contributed to data analysis and manuscript review and editing. This manuscript has been accepted as J. Fan, A. A. Forero Pico and M. Gupta, "Aerosol Jet Printed OECT Functionalization Study for Glucose Detection", Materials Advances, 2021, DOI: 10.1039/D1MA00479D.

Chapter 8 presents biosensing using OECTs with NHC functionalized gate. This work is conceptualized by Dr. Manisha Gupta. Fabrication of the OECT and Au electrode, material and device characterization, investigation of click reaction and biosensing, and analysis of data were conducted by Jiaxin Fan. The NHC ligand synthesis and deposition were performed by Seongdae Kang. The NHC ligand synthesis and deposition conditions were initially optimized by Alexandra Predy under the supervision of Dr. Florence Williams.

The work presented in chapter 9 was conceptualized by Dr. Manisha Gupta. Jiaxin Fan designed and fabricated all the OECT devices, investigated and optimized the antibody functionalization, and performed all the characterization and data analysis. The software and hardware of the data processing circuit was developed by Sheldon Parr. Seongdae Kang helped with the antibody functionalization for clinical sample testing. Dr. Manisha Gupta supervised the work. The clinical sample testing was conducted in Alberta Provincial Lab.

Acknowledgements

First and foremost, I would like to express my most sincere gratitude and appreciation to my mentor and supervisor, Dr. Manisha Gupta, who has allowed me to start my research adventure. Her enthusiasm for research has consistently motivated me throughout my Ph.D. journey. Without her constant patience, support, and guidance, this thesis would not have been possible. I am especially thankful for all the freedom and learning opportunities she has given me, letting me grow and achieve.

Many thanks to my lovely labmates and friends, Dhanvini Gudi, Darren Majak, Seongdae Kang, Payel Sen, Dipanjan Nandi, Michael Facchini-Rakovich, Junsen Gao, and Andres Alejandro Forero Pico, for maintaining a positive and friendly working environment and always helping and supporting me. I would also like to thank Sheldon Parr who has made a great contribution to the development of the COVID-19 diagnostic tool. I will always miss the coffee, lunch, and ice cream time we spent together. Thank you all for making my Ph.D. experience so enjoyable.

I would like to thank my parents who always support me unconditionally. They have never put any pressure on me and give me the freedom to pursue whatever I enjoy doing. I am so grateful to have such loving and open-minded parents. Last but not least, I would like to thank my fiancé, Enyu Zhou, who has been supportive as always, tolerates my bad temper, and boosts me up when I am down. None of these would be possible without you. Thank you for being there for me.

I would also like to acknowledge the financial supports provided by the Queen Elizabeth II Graduate Scholarship, Natural Sciences and Engineering Research Council (NSERC) Postgraduate Scholarship, President's Doctoral Prize of Distinction from

the University of Alberta, and Alberta Innovates Graduate Student Scholarship and the MNT financial assistance for fabrication and characterization costs provided by CMC Microsystems.

Table of Contents

List of Tables

List of Figures

Chapter 1

Introduction

1.1 Motivation

Monitoring physiological changes provides critical health related information. Current healthcare practices are mostly centralized and reactive. Disease prevention, early diagnosis, and management usually rely on limited physiological information collected months and years apart [2]. These tests are often performed by trained healthcare workers and require complex laboratory equipment. The wearable biosensor is a rapidly growing field that aims to tackle these limitations of the healthcare system by providing individuals with insights into their physiology [3]. Frequent measurements of physiological parameters help to establish baselines and identify abnormal signals. Wearable devices are proven to be useful in the identification of early signs of Lyme disease and inflammatory responses [4].

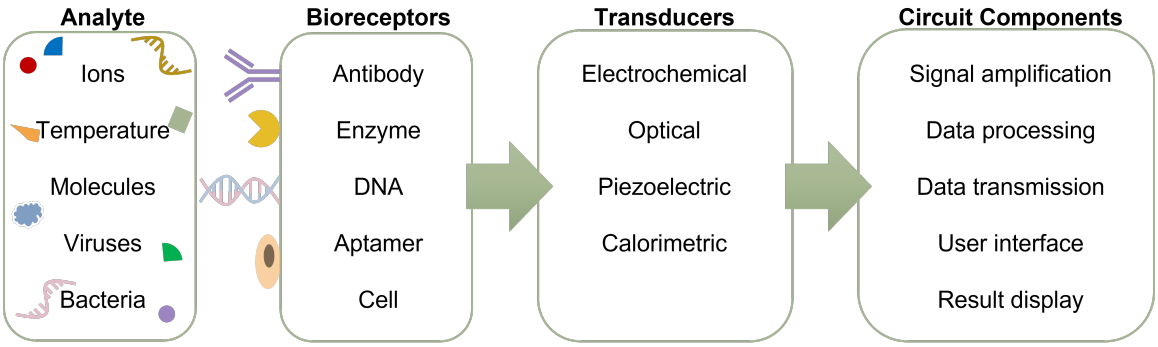

Figure 1.1: Schematic of the main components of a biosensing platform.

Over the past few decades, efforts have been devoted to the development of compact and affordable wearable biosensing platforms and point-of-care diagnostic tools. As shown in Figure 1.1, the three main components of a biosensing platform are the bioreceptor that directly interacts with the analyte, the transducer that converts the biological and chemical signal to electrical signal, and the circuit components for data processing and transmission. Among different types of transducers, electrochemical sensors have been widely used for biosensing applications. Electrochemical sensors are usually based on passive surface electrodes and use the three-electrode cell configuration that consists of a working, counter, and reference electrode. Usually, the biorecognition elements are immobilized onto the working electrode. The development of electrochemical sensors is relatively mature and many of them can be found in commercially available products. The surface electrodes are relatively robust, cover a reasonable detection range, and need simple electronic circuit components for readout [5, 6]. However, surface electrode based electrochemical sensors are restricted by their surface area. Small surface area increases the impedance and limits the active site for the interaction between the bioreceptor and the analyte. Therefore, there is a need for active components to be integrated into these sensing platforms.

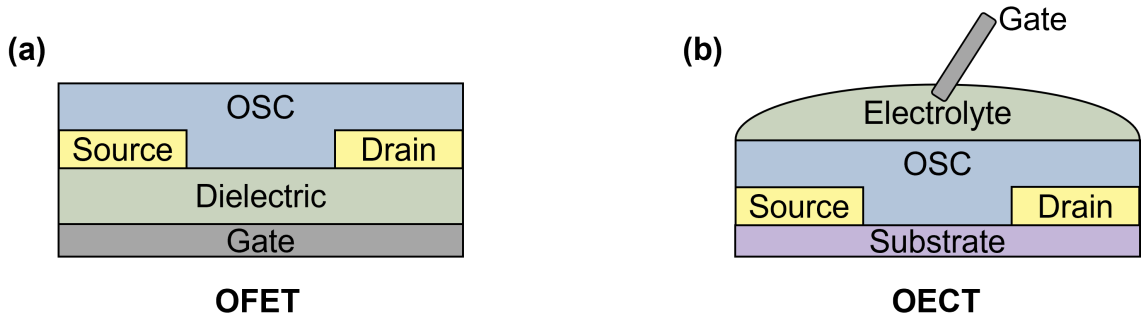

Figure 1.2: Schematic of (a) an OFET and (b) an OECT.

Field-effect transistor (FET) based sensors have been receiving increasing interest due to their intrinsic signal amplification. Conventional silicon-based transistors are usually rigid, use non-biocompatible materials, and have high processing and fabri-

cation cost. All these drawbacks could be overcome by utilizing organic semiconductors (OSCs). OSCs are mechanically flexible, biocompatible, solution-processable, and compatible with large-scale low-cost fabrication techniques. Their properties could be tuned by modifying chemical structures. Hence, organic thin-film transistors (OTFTs), such as organic field-effect transistors (OFETs) and organic electrochemical transistors (OECTs) are promising candidates for biosensing applications. The basic device structures of OFET and OECT are shown in Figure 1.2. The performance of OFET is greatly dependent on the OSC crystallinity, metal/OSC contact quality, and the OSC/dielectric interface quality. For OFET based biosensors, the biological and chemical signal is usually transduced into an electrical signal through the changes in the effective gate voltage and/or the charge carrier density near the OSC/dielectric interface, which is induced by the bioreceptor-analyte interaction. For OECTs, the dielectric layer is replaced by a liquid/gel electrolyte and the channel material is ion-permeable OSC. The operation of OECT relies on the bulk channel doping/dedoping modulated by the ions injected into the channel from the electrolyte. OECTs exhibit great stability in aqueous environments, require low operation voltages (usually less than 1 V) that prevent undesired redox reactions, and have high transconductance. In sensing applications, transconductance is directly correlated with the sensitivity [7]. These features of OECT make it more suitable for biosensing applications.

Even though OTFTs have been employed as transducers to detect various analytes, there is still room for improvement. Selectivity and sensitivity are the key parameters for evaluating the performance of a biosensor. To meet the demand for sensing the specific biological analyte, organic transistors need to be functionalized with biorecognition elements to improve the device-analyte interactions. The sites of modification and functionalization methods need to be considered for device functionalization [8]. Functionalizing the OSC layer is a widely used approach for improving selectivity and sensitivity [9]. This approach results in direct response to the interaction with the analyte, but certain immobilization techniques could damage the channel material

and lead to significant deterioration of device performance. Gate and dielectric functionalization are alternative approaches that improve the sensing selectivity without affecting the channel electrical properties. Different functionalization methods may be selected based on the modification site and the type of biomolecule that needs to be attached. It is important to establish strong and stable bonds between the biomolecule and the surface to ensure reliable sensor performance.

Another challenge for the commercialization of custom-designed biosensing platforms is the high fabrication costs. Most of the surface electrodes and electronic devices are still produced by conventional microfabrication methods in a cleanroom environment. Material patterning and deposition are performed as separate steps. Photolithography is the main technique used for material patterning. A photomask is required to transfer the designed patterns onto the substrate as photoresist patterns. Then a series of material deposition and chemical treatments, such as sputtering, etching, and liftoff, is carried out to produce the patterns of the desired materials. Microfabrication possesses several advantages. It is capable of producing high-quality materials and contacts with pattern size in the sub-nanometer range and provides precise control of the shape and size. Hence, with optimized designs and processes, microfabrication is cost-effective, as the desired patterns can be created over the entire substrate with a high density and batch processed. However, tailoring the biosensing platforms for precision health monitoring requires frequent change of the design, which requires a new photomask each time when using microfabrication and results in high time and material consumption. The invention of organic semiconductors paves the path for manufacturing electronics with low-temperature solution-processable techniques, such as spin-coating, drop-casting, and printing techniques. Creating electronics by diverse printing techniques has emerged as a new industry known as printed electronics. Different additive manufacturing technologies are utilized for printed electronics, where the material is deposited and patterned at the same time. Some commonly used printing techniques are screen-printing, gravure

printing, inkjet printing, and 3D printing. 3D printing is a digital process, in which a 3D model of the object is designed and sliced into layers using software, and the object is built layer by layer using different technologies, such as fused deposition modeling (FDM), stereolithography (SLA), flow-based direct writing, and aerosol jet (AJ) printing. A wide range of materials, including metals, semiconductors, and dielectrics, can be deposited by 3D printing. 3D printing is compatible with various flexible substrates and is possible for large-scale production. Moreover, the patterns can be easily changed by modifying the 3D model using CAD software. Even though the performance of printed devices may not be comparable to microfabricated devices, it is still sufficient for certain biosensing applications. Combining with the fast prototyping feature, this makes 3D printing an ideal technique for fabricating affordable customized biosensors.

The goal of this work is to optimize and functionalize 3D printed OECT biosensors that can be integrated into portable biosensing platforms. OECT is chosen as the transducer due to several advantages. OECTs have a simple device structure that is desired for in-expensive printing techniques. Moreover, OECTs demonstrate high intrinsic signal amplification with low operation voltages and compatibility with aqueous media, which are the key requirements for biosensing application. To fulfill the goal and address the challenges mentioned above, the first step is to select suitable materials for printing OECT and optimize the printing and processing parameters. Understanding the influences of geometry on electrical characteristics provides more insightful information for choosing suitable device designs for specific sensing applications. OECTs have intrinsic ion sensitivity, and certain molecules could be detected by simply changing the gate material. However, functionalization is still critical to expand the sensing capability and improve the selectivity of OECTs. To develop various biosensors, both physisorption and chemisorption are utilized in this work to modify the printed OECTs. Optimization of the device functionalization is based on the choice of modification sites, the amount of material for the reaction, and adequate

surface area for biomolecule immobilization and/or desired electrochemical reactions. This work contributes to the development of affordable biosensing platforms.

1.2 Outline

This thesis is organized into 10 chapters, beginning with the motivation of the work in chapter 1.

Chapter 2 is the background chapter. In this chapter, a brief introduction of the existing biosensor technologies, the working principle, materials, and fabrication methods of OECTs, and surface functionalization techniques are presented with relevant literature.

Chapter 3 explains the material selection for both nScrypt and Optomec AJ5X 3D printing systems and the important processing parameters for each system. The optimized printing and annealing parameters for each material that is used to build OECT in the later chapters are presented in this chapter.

Chapter 4 reports the development of fully printed OECTs by using the nScrypt 3D printing system. The device performances of OECTs assembled on different flexible substrates are compared. These printed OECTs demonstrated intrinsic ion and pH sensitivity.

Chapter 5 presents the optimization of aerosol jet printed OECTs with two different contact materials, Ag and Au. The influences of device geometry on the device performance were studied. The optimized OECT designs were used for developing sensors in the later chapters.

Chapter 6 demonstrates molecular detection with AJ printed OECTs. An unfunctionalized OECT was used to sense the faradaic current induced by the electrooxidation reaction of Δ^9-THC molecules at the Pt gate electrode. Spike tests were conducted with Δ^9-THC dissolved in synthetic saliva buffer. The Δ^9-THC concentration correlated with the change of drain current. This chapter demonstrates the potential of using AJ printed OECTs as disposable salivary Δ^9-THC sensors.

Chapter 7 reports the functionalization study of glucose sensors based on AJ printed OECTs. The glucose oxidase enzyme was physically adsorbed onto OECT to detect the glucose concentrations. Four different functionalization configurations were used to study the effects of functionalization sites and the benefits of using biomaterials and nanomaterials.

Chapter 8 presents a biosensor platform based on AJ printed OECT and an external printed Au gate functionalized with alkyne-NHC. The deposition of alkyne-NHC was confirmed by various methods. Biotin molecules were immobilized onto the Au electrode surface via click chemistry. Biosensing was demonstrated by detecting streptavidin-biotin binding.

Chapter 9 describes the development of an OECT based rapid COVID-19 diagnostic tool. The biosensor was based on an AJ printed OECT with an in-plane Au gate functionalized with SARS-CoV-2 antibody via chemisorption. The antibody-antigen binding was used to detect the presence of the virus. A custom designed circuit was integrated for user interface, signal processing, and data collection.

Chapter 10 summarizes the primary outcomes and presents the future perspectives of this thesis.

Chapter 2

Background

2.1 Biosensors

Biosensors have demonstrated their potentials in the applications of various fields, including agriculture, environmental monitoring, food industry, and medical science. Biosensors are compact analytical tools that convert biological signals into measurable electrical signals [10, 11]. The three key components of a biosensor are the biorecognition elements integrated on the biosensor surface for recognizing the target analyte, the transducer component that is responsible for the transduction of the biological response into an electrical signal, and the electronic system for the signal amplification and processing, the data transmission, and the result display. The development of biosensors is multidisciplinary research that requires knowledge and expertise from biology, chemistry, and engineering [12]. Flexible and wearable biosensors have gained increasing attention in healthcare applications ranging from rapid disease diagnostics [13, 14], continuous monitoring of chronic diseases [15–18], to the controlled delivery of therapeutic drugs [19, 20].

In the traditional clinical settings, blood and urine samples are collected routinely and then analyzed by trained workers using bulky and expensive analytical instruments. As the level of the analyte of interest is not continuously monitored, some changes may not be accurately captured. In addition, numerous medical diagnoses are based on blood and urine samples, which are not suitable for long-term continu-

ous monitoring. Wearable biosensors are capable of real-time quantification of critical biomarkers and metabolites. Tremendous efforts have been made towards developing wearable biosensors for the non-invasive detection of biomarkers in different body fluids, such as saliva, sweat, tear, interstitial fluids, and breath. Wearable biosensors offer more dynamic information about the target analytes and a wide range of health conditions, and hence are considered as important tools for future deployment of precision health which will reduce healthcare system burden by promoting decentralized healthcare delivery [21–24]. There are unique challenges in developing flexible biosensors for wearable personal health monitoring. The transducer is assembled on a substrate with bioreceptors specific to the analyte of interest immobilized onto the transducer. In order to use the flexible biosensor for healthcare monitoring, it should selectively detect the target analyte with linearity in the desired concentration range. The substrate selection is an essential step for fabricating wearable biosensors, as it forms the foundation and the primary mechanical support of the entire system [21, 22]. The materials selected for the transducer should be susceptible to the same mechanical deformation as the substrate without delamination and performance deterioration [25]. Therefore, all elements of the biosensor should have desired stability, mechanical flexibility, and biocompatibility, preventing undesired interaction and damage to the surrounding physiological environment.

Among different types of biosensors, electrochemical biosensors have been most studied for wearable applications due to their unique properties. Electrochemical biosensors usually consist of a working, reference, and counter electrodes. The working electrode is the site of signal transduction, the reference electrode serves as a potential reference point, and the counter electrode is used to complete the electrical circuit such that the current can flow between the working and counter electrodes and be recorded. The analyte detection is achieved by sensing the local impedance or potential changes induced by the electrochemical reactions at the working electrode surface. The electrode material, surface modification, and electrode dimension have

great influences on biosensor performance. However, using this type of electrodes for recording physiological and biological signals is often challenging and requires external amplification [26, 27]. Therefore, various types of transducers have been explored for electrochemical biosensors.

2.2 Organic Electrochemical Transistor (OECT)

Organic thin film transistors (OTFTs) have attracted considerable attention in the recent few decades for a wide range of applications, especially in the field of chemical and biological sensing, as they have unique properties such as solution processability, mechanical flexibility, and lightweight. Two main types of OTFTs that have been extensive studies for biosensing applications are organic field effect transistors (OFETs) and organic electrochemical transistors (OECTs). Both these devices are three terminal devices with source, drain, and gate electrodes and show similar current-voltage (IV) characteristics as metal-oxide semiconductor field effect transistors (MOSFETs). For a conventional OFET, the source and drain contacts are connected by an organic semiconductor (OSC) channel, and the gate electrode is separated from the channel by a thin dielectric layer. The channel current of an OFET is modulated by the gate voltage through field-effect doping which only happens near the interface of the OSC and the dielectric. Similar to MOSFETs, the capacitance of gate dielectric and the interface quality have significant impacts on the performance of OFETs. Electrolyte-gated organic field-effect transistors (EGOFETs) are a special type of OFET. In this case, an electrolyte is used instead of the gate dielectric layer. EGOFETs operate similarly to the conventional OFETs. Upon the application of a gate voltage, electric double layers (EDLs) form at both the gate/electrolyte interface and the electrolyte/OSC interface. These EDLs can be viewed as nanometer-thick capacitors which result in a much larger overall gate capacitance as compared to the capacitance obtained by conventional gate dielectric materials [28]. The polarization of the electrolyte induces a large electric field near the surface of OSC, leading to

the accumulation/depletion of charge carriers in the OSC. EGOFETs operate with low voltages as a result of the enhanced gate capacitance and charge carrier density [29]. For an OECT, an ion-permeable electroactive conducting polymer film is used as the channel material connecting the source and drain electrodes, and an electrolyte medium is used between the channel and the gate electrode. In contrast to OFETs, upon the application of a gate bias, the ions in the electrolyte are driven into the channel film, and this process modulates the channel current due to reversible electrochemical doping/dedoping of the bulk conducting polymer film. This bulk gating effect results in both low operation voltage and high capacitance [30]. The biosensors in this thesis were developed using OECTs through various device configuration and functionalization techniques, as OECTs have a simple device structure that is compatible with printing techniques, operate stably in aqueous media with low voltages, and show high transconductance.

2.2.1 OECT Working Principle

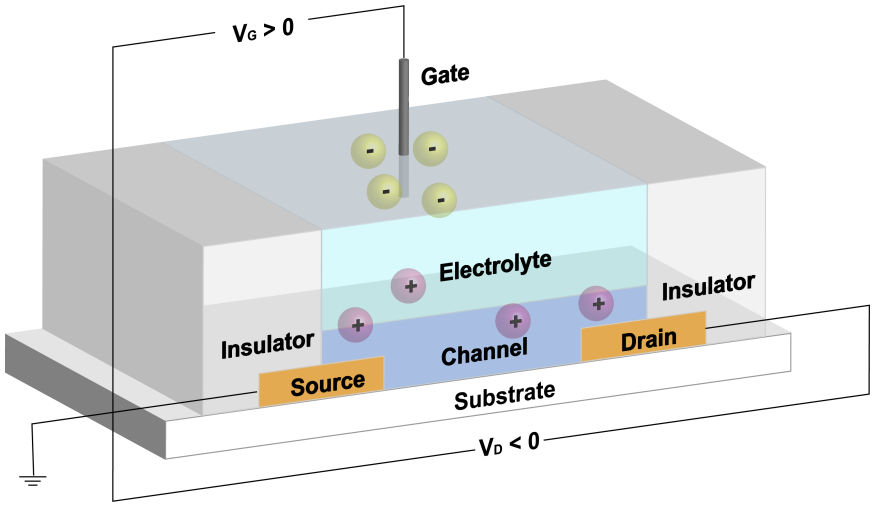

Figure 2.1: Schematic of a p-type OECT.

Figure 2.1 shows the schematic of a p-type OECT. The device physics of a p-type depletion mode OECT has been explained by Bernards *et al.* [31] and Friedlein *et al.* [32]. This model provides a quantitative way to predict the OECT's behaviors.

According to the Bernards model, an OECT can be viewed as an electronic circuit, which describes the electronic charge flow obeying Ohm's law, and an ionic circuit, which describes the flow of ions. The electronic circuit is considered as a resistor, and the drift of electronic charges in the channel is affected by the local potential, which behaves similarly to the charge drifts in MOSFET. The ionic circuit describes the ionic charge transport in the direction of the gate, electrolyte, and channel, which is modeled as a capacitor connected in series with a resistor [32]. The resistor describes the ionic strength and conductivity of the electrolyte, and the capacitor describes the polarization at the gate/electrolyte and channel/electrolyte interfaces. The source and drain electrodes form contacts with the channel, in which an electric current flows in response to a potential difference. Conventionally, a voltage is applied to the drain contact across the grounded source contact (V_D). The potential applied at the gate electrode (V_G) modulates the channel current (I_D) by changing the doping state and the conductivity of the channel material. When applying a negative drain voltage ($V_D < 0$) and zero gate voltage ($V_G = 0$), the device is ON. When a positive gate voltage ($V_G > 0$) is applied through the electrolyte, the cations in the electrolyte are driven into the porous channel film and compensate for the negative charges on the PSS chain. To maintain the charge neutrality, the hole density within the channel reduces, and therefore, I_D decreases due to the reduction in channel conductivity, which turns the device to its OFF state [31]. The steady-state characteristic of OECT are similar to that of a MOSFET. Therefore, the dependence of I_D as a function of V_G could be expressed in the following form:

$$I_D = \frac{Wd}{L}\mu C^*(V_T - V_G + \frac{V_D}{2})V_D \tag{2.1}$$

where W, L, and d is channel width, length, and thickness, respectively. μ is hole mobility. C^* is the capacitance per unit volume that could be extracted from the transient current response. V_T is the threshold voltage. At saturation, where $V_D =$

$V_G - V_T$, the saturation current ($I_{D,SAT}$) could be expressed as follows:

$$I_{D,SAT} = \frac{Wd}{2L}\mu C^*(V_T - V_G)^2 \tag{2.2}$$

where the symbols have the usual meanings as described above. The magnitude of I_D is directly proportional to both the channel width to length ratio and the channel thickness, which is different from the behavior of MOSFET. The dependence of drain current on channel thickness is a unique property for OECT due to the ion penetration from the electrolyte which changes the conductivity of the entire channel film [33].

Transconductance (g_m) is an important parameter for OECT characterization and defined as $g_m = \Delta I_D/\Delta V_G$. It describes how much the change in the gate voltage is reflected on the change of drain current, and therefore it determines how effectively the chemical or biological signal is transduced into an electrical signal for sensing applications. The transconductance of an OECT is expressed as follows:

$$g_m = \frac{Wd}{L}\mu C^*(V_T - V_G) \tag{2.3}$$

where the symbols have the same meanings as described above. Rivnay *et al.* have compared the performances of OECTs with different channel thicknesses and demonstrated that the OECT's transconductance is directly proportional to the channel thickness due to the increase in the channel capacitance [33]. The large volumetric capacitance also results in high transconductance at low operation voltage. The value of C^* is estimated by the amount of charge injected (Q) when a pulsed gate voltage is applied. Channel current transient response can be used to estimate the time constant (τ) of an OECT. Even though devices with a thicker channel have higher transconductance, they also show a slower response time [33]. Therefore, the channel dimension needs to be taken into consideration when designing devices for different applications.

Even though the model of OECT is based on a p-type depletion mode device, generally, the OECT could be either p-type or n-type and either depletion mode

(normally ON) or accumulation mode (normally OFF) based on the properties of the channel material.

2.2.2 OECT Materials

Substrate

The choice of substrate is crucial to the device fabrication, as the substrate is the foundation on which the biosensor is constructed [25]. To develop flexible biosensors, the substrate should have good mechanical flexibility, chemical compatibility with the wet processes, and thermal stability to withstand the processing and annealing temperatures. Moreover, strong adhesion between the deposited materials and the substrate is necessary. For OECTs, the substrate should be electrically insulating and non-electroactive. Since biosensing requires the direct contact of the devices with the physiological environments, the substrates should also have excellent biocompatibility and not induce any toxic effects to the surrounding biological system during testing [34]. Parylene C is a semi-crystalline polymer and has been widely used as the substrates for microfabricated OECTs due to its mechanical flexibility and biocompatibility [7, 35]. By carefully controlling the deposition parameters, parylene C films of only several micrometers thick could be achieved and have been used to fabricate ultra-flexible bioelectronic devices. Owing to the low temperature processability of conducting polymers, paper and plastic films can also be used as the substrates for OECTs. Some popular plastic substrates are polyethylene terephthalate (PET) [36, 37], polyimide [16, 38], polyethylene naphthalate (PEN). Silk fibroin [39], textile [40], and paper [41] substrates have also been used for developing flexible OECTs.

Channel Materials

The channel of an OECT typically consists of conducting polymers that are based on π-conjugated systems. A conjugated polymer is characterized by a backbone of alternating single and double bonds, which contribute to the optical, electrochemical,

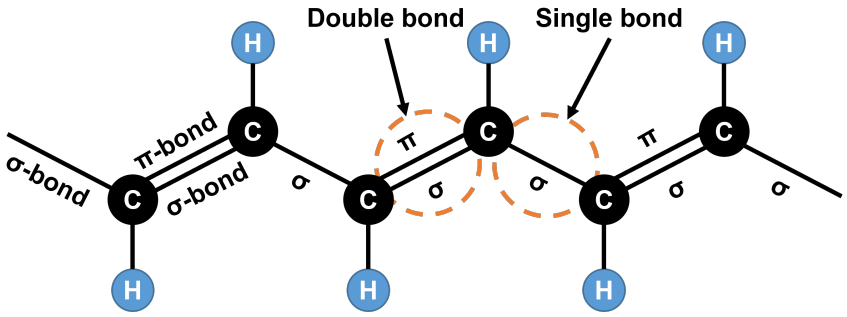

Figure 2.2: Chemical structure of polyacetylene demonstrating π- and σ-bonds.

and electrical properties. Polyacetylene (Figure 2.2) is the first synthesized conducting polymer discovered by Ito *et al.* [42]. Polyacetylene is used as an example here to illustrate the conduction principle in conducting polymers. The carbon atoms on polyacetylene are sp^2-hybridized. Each carbon atom has four valence electrons, three sp^2-orbitals form a triangular plane, and the remaining p_z-orbital is oriented perpendicular to the plane. The overlap of the sp^2-orbitals from two adjacent carbon atoms forms a σ-bond, and the overlap of the p_z-orbitals forms a π-bond. σ-bonds constitute the backbone of the π-conjugated polymer, and due to the large energy gaps present between the occupied bonding orbitals and the empty anti-bonding orbitals, the electrons from σ-bonds are usually localized and do not contribute to electrical conduction. Therefore, σ-bonds are more stable and hold the molecular structure together. Whereas for π-bonds, there are smaller energy gaps between the bonding and anti-bonding orbitals. Therefore, π-electrons are more likely to be delocalized and contribute to the electrical conducting property. Similar to inorganic semiconductors, conducting polymers have very low conductivity when they are not doped. A conjugated polymer can be either in its oxidized state, known as p-doped, or reduced state, known as n-doped. Moreover, the channel material needs to have both electrical and ionic conductivity for OECTs to function properly. To be used as the channel for an OECT, the material should be ion permeable and can be electrochemically doped/dedoped when interacting with the ions from the electrolyte. The first OECT was demonstrated by White *et al.* [43] with polypyrrole (PPy) (Figure 2.3 (a)) as the

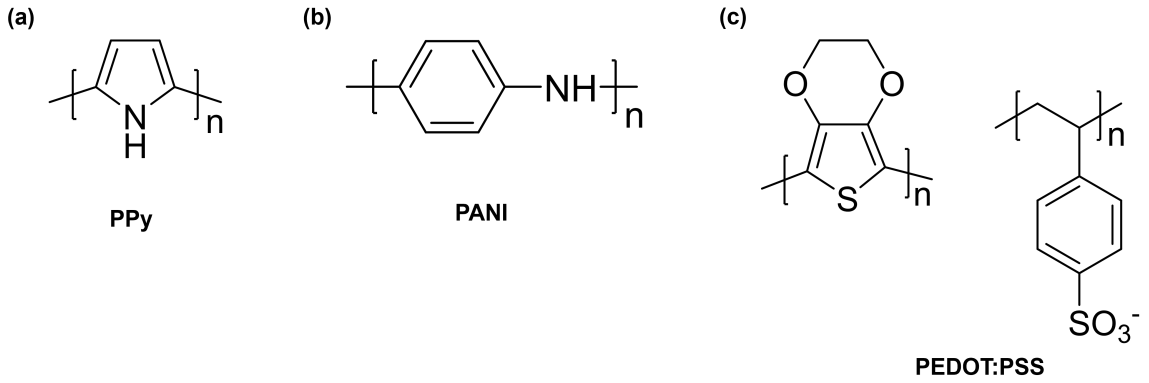

Figure 2.3: Chemical structures of p-type conducting polymers.

channel material. PPy based OECTs are p-type accumulation mode devices. When a negative gate voltage is applied, anions in the electrolyte penetrate the channel film and oxidize PPy to its doped state as shown in the following chemical reaction:

$$PPy + Y^- \Longleftrightarrow PPy^+ : Y^- + e^- \tag{2.4}$$

where Y^- is the anion from the electrolyte [44]. The conductivity of PPy is sensitive to pH. Nishizawa *et al.* utilized the pH sensitive property of PPy and developed a penicillin sensor [45]. The development of PPy based OECT is relatively slow as compared to the other channel materials mainly due to its poor electrochemical and chemical stability [46]. PPy loses its conductivity when being over-oxidized either by the application of a high positive potential (>0.5 V vs saturated calomel electrode (SCE)) or the exposure to water and oxygen, which leads to the device deterioration [47].

Polyaniline (PANI) is another p-type conducting polymer that has been investigated as the channel material for OECT, and its chemical structure is shown in Figure 2.3 (b). PANI has three redox states: a fully reduced leucoemeraldine state, a partially oxidized emeraldine state, and a fully oxidized pernigraniline state. Both the fully reduced leucoemeraldine state and oxidized pernigraniline state are the dedoped forms of PANI. The conductivity of the neutral emeraldine base is lower than 10^{-10} S/cm. Upon protonation, the insulating emeraldine base becomes a conducting

emeraldine salt with a conductivity increase to $\sim$ 100 S/cm [48]. Similar to PPy, PANI is also sensitive to the electrolyte pH. One major drawback of PANI is the loss of conductivity when pH is above 5.5, which limits the biosensing capability of PANI based OECTs [44, 49]. Several strategies have been employed to overcome this issue. By incorporating poly(styrenesulfonate) as the counter-ion, Bartlett *et al.* were able to extend the working range of PANI film to neutral pH [50]. Raffa *et al.* demonstrated that by sultonation, the conductivity of PANI at low pH was unaffected and at neutral pH was dramatically improved [51].

The most popular channel material for OECTs is poly(3,4-ethylenedioxythiophene) polystyrene sulfonate (PEDOT:PSS) due to its high conductivity (up to $\sim$1000 S/cm), high stability, and commercially availability [44, 46, 52]. PEDOT:PSS as shown in Figure 2.3 (c) is a polymer mixture consisting of the conjugated polymer PEDOT and the dopant PSS. The sulfonate groups (SO_3^-) on the PSS chain act as acceptors for the holes to form in the PEDOT backbone. When PEDOT:PSS is used as the channel of OECT, the cations in the electrolyte can enter the polymer film and compensate for the negative charges on the PSS chain to reduce PEDOT from its highly conducting oxidized state ($PEDOT^+$) to its less conducting neutral state ($PEDOT^0$). The process is shown in the following reaction:

$$PEDOT^+ : PSS^- + M^+ + e^- \Longleftrightarrow PEDOT^0 + M^+ + : PSS^- \tag{2.5}$$

where M^+ is a cation from the electrolyte and e^- is the charge injected from the drain. This process is well observed in the experiment as a color change from light blue (oxidized state) to dark blue (neutral state). Moreover, PEDOT:PSS is commercially available as aqueous dispersions and is compatible with various thin film deposition methods using solution processing techniques [53].

Compared to the p-type conducting polymers, the development of n-type conducting polymers is relatively slow, as n-type conducting polymers are usually unstable and degrade rapidly with the presence of oxygen and water. OECT based on n-type

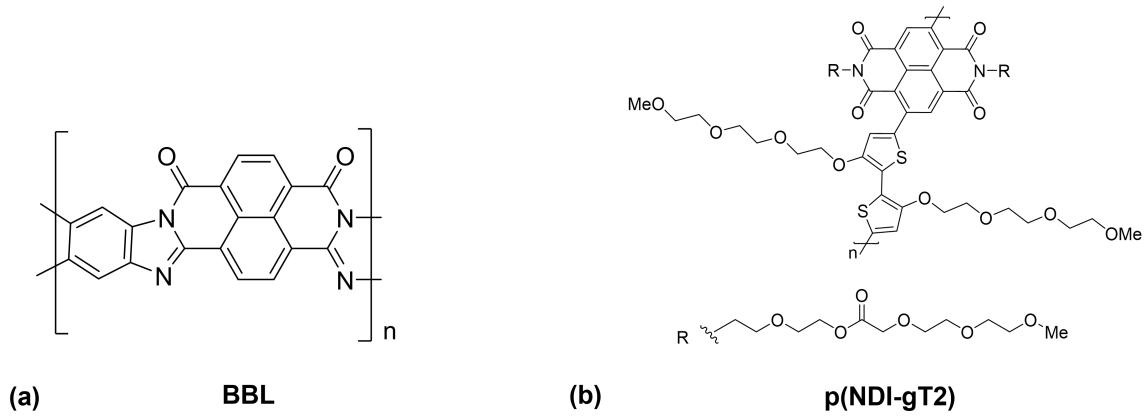

Figure 2.4: Chemical structures of n-type conducting polymers.

channel material showing water stability was first demonstrated by Giovannitti *et al.* in 2016, and the active material is a donor–acceptor-conjugated copolymer based on the electron-rich thiophene and the electron-deficient 2,6-dibromonaphthalene-1,4,5,8-tetracarboxylic diimide-co-monomers p(gNDI-gT2) [54]. The structure of p(gNDI-gT2) is shown in Figure 2.4 (a). When p(gNDI-gT2) is doped by an electrolyte (100 mM NaCl) under the presence of oxygen, both holes and electrons can be transported along its backbone. OECT based on p(gNDI-gT2) exhibits ambipolar properties. When negative drain and gate voltages are applied, the OECT behaves as an accumulation mode p-type device, and holes are the main charge carriers. Whereas when positive drain and gate voltages are applied, electrons are the main charge carriers, and the OECT works as an n-type accumulation mode device [44, 54].

Sun *et al.* have demonstrated the use of poly(benzimidazobenzophenanthroline) (BBL) as the active material for high-performance n-type OECT [55]. BBL is classified as a ladder polymer based on its double-stranded and highly conjugated macromolecular structure as shown in Figure 2.4 (a) [56]. BBL has high electrical conductivity due to its highly planar backbone structure which promotes intramolecular charge transportation. Under positive drain and gate voltages, the cations in the electrolyte penetrate the BBL polymer film, and BBL is reduced to maintain charge neutrality. As electrons are the main charge carriers, an increase in the drain current

is expected. Therefore, an increase in the applied gate bias leads to an increase in the drain current, and the OECT based on BBL is an n-type accumulation mode device. High electrical conductivity along with high electron affinity of BBL results in high transconductance (up to 9.7 mS) of BBL based OECTs [55]. High charge capacity of BBL also contributes to the high transconductance of BBL based OECTs. When compared to PEDOT:PSS, which has a volumetric capacitance of about 40 F cm^{-3}, BBL has a high C^* value of about 900 F cm^{-3} [57]. When compared to NDI based n-type conducting polymer, BBL does not require side chain modifications to improve its solubility, which increases the film crystallinity and the charge carrier mobility by decreasing the π-π stacking distance. However, the major drawback of using BBL as the channel for OECT is the poor ionic transport which limits the time constant of the device and results in a very slow switching speed [44, 55].

Gate Materials

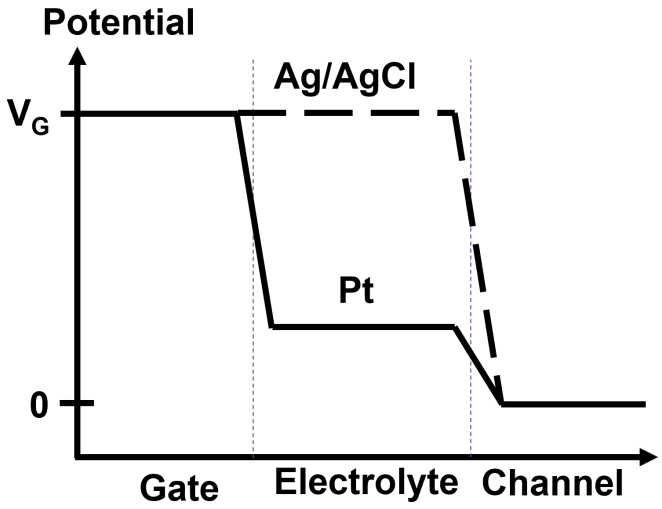

Figure 2.5: Schematic of the potential profile across the gate, electrolyte, channel direction for an Ag/AgCl and Pt gate electrode.

As a result of gating through an electrolyte, the property and geometry of gate material also affect the behavior of OECT [52]. Changing the gate material and size affects the potential distribution across the gate, electrolyte, and channel interface.

When a polarizable gate electrode, such as gold (Au) and platinum (Pt), is used, the capacitor (C_{eq}) in the ionic circuit model is equivalent to two capacitors in series corresponding to the electrical double layer (EDL) formed at the gate/electrolyte interface (C_{GE}) and the channel capacitance (C_{CE}). Their relationship is expressed in Equation 2.6. As the two capacitors are in series, the applied gate potential drops across the interface with lower capacitance. When a non-polarizable electrode, such as silver and silver chloride (Ag/AgCl), is used as the gate electrode, the electrons flow freely across the electrode surface and the electrolyte, and the potential drop at the gate/electrolyte interface is negligible. Figure 2.5 illustrates the potential profile across the OECT when using polarizable and non-polarizable gate electrodes.

$$\frac{1}{C_{eq}} = \frac{1}{C_{GE}} + \frac{1}{C_{CE}} \tag{2.6}$$

Several studies have demonstrated the effect of gate material on OECT's responses. Lin *et al.* [58] demonstrated that the transistor current modulation could be achieved either by redox reaction with the electrolyte (Faradaic regime) or by charging of ionic double layer (non-Faradaic regime). They have also observed that the gate capacitance affected the effectiveness of gating in the non-Faradaic regime. Tarabella *et al.* [59] have observed that the Ag gate electrode showed a larger channel current modulation as compared to the Pt gate electrode. This observation was attributed to the redox reactions that occurred between the Ag electrode and the halide electrolyte. In contrast, when using a Pt gate electrode in the same electrolyte, the process is non-Faradaic, and the potential acting on the channel is lower than the applied gate voltage resulting in less effective gating. Cicoira *et al.* [60] have studied the influence of relative gate size on the response of OECT working in both non-Faradaic and Faradaic regimes using planar Pt gates. They have found that with the same channel area, the device with smaller gate area shows higher sensitivity with lower background noise for detecting H_2O_2. Tang *et al.* [61] have demonstrated that the activated carbon gate electrode had higher current modulation as compared to the

PEDOT:PSS gate electrode of similar size, and this was attributed to the large specific area of activated carbon which leads to high specific double-layer capacitance and electrostatic charge capacity.

Pt electrode is electrocatalytically involved in different redox reactions. Utilizing the electro-oxidative properties, various molecules, including hydrogen peroxide (H_2O_2) [60], dopamine [62], and delta-9-tetrahydrocannabinol [63] have been detected using OECTs with unmodified Pt gates. Utilizing the catalytic effect of Pt on the decomposition of H_2O_2, enzymatic sensors based on OECTs for detecting glucose [64, 65] and lactate [16] have been developed. Due to excellent biocompatibility, structural versatility, and broad compatibility with functionalization techniques, Au has also been used as the gate material for integrating bioreceptors to develop OECT based biosensors [66–70]. Nanomaterials, such as metal nanoparticles [37, 71], TiO_2 nanotube arrays (TNTAs) [72], and carbon nanomaterials and composites [73, 74] have been incorporated to the gate of OECT for different sensing applications. Nanomaterials help to increase the area of the active site to promote the desired electrochemical reactions and thus improving the sensing range and sensitivity of OECT based biosensors.

2.3 Surface Functionalization

Surface functionalization is a critical step in constructing a biosensor. The incorporation of biorecognition elements onto the biosensor enables the effective detection of the analyte of interest. The selectivity of a biosensor relies on the specific affinity between the biorecognition element and the target analyte. Enzymes, antibodies, nucleic acid (DNA), aptamers, and molecular imprinted polymers (MIPs) are some examples of bioreceptors that have been explored for biosensing applications.

2.3.1 Bioreceptors

Enzymes are proteins with specific 3D structures acting as catalysts. Enzymes are capable of capturing and converting the target molecules into measurable products without being consumed [75]. One of the most studied enzymatic biosensors is the glucose sensor. Glucose oxidase catalyzes the oxidation of glucose molecules and produces hydrogen peroxide, which is then electrochemically detected. Enzymes are highly specific and their 3D structures need to be maintained to ensure proper function and activity. One of the common problems with enzymes as bioreceptor is the loss of catalytic activity after immobilization, which is mainly due to the binding site being blocked after attaching to the surface [76].

Antibodies are Y-shaped proteins that are typically around 150 kDa in size [77]. Antibodies share a similar structure that is consisted of fragment crystallizable (Fc) and fragment antigen-binding (Fab) regions. The Fc region interacts with the receptors on the cell surface, and the Fab region binds to the antigen [78]. The antibodies with a high affinity to a specific analyte are less likely to cross-react with other molecules, and this is an ideal property for biosensor integration. Therefore, antibodies have been widely used in the development of biosensors. Biosensors developed using antibody-antigen interaction are known as immunosensors. The major drawback of using antibodies is the high cost of production and purification process, which could also be complex and time consuming [77].

Genosensors are developed based on DNA complementarity. After identification of the target DNA sequence, the complementary DNA fragment can be synthesized and immobilized onto the transducer surface [79]. However, genosensors have limited application which is mainly focused on nucleic acid detection.

Aptamers are oligonucleotide or peptide molecules that are capable of binding to a broad range of analytes including metal ions, molecules, proteins, viruses, bacteria, and whole cells [80]. Aptamers can be synthesized in vitro with selective high affinity

to the target analyte [77]. Aptamer based biosensors are known as aptasensors and have gained increasing attention due to their high affinity, selectivity, and relative low-cost and easy fabrication process [5, 81].

Molecular imprinted polymers (MIPs) are synthesized using a template polymer matrix mimicking natural bioreceoptors to recognize the target molecules [77]. MIPs have been integrated with different transducers and demonstrated high sensitivity and selectivity [82]. As MIPs are synthetic biorecognition elements, they have great stability, reproducibility, and tunability [77].

In this thesis, we have selected enzymes and antibodies as the bioreceptors for developing OECT based biosensors due to their well-studied properties and commercial availability.

2.3.2 Functionalization Techniques

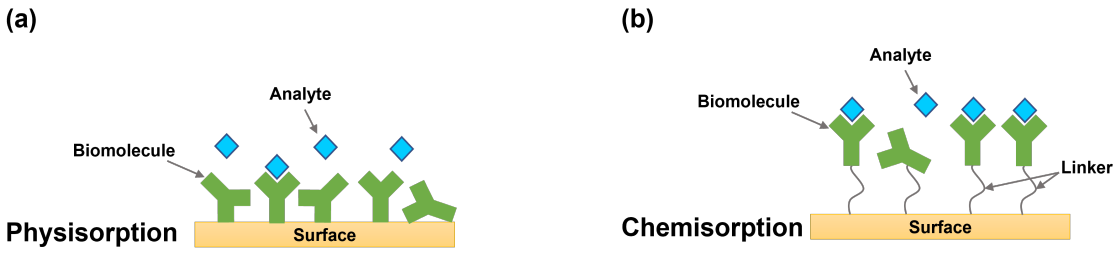

Figure 2.6: Schematic of (a) physisorption and (b) chemisorption.

Two main categories of functionalization techniques are physical adsorption (physisorption) and chemical adsorption (chemisorption). Physisorption is the simplest approach for biomolecule immobilization. In this case, the functionalization is achieved by immersing the surface in the stock solution containing the biomolecules for a certain period and washing the surface with buffer to remove the loose molecules. Since physisorption is a spontaneous process, the functionalities of the biomolecules are well preserved; however, the biomolecules are bound to the surface with only weak forces, such as electrostatic force due to hydrophobic interaction, Van der Waals forces, and hydrogen bonding. Physisorption is a reversible process. Change

in the environment temperature, pH, or ionic strength may lead to the desorption of the biomolecules, which induces errors and noises during sensing. The immobilized biomolecules are randomly oriented on the surface; hence the active site of the biomolecule may be blocked as shown in Figure 2.6 (a). Physisorption is non-specific to the biomolecule of interest; hence, other molecules in the electrolyte or the testing analyte could be immobilized onto the transducer surface and interfere with the signal transducing. Therefore, biosensors based on physisorption may suffer from high operational noise and low storage stability.

Chemisorption is a more prominent approach for surface functionalization. In contrast to the weak bonding of physisorption, chemisorption is characterized by the strong covalent bonding. The transducer surface is first activated with linker molecules containing functional groups such as amine, hydroxyl, thiol, and carboxylic groups, and then the biomolecules are attached to the linker and immobilized onto the surface as shown in Figure 2.6 (b). Biosensors modified via chemisorption are more stable, which is attributed to the strong binding between the biomolecule and the surface. Also, the immobilization and orientation can be controlled by modifying the biomolecules with specific functional groups, hence improving the specificity and homogeneity of the transducer surface, which benefits the development of multiplexed biosensing platforms. One of the major drawbacks of chemisorption is that the process may use harsh solvents and chemicals which could damage both the biomolecule and the device, leading to poor sensing performance.

2.3.3 Functionalization Site

For an OECT, bioreceptors can be immobilized onto either the channel or the gate region, as both surfaces are in direct contact with the electrolyte and the analyte. Functionalizing the channel provides a direct response when the analyte interacting with the channel. Various biorecognition elements have been conjugated to the channel of OECT for glucose [83], prostate specific antigen (PSA) [71], human influenza

virus [84], ions [85], and E. coli bacteria [86] detection. The major disadvantages of modifying the channel are that PEDOT:PSS has low biofunctionality that limits the molecule attachment, the channel conductivity may be disrupted after biomolecule immobilization, and the biomolecules may denature due to high-temperature curing [87].

Since the gate electrode is completely isolated from the channel, functionalizing the gate electrode does not affect the performance of the channel [8, 87]. Various functionalization materials and processes can be performed on the gate electrode without influencing the channel conductivity. There are more choices of gate material, and thus more functionalization techniques could be utilized [87]. Antibodies [67, 88], enzymes [73, 89, 90] , peptides [69], cells [91], DNA [68], aptamers [92, 93], and MIPs [70, 94] have been integrated to the gate of OECT to develop biosensors for various biosensing applications.

2.4 Fabrication Techniques

Most of the reported OECTs are fabricated by conventional microfabrication techniques. Advantages of microfabrication include the precise control of the feature size down to the submicron range, the high material quality for reliable contacts, and the reproducibility of device dimension and performance [95, 96]. Microfabrication requires expensive equipment and cleanroom facilities. Material deposition and patterning usually require separate steps. Patterning of the channel material usually requires special photoresists, as the standard materials and chemicals for photolithography damage the PEDOT:PSS films. Therefore, the fabrication cost of disposable OECT based biosensors when using microfabrication is still very high. Due to the solution processability of conducting polymer and the simple device structure, OECTs can also be fabricated using low temperature solution processing techniques, such as spin-coating and various printing techniques. Printing techniques, such as screen printing [36, 97–99], inkjet printing [100–102], 3D printing [103, 104], and aerosol

jet printing [63, 105], have been used for fabricating OECTs. These techniques are compatible with various substrates, and each layer of the material is deposited and patterned at the same time during the process. Printing techniques offer the advantages of more flexibility in device design, fewer fabrication steps, less material wastage, and possibility of large area continuous production using roll-to-roll processing. Therefore, utilizing printing techniques, without the need for cleanroom environment, greatly reduces the fabrication cost for manufacturing the OECT based biosensors.

2.4.1 nScrypt Printing System

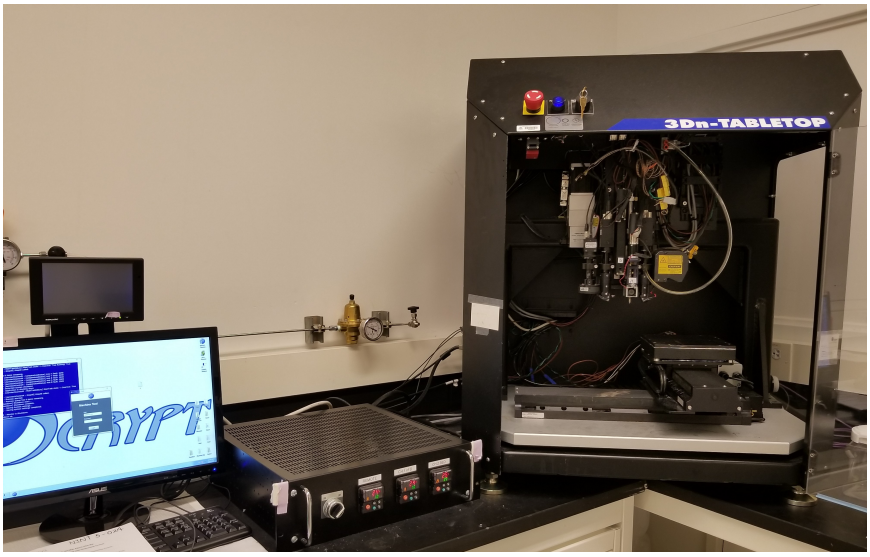

Figure 2.7: nScrypt 3Dn tabletop micro-dispensing and 3D printing system.

Some of the OECT devices described in this thesis were fabricated using nScrypt 3Dn tabletop micro-dispensing and 3D printing system, which is shown in Figure 2.7. This system is equipped with two pumps: SmartPump™ and nFD™ pump. SmartPump™ shown in Figure 2.8 utilizes flow-based direct-write technique, in which the fluid is pushed under a mechanical pressure through a ceramic nozzle with a micrometer-sized opening, and a continuous stream of ink is deposited onto the substrate. The amount of ink deposited is controlled by both the valve opening and

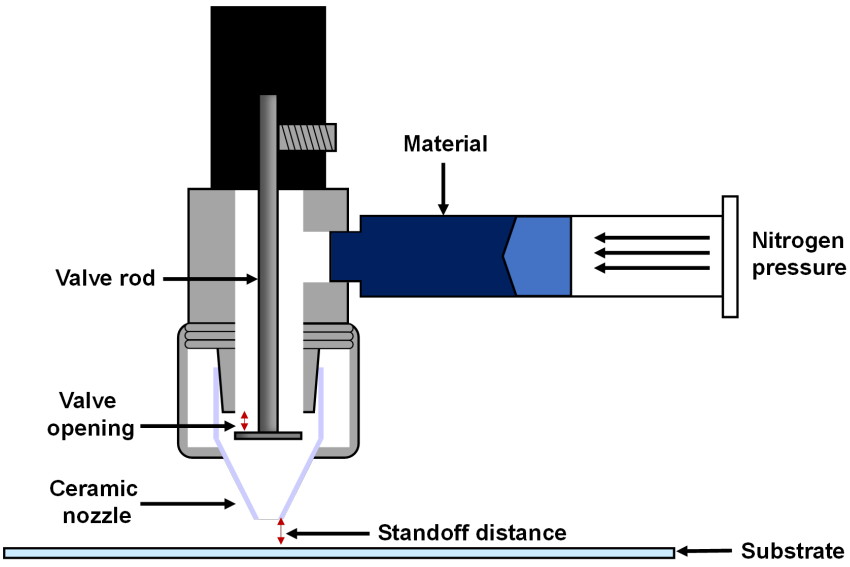

Figure 2.8: Schematic of flow-based direct writing used in the nScrypt 3D printing system.

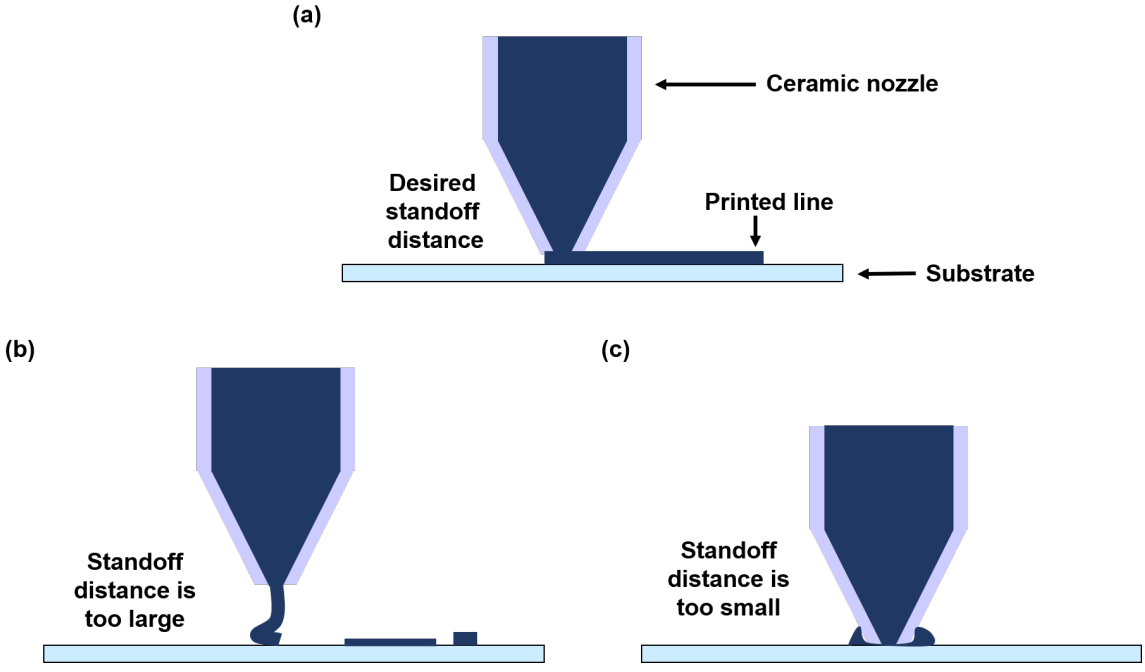

Figure 2.9: Schematic diagram illustrating the effect of standoff distance for nScrypt 3D printing system. (a) Desirable standoff distance. (b) Standoff distance is too high, and it results in discontinuous printed line. (c) Standoff distance is too small, which results in wider linewidth and non-uniform line surface.

nitrogen pressure for ink flow. The system is capable of printing inks with large viscosity ranges from 1 to 1,000,000 centipoise (cps). However, Smartpump™ is more

suitable for printing high viscosity inks, as inks with very low viscosity are more likely to overflow and spread. The ink surface tension and the substrate wettability are important parameters that influence the quality of the printing, and a high contact angle is usually preferred to maintain the printed linewidth. In addition, heating the substrate also helps to reduce the ink spread by accelerating solvent evaporation while printing. nScrypt provides ceramic nozzles with inner diameters (I.D.) ranging from 12.5 to 125 μm. The selection of nozzle size is based on material properties such as particle size, surface tension, and viscosity. The particle size is preferably more than 10 times smaller than the nozzle inner diameter to avoid clogging. Another key parameter for optimal printing results is the small distance between the nozzle and the substrate, also known as the standoff distance. It is crucial to set a suitable standoff distance for the desired amount of material to be uniformly deposited onto the substrate. The printed linewidth should be between the nozzle inner diameter and outer diameter. If the standoff distance is too large, it results in discontinuous ink deposition. When the nozzle is in direct contact with the substrate, both the nozzle and the substrate will be damaged. When the standoff distance is too small, the material is squeezed out of the outer diameter of the nozzle resulting in non-uniform lines that have thicker edge and are very thin or discontinuous in the middle. Occasionally, this can be resolve by reducing ink flow by lowering the nitrogen flow, adjusting the valve opening, or increase the printing speed. Therefore, for a uniform and continuous printed film, it requires the correct combination of the valve opening, the nitrogen pressure, the nozzle size, the standoff distance, the bed temperature, the speed of printing, and an adequate amount of line overlap. nFD pump is based on one of the most widely used 3D printing technology - fused deposition modelling (FDM). A thermoplastic filament is fed through a heated nozzle, and the 3D object is printed layer-by-layer. The extruder temperature, the filament feeding speed, the printing speed, the standoff distance, and the layer height are the key parameters to adjust for achieving optimal printing results.

2.4.2 Optomec Aerosol Jet 5X System

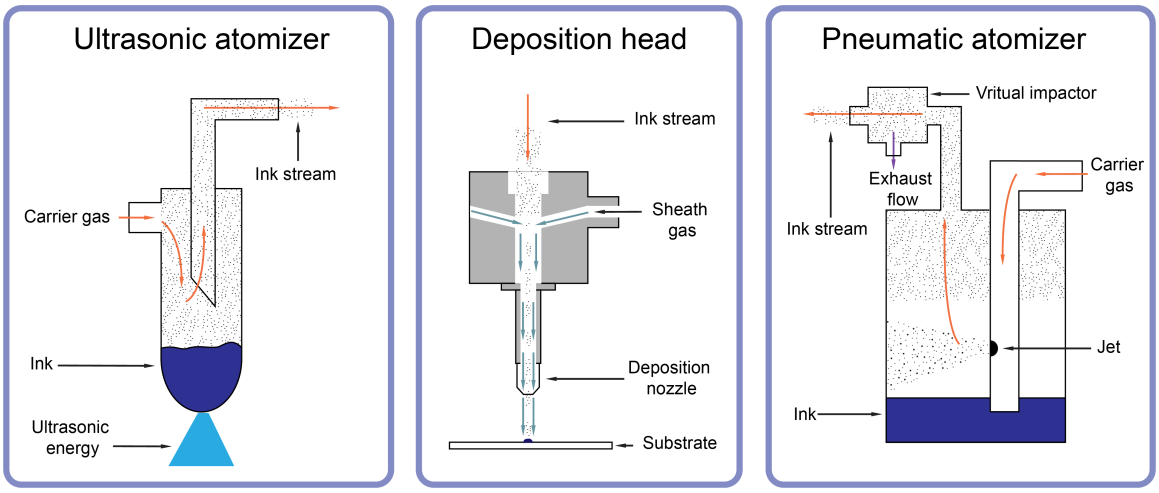

Figure 2.10: Schematic of the processes involved in aerosol jet printing.

Aerosol jet (AJ) printing is a non-contact direct-write 3D printing technique. Figure 2.10 shows an overview schematic of the processes involved in AJ printing. Submicron ink droplets are first generated by ultrasonic or pneumatic atomization. The ink stream is directed into the deposition head by a carrier gas flow. In the deposition head, the ink stream is then focused by a sheath gas flow to form a coaxial stream before being emitted through the deposition nozzle. This results in a concentrated ink stream with a width that is only a fraction of the nozzle orifice and reduces the chance of nozzle clogging [106, 107]. Inks, pastes, and particulate suspensions, having a particle size less than 500 nm and a viscosity range of 1 to 1000 cps, may be atomized and deposited by the AJ printing method. The majority of the devices in this thesis were fabricated using Aerosol Jet 5X (AJ5X) system manufactured by Optomec as shown in Figure 2.11. Optomec AJ5X is based on AJ printing technology and designed for 3D printed electronics. The system contains two different atomizers, an ultrasonic atomizer (UA) and a pneumatic atomizer (PA) for printing inks with various properties. UA requires only a small amount of ink (1 – 2 mL) and is capable of atomizing inks with a viscosity of lower than 10 cps. The ink is contained in a glass vial and positioned above a transducer in a water reservoir. The glass vial has

Figure 2.11: Optomec Aerosol Jet 5X system.

a very thin bottom wall to enable effective ultrasonic power transduction. The ink mist density is adjusted by both the ultrasonic vibration intensity and the water bath temperature. Inks with high vapor pressure solvents can be used on UA. Whereas PA is capable of atomizing inks with a viscosity up to 1000 cps, but a higher ink volume (10 – 30 mL) is needed for generating the aerosol. The fluid in the atomizer jar is sheared into small droplets by a high-velocity gas flow. As the gas flow rate for ink atomization is too high for the deposition head, the ink stream is directed through a virtual impactor where the ink stream is concentrated by removing excess atomization gas flow before entering the deposition head [108]. PA also has a heater band around the atomizer jar for reducing the ink viscosity and a magnetic stirrer for maintaining the ink homogeneity. Since a high gas flow rate is used for producing aerosols, solvents with low to medium vapor pressure are preferred on PA. High vapor pressure solvents lead to excessive drying of the ink, resulting in powdery deposition

with porous printed films. Therefore, in this thesis, UA was mainly used for printing low viscosity materials including metal inks for contacts and conducting polymer for channel, and PA was only used for printing the high viscosity material that is used as the insulating layer of OECT.

Depending on the ink properties and nozzle size, AJ printing is capable of printing features with a linewidth less than 10 μm and thickness less than 100 nm. Utilizing a coaxial sheath gas flow has provided unique advantages to AJ printing. The collimated aerosol flow has more tolerance in the standoff distance (1 - 5 mm), and this enables more flexibility in printing on non-planar substrates. In additions, unlike the techniques used by the nScrypt 3D printer where the printed linewidth is limited by the nozzle diameter, AJ printing is capable of controlling the printed line dimensions by changing the sheath and carrier flow rates without the need to switch nozzle [107, 109]. The quality of printed lines depends on multiple factors, including nozzle diameter, gas flow rates, printing speed, and printing bed temperature. One of the main goals of AJ printing parameter optimization is to minimize overspray and have a more defined edge. Overspray deposits are ink droplets with insufficient inertia and deviated from the center of the deposition. Overspray results in broadly distributed patterns near the edge of the printed pattern[106, 108]. Optomec AJ5X system also has built-in laser (830 nm) and UV-lamp (405 nm) for post-treatment of printed materials.

2.5 Characterization Techniques

2.5.1 Profilometry

Alpha-step IQ profilometer was used in this work to determine the thickness of printed films. This instrument is a stylus profilometer in which a probe moves across the surface of the sample to determine the sample height and roughness.

2.5.2 Four-Point Probe

Lucus Pro4 4000 sheet and bulk resistivity measurement system with Keithley 2601A sourcemeter was used in this work to measure the resistivity of the printed thin film samples. This equipment has four equally spaced probes where the current is sourced through the outer two probes and the voltage is measured by the inner two probes. The four-point probe setup is used to eliminate the effect of contact resistance to achieve more accurate measurements. The sheet resistance is measured by the four-point probe system, and the bulk resistivity and conductivity could be calculated based on the sample thickness.

2.5.3 Fluorescence Imaging

ChemiDoc MP Imager was used in this work to verify the surface functionalization. The samples modified with fluorescent molecules or fluorophores are first illuminated with light of a specific wavelength. An excitation filter is used to select the excitation wavelength from the broad spectrum of the light source. The fluorophores absorb the light of excitation wavelengths and emit light of longer wavelengths. An emission filter is used to block the exciting light and allow only the emitted light to pass, such that only the fluorescent objects are visible.

2.5.4 Keithley Sourcemeter

Keithley 4200SCS semiconductor characterization system and a Keithley 2612B dual channel sourcemeter were used in this thesis to measure the electrical characteristics of OECT devices. The sourcemeter is capable of precisely supply and measure a voltage and current simultaneously. The current voltage (IV) characteristics, transfer characteristics, and transient gate current of printed OECTs were measured using the Keithley systems.

2.5.5 Cyclic Voltammetry (CV)

CV is an electrochemical technique that is used to study the oxidation and reduction processes of molecules. All the CV measurements in this thesis were carried out using a Gamry Reference 600+ potentiostat and a three-electrode electrochemical cell configuration. The three-electrode setup consists of a working electrode, a Ag/AgCl reference electrode, and a Pt counter electrode. The potential is applied between the working and reference electrodes and changes linearly with time at a constant rate, and the current between the working and counter electrodes is measured.

2.5.6 Electrochemical Impedance Spectroscopy (EIS)

The same three-electrode setup used in CV measurement was also used for EIS measurements in this work. EIS applies a low amplitude alternating current (AC) potential at a wide range of frequencies, and the impedance spectrum of the electrochemical cell is obtained by measuring the magnitude and phase change of the current. The complex impedance can be presented as Bode and Nyquist plots. For a Bode plot, the magnitude and phase angle of impedance are plotted against the frequency. The complex impedance can be divided into real and imaginary components. In a Nyquist plot, the negative imaginary impedance is plotted against the real impedance. Each point on the Nyquist plot is corresponding to the impedance measurement at a different frequency. Electrode double layer capacitance, electrode kinetics, diffusion layer, and solution resistance are the common cell elements and characteristics that contribute to the measured impedance spectra. Equivalent circuit model fitting is the most common method used to analyze the EIS data. Common electrical elements such as resistors, capacitors, and inductors are used along with some specialized electrochemical elements to model the equivalent circuit.

2.5.7 Scanning Electron Microscope (SEM)

In SEM, the sample is scanned by a focused beam of electrons in a raster pattern. These electrons interact with the atoms in the sample, which produce signals that provide both morphological and compositional information about the sample. The secondary electron detector collects the secondary electrons emitted by the atoms that are excited by the electron beam. As secondary electrons have low energy, only electrons near the surface of the sample could escape and be collected by the detector. Therefore, secondary electrons provide morphological and topological information of the sample. Whereas back-scattered electrons have much higher energy than the secondary electrons, and they are used for demonstrating the contrasts of phases in multiphase samples. When the electron beam kicks out an inner shell electron from the sample, this leaves a hole that an electron with higher energy can fill. When the higher-energy electron fills the shell, it leads to the emission of characteristic X-rays that can be detected by energy-dispersive spectroscopy. These characteristic X-rays are unique to each element in the periodic table and can be used to identify the abundance and distribution of elements in the sample.

2.5.8 Fourier Transform Infrared (FTIR) Spectroscopy

FTIR spectroscopy is based on the principle that different bonds absorb light at different frequencies. FTIR measures the absorption infrared (IR) spectra which can be used to identify or quantify the material of the sample. In this work, an attenuated total reflection (ATR) accessory was used to measure the samples, and a diamond ATR crystal is used in the setup. The sample is placed on top of the ATR crystal with good contact. The ATR crystal has a higher refractive index than the sample. When the IR beam is directed onto the crystal at a certain angle, the IR beam is reflected internally, which creates an evanescent wave that penetrates a few micrometers into the sample. When the sample absorbs the IR energy, the evanescent wave will be attenuated, and this change is recorded by the detector by measuring the IR beam

exiting the opposite end of the crystal.

2.5.9 X-ray Diffractometer (XRD)

XRD is used to determine the crystal structure of materials. A monochromatic X-ray is incident onto the sample, and the intensities and scattered angles of the diffracted X-ray beam are measured. As the samples used in this work were mainly thin films, small incidence angles were used in the XRD measurement to avoid strong signals from the substrate. The interplanar lattice spacing (d) can be obtained from the peak of XRD data using Bragg's law:

$$n\lambda = 2dsin\theta \tag{2.7}$$

where λ is the wavelength of the incident X-ray. θ is the angle of incidence calculated from the peak position 2θ. n is an integer.

2.5.10 Atomic Force Microscope (AFM)

AFM is a sub-nanometer resolution surface scanning technique that is used to collect the topography information for the samples in this work. The AFM data is collected by scanning the surface of the sample using a cantilever with a very sharp tip attached to the end. The cantilever deflects when the tip contacts the surface, and the image is generated by measuring the cantilever deflection using various methods. AFM has different imaging modes that are classified based on the tip motion. Tapping mode was used to scan the printed thin films in this work to determine the surface roughness.

Chapter 3

Material Selection and Printing Optimization

In this chapter, the choice of materials and the printing processes developed using the two 3D printing systems, nScrypt and Optomec aerosol jet 5X, are described. The material selection and printing parameter optimization were based on the results of various material characterization techniques to achieve optimal properties for OECT development. This chapter starts with the choice of materials: substrate, metal inks for contacts, organic semiconductor inks for the channel, and insulators. Then the main process parameters for each system were described and optimized.

3.1 Material Selection

3.1.1 Substrates

As the goal is to develop fully printed flexible biosensors, the substrate should have good mechanical flexibility, chemical compatibility with the ink and solvents, and thermal stability withstanding the ink annealing processes. For OECTs, the substrate should be electrically insulating and non-electroactive. Substrate wettability is also important to improve the quality of printed features. A high contact angle is usually preferred to reduce the material spreading and achieve fine features.

For initial material testing conducted on both 3D printing systems, glass slides were used as the substrate due to their great chemical compatibility, capability to withstand

high temperature, and compatibility with various characterization techniques. To develop OECTs, printed polylactic acid (PLA), printed polydimethylsiloxane (PDMS), commercially available polyethylene terephthalate (PET), and commercially available polyimide (Kapton) substrates were investigated. On the AJ5X, only commercially available substrates, PET and Kapton, were chosen as the substrate for building printed OECTs.

3.1.2 Metal Inks for Contacts

Silver as opposed to gold, which is often used as the contact material in conventional microfabrication techniques to form high quality contact, was first chosen as the material for printing the source and drain contacts and the conductive traces. This is because bulk silver has a low resistivity of 1.59 x 10^{-6} Ω-cm [110], and it is a more economical option compared to gold, and there are many commercially available silver conductive inks. Another advantage is that silver inks usually require lower curing temperature (<200℃) which is more suitable for printing on flexible polymer substrates.

On the nScrypt printer, the initial trials were performed using water based silver conductive ink (WB-1075, Conductive Compounds, Inc.) that only needs a post-processing temperature of 100℃ . However, this ink did not provide the desired properties for printing. The ink dries while being printed, and this leads to frequent nozzle clogging. Hence, the water-based silver ink was not successfully printed. Then, DuPont CB028 silver conductive paste was tested on the nScrypt 3D printing system. DuPont CB028 is a screen-printing ink consisted of micron-sized silver flakes and polymer additives for enhancing flexibility. Due to the large flake size and high viscosity (15,000 – 30,000 cps), 125 μm (I.D.) nozzle was used for printing CB028. The nozzle size and large flake size limited the printed feature sizes and the printed film thickness.

On the Optomec AJ5X system, water-based Ag nanoparticle (NP) ink (Clariant

EXPT Prelect TPS 50G2) was initially used for making source and drain contacts for OECTs. The printing parameters were optimized based on the starter recipe provided by Optomec. Even though external wire electrodes have worked well as the gate electrode for OECT, in-plane electrodes are still needed to integrate the OECT based biosensors with other circuit components for developing biosensing platform. In this thesis, Pt NP ink (UT DOTS, Inc.) was used to print the in-plane gate electrode for OECT based glucose sensor. Due to the excellent chemical stability and biocompatibility of gold, Au NP ink (UT DOTS, Inc.) was used to print source, drain, and gate for the OECT based biosensors.

3.1.3 Organic Semiconductor Inks for Channel

In this thesis, only one channel material, PEDOT:PSS, was studied. PEDOT:PSS has demonstrated excellent stability in aqueous environments and is the most used channel material for OECT. On the nScrypt 3D printing system, ORGACON™ clear conductive screen-printing ink (EL-P 5015) was tested. This ink has high viscosity of >100,000 cps, and a proprietary ink recipe to prevent the dissolution of printed films. For the AJ5X 3D printing system, we have used PEDOT:PSS aqueous dispersion in water (Clevios PH-1000) due to its high conductivity. Two ink formulations were used for printing the channel in order to reduce the swelling of the PEDOT:PSS film. Ethylene glycol (EG) (Sigma Aldrich) was added to improve the conductivity of PEDOT:PSS. Dodecylbenzene sulfonic acid (DBSA) (Sigma Aldrich) was added to adjust the surface tension. (3-glycidyloxypropyl) trimethoxysilane (GOPS) (Sigma Aldrich) was added as the crosslinker to prevent the dissolution of PEDOT:PSS films. The two different recipes are listed in Table 3.1.

3.1.4 Insulators

The insulator passivates the source and drain contacts and prevents them from contacting the electrolyte. The insulator also helps to prevent oxidation and formation

Table 3.1: PEDOT:PSS ink recipes.

	PH-1000	EG	DBSA	GOPS
Recipe A	5 mL	1.25 mL	0.0125 mL	0.06 mL
Recipe B	5 mL	0.256 mL	0.0050 mL	0.05 mL

of tarnish for silver electrodes and traces. For nScrypt, PLA was used as the insulator for devices printed on PLA substrate to provide better adhesion. PDMS was used as the insulator for devices printed on the other type of substrates. For AJ5X, acrylic-based adhesive (Henkel Loctite AA 3104) and UV-curable PDMS (Shin-Etsu KER-4690A/B) were used as the insulator.

3.2 Printing Optimization

3.2.1 nScrypt

nScrypt 3Dn tabletop micro-dispensing and 3D printing system have two pumps: a Smartpump that is based on flow based direct write and an nFD pump that is based on fused deposition modeling. Some printing parameters affect printing results for both pumps and there are some unique parameters for each pump. The printing parameters for nScrypt are listed below:

1. Nozzle diameter – the opening diameter of the ceramic nozzle. It is selected based on the ink properties such as viscosity and particle size. The printed linewidth should be larger than the nozzle inner diameter (I.D.) and similar to the nozzle outer diameter (O.D.) for both pumps.

2. Dispensing gap – the small distance between the substrate and the nozzle. This parameter affects the continuity and shape of the printed traces for both pumps.

3. Valve opening – the distance of the valve rod moves. It controls the flow of ink for the Smartpump. A small valve opening limits the ink flow and a large valve opening allows more ink flow.

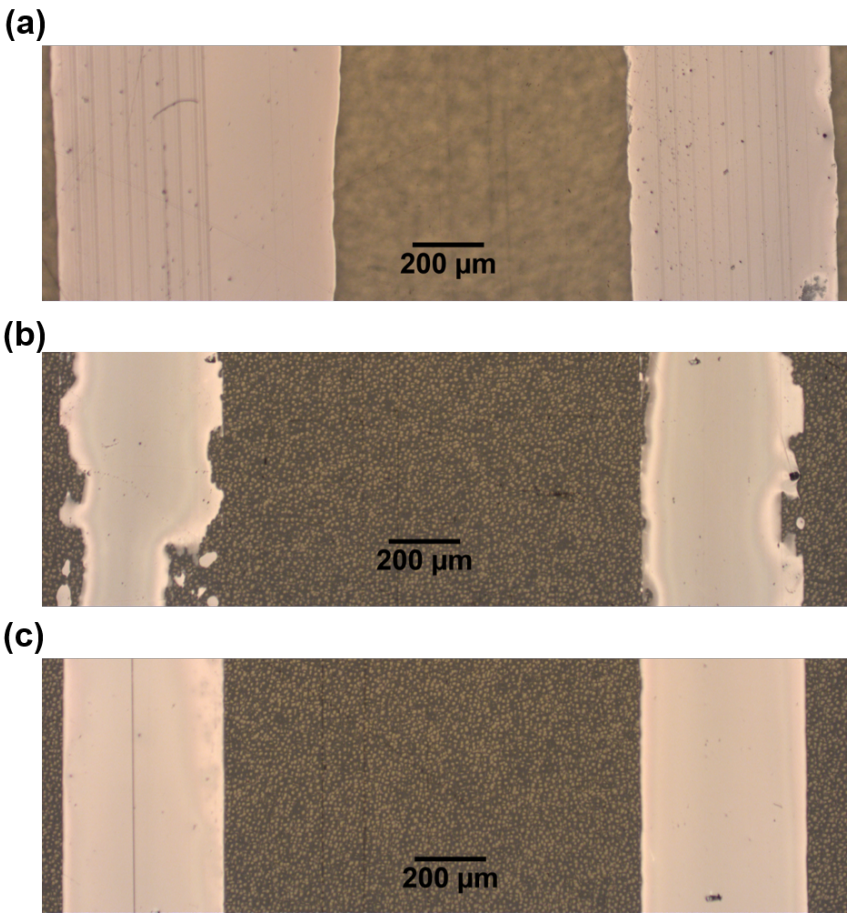

Figure 3.1: Microscope images of DuPont CB028 silver ink printed with the dispensing gap that is (a) too small, (b) too large, and (c) at optimal height.

4. Valve speed – the speed at which the valve rod moves to the open and close positions. This parameter affects the quality of the beginning and the end of the printed line. A slow speed may result in an insufficient material deposition for the beginning of the line and excess material deposition for the end of the line.

5. Nitrogen pressure – the carrier gas for feeding the material for the Smartpump. This pressure controls the material feeding speed. Higher nitrogen pressure is normally required to push more viscose material to the nozzle.

6. Printing speed – the speed at which the printer bed moves. This parameter controls the amount of material deposited and the printed line shape for both pumps.

7. Bed temperature – the printer bed temperature. Higher temperature helps

to reduce ink spread for the Smartpump. Heat printer bed also enhances the first layer adhesion and prevents material warping due to thermal contraction for the nFD pump.

8. Extruder temperature – nozzle temperature for the nFD pump. It is set to the printing temperature of the thermoplastics.

9. Filament feeding speed – the speed at which the filament is fed to the nozzle for the nFD pump. This parameter controls the amount of material extruded. This speed should be reduced for smaller nozzle diameters to avoid material overflow and tip damage.

For the Smartpump, dispensing gap, valve opening, and printing speed are the most important parameters to adjust to ensure that the deposited material forms uniform and continuous lines. For the nFD pump, dispensing gap, material feeding speed, and printing speed are the most critical processing parameters that need to be adjusted to achieve optimal printing results. To print continuous films, the pattern infill should be designed such that there is approximately 10% overlap between adjacent lines. The effect of dispensing gap is demonstrated in Figure 3.1, these silver traces were printed with DuPont CB028 ink and using the same printing parameters except different dispensing gaps. When the tip was too close to the substrate, it scratched the substrate, and this resulted in ink overflowed as shown in Figure 3.1 (a). When the dispensing gap was too large, the ink was unevenly distributed, and the printed pattern was discontinuous as shown in Figure 3.1 (b). Figure 3.1 (c) illustrates the desired printing results with an optimal dispensing gap along with material feeding and printing speed. The optimized printing parameters and annealing conditions for various materials are listed in Table 3.2.

As the materials selected for nScrypt have high viscosities and/or large particle sizes, the thickness of printed films was in the range of micrometers. These optimized printing and annealing conditions were used to fabricate OECTs in chapter 4.

Table 3.2: Optimized printing and annealing parameters for materials printed by nScrypt 3D printer.

	CB028	**EL-P5015**	**PDMS**	**PLA**
Pump	Smartpump	Smartpump	Smartpump	nFD pump
Tip size (I.D./O.D) [μm]	125/175	50/75	75/125	125/175
Dispensing gap [mm]	0.12	0.09	0.13	0.1
Bed temperature [℃]	R.T.	R.T.	45	70
Valve opening [mm]	0.08	0.06	0.06	-
Extruder temperature [℃]	-	-	-	230
Feeding speed [mm/s]	-	-	-	1
Printing speed [mm/s]	15	5	5	10
Infill [mm]	0.15	0.1	0.15	0.1
Annealing conditions	1 hr at 160℃	15 mins at 130℃	3 hrs at 70℃	-
Average Thickness [μm]	9.0 $\pm$ 2.4	2.5 $\pm$ 0.6	6.9 $\pm$ 0.5	-
Average Resistivity	13.0 $\pm$ 2.4 $\mu\Omega$-cm	50.9 $\pm$ 16.1 mΩ-cm	-	-

3.2.2 Optomec AJ5X

As Optomec AJ5X 3D printing system has two different atomizers, ultrasonic atomizer (UA) and pneumatic atomizer (PA), there are unique process parameters for each atomizer and some common process parameters. The important process parameters and their effects on printing results are listed below:

1. Sheath gas flow rate – the nitrogen flow rate for shielding the carrier gas flow coming from either the UA or PA in the deposition head. This parameter controls the printed linewidth and helps to reduce overspray. The sheath flow rate should be higher than the carrier flow rate to control the linewidth and prevent material from contacting the nozzle sidewall.

2. Atomizer flow rate for UA – the carrier flow rate delivering the material to the deposition head. For UA, the atomizer flow rate does not affect the ink atomization. A higher atomizer flow rate increases the amount of ink deposited.

3. Atomizer flow rate for PA – the high-velocity nitrogen stream used in PA to atomize the ink. This parameter is adjusted to achieve the optimal material atomization rate.

4. Exhaust flow rate for PA – the flow rate stripping material from the main

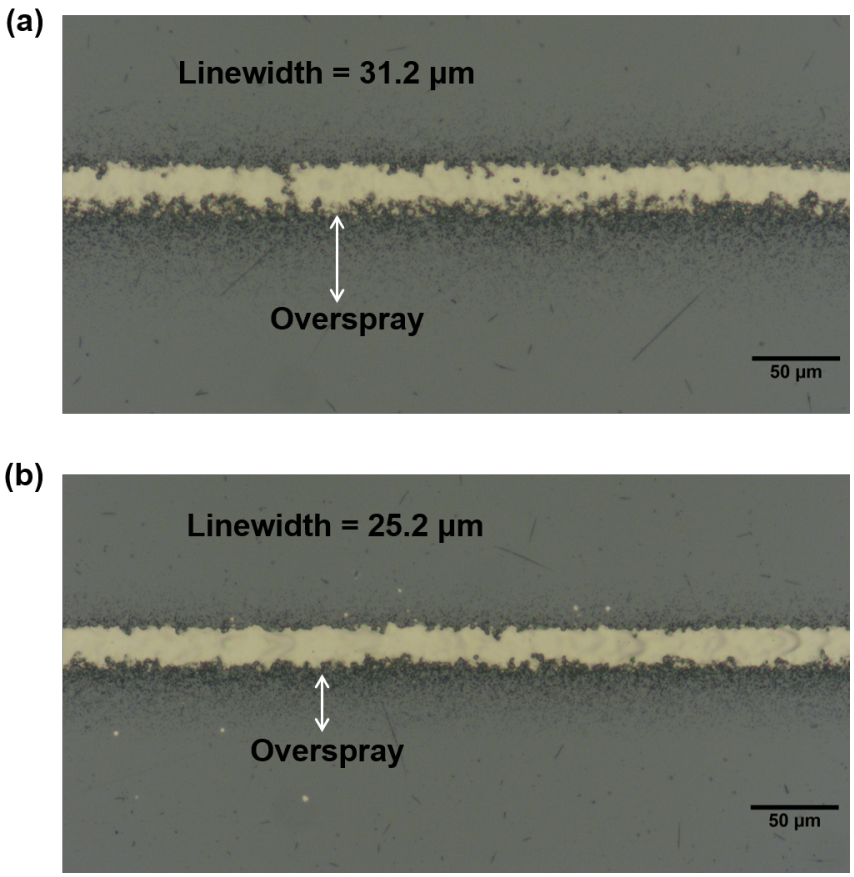

Figure 3.2: Microscope images of Au traces printed by AJ5X. Both lines were printed with same process parameters except different sheath flow rate. (a) Au line printed at sheath flow rate of 27 ccm. (b) Au line printed at sheath flow rate of 54 ccm.

atomizer flow out of the virtual impactor. The carrier flow rate for PA is the difference between the atomizer flow rate and the exhaust flow rate. Increasing the carrier flow rate, which could be achieved by either increasing the atomizer flow rate or reducing the exhaust flow rate, leads to more material deposition. If the exhaust flow rate is larger than the atomizer flow rate, the material is completely vented out of the system.

5. Ultrasonic power – the ultrasonic energy for atomizing ink in UA. This parameter controls the ink atomization. Different materials may require different energy to generate aerosol.

6. Bath temperature – the temperature setting of the water chiller to regulate the

ultrasonic bath temperature. Higher bath temperatures facilitate the ink atomization in UA.

7. Pneumatic heater/stirrer – the temperature and magnetic stir controls for the PA ink jar. Higher temperatures help to reduce material viscosity and facilitate material atomization. Stirring helps to maintain the homogeneity of unstable materials and temperature uniformity when heating.

8. Deposition nozzle diameter – the size of nozzle tip opening. The nozzle diameter could limit the printed feature size.

9. Standoff distance – the distance between the nozzle and the substrate. As AJ printing is a non-contact printing method, the standoff distance is in the range of 3 to 5 mm and has a relatively larger tolerance than the nScrypt 3D printing system.

10. Process speed – the speed at which the nozzle and printer bed move during material deposition. Increased printing speed results in narrower linewidth.

11. Bed temperature – the printer platen temperature. Higher temperatures help to reduce the material spread by evaporating excess solvent while printing.

Optomec AJ5X works well with low viscosity inks and is capable of printing much smaller features. For aerosol jet printing, the ratio of the sheath flow rate to the carrier flow rate plays a key role in printing optimization, and this ratio can be used to tune the linewidth without changing the nozzle. Figure 3.2 shows the microscope images of printed Au lines with different sheath flow rates. The effect of increasing sheath flow rate on reducing the overspray and the linewidth was demonstrated. Besides the mentioned parameters, infill is another important parameter to ensure the continuity of printed films. Table 3.3 lists all the optimized printing parameters and annealing conditions for different materials printed using AJ5X.

With the optimized condition, we were able to achieve printed Ag films with a resistivity that is about 3 times of bulk Ag (1.6 $\mu\Omega$-cm [110]) and printed Au film with a resistivity that is about 6 times of bulk Au (2.4 $\mu\Omega$-cm [110]). Figure 3.3 shows the SEM images of printed Au films with different printing conditions. The

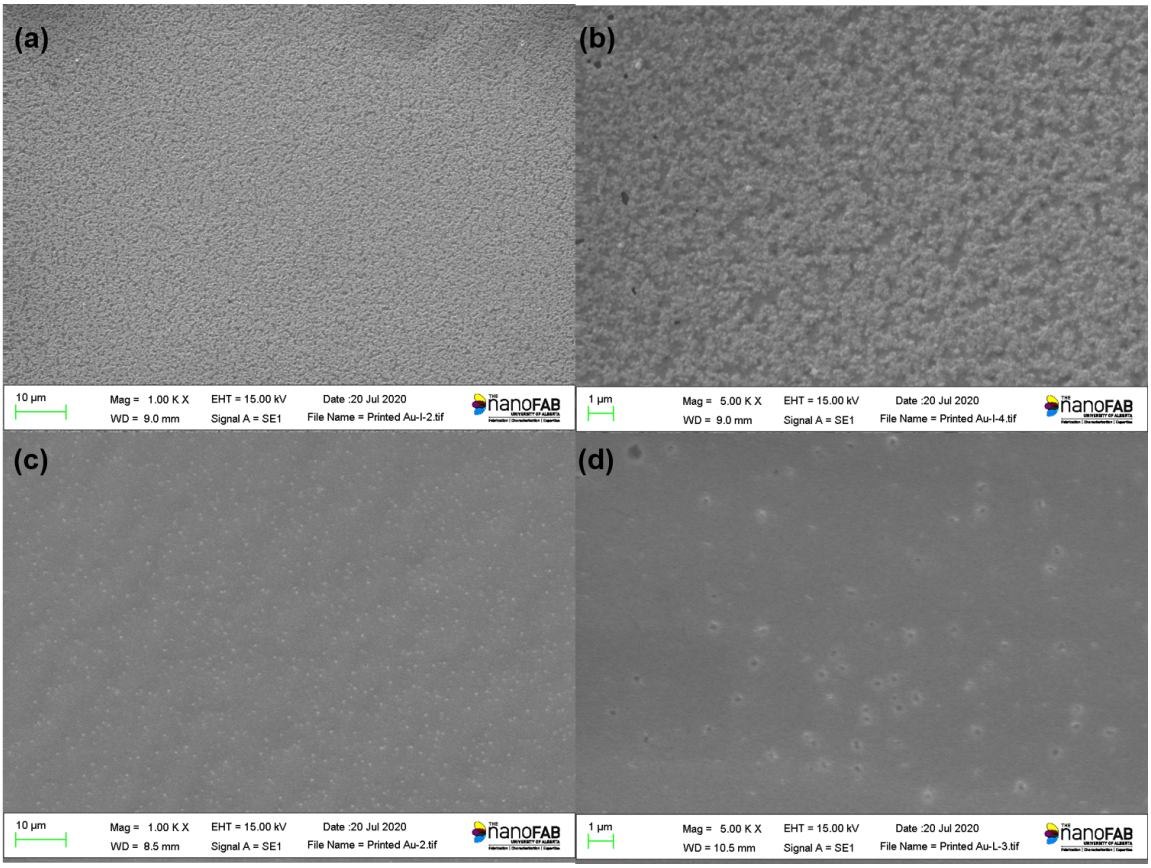

Figure 3.3: SEM images of Au films printed using UA with atomizer flow rate of (a),(b) 25 ccm, and (c),(d) 27 ccm.

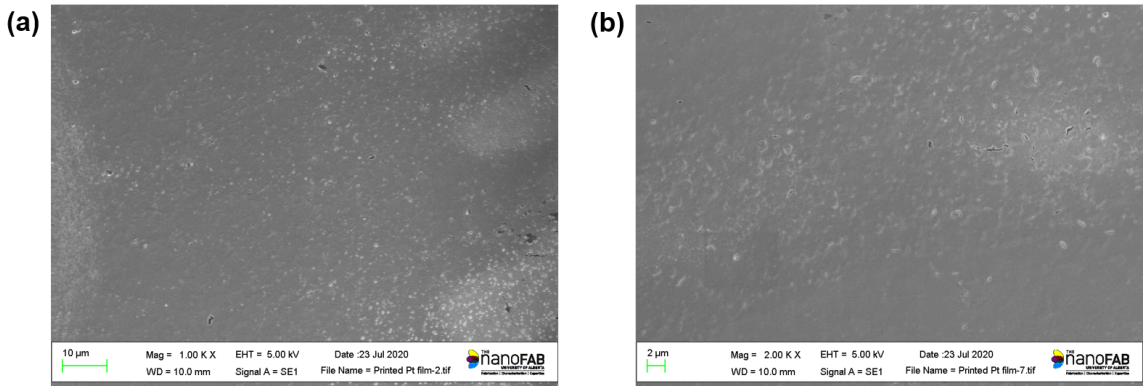

Figure 3.4: SEM of AJ printed Pt films on Kapton substrate.

film printed with a lower atomizer flow rate looks much rougher due to small voids in the film. A more continuous film was achieved with an increased atomizer flow rate. It is worth noting from the table that the printed Pt films had poor conductivity when compared with bulk Pt (10.6 $\mu\Omega$-cm [110]). This is due to the low solid content of

Table 3.3: Optimized printing and annealing parameters for materials printed by Optomec AJ5X 3D printer.

	Clariant Ag NP	UTDOTS Pt NP	UTDOTS Au NP	PEDOT:PSS Recipe A	PEDOT:PSS Recipe B	Loctite AA 3104	UV-curable PDMS
Atomizer	UA	UA	UA	UA	UA	PA	PA
Tip size [μm]	150	150	150	150	150	300	300
Bed temperature [°C]	R.T.	80	80	R.T.	R.T.	R.T.	R.T.
Bath temperature [°C]	27	30	25	30	30	N/A	N/A
Standoff distance [mm]	3	3	3	3	3	4	4
Sheath flow rate [ccm]	50	30	30	35	35	60	60
Atomizer flow rate [ccm]	30	18	27	20	20	1000	1340
Exhaust flow rate [ccm]	N/A	N/A	N/A	N/A	N/A	960	1320
Process speed [mm/s]	8	8	5	10	5	10	3
Layer of printing	2	1	1	2	2	1	1
Infill [μm]	10	10	10	30	30	100	30
Annealing conditions	overnight at 130°C	Laser sintering (150 mW)	1 hr at 280°C	20 mins at 130°C	20 mins at 130°C	UV	UV then 130°C for 30 mins
Average thickness [μm]	2.44 ± 0.03	0.20 ± 0.01	0.58 ± 0.09	0.38 ± 0.02	0.79 ± 0.02	2.23 ± 0.22	1.12 ± 0.16
Resistivity	4.74 ± 0.51 $\mu\Omega$-cm	0.14 ± 0.02 Ω-cm	14.23 ± 2.19 $\mu\Omega$-cm	3.99 ± 0.49 Ω-cm	24.75 ± 1.83 mΩ-cm	-	-

the ink that results in small cracks in the annealed film as shown in the SEM images in Figure 3.4. PEDOT:PSS films based on recipe A demonstrated higher resistivity when compared to PEDOT:PSS films based on recipe B. Lower EG content of recipe B also helped to reduce film swelling when measuring with electrolyte resulting in less variation in consecutive IV measurements for individual OECTs.

Chapter 4

3D Printed High Transconductance Organic Electrochemical Transistors On Flexible Substrates[1]

Jiaxin Fan[1], Carlo Montemagno[2], Manisha Gupta[1*]

[1]Department of Electrical and Computer Engineering, University of Alberta, Edmonton, Canada.

[2]Department of Chemical and Materials Engineering, University of Alberta, Edmonton, Canada.

4.1 Keywords

3D printing, organic electrochemical transistor, printed electronics, ion sensing

4.2 Abstract

Solution-processable organic semiconducting materials have been utilized for low-cost disposable flexible electronics applications through additive printing techniques. Organic electrochemical transistors (OECTs) are powerful devices for biosensing due to their simplicity, stability in aqueous media and high transconductance. Here, we report fully 3D printed functional OECTs using fused deposition modelling (FDM) and

[1]This manuscript is published as J. Fan, C. Montemagno, and M. Gupta, "3D printed high transconductance organic electrochemical transistors on flexible substrates," Organic Electronics, vol. 73, pp. 122–129, 2019, doi: 10.1016/j.orgel.2019.06.012.

direct writing 3D printing techniques using PEDOT:PSS as the channel material with silver as the source/drain material. These devices demonstrate high transconductance of 12.1 ± 0.4 mS, low operating voltage and high current ON/OFF ratio. They have a threshold voltage in the range of 0.66 ± 0.01 V. These printed OECTs demonstrate good stability and robust behavior after several measurement cycles. We demonstrate pH and K^+ ion sensing using these printed OECTs with high sensitivity of -26.4 mV/pH and 240 mV/decade (higher than the Nernst limit of 59.2 mV/decade). These devices can be utilized for biosensing and logic circuitry for different wearable and standalone sensing applications.

4.3 Introduction

Organic electrochemical transistors (OECTs) have attracted increasing attention due to their intrinsic advantages, such as biocompatibility, ease of fabrication, high sensitivity, low operating voltage, and stability in aqueous environment. Thereby, OECT has been studied extensively for its application in chemical and biological sensing and has demonstrated capability for ion [85, 111, 112], pH[113, 114], protein[115], label-free DNA[116], glucose[65, 73, 117, 118], lactate[119], and dopamine[62, 120, 121] detection. Unlike organic field effect transistors (OFETs) based sensors, where the electrolyte is separated from the channel by a thin layer of dielectric to minimize ion penetration, OECTs are directly gated through an aqueous electrolyte, in which the ion exchange between the channel and electrolyte modulates the conductivity of the polymer film and determines the ON/OFF state of the device. Most of these devices are based on a solution-processable semiconducting polymer channel, which provides unique opportunities to be integrated as components for logic circuits [55, 122, 123], transducers and/or disposable sensors into flexible, wearable and portable biomedical devices for biosensing applications [8, 40, 41, 124–126] via low-cost printing techniques including screen printing [36, 97, 127, 128], inkjet printing [102, 129–131], and 3D printing.

3D printing, an additive manufacturing technique, is a process in which an object is built by stacking thin layers of materials using a digital 3D model of the object. 3D printing has emerged as an important technology for printed electronics as it inexpensive and is compatible with various flexible substrates[132] with fast prototyping. Some common technologies utilized for 3D printing are: fused deposit modelling (FDM), stereolithography (SLA), and flow-based techniques. FDM is a widely used 3D printing technique, in which a pre-shaped thermal plastic filament is extruded through a heated nozzle. This is a low-cost 3D printing technique that provides freedom for more customized substrates and encapsulations. Whereas flow based direct writing utilizes micro-dispensing technology in which a fluid is delivered under a positive mechanical pressure through a 100-micrometer sized nozzle, and a continuous flow of ink is deposited onto the substrate [133]. As many organic semiconducting materials are solution processable, flow based direct writing is well suited for maskless patterning, which makes it easier to customize the design and is economical. Compared to traditional microfabrication techniques, 3D printing utilizes additive techniques such that the devices can be fabricated with a single system, which reduces the complexity and number of steps required for device fabrication. 3D printing also provides more freedom in device design and customization by simply modifying the digital 3D model of the object to be printed. Compared to the other printing techniques, such as screen, inkjet and flexographic, 3D printing is more compatible with a large variety of substrates, ranging from rigid substrates to flexible PET films, and can be used for 3D printed customized substrates. Moreover, the substrate does not need to be flat, some 3D printing systems are able to pattern on a uneven substrate by mapping out the 3D profile of the substrate with a laser height sensor or by preloading the 3D model of the substrate.

In this work, we have utilized FDM and direct writing 3D printing techniques to develop OECTs. We have selected poly (3, 4-ethylenedioythiophene)-poly (styrenesulfonate) (PEDOT: PSS) as the active channel material of the OECT, since it exhibits

great stability [134, 135], high electrical conductivity, and it has been tested with a range of different cell lines and shows good biocompatibility [136]. The OECTs based on PEDOT:PSS are p-type depletion mode (normally ON) devices. To effectively transduce chemical and biological signals, high gain is essential for sensor designs as it associates with high sensitivity [7]. In comparison to surface electrodes, OECTs exhibit a larger output signal for the same input due to their high transconductance [7]. In order to improve biocompatibility and conformality and optimize printing parameters, we have fabricated OECTs on different substrates, soft polylactic acid (PLA) filaments printed using FDM technique, polydimethylsiloxane (PDMS) deposited using direct writing technique, and also commercially available thin film substrate, polyethylene terephthalate (PET). Commercially available silver conductive paste was patterned on each type of substrate to form source and drain contacts using direct writing technique. PEDOT:PSS ink was deposited between the source and drain electrodes to form channel region by direct writing technique. The performance of devices developed on soft PLA and PET substrate were compared, and devices printed on PDMS substrate were used for conducting preliminary ion concentration and pH sensitivity tests. We have successfully 3D printed functional OECTs that show high transconductance and sensitivity to ion concentrations.

4.4 Experimental Section

4.4.1 Device Fabrication

nScrypt 3Dn direct print dispensing and 3D printing system was used to fabricate the 3D printed OECTs. The nScrypt printer has two different pumps, where Smartpump™ uses flow based direct writing technique and nFD pump is based on FDM technique. Smartpump™ was used to dispense liquid inks, such as silver paste for source and drain contact, channel material, and PDMS insulating cover. nFD pump was used to print soft PLA substrate and insulating cover. The printer has X/Y/Z

resolution of 0.5 μm. However, the printed feature size depends on the nozzle size, viscosity and particle size of the ink, and wettability of the substrate. For example, the silver conductive paste (DuPont CB028) for printing source and drain contact, has a viscosity of 18,000 cps and average particle size of approximately 10 μm. Due to the large size of the ink particles, a 125 μm (I.D.) nozzle was used to dispense the paste to prevent clogging the nozzle. The silver lines printed on glass has an average linewidth of 175 μm and thickness of 20 μm. The device patterns were designed using pCAD and AutoCAD software and converted to g-code by Slic3r software when using nFD pump. We have fabricated the OECTs on different substrates namely, printed soft polylactic acid (PLA), printed polydimethylsiloxane (PDMS) (SYLGARD® 184 Silicone Elastomer Kit), and adhesion promoted polyethylene terephthalate (PET) films (DuPont Teijin Films, 125 μm thick). Soft PLA and PDMS were also used as insulating layer to prevent source and drain from contacting the electrolyte, which also defines the active channel region. Soft PLA filament (Orbi-tech) was directly extruded by nFD pump to form substrate and mask. PDMS mixing with curing agent (10:1) was printed as substrate and mask using Smartpump™ and baked at 70℃ for 3 h in oven. For the all the devices silver contacts for source and drain were printed using commercially available silver conductive paste (DuPont CB028) and annealed at 120℃ for 2 h when deposited on soft PLA substrate and 160℃ for 1 h when printed on PET and PDMS substrates, as soft PLA substrate has lower melting point and starts to deform when heated above 120℃ . The channel material, commercially available poly(3,4-ethylenedioxythiophene)-poly(styrenesulfonate) (PEDOT: PSS) (Orgacon EL-P 5015) aqueous dispersion, was deposited between source and drain contacts using Smartpump™. For OECTs 3D printed on soft PLA substrate, the channel was cured at 120℃ for 30 min, and for devices assembled on PET and PDMS substrates, the channel was cured at 130℃ for 20 min due to the same reason mentioned for silver annealing.

4.4.2 Material and Electrical Characterization

The thickness of printed channel was determined using a two-dimensional surface topography profiler Alpha-Step IQ. Four-point probe station (Pro 4000) with Keithley 2601A source meter was used to measure the sheet resistance of the PEDOT:PSS films of different thicknesses. Glancing angle X-ray diffraction (GXRD) studies were carried out on Rigaku Ultimate IV system with Cu source operated at 40 kV and 44 mA, and JADE software was used for XRD spectra analysis. Zeiss EVO M10 scanning electron microscope (SEM) was used to investigate the surface morphology of printed PEDOT:PSS sample.

All the electrical characterization of the OECTs was conducted using a Keithley 4200 Semiconductor Characterization System (SCS) parameter analyzer along with a probe station. Device output curves were generated by measuring current between source and drain (I_D) while sweeping the voltage between source and drain (V_D) at different gate bias (V_G). Transfer curve at different drain bias and the corresponding transconductance were extracted from the measured data. All the device characterization was conducted with 100 mM NaCl in deionized water as the electrolyte. A silver wire was first cleaned with nitric acid for 30 min and then dipped into 12 wt% bleach solution for 30 min to form Ag/AgCl and used as an external gate electrode. The electrolyte was added to the channel of each device with a micropipette and left for several minutes before testing to ensure repeatable measurements.

For ion concentration detection, the electrolytes with different potassium ion (K^+) concentrations (1 mM, 10 mM, 100 mM, and 1000 mM) were prepared by dissolving appropriate amount of KCl in DI water. For pH sensitivity tests, the testing electrolytes were prepared by first diluting 10x phosphate buffered saline (PBS) solution (Fisher BioReagents) to 0.1x PBS solution with DI water. The pH of the solution was tuned by adding 1 M hydrochloric acid (HCl) and measured with a VWR B10P Benchtop pH meter. The OECT was washed with DI water and dried with com-

pressed air between each measurement cycle to avoid contaminations.

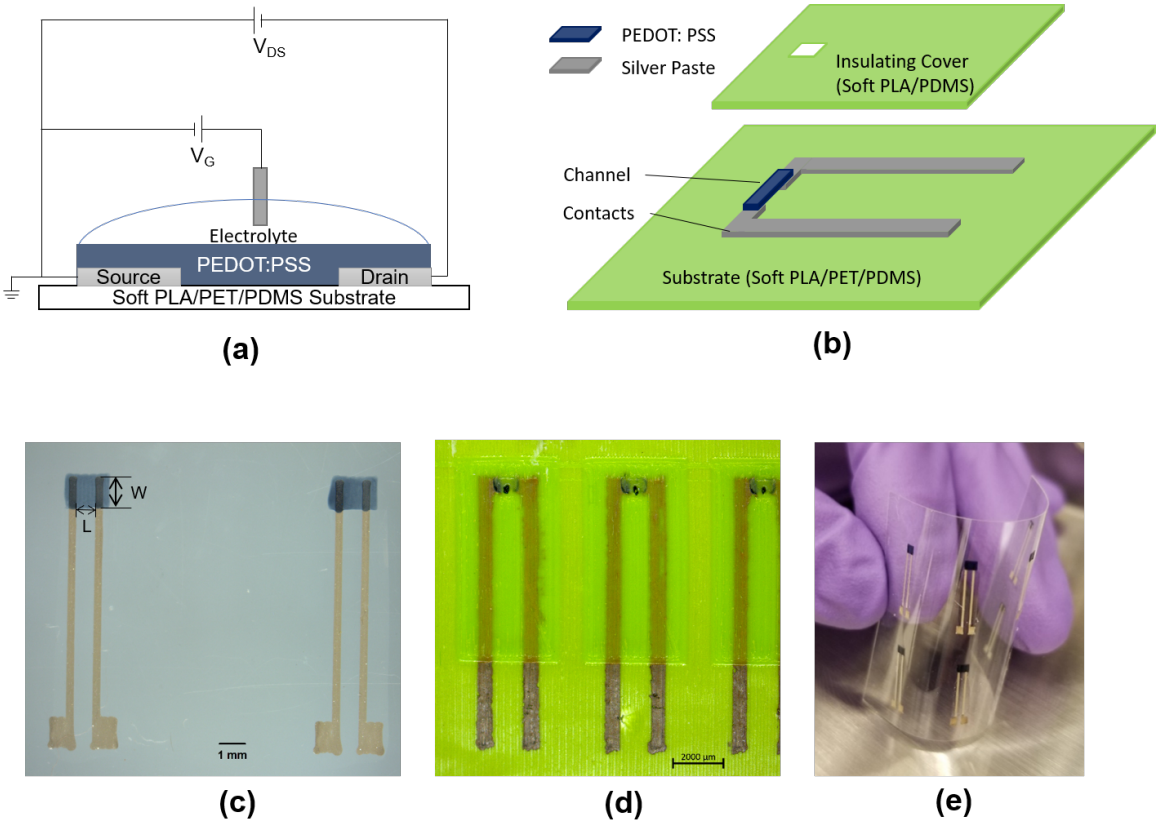

Figure 4.1: (a) OECT architecture with PET/PDMS substrate. (b) OECT schematic with 3D printed soft PLA as substrate and insulating layer. The channel width and length are defined by the opening on the insulating cover. (c) Microscopic image of OECTs assembled on PET substrate, the source and drain are the printed silver paste, the bluish color is the PEDOT:PSS channel with length (L) and width (W), and the printed PDMS cover is transparent and not visible in the image. (d) Microscope image of OECTs on printed soft PLA substrate. The opening on the soft PLA insulating layer defines the channel dimension. (e) Photo of OECT array printed on PET substrate showing flexibility.

4.5 Results and Discussion

4.5.1 Device Structure

Figure 4.1 (a) shows the schematic of a printed OECT. The OECTs developed for this work were assembled on polyethylene terephthalate (PET) films and 3D printed soft polylactic acid (PLA) substrates (Figure 4.1 (b)). Silver conductive ink was

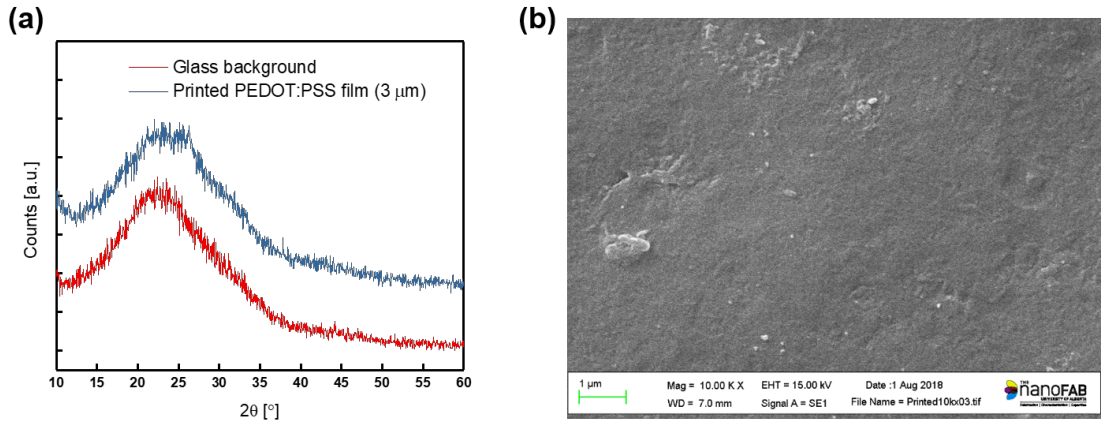

Figure 4.2: (a) Glancing angle X-ray diffraction (XRD) spectra of 3 μm thick 3D printed PEDOT:PSS film on glass substrate. (b) Scanning electron microscopic (SEM) image showing morphology of 3D printed PEDOT:PSS film.

dispensed onto the substrate to form source, drain, and gate electrode. PEDOT: PSS aqueous dispersion was dispensed on top of source and drain electrode to form active sensing area. For the devices assembled on PET film, even though the entire printed PEDOT:PSS area was used for sensing, the channel length was defined as the distance between the source and drain electrode excluding the overlap as shown in Figure 4.1 (c). Whereas for the device with printed soft PLA substrate (Figure 4.1 (d)), the opening on the soft PLA mask defined the active channel area. The devices developed on the PET film have an average channel thickness of d = 2.5 $\pm$ 0.2 μm (n = 8), which is much thinner than the channel of the devices printed on soft PLA substrate d = 7.1 $\pm$ 0.3 μm (n = 9). Finally, a layer of PDMS or soft PLA was printed to prevent the source and drain electrode from being in direct contact with the electrolyte (100 mM NaCl solution). An Ag/AgCl wire is used as external gate electrode for all devices.

4.5.2 Material Characterization

The PEDOT: PSS films 3D printed on glass slide and annealed at 130℃ for 20 min were characterized. Four-point-probe, X-ray diffraction (XRD), and scanning electron

microscope (SEM) was used to measure the electrical conductivity, crystallinity, and morphology of the annealed PEDOT: PSS films. The average conductivity for 3D printed film with an average thickness of 3.5 μm is 15.7 $\pm$ 0.3 S/cm (n = 5). The glancing angle XRD spectra of 3D printed PEDOT: PSS film is shown in Figure 4.2 (a). There was no significant peak being observed, which indicates that the PEDOT: PSS film is amorphous in nature. Figure 4.2 (b) shows the SEM image PEDOT:PSS film deposited by 3D printing method. There is no significant gap or crack observed for the sample, which indicates that 3D printing is a reliable method to achieve continuous PEDOT:PSS film.

4.5.3 OECT Characterization

The behavior of PEDOT: PSS based OECTs can be described as an electronic circuit, for hole transport within the conducting polymer, integrated with an ionic circuit, for ion transport between electrolyte and the porous channel [31]. Figure 4.3 shows the output characteristics, transfer curves, and transconductance of two devices developed for this work. Figure 4.3 (a), (c) shows the output characteristics of a typical OECT printed on PET film with 3D printed channel (W = 912 μm, L = 694 μm, d = 2.6 μm) and a fully 3D printed OECT with printed soft PLA substrate (W = 177.5 μm, L = 117.5 μm, d = 7.5 μm), and the corresponding transfer curves are shown in Figure 4.3 (b), (d), respectively. For all the IV-characteristic measurements, the drain bias, V_D, was varied from 0 to –0.8 V and the gate bias, V_G, was varying from 0 V to 1 V with a step size of 0.1 V. The output characteristics of all devices developed for this work have shown p-channel behavior. The magnitude of drain current (I_D) decreases with the increase of gate voltage (V_G), which indicates that these devices operates in depletion regime[31]. Upon an application of positive gate voltage, the cations from the electrolyte penetrate into the porous PEDOT:PSS channel and compensate the sulphonate anions on the PSS chain. Therefore, the hole density decreases leading to the decrease in channel conductivity, which reduces the drain current and turns OFF

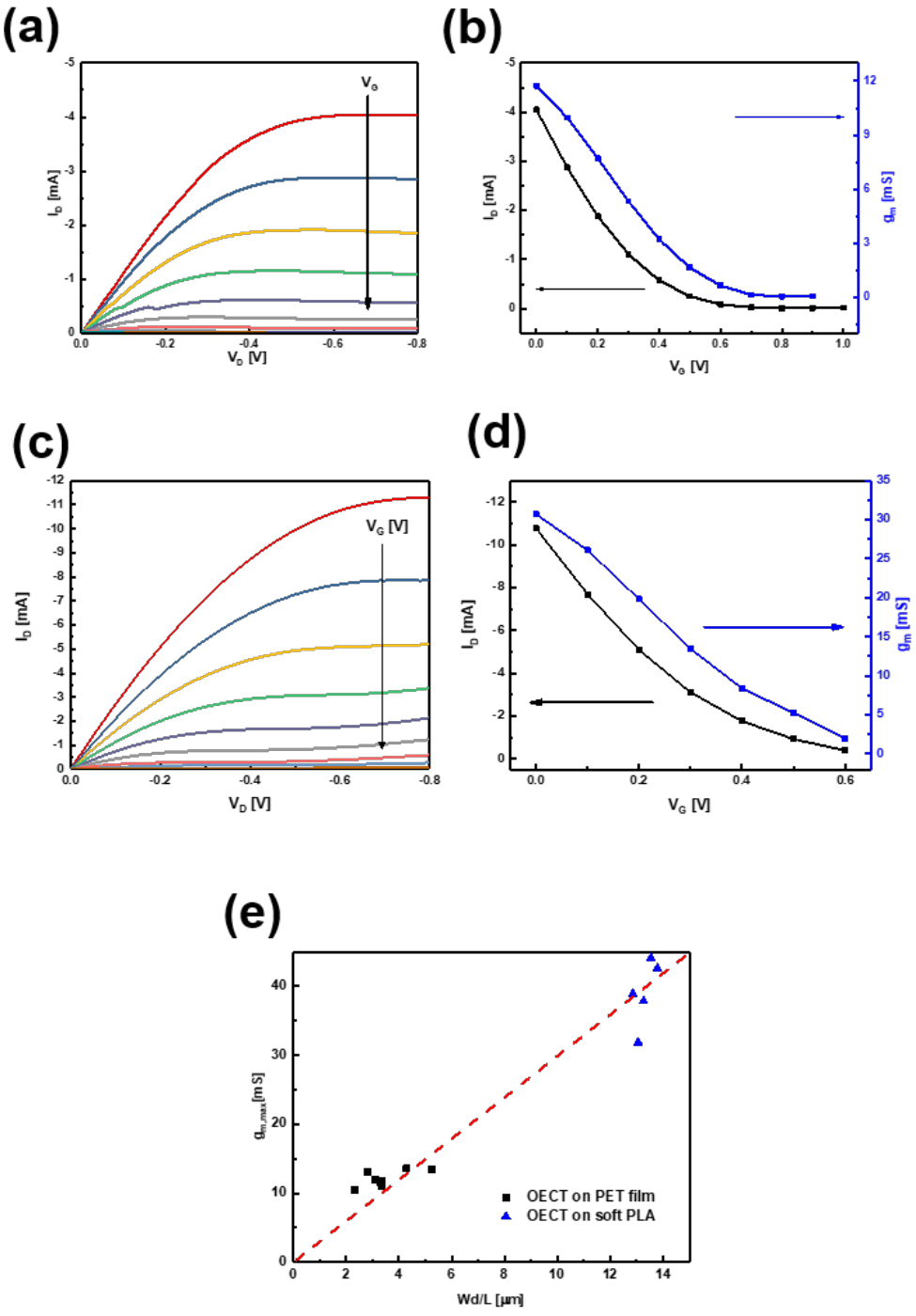

Figure 4.3: (a) Output characteristics of an OECT printed on PET film (W = 912 μm, L = 694 μm, d = 2.6 μm) for V_G from 0 V (top curve) to 0.8 V (bottom curve). (b) Transfer curve for V_D = -0.7 V, and the corresponding transconductance with $g_{m,max}$ = 11.7 mS. (c) Steady-state characterization of a fully printed OECT with

soft PLA substrate and cover (W = 178 μm, L = 118 μm, d = 7.5 μm) for V_G from 0 V (top curve) to 0.8 V (bottom curve). (d) Transfer curve for V_D = -0.7 V and the corresponding transconductance with peak, $g_{m,max}$ = 30.7 mS. (e) Scaling of peak transconductance ($g_{m,max}$) with channel geometry (Wd/L) for devices printed on PET substrate (black squares) and on soft PLA substrate (blue triangles). Red dashed line shows the peak transconductance is linearly correlated with the channel geometries, which could be used for device performance optimization with limited surface area.

the device. The magnitude of drain current increases with the increase of magnitude of drain voltage under linear regime and saturates when the magnitude of drain voltage is further increased due to channel pinch-off. The threshold voltage, V_T, can be then extracted from the transfer curve using equation 4.1:

$$I_D^{SAT} = \frac{Wd}{L}\,\mu C^*(V_T - V_G)^2 \tag{4.1}$$

where I_D^{SAT} is the saturation drain current, W is the channel width, L is the channel length, d is the channel thickness, μ is the hole mobility of PEDOT:PSS, C^* is the capacitance per unit volume of the channel, and V_G is the applied gate voltage. Threshold voltage extracted for devices on PET film with printed channel is V_T = 0.66 $\pm$ 0.01 V (n = 8) and for devices with printed soft PLA substrate is V_T = 0.74 $\pm$ 0.03 V (n = 4). All the 3D printed OECTs in this work exhibit low voltage operation, which is a typical for OECTs, and this is attributed to the mixed ionic-electronic conduction property of the channel material, PEDOT:PSS. In this case, the gate bias modulates the cation penetration from the electrolyte, which directly controls the doping of the channel, and therefore, leads to large volumetric capacitance [30, 137]. The current ON/OFF ratio is determined by taking the drain current ratio at V_G = 0 V and V_G = 1 V from the transfer curve. The extracted ON/OFF ratio is 570 for the OECTs 3D printed on PET film and 1330 for the OECTs printed on soft PLA substrate.

Transconductance is another important device parameter which determines how effectively the transducer can convert the chemical or biological signals. Transconductance of a transistor is defined as $g_m = \Delta I_D/\Delta V_G$ and can be expressed in the

following form for an OECT operating in saturation regime [33]:

$$g_m = \frac{Wd}{L}\ \mu C^*(V_T - V_G) \tag{4.2}$$

As shown in Figure 4.3 (b), the transconductance of the OECT 3D printed on PET film has a peak value of g_m = 11.7 mS at V_G = 0 V. Devices of similar channel dimensions have transconductance peak value of g_m = 12.1 ± 0.4 mS (d = 2.5 ± 0.2 μm) at V_G = 0 ∼ 0.1 V and μC^* = 59.2 ± 5.6 $FV^{-1}s^{-1}cm^{-1}$ calculated from equation 4.2. A much higher transconductance peak g_m = 30.7 mS was observed at V_G = 0 V as shown in Figure 4.3 (d) for an OECT 3D printed on soft PLA substrate, and devices of similar channel dimensions have average peak transconductance of g_m = 31.8 ± 6.7 mS (d = 7.1 ± 0.3 μm) and μC^* = 39.8 ± 3.4 $FV^{-1}s^{-1}cm^{-1}$ calculated from equation 4.2. As OECT's transconductance depends on not only the lateral dimensions of the channel, but also the thickness [33, 138]. Figure 4.3 (e) shows the correlation between the scaling of peak transconductance extracted at V_D = -0.7 V and the OECT channel dimensions for 3D printed OECTs assembled on both PET and printed soft PLA substrate. The transconductance is directly proportional to the channel geometry based on equation 4.2, which can also be observed in our results. With limited surface area, the sensitivity of OECT based biosensor can be enhanced by increasing the channel W/L ratio and channel thickness. Even though devices with thicker channel show higher transconductance, which indicates higher sensitivity for sensing applications, they also have slower response, as more cations are required in order to fully de-dope the thicker channel and turn the device OFF. Thicker channel devices (higher stored charge) are more sensitive to weak signals, whereas thinner channel devices (lower stored charge) have faster response. Therefore, based on experimental needs, one can easily design an OECT array with neighboring devices having different channel thickness using 3D printing technique, which require more complicated steps when fabricated with traditional microfabrication techniques.

Table 4.1 contains device parameters, including lateral channel dimension, channel

Table 4.1: Comparison of OECTs fabricated with different techniques. Device parameters including lateral channel dimension, channel thickness (d), peak saturation transconductance ($g_{m,max}$), current ON/OFF ratio ($I_{D,ON}/I_{D,OFF}$), and threshold voltage (V_T) are listed in the table.

Fabrication technique	**Contact material**	**Channel material & lateral dimension**	**d [μm]**	**$g_{m,max}$ [mS]**	**$I_{D,ON}/I_{D,OFF}$**	**V_T [V]**	**Ref.**
3D printed OECT on printed soft PLA	Ag	PEDOT:PSS W/L = 1.6 ± 0.1	7.1 ± 0.3	38.9 ± 2.4	1.33×10^3	0.74 ± 0.03	This work
3D printed OECT on PET film	Ag	PEDOT:PSS W/L = 1.3 ± 0.1	2.5 ± 0.2	12.1 ± 0.4	5.70×10^2	0.66 ± 0.01	This work
Microfabricated OECT	Au	PEDOT:PSS W/L = 1	0.4	4.02	N/A	N/A	[7]
	Au	PEDOT:PSS W/L = 2	0.4	2.7	N/A	N/A	
	Au	PEDOT:PSS W/L = 2	0.14	$\sim$2	$\sim 10^5$	N/A	[138]
	Au	PEDOT:PSS W/L = 0.25	0.17	3.2	5.41×10^2	0.52	[139]
Screen printed OECT	PEDOT :PSS	PEDOT:PSS W/L = 0.0625	N/A	N/A	~ 2	N/A	[98]
	PEDOT :PSS	PEDOT:PSS W/L = 0.125	N/A	N/A	~ 1.25	N/A	
Inkjet printed OECT	Ag	PEDOT:PSS W = 100 μm	0.18	N/A	1×10^2	N/A	[140]
	PEDOT :PSS	PEDOT:PSS W = 850 μm	2	0.12	N/A	N/A	[100]
	PEDOT :PSS	PEDOT:PSS Active channel area = 1.3 mm^2	N/A	N/A	5.00×10^2	N/A	[102]
	PEDOT :PSS	PEDOT:PSS W/L = 2/3	N/A	1.67	2.00×10^2	>1.5	[101]

thickness, source/drain electrode material, peak transconductance, ON/OFF ratio and threshold voltage, of the two kinds of OECTs developed for this work and literature results of OECTs fabricated with other techniques. The OECTs from this work demonstrate considerably higher transconductance and comparable ON/OFF ratio as compared to other studies. However, the ON/OFF ratio of 3D printed OECTs is significantly lower compared to the microfabricated devices. This can be attributed to the thicker channels in our printed devices which makes it quite difficult to dedope them completely and also due to the 3D printed Ag electrode. Ag electrode can have a thin oxidized layer on the top which can lead to poor interface with the PEDOT:PSS channel. This will lead to higher contact resistance at the channel and electrodes and this problem is not observed with Au electrodes. In other reported work, with microfabricated devices with Au electrodes higher ON/OFF ratio of 10^5 has been measured [138].

4.5.4 Ion Concentration and pH Sensitivity Tests

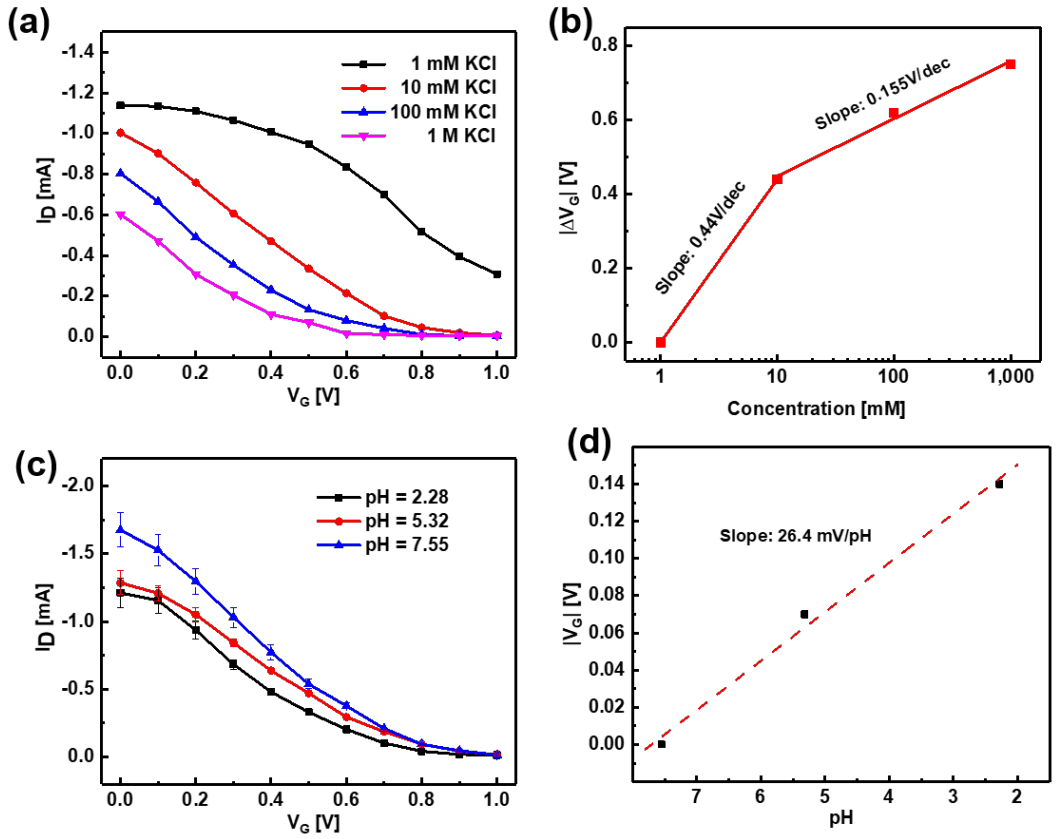

Figure 4.4: Preliminary ion concentration and pH sensing results based on OECTs 3D printed on PDMS substrate. (a) Transfer curves of OECT tested at drain bias of V_D = -0.1 V with KCl solution of different concentrations (1 mM, 10 mM, 100 mM, and 1 M). (b) Shift in V_G ($|\Delta V_G|$) as a function of KCl solution concentration extracted from shifting the transfer curves in figure 4.4 (a). A logarithmic correlation between $|\Delta V_G|$ and K^+ concentration can be observed from the curve with a sensitivity of 240 mV/dec which is higher than the Nernst limit of 59.2 mV/dec. (c) Transfer curves of OECT tested at drain bias of V_D = -0.1 V with PBS of different pH values (2.28, 5.32, 7.55). (d) Shift of V_G as a function of the pH value of the PBS solution extracted from shifting the transfer curves in Figure 4.4 (c) and it shows a linear correlation between ($|\Delta V_G|$) and pH value with a slope of -26.4 mV/pH.

We have conducted both ion and pH testing on these 3D printed OECT devices. Preliminary ion concentration sensing tests were conducted with OECTs assembled on PDMS substrate as described in method section. Figure 4.4 (a) shows the transfer characteristics (biased at V_D = -0.1 V) of a printed OECT measured in KCl solution

with different concentrations (1 mM, 10 mM, 100 mM, and 1 M). It can be clearly observed that as the cation concentration (K^+) increases, the drain current decreases for the same gate bias. This change of OECT behavior with different cation concentration is due to the shift in the threshold voltage, and the transfer curves can be merged into a single curve by horizontally offset all transfer curves to the right. As shown in Figure 4.4 (b), the shift of gate voltage, ΔV, shows logarithmic dependence on the K^+ concentration with slope of 240 mV/dec. The 3D printed OECTs exhibited K^+ ion sensitivity higher than the Nernst limit of 59.2 mV/dec, which is attributed to their high transconductance due to the thicker channels. From the trend of the curve, we can predict that the slope will further decrease as the concentration increases and eventually becomes zero for higher concentrations. More detailed experiments will be conducted in the future to obtain the limit of detection (LOD) for these 3D printed devices, which could be much lower than 1 mM. The pH sensitivity tests were carried out with 0.1x PBS with different pH values (7.55, 5.32, and 2.28). Similarly, the transfer curves of printed OECTs measured in PBS solutions with different pH values are shown in Figure 4.4 (c). In this case, as the pH decreases, the hydrogen ion (H^+) concentration in the solution increases, more cations are available in the solution to de-dope the PEDOT:PSS channel, and therefore the threshold voltage shifts to lower values. Figure 4.4 (d) shows the relative shift in gate voltage as a function of different pH values (ΔV/pH), and a linear relationship with a slope of -26.4 mV/pH is observed. Table 2 shows the comparison of K^+ ion and pH sensitivity along with peak transconductance of the devices developed for this work and other literature results. The 3D printed OECTs exhibit similar or higher K^+ sensitivity to the microfabricated OECTs from other studies. Scheiblin *et al.* have obtained pH sensitivities of -73 mV/pH and -44 mV/pH for OECT-only pH sensors with modified gate materials: IrOx and polyaniline (PANI) respectively [113]. In this case, the pH sensitivities of the OECTs were enhanced due to the pH sensitive gate materials, whereas in this work, we have demonstrated the intrinsic pH sensitivity of OECTs. PEDOT:PSS

based OECTs have been demonstrated with intrinsic ion sensitivity and pH sensitivity [111, 112, 114]. However, to achieve selective sensing and improve the ion and pH sensitivity, functionalization of PEDOT:PSS surface and/or applying active gate materials is required, and this will be studied in the future.

Table 4.2: Comparison of peak transconductance ($g_{m,max}$) and sensitivity to change in ion concentration ($\Delta V/\Delta C$) or pH ($\Delta V/pH$) of OECT fabricated with different techniques

Fabrication technique	**Gate material**	**$g_{m,max}$ [mS]**	**$\Delta V/\Delta C_{K^+}$ [mV/dec]**	**$\Delta V/pH$ [mV/pH]**	**Reference**
3D printed OECT-only	Ag/AgCl	12.1 ± 0.4	440	-26.4	This work
3D printed OECT-inverter	Ag/AgCl	16.63	366.67	N/A	[123]
Microfabricated OECT	Ag/AgCl	N/A	59.4	N/A	[111]
	Ag/AgCl	~ 3	414	N/A	[112]
Screen printed OECT-only	IrOx	~ 0.12	N/A	-73	[113]
	Polyaniline	~ 0.21	N/A	-44	

4.6 Conclusion

We have demonstrated fully printed functional OECTs utilizing a single 3D printing system. Two different substrates one printed soft PLA and another a commercial substrate, PET film, were utilized for the work to demonstrate that both can be implemented for flexible devices. The printed OECTs demonstrate comparable results to the devices fabricated using microfabrication techniques with a high transconductance of 12.1 ± 0.4 mS and high current ON/OFF ratio in the range of 10^2. Due to the high transconductance they demonstrate high sensitivities to K^+ ion (as high as 240 mV/dec – higher than the Nernst limit) and pH detection (-26.4 mV/pH). Thus, we have demonstrated high performance, reliable and repeatable flexible OECT devices can be fabricated by simple and economical 3D printing techniques which paves the way for affordable and customized biosensing and bio wearables application.

Chapter 5

Aerosol Jet Printed OECT Device Optimization

5.1 Introduction

Printed and flexible electronics is an emerging area that has been widely investigated for biosensing applications in the past few decades. Efforts have been made to develop fully printed flexible biosensors and electronic circuits which consist of multifunctional materials and devices. Owing to the mechanical flexibility, the low temperature solution processability, and the versatility of organic semiconductors (OSCs), both OFETs and OECTs are promising candidates to be implemented as various components for printed electronics. As mentioned in the background chapter, both OFETs and OECTs are three-terminal devices with source, drain, and gate contact. OFETs adopt a similar structure to the conventional FETs, where a dielectric layer is sandwiched between the organic semiconductor channel and the gate. The gating of OFETs is through a purely capacitive effect across the dielectric layer, which modulates the charge carrier concentration near the dielectric/OSC interface in the channel. For OECTs, the dielectric layer is replaced by an aqueous electrolyte that is in direct contact with an ion-permeable OSC channel. In this case, the channel current modulation is achieved by electrochemical doping/dedoping of the channel facilitated by ion injection.

Due to the lack of a dielectric layer in the structure of OECT, the transport of

charge carriers is not dominated by the interface quality between the organic semiconductor and the dielectric layer. Moreover, the interaction between the channel and ions in the electrolyte happens throughout the entire channel, and this leads to high capacitance. Therefore, OECTs have low operation voltage, usually less than 1 V, and is more suitable for working in aqueous media to avoid undesired electrochemical oxidation and reduction reactions. The large volumetric capacitance also leads to high transconductance (g_m). Transconductance represents the change of drain current in response to the change of the gate voltage, and it is the device parameter that governs the signal amplification and affects the sensitivity of the biosensor. Hence, understanding the correlation between device properties and device geometry is important for designing the biosensor for desired applications.

In this chapter, OECTs were fabricated using an AJ5X 3D printing system with the optimal material printing parameters and annealing conditions described in chapter 3. As mentioned in chapter 2, channel dimensions and gate materials affect the electrical characteristics of OECTs. This chapter focuses on the study of the influence of geometry variations on the device properties illustrated using two types of OECTs developed in this thesis, OECTs with Ag contacts (Ag-OECTs) and OECTs with Au contact (Au-OECTs). This study is important to biosensor development for tuning device properties to achieve optimal sensing performance.

5.2 Experimental Details

5.2.1 Ag-OECT Fabrication

Ag-OECTs are printed using the Optomec AJ5X 3D printing system on flexible PET substrates. Commercially available silver Ag NP ink (Clariant EXPT Prelect TPS 50G2) was first diluted with DI water with a volume ratio of 1:1. The diluted Ag NP ink was then used for printing the source and drain contacts of OECT using UA. The printed Ag traces were annealed in an oven overnight at 130℃. The PEDOT:PSS ink

was prepared by mixing PEDOT:PSS (Clevios PH-1000) solution with 20% ethylene glycol (EG) (Sigma Aldrich), 0.1% of dodecylbenzene sulfonic acid (DBSA) (Sigma Aldrich), and 0.9% of (3-glycidyloxypropyl) trimethoxysilane (GOPS) (Sigma Aldrich). The PEDOT:PSS ink was then deposited by UA to form the channel region on the printed Ag source and drain and annealed for 20 minutes at 130℃. A UV-curable acrylic adhesive (Henkel Loctite AA 3104) layer was printed to passivate the source and drain electrodes to prevent shorting from the electrolyte. The passivation layer was dispensed on the electrodes by PA and cured on-the-fly with the built-in UV lamp (405 nm, 5 mW).

5.2.2 Au-OECT Fabrication

Au-OECTs were fabricated using the Optomec Aerosol Jet 5X 3D printer on flexible polyimide (Kapton) substrates. Gold nanoparticle (Au NP) ink (UT Dots, Inc.) was deposited using UA to form source, drain, and gate electrodes and all the metal interconnects. The printed Au traces were annealed at 280℃ for 1 hour. The channel of OECT was printed using poly(3,4-ethylenedioxythiophene) polystyrene sulfonate (PEDOT:PSS) mixture composed of 94% Heraeus Clevios™ PH 1000, 5% ethylene glycol (EG), 0.1% dodecylbenzenesulfonic acid solution (DBSA) (70 wt.% in isopropanol), and 1wt.% (3-glycidyloxypropyl) trimethoxysilane (GOPS) ($\geq$ 98%) and annealed at 130℃ for 20 minutes. Finally, a layer of UV-curable polydimethylsiloxane (PDMS) (Shin-Etsu Chemical Co., Ltd.) was deposited by PA to protect the metal traces from shorting with the liquid electrolyte. The PDMS insulating layer was cured with UV on-the-fly while printing and then baked at 130℃ for 30 minutes to fully anneal the layer.

5.2.3 Electrical Characterization

For Ag-OECTs, electrical measurements were performed at room temperature using a Keithley 2612B sourcemeter controlled by LabVIEW, and a sweep rate of approxi-

mately 500 mV/s was used for all the measurements. The characterization was carried out using an external Ag/AgCl wire as the gate electrode and 100 mM NaCl as the electrolyte. The output characteristics were measured by sweeping the drain bias (V_D) from 0.2 V to -0.6 V with a step size of -0.02 V for each gate bias (V_G) ranging from 0 to 1 V with a step size of 0.1 V. The IV sweep started from 0.2 V to confirm that the device is off at $V_D = 0$ for all V^G biases. The transfer characteristics and transconductance were extracted from the measured output characteristics at a fixed drain bias (V_D = -0.6 V). A sweep rate of approximately 500 mV/s was used for all the measurements.

For Au-OECTs, the electrical characteristics were measured using a Keithley 4200 SCS semiconductor parameter analyzer. An in-plane printed Au gate electrode and 1xPBS solution as the electrolyte were used for all the measurements. The output characteristics were measured by sweeping V_D from 0.2 V to -0.6 V for each constant V_G stepped from -0.4 to 1.6 V with a step size of 0.1 V. The transfer curves were measured by sweeping the V_G from -0.4 V to 1.6 V for each constant V_D from -0.1 V to -0.6 V. The pulse measurements were carried out by applying pulsed gate voltage of different amplitudes to a device under constant V_D and the gate transient current was measured.

5.3 Results and Discussions

5.3.1 Ag-OECT Optimization

Figure 5.1 shows both the top view and the side view schematics for the Ag-OECTs developed for this work. An external Ag/AgCl electrode was used as the gate electrode for device characterizations. Three device geometry parameters as indicated in the schematic were varied for this study, and they are the channel length (L), the channel width-to-length ratio (W/L), and the channel thickness (d). OECTs with two channel lengths, L = 100 and 250 μm, were designed; however, the average resulting channel

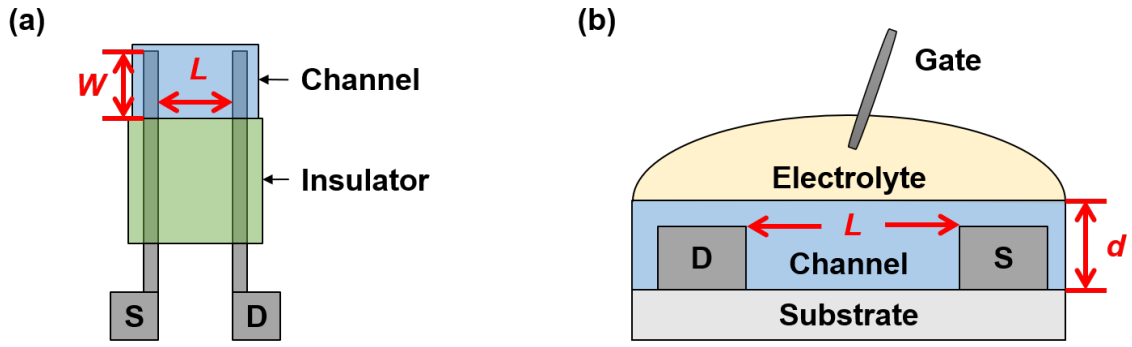

Figure 5.1: (a)Top-view and (b) side-view schematics of the Ag-OECT illustrating the channel geometries.

lengths are 90.3 ± 1.7 and 240.1 ± 2.8 μm due to printing variations. For each channel length, the channel width was varied to obtain different values of W/L. For Ag-OECTs with a channel length of 90 μm, the average W/L values are 1, 2, and 4. For devices with a channel length of 240 μm, the resulting average W/L values are 1, 2, and 5. For each combination of channel length and W/L, the channel thickness was varied by increasing the number of printed PEDOT:PSS layers. The average thickness is approximately 200 nm and 400 nm for one layer and two layers of printed PEDOT:PSS, respectively.

Figure 5.2 shows typical current-voltage (I-V) characteristics and transfer characteristics (V_D = -0.6 V) of fully printed Ag-OECTs with the same W/L of 1 and different channel lengths and thicknesses. In all these cases, the magnitude of I_D decreases as V_G increases indicating typical p-type depletion mode behaviors as expected. According to Bernards model, the steady-state characteristics of an OECT can be described using the following equation [31]:

$$I_D = \left\{ \begin{array}{lll} \mu C^* \frac{W}{L} d[V_T - V_G + \frac{V_D}{2}]V_D, & \text{for} & V_D > V_G - V_T \\ \mu C^* \frac{W}{2L} d[V_T - V_G]^2, & \text{for} & V_D < V_G - V_T \end{array} \right\} \quad (5.1)$$

where μ is the hole mobility of PEDOT:PSS; C^* is the volumetric capacitance; V_T is the threshold voltage. For OECTs, the magnitude of I_D scales with W/L like conventional MOSFETs. In addition, I_D also scales with the channel thickness, which is also observed in our results. Since the devices characterized in Figure 5.2 (a) and

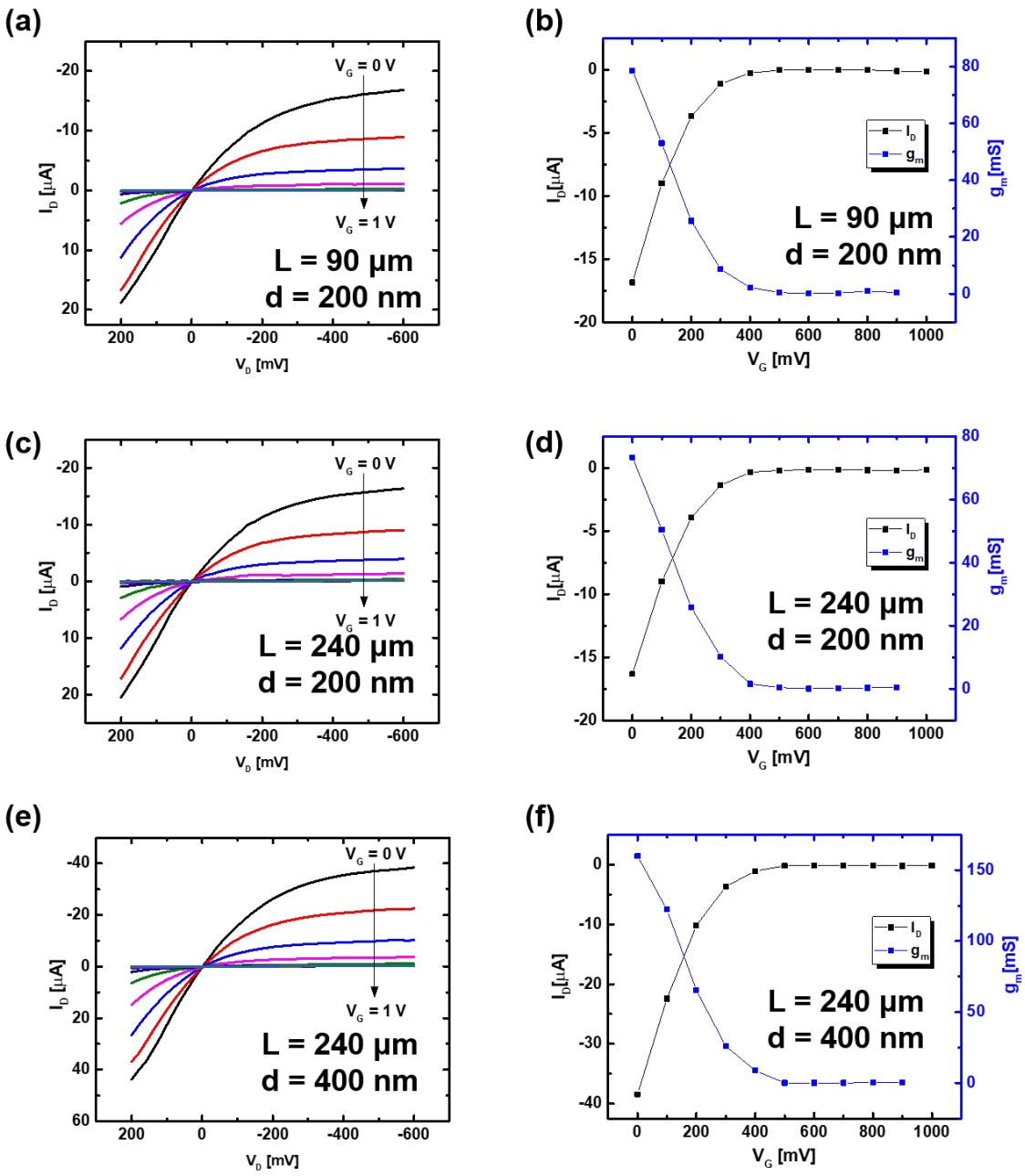

Figure 5.2: Electrical characteristics of Ag-OECTs with W/L = 1 and different channel length and thickness. (a) I-V and (b) transfer characteristics of an Ag-OECT with L = 90 μm and d = 200 nm. (c) I-V and (d) transfer characteristics of an Ag-OECT with L = 240 μm and d = 200 nm. (e) I-V and (f) transfer characteristics of an Ag-OECT with L = 240 μm and d = 400 nm.

Figure 5.2 (c) have the same channel thickness and W/L, it can be observed that both devices show similar I_D levels despite having different channel lengths. Figure 5.2 (c)

and (e) shows the output characteristics of two OECTs with the same channel lateral dimensions and different thicknesses, and the OECT with a thicker channel has a high I_D. The on-off current ratio ($I_{D,ON}/I_{D,OFF}$) can be extracted from the transfer curve by taking the drain current ratio at $V_G = 0$ V and $V_G = 0.8$ V. As observed in Figure 5.2 (b),(d),(f), the off-state drain current for the printed OECTs falls in the same range ($< 1\mu$A).

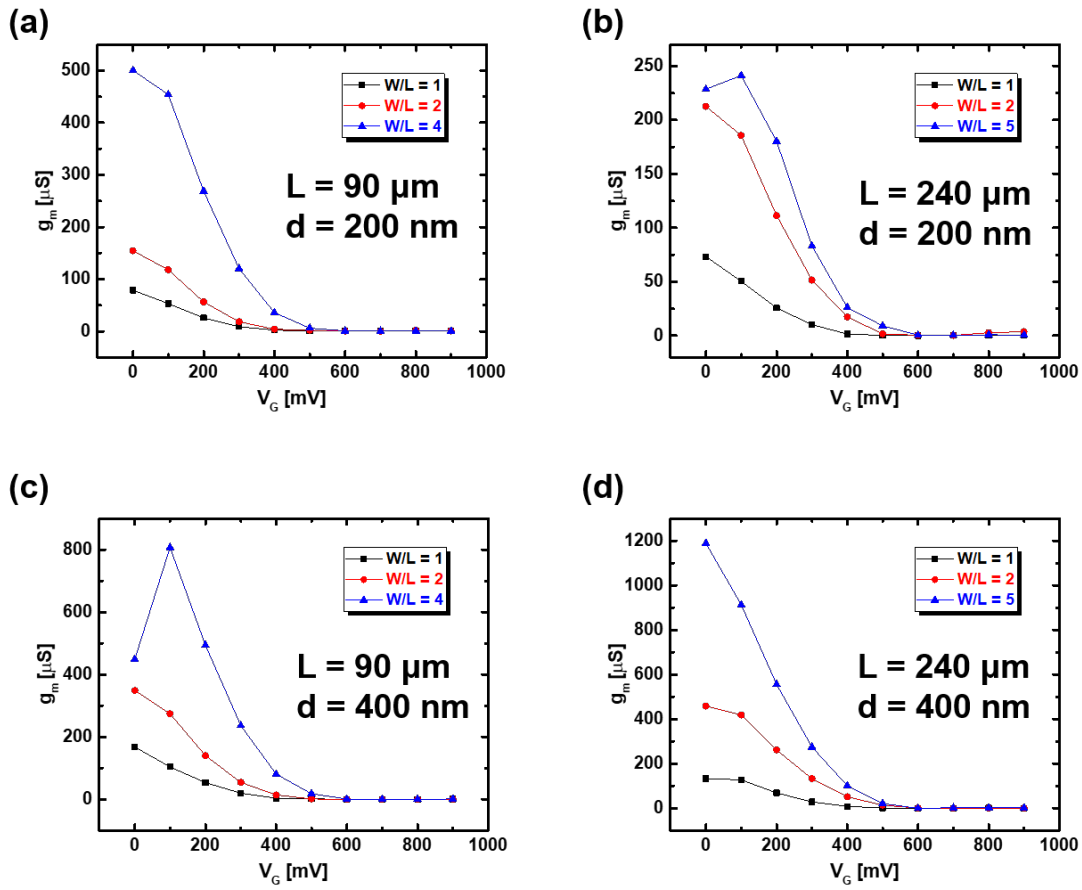

Figure 5.3: g_m curves extracted from the transfer curves at V_D = -0.6 V showing the effect of W/L for Ag-OECTs with channel dimensions of (a) L = 90 μm and d = 200 nm, (b) L = 240 μm and d = 200 nm, (c) L = 90 μm and d = 400 nm, (d) L = 240 μm and d = 400 nm.

Figure 5.2(b),(d),(f) also shows the transconductance curves extracted from the plotted transfer curves. Transconductance (g_m) can be obtained by taking the deriva-

tive of Equation 5.1 and expressed as follows:

$$g_m = \left\{ \begin{array}{ll} -\mu C^* \frac{W}{L} d\, V_D, & \text{for} \quad V_D > V_G - V_T \\ \mu C^* \frac{W}{L} d\, [V_T - V_G], & \text{for} \quad V_D < V_G - V_T \end{array} \right\} \tag{5.2}$$

where the symbols have their usual meanings. Several studies have demonstrated the transconductance of OECT scales with both W/L and the channel thickness [33, 140–142]. This is a unique property that differentiates OECT from other types of FETs [32]. Figure 5.3 shows the transconductance curves extracted for devices with different W/L. On comparing the g_m curves for devices with different channel geometries, it is observed that g_m is proportional to both W/L and d of the OECT. In all these cases, the peak transconductance ($g_{m,max}$) occurs at a gate voltage of 0 or 0.1 V indicating low operation voltages, which is a desired property for biosensing applications. In Figure 5.4 (a), the peak transconductance values extracted for V_D = -0.6 V are plotted against the channel geometry (Wd/L) showing a linear correlation with a correlation factor R = 0.99.

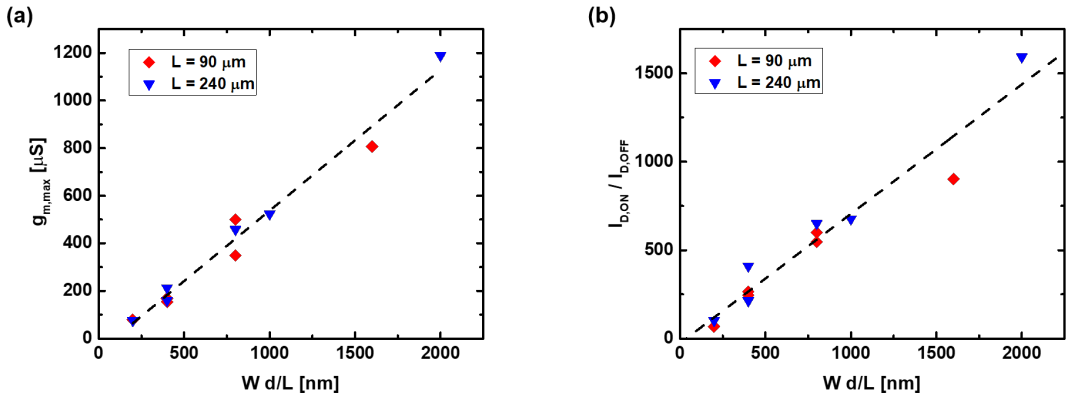

Figure 5.4: (a) Scaling of peak transconductance and (b) scaling of drain current on-off ratio with channel geometry.

Table 5.1 lists the key device parameters extracted for Ag-OECTs with different channel dimensions. The extract device parameters include $g_{m,max}$, V_T, $I_{D,ON}/I_{D,OFF}$, and μC^*. The V_T values were extracted graphically by taking the x-intercept of $\sqrt{I_D}$ vs V_G in saturation from Equation 5.1.

Table 5.1: Device dimensions and parameters of Ag-OECTs.

L [μ**m**]	**W/L**	**d** [**nm**]	$\mathbf{g_{m,max}}$ [μ**S**]	$\mathbf{V_G(g_{m,max})}$ [**mV**]	$\mathbf{V_T}$ [**mV**]	$\mathbf{I_{D,ON}/I_{D,OFF}}$	$\mu\mathbf{C^*}$ [**F cm^{-1} V^{-1} s^{-1}**]
90	1	200	78.63	0	396	68.1	9.93
90	1	400	168.1	0	435	244.6	9.66
90	2	200	154.32	0	409	265.0	9.43
90	2	400	348.65	0	448	546.5	9.73
90	4	200	500.35	0	474	599.8	13.19
90	4	400	807.26	100	526	901.9	11.84
240	1	200	75.4	0	414	101.8	9.11
240	1	400	160	0	460	213.3	8.70
240	2	200	212.64	0	461	409.5	11.53
240	2	400	458.04	0	534	650.8	10.72
240	5	200	523.09	100	540	676.2	11.89
240	5	400	1188.85	0	563	1593.1	10.56

From Table 5.1, higher threshold voltages are observed for the OECTs with the thicker channel, as a large gate voltage is required to drive more cations to fully dedope the entire channel and turn the device off. Similarly, for the OECTs with the same channel length and thickness but larger channel width, more ions are needed to fully turn the device off, and hence a larger V_T was observed from this study. Since all the listed in the table Ag-OECTs had similar off currents levels, $I_{D,ON}/I_{D,OFF}$ is mainly determined by the on-state drain current, which is also scaled with the channel geometry as described in Equation 5.1. Therefore, $I_{D,ON}/I_{D,OFF}$ for these printed Ag-OECTs is linearly correlated with Wd/L with a correlation coefficient of R = 0.97 as shown in Figure 5.4 (b).

Charge carrier mobility and capacitance per unit area are important material prop-

erty parameters that influence the on-state drain current and the transconductance of FETs. As the operation of OECT relies on both efficient lateral electronic transport in the channel film and vertical ionic transport for ions moving in and out of the channel, Inal *et al.* have purposed that the product of charge carrier mobility and capacitance per unit volume (μC^*) can be used as a standard parameter for the direct comparison of active channel materials used for OECTs [30]. As the same PEDOT:PSS ink formulation was used for printing the Ag-OECTs, the μC^* did not show any correlation with the channel geometry variation. The average μC^* for PEDOT:PSS based OECTs is 10.52 ± 1.35 (n = 12) F V^{-1} s^{-1} cm^{-1}. The extracted μC^* value is lower than the average values observed in other studies, which are likely due to different fabrication methods and possible defects in the printed PEDOT:PSS films.

Based on these results, it was observed that devices with higher W/L and d demonstrated higher $I_{D,ON}$ and g_m, and hence are preferred for high sensitivity sensor development. Ag-OECTs with small W/L and lower channel thickness have lower $I_{D,ON}$ and g_m, and hence, external signal amplification may be required when using them as biological and chemical sensors. However, these devices also have lower V_T, which may be beneficial for applications that require low operation voltage and power consumption. In addition, one drawback of OECT is its slow response speed, as the operation relies on ions moving in and out throughout the entire channel thickness. OECTs with thinner channel have faster speed as compared to devices with thicker channel, and hence are more suitable for applications that require rapid changes [7]. One of the intriguing features of OECT is the dependence of device properties on channel thickness. This enables alternation of device sensitivity without the need of changing device lateral dimension. From these results, Ag-OECTs based on two layers of printed PEDOT:PSS with a channel dimension of L = 100 μm and W/L = 4 were small and demonstrated decent transconductance and low operation voltages. Therefore, they were selected for developing the delta-9-tetrahydrocannabinol

(Δ^9-THC) and glucose sensors.

5.3.2 Au-OECT Optimization

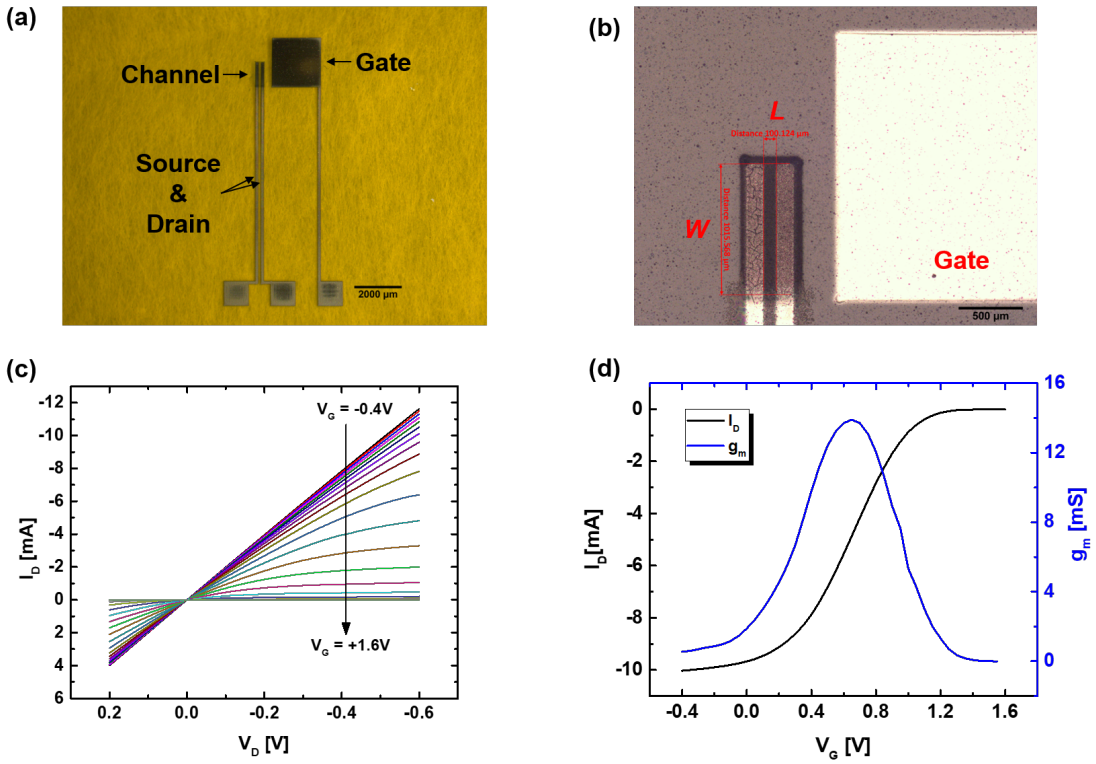

Figure 5.5: (a) Microscope image of an Au-OECT with W/L = 10 and gate size = 4 mm^2. (b) Zoom-in microscope image of the same device showing the measured channel dimensions. (c) I-V characteristics of an Au-OECT with W/L = 10 and gate size = 4 mm^2 measured with 1xPBS as the electrolyte. (d) Transfer and transconductance curves of the same device measured at V_D = -0.6 V.

Even though the printed Ag-OECTs demonstrated decent device performance, there are still some drawbacks to use silver as the contact material. Silver is more reactive than gold. During the device fabrication, silver oxide and silver sulfide may form in the air on the printed electrodes and lead to poor contact with PEDOT:PSS film. The formation of silver tarnish on the printed silver traces deteriorates the device performance. Gold has higher conductivity and better work function alignment with PEDOT:PSS facilitating charge injection; therefore, devices with gold contacts demonstrate improved performance [104]. In addition, gold is well-known for its

excellent biocompatibility. Hence, in this thesis, OECTs with printed Au electrodes were developed and the effect of channel and gate geometrical variations on device performance was studied.

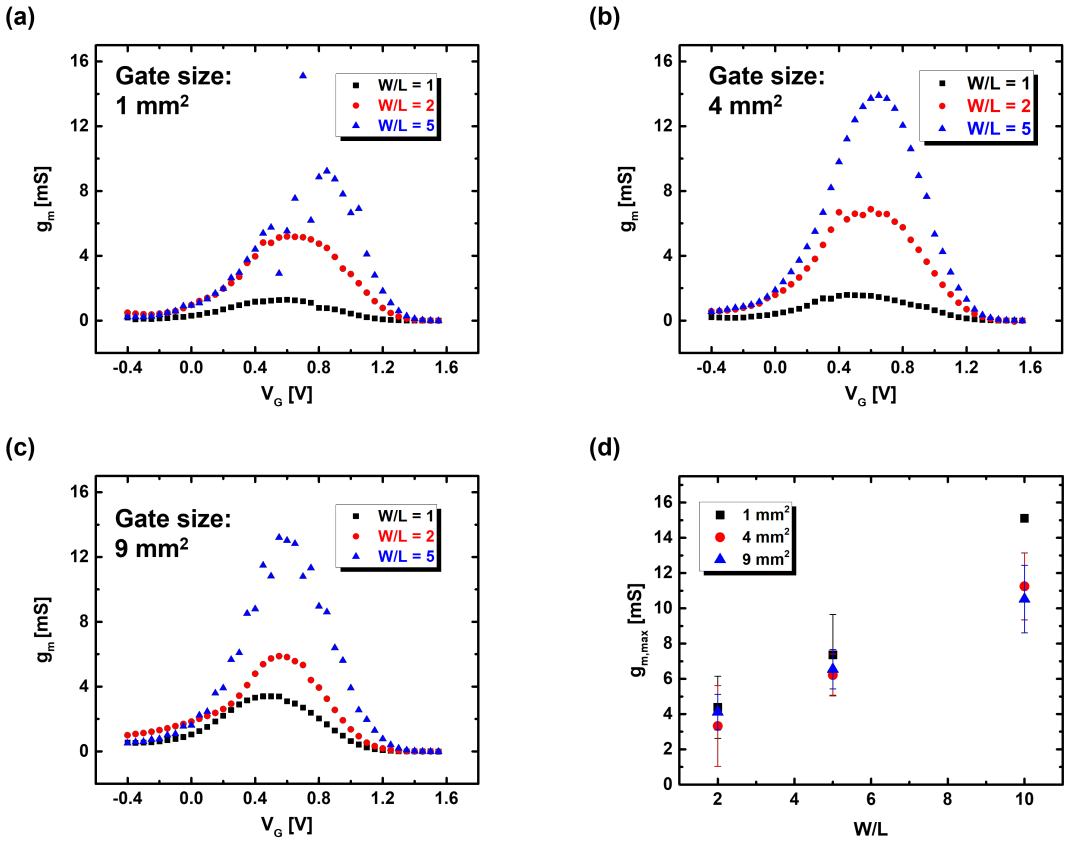

Figure 5.6: Scaling of g_m with W/L extracted from transfer curves measured at V_D = -0.6 V for Au-OECTs with gate size of (a) 1 mm^2, (b) 4 mm^2, and (c) 9 mm^2. (d) Average peak transconductance plotted against W/L for Au-OECTs with different gate sizes. Error bar represents the standard deviation calculated from 5 devices, except only one measurement was collected for OECT with W/L = 10 and gate size of 1 mm^2.

Au-OECTs had a similar device structure as the Ag-OECTs, except that an in-plane printed Au gate was implemented in the device design. Having in-plane gates simplifies the steps required for integrating the OECT with other circuit components for developing biosensing platforms. Figure 5.5 (a) is the microscope image of an Au-OECT showing the device layout. All the Au-OECTs had a constant channel length (L = 100 μm). Two-layer printed channel with an average thickness of 791.3

± 16.9 nm was used for all Au-OECTs. The channel width was varied to achieve different width-to-length ratios (W/L = 2, 5, and 10). As discussed in chapter 2, Au is a polarizable electrode, and the potential drop at the gate/electrolyte is affected by the gate geometry [52]. To study the influence of gate size on the device performance, the printed gate electrode was designed as a simple square shape and its side length was varied to obtain three gate sizes of 1, 4, and 9 mm^2. The microscope image of the Au-OECT shown in Figure 5.5 (a) had a gate size of 4 mm^2 and W/L of 10, and a zoom-in view of the same device is shown in Figure 5.5 (b) illustrating the defined channel parameters.

I-V characteristics of a typical printed Au-OECT (W/L = 10, gate size = 4 mm^2) is shown in Figure 5.5 (c), and a p-type depletion mode behavior was observed. As expected, a higher gate voltage was required to fully turn off the device when using Au as the gate material. As observed from the transfer and transconductance curves in Figure 5.5 (d), the corresponding gate voltages for peak transconductance (V_G ($g_{m,max}$)) were higher for Au-OECTs as compared to the V_G ($g_{m,max}$) values for Ag-OECTs. Since all the Au-OECTs had similar channel thickness, the peak g_m values were plotted only against W/L for OECTs with different gate sizes. As described by Equation 5.2, a linear correlation between the W/L and peak g_m can be observed from Figure 5.6.

As shown in Figure 5.5 (c), Au-OECTs did not saturate. Hence, the device parameter extractions were based on the linear region equations. In addition, linear extrapolation method was used to extract V_T [143–145]. The first step is to find the maximum slope ($g_{m,max}$) of the transfer curve. Then, extrapolating the portion of the transfer curve with maximum slope to find the x-intercept, and V_T is calculated by:

$$V_T = V_x - \frac{V_D}{2} \tag{5.3}$$

where V_x is the x-intercept linearly extrapolated from the transfer curve at its maximum slope. The extracted device parameters for Au-OECTs with different device

geometries are listed in Table 5.2.

Table 5.2: Device dimensions and parameters of Au-OECTs.

Gate size [$\mathbf{mm^2}$]	**W/L**	$\mathbf{g_{m,max}}$ [mS]	$\mathbf{V_G(g_{m,max})}$ [V]	$\mathbf{I_{D,ON}/I_{D,OFF}}$	$\mathbf{V_T}$ [V]	$\mu\mathbf{C^*}$ [$\mathbf{F\ cm^{-1}\ V^{-1}\ s^{-1}}$]
1	2	1.28	0.60	129.21	1.16	13.50
1	5	5.19	0.60	522.20	1.28	21.87
1	10	15.11	0.70	637.74	1.32	31.83
4	2	1.58	0.45	476.79	1.12	16.67
4	5	6.88	0.60	1247.38	1.19	28.96
4	10	13.90	0.65	1777.19	1.24	29.28
9	2	3.40	0.45	977.80	1.19	35.80
9	5	5.88	0.55	1262.89	1.10	24.79
9	10	13.21	0.55	1462.56	1.15	27.82

From Table 5.2, it can be observed that both the peak transconductance and on-off current ratio increase with the increase of channel width-to-length ratio following Equations 5.1 and 5.2, and they are not directly correlated with the change of gate geometry. The main device parameter affected by the gate size is the threshold voltage. For devices with the same lateral channel dimensions, a smaller threshold voltage is observed in Table 5.2. As mentioned in chapter 2, Bernards model considered an OECT as two circuits: an electronic circuit that consists of a resistor and describes the electronic charge flow in the channel between the source and drain contact, and an ionic circuit that consists of a capacitor and a resistor in series and describes the flow of ions in the direction of gate, electrolyte, and channel [31]. The overall capacitor (C_{eq}) in the ionic circuit is equivalent to two capacitors in series that are used to model the electrical double layer formed at the gate/electrolyte interface (C_{GE}) and

the channel capacitance (C_{CH}) [32]. The correlation is expressed in Equation 5.4:

$$\frac{1}{C_{eq}} = \frac{1}{C_{GE}} + \frac{1}{C_{CH}} \tag{5.4}$$

When a small polarizable gate electrode is used, the applied gate potential drop across each capacitor is inversely proportional to their capacitance [52]. As the gate area increases, the potential drop at the gate/electrolyte interface reduces resulting in more effective gating, decrease of the threshold voltage, and shift of the $V_G(g_{m,max})$ to lower values.

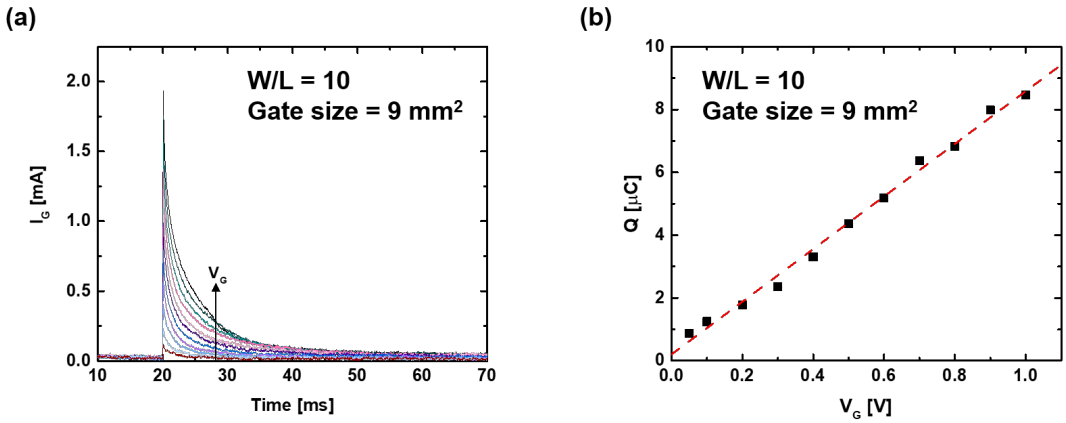

Figure 5.7: (a) Transient gate current (I_G) measured at constant V_D and pulsed V_G with amplitude ranging from 0.1 to 1 V with a step size of 0.1 V. (b) Injected charge (Q) as a function of V_G. The linear fit shows R = 0.99 with a slope corresponding to the C_{CH} of the device.

The average μC^* for Au-OECTs is 25.61 ± 7.19 (n = 9) F V^{-1} s^{-1} cm^{-1}. Even though both Ag-OECT and Au-OECT are based on PEDOT:PSS, different ink formulations were used for the channel printing. As described in chapter 3, the ink formulation used for printing Au-OECTs demonstrated higher conductivity as compared to the ink formulation used for printing Ag-OECTs; and hence, a higher average μC^* was observed. For Au-OECTs, to extract the volumetric capacitance and charge carrier mobility, the gate transient current (I_G) was measured at constant V_D = -0.6 V for pulsed gate voltage with increasing amplitude as shown in Figure 5.7 (a). The ionic charge (Q) injected into the channel was estimated as the area under the I_G curves for

each applied gate pulse as shown in Figure 5.7 (b). The slope of the Q vs V_G curve is the corresponding channel capacitance (C_{CH}). Volumetric capacitance for each device is extracted by dividing the C_{CH} by the volume of the channel. The average volumetric capacitance extracted for Au-OECT using this method is 26.46 ± 3.21 (n = 9) F/cm^3. The average μ is 0.98 ± 0.29 (n = 9) cm^2/Vs. The extracted C* and μ values are lower than the values observed in other literature [30, 33, 146]. Low C* value may be due to lower EG content used in this ink formulation that reduces the hydration and the charge capacity of PEDOT:PSS [146]. Low μ may be attributed to the printed film quality. Another reason for lower C* and μ may be higher parasitic series resistance between the metal contact and the PEDOT:PSS film which limits the device performance [32, 147, 148]. The contact resistance is probably higher for printed OECT as compared to the high quality contact of microfabricated OECTs. Further studies are required to verify these hypotheses.

Hence, for Au-OECTs, the magnitude of I_D, g_m, and $I_{D,ON}/I_{D,OFF}$ increase with W/L. V_T decreases as the gate size increases due to increased C_{GE}. This is a signature feature of OECT, which is useful for tuning parameters to acquire desired sensing range. Smaller Au gate may not be as efficient as the Ag/AgCl or larger Au gate, but by utilizing the change of effective gate voltage, molecular sensing using OECT could be achieved [15, 63, 70, 118, 121]. Based on these optimization, Au-OECT with channel W/L of 10 was selected for detecting binding of biotin and streptavidin using the NHC-modified gate electrode. The Au-OECT with W/L of 10 and gate size of 9 mm^2 was chosen for the development of point-of-care SARS-CoV-2 detection device to ensure high transconductance at low gate voltage and an adequate amount of antibody attachment for higher sensitivity.

5.4 Conclusion

A systematic study of the influences of device geometry on the OECT performance was conducted in this chapter. The study was based on two types of OECTs with

different contact and gate materials. It was observed that for both types of OECTs, g_m, $I_{D,ON}/I_{D,OFF}$ ratio, and V_T are proportional to the W/L and channel thickness. With a different gate material, the device performance is also affected by the gate geometry. Based on these observations, devices with different geometries and materials were selected for different sensing applications in the next few chapters.

Chapter 6

Unfunctionalized Aerosol Jet Printed OECT for Delta-9-tetrahydrocannabinol (Δ^9-THC) Sensing

6.1 Introduction

As demonstrated in many other studies and described in chapter 2 and chapter 4 of this thesis, PEDOT:PSS based OECTs have intrinsic ion sensitivity; and hence, they can be directly used for ion concentration detection [85, 104, 111]. Taking the advantages of electrochemical redox properties of certain molecules, molecular detections could be achieved using unfunctionalized OECTs. One common example is hydrogen peroxide (H_2O_2). There have been numerous enzymatic biosensors developed based on the electrochemical oxidation of H_2O_2 at platinum (Pt) electrode including commercially available glucose sensors. Cicoira *et al.* have demonstrated the detection of H_2O_2 using an OECT with planner Pt gate [60]. Dopamine sensing using OECT with Pt gate was also demonstrated in several studies [62, 120, 121]. The working principle is based on the electro-oxidation of dopamine molecules on the Pt gate surface, which induces Faradaic current that modulates the effective gate voltage and leads to change in the drain current [62]. The same basis may be applied for other chemical and drug detection.

Delta-9-tetrahydrocannabinol (Δ^9-THC) is the main psychoactive ingredient in cannabis products, which can impair the ability to drive safely and increase the risk of fatal accident. Conventional Δ^9-THC testing is performed in centralized laboratories using bulky and complex instruments such as liquid chromatography (LC) and gas chromatography-mass spectrometry (GC-MS). With the legalization and decriminalization of cannabis in various jurisdictions, it is an urgent need to develop a sensitive and accurate disposable biosensor for roadside testing of Δ^9-THC. Δ^9-THC can be detected in various body fluids, such as blood, urine, and saliva. Blood and urine tests are not practicable for roadside screening, whereas saliva sample is easy to collect and more suitable for on-site testing. Moreover, Δ^9-THC exists in saliva at a measurable amount and its level peaks within 1-2 hours after consumption of cannabis products [149]. Therefore, testing salivary Δ^9-THC is highly suitable for on-site roadside screening [150–153].

Electrochemical biosensors based on passive electrodes could be made into portable and disposable sensors, but they often suffer from low signal-to-noise ratio and requires external signal amplifications. Due to low dissolution of Δ^9-THC in aqueous media, the common procedure for sensing Δ^9-THC using electrochemical electrodes usually involves drop-casting of the cannabinol solution dissolved in organic solvent onto the surface of the electrode first, and the measurement is performed after the solvent has fully evaporated. This step is necessary to concentrate the analyte onto the electrode surface [154–156]. Such a method is difficult to be implemented for roadside tests, as there may also be interference from other electroactive substances in saliva.

OECT has intrinsic signal amplification, low operation voltages, and excellent stability when operating in aqueous environments; therefore, it is a promising candidate for developing biosensors for various applications. In this work, we have demonstrated the detection of Δ^9-THC molecules in synthetic saliva buffer using an unfunctionalized aerosol jet printed OECT with PEDOT:PSS channel and an external Pt gate.

In this approach, we have utilized the electrochemical property of Δ^9-THC molecules to achieve the detection.

6.2 Experimental Details

6.2.1 OECT Fabrication

The OECTs were fabricated using Optomec Aerosol Jet 5X printing system on 24.5 μm thick flexible Kapton substrates. The source and drain contacts were printed by ultrasonic atomizer (UA) using commercially available silver (Ag) nanoparticle (NP) ink (Clariant EXPT Prelect TPS 50G2), which was diluted with deionized water with volume ratio of 1:1. The printed Ag traces were annealed in an oven at 130℃ overnight. The PEDOT:PSS ink consists of PEDOT:PSS (Clevios PH-1000) solution with 20% ethylene glycol (EG) (Sigma Aldrich), 0.1% of dodecyl benzene sulfonic acid (DBSA) (Sigma Aldrich), and 0.9% of (3-glycidyloxypropyl) trimethoxysilane (GOPS) (Sigma Aldrich). The PEDOT:PSS ink was then deposited by UA to form the channel region and cured at 130℃ for 20 mins to prevent the dissolution of PEDOT:PSS. Finally, an UV-curable polydimethylsiloxane (PDMS) layer was printed to passivate the source and drain electrodes. The passivation layer was dispensed on the electrodes by the pneumatic atomizer and partially cured while printing with the built-in UV lamp (405 nm, 5 mW) and post annealed at 130℃ for 30 mins.

6.2.2 Electrical Measurements

The electrical measurements were carried out using a Keithley 2612B sourcemeter controlled by a customized LabVIEW program. A platinum (Pt) wire with a diameter of 0.5 mm (267228 from Sigma-Aldrich) was used as the external gate for all the measurements. Measurements were conducted using Δ^9-THC in synthetic saliva buffer. The synthetic saliva buffer (pH = 6.2) contains 27.5 mM sodium chloride, 6.3 mM ammonium chloride, 4.9 mM sodium phosphate (monobasic), 2.9 mM potassium chloride, 1.1 mM sodium citrate (anhydrous), 0.02 mM magnesium chloride

(anhydrous), 0.27 mM sodium carbonate and 0.2 mM calcium chloride [152]. The concentrated Δ^9-THC solution was diluted using the synthetic saliva buffer to obtain different molar concentrations for testing. The output characteristics were measured using the blank synthetic saliva buffer and 1 μM Δ^9-THC solution in synthetic saliva buffer. The drain voltage (V_D) was swept from 0.2 V to -0.8 V for each gate voltage (V_G) stepped from 0 V to 1 V with a step size of 0.1 V. The synthetic saliva Δ^9-THC sensing was carried out with biasing the gate and drain under constant voltages (V_G = 1 V and V_D = -0.1 V). After the I_D settled, 10 μL of a chosen concentration of Δ^9-THC solution was added into the electrolyte at a fixed time interval and the change in the drain current (I_D) was recorded.

6.3 Results and Discussions

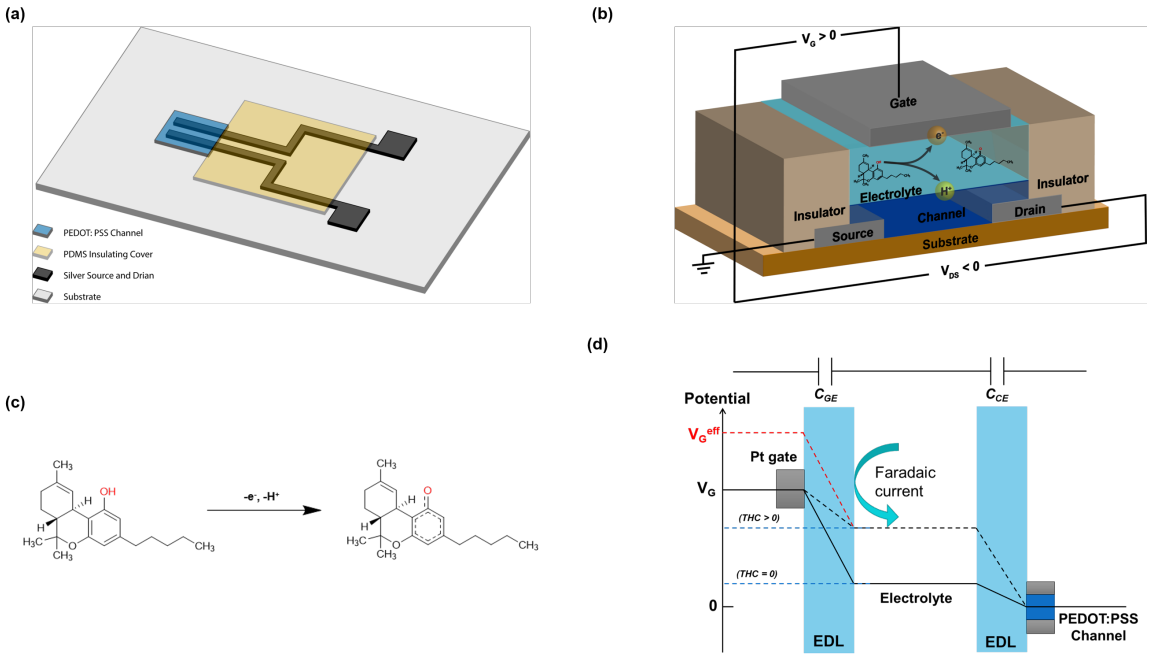

Figure 6.1: (a) Schematic of an aerosol jet printed OECT. (b) Schematic of OECT based Δ^9-THC sensor. (c) Chemical structure of delta-9-tetrahydrocannabinol (Δ^9-THC) and the electro-oxidation of the phenol group on the Δ^9-THC molecule [155, 157]. (d) Potential drops across the two electric double layers (EDLs) at the interfaces of the gate/electrolyte and the channel/electrolyte. The two capacitors, C_{GE} and C_{CE}, are shown as the electrical model to represent the EDLs. (Reproduced from Ref. [63] with permission from the Royal Society of Chemistry.)

Figure 6.1 (a) shows the schematic of the OECT used for Δ^9-THC sensing. The OECTs were printed on flexible Kapton substrates with Ag source and drain contacts and PEDOT:PSS channel. The channel dimensions were optimized as L = 100 μm, W/L = 4 and d = 560 nm. An external Pt wire was used as the gate electrode. A schematic of OECT based Δ^9-THC sensor is shown in Figure 6.1 (b). The working principle of OECT based Δ^9-THC sensor is based on the electro-oxidation reaction of phenol groups as shown in the reaction schematic in Figure 6.1 (c). As a small polarizable electrode was used as the gate in this case, the potential distribution across the gate, electrolyte, and channel interfaces is illustrated by the solid black line in Figure 6.1 (d). The applied gate voltage distributed across the two capacitors, C_{GE} and C_{CE}, which are ascribed to the electric double layers (EDLs) formed at the gate/electrolyte interface and the electrolyte/channel interface, respectively. When Δ^9-THC molecules are introduced to the electrolyte under a positive gate bias, the oxidation of the phenol group on Δ^9-THC molecule generates Faradaic current and leads to change in the potential distribution within the device as illustrated by the black dotted line in Figure 6.1 (d). $V_G{}^{eff}$ is the effective gate voltage that is required to generate the same potential profile without the Faradaic contribution as represented by the red dotted line in Figure 6.1 (d). $V_G{}^{eff}$ is directly proportional to the concentration of Δ^9-THC. Since PEDOT:PSS based OECTs are depletion mode devices, as $V_G{}^{eff}$ increases with the increase of Δ^9-THC concentration, a decrease in the magnitude of I_D is expected.

Preliminary measurement of Δ^9-THC in synthetic saliva buffer was conducted. The output characteristics of a printed OECT measured using synthetic saliva buffer with and without Δ^9-THC are shown in Figure 6.2 (a)-(b). The shift in the transfer curves for these measurements at V_D = -0.6 V is shown in Figure 6.2 (c), and a clear decrease in I_D is observed with the presence of Δ^9-THC. Since various types of ions present in the synthetic saliva buffer, a real time I_D response of aerosol jet printed OECT was measured with blank synthetic saliva buffer to determine the

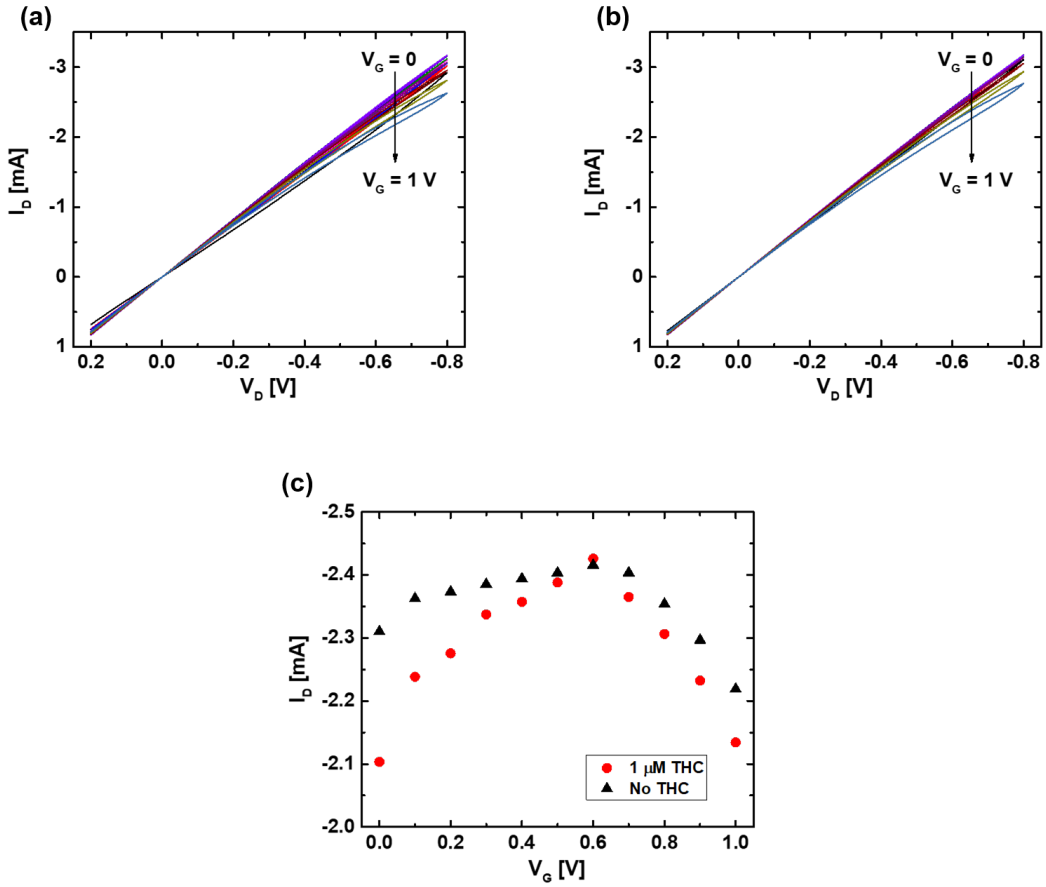

Figure 6.2: The output characteristics of an OECT measured with Pt gate and (a) 1 μM Δ^9-THC diluted in synthetic saliva buffer and (b) blank synthetic saliva buffer as the electrolyte. (c) Shift of transfer curve extracted from the output characteristics at V_D = -0.6 V for the two measurements. There is a clear decrease in the drain current with the presence of Δ^9-THC. (Reproduced from Ref. [63] with permission from the Royal Society of Chemistry.)

measurement baseline. As shown in Figure 6.3 (a), the drain current shown in red, I_D, spiked after the addition of synthetic saliva buffer, which is likely due to the sudden ion injection. We also observed that the gate current, shown in blue, I_G, had a sharp increase with a large amplitude when the solution was added. I_D settles to the same current level as before adding the synthetic saliva buffer after approximately 300 seconds. Therefore, to minimize the interference from adding synthetic saliva buffer, we waited 300 seconds between consecutive Δ^9-THC solution additions.

For synthetic saliva Δ^9-THC spike test, the OECT was biased at constant voltages,

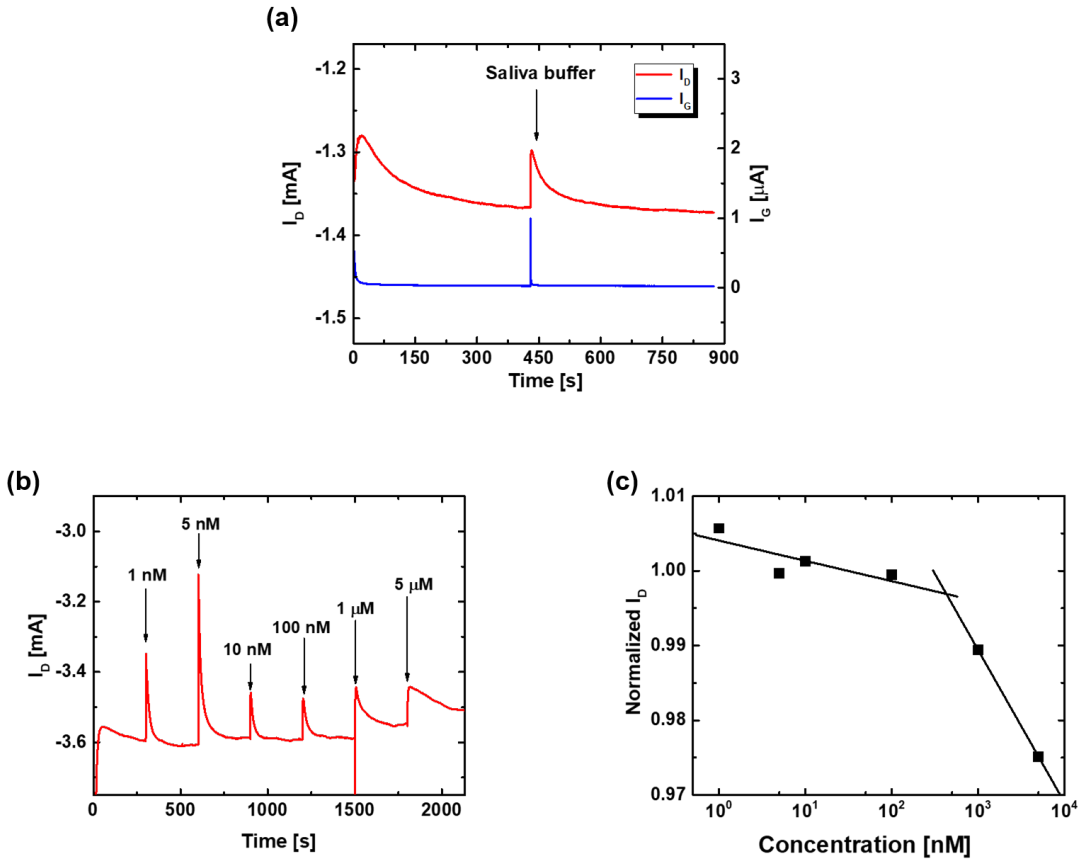

Figure 6.3: (a) I_D response of an aerosol jet printed OECT to the addition of synthetic saliva buffer. A large gate current spike is also observed when the synthetic saliva buffer is added due to a large number of cations available in the solution. (b) I_D response of an aerosol jet printed OECT to the addition of Δ^9-THC diluted in synthetic saliva buffer with different concentrations. (c) Normalized I_D of an aerosol jet printed OECT with the addition of different concentrated Δ^9-THC in synthetic saliva buffer. There are two regions of operation with slopes of -0.003 per dec for 1 – 425 nM and -0.02 per dec for 425 nM – 5 mM. (Reproduced from Ref. [63] with permission from the Royal Society of Chemistry.)

V_G = 1 V and V_D = -0.8 V, and I_D was monitored for each concentration addition. 10 μL of synthetic saliva buffer was used as the background electrolyte and left for about 300 seconds while I_D settled, and then Δ^9-THC solution in synthetic saliva buffer with concentrations ranging from 1 nM to 5 μM was added to the existing electrolyte. With each addition of Δ^9-THC solution, there is a spike in the I_D as seen in the real-time OECT I_D response shown in Figure 6.3 (b). However, due to the effect of ion injection from synthetic saliva buffer, the initial spike after adding the

sample was not considered for the sensitivity analysis. The normalized I_D extracted from the settled I_D regions of Figure 6.3 (b) has been plotted against the Δ^9-THC concentration in Figure 6.3 (c). The sensitivity curve has two distinct slope regions that intercept at 425 nM. A slope of -0.003 per dec was observed for the concentration range of 1 – 425 nM, and a slope of -0.02 per dec was observed for 425 nM – 5 μM. Since the device was not functionalized with bioreceptors for selective detection of Δ^9-THC, it had poor reproducibility for sensing Δ^9-THC in synthetic saliva buffer due to excess ions in the buffer solution.

6.4 Conclusion

In this chapter, synthetic saliva Δ^9-THC concentration sensing was achieved using an unfunctionalized OECT with an external Pt wire as the gate electrode. The working principle of OECT Δ^9-THC sensor is based on the potential change induced by the Faradaic current generated from electrochemical oxidation of Δ^9-THC molecules. These preliminary results demonstrated the potential of utilizing these OECT based biosensors for rapid roadside testing of salivary Δ^9-THC levels. Functionalization of the device with antibody or mediator is necessary to improve selectivity and sensitivity of the sensor and make it directly usable for detecting Δ^9-THC in saliva.

Chapter 7

Functionalization Study of Aerosol Jet Printed Organic Electrochemical Transistor (OECT) for Glucose Detection[1]

Jiaxin Fan, Andres Alejandro Forero Pico and Manisha Gupta*

Department of Electrical and Computer Engineering, University of Alberta, Edmonton, Alberta, T6G 1H9, Canada

*Email of corresponding author: mgupta1@ualberta.ca

7.1 Abstract

In this work, we have conducted a functionalization study on organic electrochemical transistor (OECT) for glucose detection. Functionalization method of a device for biosensing strongly affects its sensitivity and range of detection. Here, glucose sensing study was performed on aerosol jet (AJ) printed OECTs via four different functionalization configurations: unfunctionalized device with floating GOx, PEDOT:PSS channel functionalization with GOx, printed Pt gate functionalization with GOx, and sputtered Pt gate functionalization with GOx, in order to study the effect of functionalization site and utilization of nanomaterials on sensing range and sensitivity. We

[1]This manuscript is accepted as J. Fan, A. A. Forero Pico and M. Gupta, "Aerosol Jet Printed OECT Functionalization Study for Glucose Detection", Materials Advances, 2021, DOI: 10.1039/D1MA00479D.

found that the printed OECT with GOx functionalized printed Pt gate exhibits the best performance. It demonstrates a large glucose (in PBS solution) detection range between 100 nM to 50 mM with two sensitivities of 0.022NR/dec for 100 nM to 250 μM and 0.255NR/dec for 250 μM to 50 mM. The OECT with functionalized printed Pt gate was then evaluated for detection of glucose in artificial sweat buffer, demonstrating a detection range of 0.1 to 10 mM with two linear slopes of 0.068NR/dec for 100 - 500 μM and 0.384NR/dec for 500 μM - 10 mM. Also, AJ printing and laser sintering offers the benefit of simultaneous deposition and patterning of material and rapid annealing of material; and hence, it simplifies the fabrication steps and reduces the fabrication cost. These results confirm that these functionalized printed OECTs based sensors are highly promising for application as non-invasive electrochemical glucose sensors. Thus, clearly for biosensor development, the choice of functionalization site and material is very important.

7.2 Keywords

Organic electrochemical transistor; Aerosol jet printing; glucose sensor; printed electronics; GOx functionalization

7.3 Introduction

Fast and precise portable glucose detection is an increasing important requirement as the number of diabetic population is increasing and will reach approximately 700 million by 2045 [158]. Glucose concentration in blood has been widely used as a disease biomarker for the diagnostic of diabetes. As indicated by the American Diabetes Association (ADA), diabetes not only is a concern for individuals, but also poses a significant burden to the healthcare system with the average annual cost of diagnosed diabetes increased 26% from 2012 to 2017 considering inflation [159]. Monitoring the episodes of hyperglycemia and severe hypoglycemia is important for diabetic patients

to manage their conditions. Therefore, biosensors for measuring glucose level have been rapidly developed, which also drives the market growth for glucose biosensor. In 2015, the market value of glucose biosensor was estimated at 15.3 billion USD, in which the home care diagnostic segment, such as point-of-care glucose meter, accounts for the largest share of 46% [160]. The most used self-testing glucose meters are the finger-pricking devices. They are based on different types of enzyme modified electrochemical electrodes. A blood sample needs to be collected for each measurement from the patient's fingertip. Therefore, for the finger-pricking devices, the reading reflects the blood glucose level for the time window of the blood sampling, and the blood sampling process could be inconvenient for taking the measurements frequently.

Continuous glucose monitor (CGM) is a wearable device that measures the skin interstitial fluid glucose level at regular intervals and 24/7. CGM provides more information about the glycemic variability of an individual and alters the current and as well as the impending hyper- and hypoglycemia. CGM can also be used in conjunction with an insulin pump to reduce the risk of hypoglycemia for the patient [161]. Despite of the potential benefits for glycemic control, the clinical implementation of CGM is still limited due to barriers such as regular calibration requirement with blood glucose meter, sensor accuracy and reliability, and high cost [161, 162].

Studies have shown that salivary [163] and sweat [164] glucose level reflects the change in blood glucose level, and therefore can be used as the monitoring tool to assess the glycemic status of diabetic patients. These studies have offered an opportunity for the development of affordable, non-invasive, and highly sensitive disposable glucose sensors to aid the diabetes management. Organic electrochemical transistors (OECTs) have been extensively studied as biological and chemical sensors for detecting pH [113], ions [112, 120, 123], lactate [16, 119, 165], dopamine [62, 120, 121], uric acid [166], DNA [116], cell [167] and proteins [115]. Organic electrochemical transistor (OECT) is a type of organic thin film transistors (OTFTs), and it exhibits several advantages for biosensing applications, such as intrinsic signal amplification,

low operation voltages, and the ability to operate in aqueous environment. An OECT consists of metal source and drain contact, a conducting polymer channel, an aqueous or gel electrolyte in direct contact with the channel, and a metal gate electrode immersed in the electrolyte. The operation of OECT relies on the electrochemical doping/dedoping of the active channel material due to the injection of ions from the electrolyte driven by the gate bias.

To develop a high-performance biosensor, functionalization of the transducer surface is a critical step to improve the sensitivity and more importantly to achieve the selectivity to the analyte of interest. Various functionalization configurations have been implemented with OECT to expand its applications in biosensing [168]. Two commonly used categories of immobilization techniques are physisorption and chemisorption. Physisorption is the simplest method for macromolecule immobilization. In this case, the surface functionalization is achieved by immersing the surface in the biomolecule solution for fixed durations, and the biomolecules are bound to the surface by weak forces, such as van der Waals forces and electrostatic forces. Physisorption is a cost-effective method, and the conformation and activity of the biomolecules are well preserved after immobilization [169]. Some limitations of physisorption are desorption from the carrier surface and low immobilization efficiency [170]. Chemisorption normally requires multiple steps, in which the surface is first modified with functional groups, and the biomolecules are attached to the surface via strong covalent bonds. Chemisorption forms strong linkages between the biomolecules and the surface, and hence the modified surface is more stable. With the assistance of self-assembled monolayers (SAM), the site-directed attachment can be achieved, which results in a more homogenous surface and improves the immobilization efficiency [169]. However, chemisorption may involve toxic solvents and chemicals, and the biomolecule may lose its functional conformation after immobilization [170]. Nanomaterials have unique properties, and they have been incorporated into various fields. For biosensor device development, nanomaterials have been demonstrated

to enhance the immobilization of biomolecules and promote desired electrochemical reaction due to their large surface area [170, 171].

Another key factor to consider for biosensor design is the region of modification. For an OECT, the channel and gate are the two main sites for functionalization, as they are in direct contact with the electrolyte and the analyte. Depending on the requirements for a specific analyte detection and sensing mechanism, each functionalizing site poses its advantages. When the channel is functionalized, the interaction between the analyte and channel leads to direct device response [8]. The modification of channel interface leads to the change in the interfacial potential, and the binding of analyte modulates the channel current [71, 84, 86]. However, certain functionalization techniques damage the channel material, which results in low sensing performance. Whereas for gate functionalization, the channel remains intact after modification. Furthermore, as OECTs have high transconductance (g_m), any small changes at the gate caused by the interaction with the analyte will be transduced into apparent changes in the channel current [8]. OECTs are commonly fabricated with microfabrication techniques, but they can also be fabricated by various printing techniques such as screen printing [172], inkjet printing, 3D printing [103, 104, 123] and aerosol jet (AJ) printing [63, 105]. Printing technologies provide the benefits of versatility and wide-range material compatibility, and they allow patterning and depositing the material for each layer simultaneously, which reduces the steps and cost of fabrication [8]. As compared to other printing techniques, AJ printing is a non-contact technique, and by utilizing a sheath gas flow along with the carrier gas flow, it is capable to print features that are in the size of a fraction of the nozzle size.

In the past two decades, quite a few research groups have demonstrated OECT based glucose sensors, both functionalized and unfunctionalized, which have exhibited low limit of detection, high sensitivity, and high linearity range [65, 72, 73, 173]. Here, we have conducted a detailed study of which OECT functionalization configuration works the best for glucose sensing. We used fully aerosol jet printed OECTs

with Ag source and drain contact, poly(3,4-ethylenedioxythiophene): polystyrene sulfonate (PEDOT:PSS) channel, and printed/sputtered in-plane Pt gate. The detection of glucose was carried out using the printed OECT with glucose oxidase (GOx) in four different configurations: unfunctionalized OECT with floating GOx, functionalized channel, functionalized printed Pt gate, and functionalized sputtered Pt gate. Physisorption technique was utilized for GOx immobilization for all functionalization cases in this work. The performance of these four types of sensors were evaluated by their detection range, sensitivity, and feasibility as sweat glucose sensor. The sensor speed was not evaluated in this work, as the OECT's response time mainly depends on its channel thickness and ionic transportation [33, 174], which were kept the same for all four functionalization configurations. Based on this study, we observe the functionalized printed Pt gate demonstrated the best glucose sensing performance. This is due to the higher surface area of the printed nanoparticle based Pt gate which makes it very effective for GOx adsorption.

7.4 Material and Method

7.4.1 Device Fabrication

OECTs were printed on polyimide films (Kapton Type HN Films purchased from Cole-Parmer, 25.4 μm thick) using Optomec Aerosol Jet 5-axis (AJ5X) 3D printing system. The system is equipped with two atomizers: ultrasonic (UA) and pneumatic (PA). The UA and PA are used to dispense low and high viscosity materials, respectively. The device layouts were designed in AutoCAD 2018 software and exported as the compatible script for printing by VMTool developed by Optomec. Commercially available silver (Ag) nanoparticle (NP) ink (Clariant EXPT Prelect TPS 50G2) was first diluted with deionized (DI) water with volume (v/v) ratio of 1:1. The diluted Ag NP ink was then used for printing the source and drain contacts of OECT using UA. Two layers of wet printing were used to ensure the continuity of the re-

sulting Ag traces. The thickness of the Ag film is 2.44 ± 0.03 μm after curing in oven overnight at 130℃ and the average conductivity is 2 x 10^5 S/cm. Conductive platinum (Pt) nanoparticle (NP) ink (UT DOTS, INC.) was used for printing the in-plane gate electrode for OECT. The Pt NP patterns were laser sintered by 830 nm laser with 100 mW power. The resulting Pt film has an average thickness of 200 ± 4 nm and conductivity of 7.05 S/cm. The PEDOT:PSS ink was prepared by mixing PEDOT:PSS (Clevios PH-1000) solution with 20% ethylene glycol (EG) (Sigma Aldrich), 0.1% of dodecylbenzene sulfonic acid (DBSA) (Sigma Aldrich), and 0.9% of (3-glycidyloxypropyl) trimethoxysilane (GOPS) (Sigma Aldrich). The PEDOT:PSS ink was then sonicated for 1 hour and filtered through 0.45 μm nylon syringe filter to eliminate any large particles. The filtered ink was then deposited by UA to form channel region on the printed Ag source and drain. UV-curable polydimethylsiloxane (PDMS) (Shin-Etsu KER-4690A/B) was used to passivate the source and drain electrode to prevent shorting from the electrolyte. The PDMS solution was diluted with hexane with a v/v ratio of 3:1. The diluted PDMS ink was dispensed on the electrodes by PA and cured on-the-fly with UV (405 nm 5 mW). A final bake at 130℃ for 30 mins was done on hotplate to ensure the PDMS layer was fully crosslinked.

For devices with sputtered Pt gate electrode, silicon (Si) wafers coated with 500 nm thermal oxide (SiO_2) were used as the substrate. The SiO_2/Si wafer was cleaned in piranha solution for 15 mins and thoroughly rinsed with DI water and dried with nitrogen. The wafer was immediately treated in an automatic hexamethyldisilizane (HMDS) vapour prime oven to promote photoresist adhesion. After patterning with AZ5214 photoresist and MF390 developer, 10 nm of titanium (Ti) and 100 nm of platinum (Pt) were subsequently deposited using a magnetron sputter system, and lift-off was performed in acetone to form the Pt gate electrode. The OECT devices were then printed on the SiO2/Si substrate and next to the patterned Pt gate electrode using the same steps mentioned above.

7.4.2 Enzyme Immobilization

Glucose oxidase (GOx) (from Aspergillus niger, Sigma Aldrich, G2133) was first dissolved in 1x phosphate buffer saline (PBS) (Fisher Scientific) solution (pH = 7.4) to make 32 mg/mL GOx solution. 1 wt% CHIT solution was prepared by dissolving low molecular weight chitosan (CHIT) (Sigma Aldrich) in 1% acetic acid (Sigma Aldrich). The GOx and CHIT solution with a volume ratio of 1:1 was mixed to prepare the final stock solution for functionalization with a GOx concentration of 16 mg/mL. To functionalize the OECT, 3 μL of GOx stock solution was drop-cast using a micropipette onto the channel or the gate region. The device was left to dry for 72 hours at 4℃ . After the GOx immobilization, the functionalized area of the device was rinsed three times with PBS solution and finally with DI water to remove any loose material. The devices were then tested. The enzyme stock solution concentration was optimized based on the performance of OECT based glucose sensor with functionalized channel and printed Pt gate. Supplementary Figure A.1 shows the real time I_D measured for OECTs functionalized with 3 μL of 8 mg/mL GOx stock solution. Smaller detection ranges of 0.2 to 2 mM and 0.1 to 5 mM were observed for OECTs with functionalized channel and functionalized printed gate, respectively. These ranges are not sufficient for detecting the glucose level in sweat. Therefore, the final GOx stock solution of 16 mg/mL was used to extend the range of detection.

7.4.3 Device Characterization

All the electrical measurements were performed at room temperature using a Keithley 2612B source meter controlled by LabView. Each device was characterized using 1x PBS solution as the electrolyte and printed in-plane Pt gate to evaluate their device performance before functionalization. The current-voltage (I-V) characteristics of the devices were collected by biasing the gate voltage (V_G) from 0 V to 1 V with a step of 0.1 V while sweeping the drain voltage (V_D) from 0.2 V to -0.8 V with step size of -0.02 V and measuring the drain current (I_D). The transfer curve (I_D

vs V_G) and transconductance ($g_m = \Delta I_D/\Delta V_G$) were extracted from the device I-V characteristics.

The glucose sensing was conducted by biasing the OECT with constant V_D (-0.2 V) and V_G (0.6 V) and measuring I_D as a function of time. 5 μL of PBS solution was added initially as the background electrolyte, and then 5 μL of D-glucose (Sigma Aldrich) dissolved in PBS with incremental concentrations (100 nM to 50 mM) was consecutively added to the electrolyte at fixed time intervals. For floating GOx experiments, 3 μL of GOx solution (16 mg/mL in PBS) was added to the electrolyte before adding glucose solutions.

To compare the glucose sensitivity over different devices, the change of drain current after adding different concentrated glucose solutions was normalized as following:

$$NR = |\frac{I_D^{conc=0} - I_D^{conc>0}}{I_D^{conc=0}}| \tag{7.1}$$

where NR is the normalized I_D response $I_D^{conc=0}$ represents the drain current before adding glucose to the electrolyte, and $I_D^{conc>0}$ is the drain current after adding glucose solution of a specific concentration.

Artificial sweat buffer was prepared according to the ISO standard ISO-3160-2, which contains 20 g/L NaCl, 17.5 g/L NH_4Cl, 5 g/L acetic acid and 15 g/L lactic acid, and the pH of the solution was adjusted to 4.7 using sodium hydroxide (NaOH). Glucose sensing was conducted in the artificial sweat buffer using the same procedure as the one used for glucose sensing in PBS.

7.5 Results and Discussion

7.5.1 Sensor design and sensing mechanism

Figure 7.1 shows the microscope images of the OECT based glucose sensors developed for this work using four functionalization configurations. For the unfunctionalized OECT with floating GOx, the OECT with printed Pt gate was directly used for glucose detection with GOx added to the electrolyte during the measurement. In

this case, there is no loss for the enzyme amount, and the biofunction of the enzyme remains unaffected. For the functionalized channel, the GOx was immobilized to the channel of the OECT via physisorption as shown Figure 7.1 (b). This configuration was compared with the OECT with functionalized printed Pt gate to determine which functionalization site is preferable. To study the effect of nanomaterials, two functionalized gate configurations were utilized: Pt gate deposited by magnetron sputtering and printed Pt gate using nanoparticle based ink. All the OECTs used in this work have similar dimensions: a gate size of 1 mm^2, a channel length of 100 μm, an average channel width-to-length ratio of 4, and an average channel thickness of 560 nm.

Figure 7.2 (a) - (b) shows the typical output and transfer characteristics of a printed unfunctionalized OECT measured with the printed Pt gate and PBS solution as the electrolyte. When both the channel and gate electrode are immersed in an electrolyte and a positive gate bias is applied, the cations in the electrolyte penetrate the channel and compensate the negative charges on PSS, reducing PEDOT to its less conducting neutral state. This leads to a decrease in the magnitude of drain current. From the transfer characteristics (Figure 7.2 (b)), we observed that these printed OECTs exhibit typical p-type depletion (normally ON) mode behavior as expected. An overall gate to drain bias difference of less than 1 V is preferred in order to avoid water electrolysis. Hence, a constant drain bias, V_D, of -0.2 V was selected for the glucose spike tests. From the transconductance (g_m) curves (Figure 7.2 (c)), the maximum transconductance ($g_{m,max}$) for V_D = -0.2 V appears near V_G value of 0.6 to 0.7 V. Therefore, to maximize the device sensitivity, a gate bias, V_G, of 0.6 V was used for conducting the real time glucose sensing, I_D, measurements.

The glucose sensing mechanism using GOx for functionalization has been explained by other research groups [73, 117, 118, 175]. This is based on the enzymatic reaction of GOx and the glucose molecules and the oxidation of the hydrogen peroxide (H_2O_2)

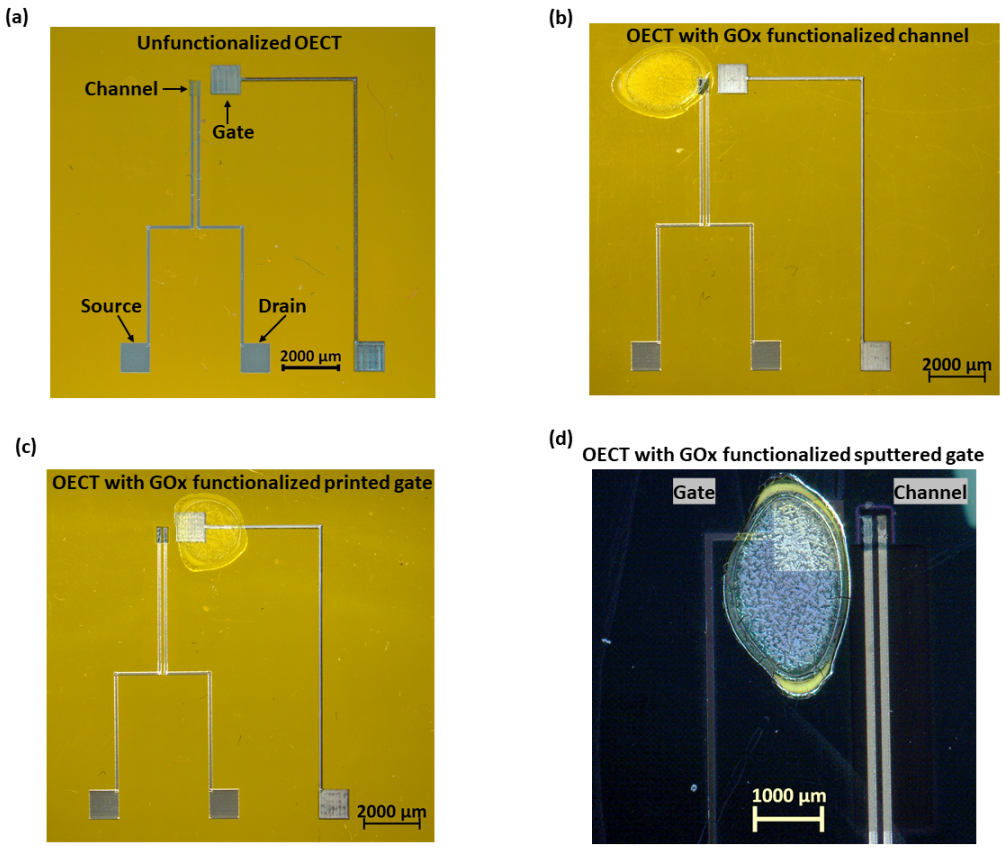

Figure 7.1: Printed OECTs based glucose sensors developed for this work. (a) Microscope image of a printed unfunctionalized OECT on Kapton substrate with printed Ag source and drain contact, PEDOT:PSS channel, and in-plane Pt gate without any modifications. The metal traces were passivated with PDMS mask to prevent shorting during the measurement. (b) Microscope image of a fully printed OECT on Kapton substrate with channel functionalized with GOx for glucose sensing. (c) Microscope image of a printed OECT on Kapton substrate with GOx functionalized printed Pt gate for glucose sensing. (d) Microscope image of a printed OECT on SiO_2/Si substrate with GOx functionalized sputtered Pt gate.

at Pt gate electrode under positive bias as shown in the following chemical reactions:

$$\text{D-glucose} + O_2 \xrightarrow{\text{GOx}} \text{D-glucono-1,5-lactone} + H_2O_2 \tag{7.2}$$

$$H_2O_2 \rightarrow O_2 + 2H^+ + 2e^- \tag{7.3}$$

where O_2 is oxygen molecule, H^+ is hydrogen ion, and e^- represents electron. As small enough voltages are selected to bias the OECT to prevent the electrolysis of water, the device operates in the non-Faradaic regime. From the reaction shown in equation

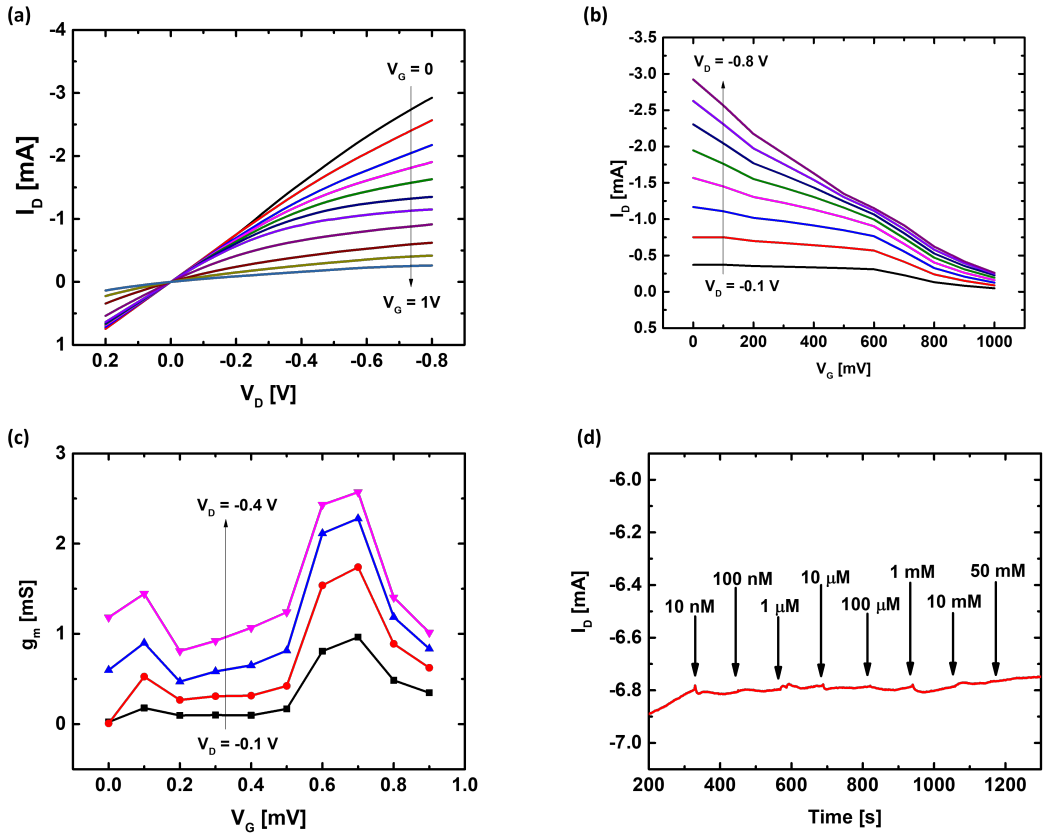

Figure 7.2: (a) Typical output characteristics of a printed OECT measured with PBS electrolyte under different V_G (0 to 1 V). (b) Transfer characteristics under different V_D (-0.1 V to -0.8 V) of a printed unfunctionalized OECT. (c) gm curves extracted for V_D ranging from -0.1 to -0.4 V. (d) I_D shows negligible change with the increase in glucose concentration for an OECT without any GOx functionalization.

7.2, it can be observed that the D-glucose molecules are oxidized to D-glucono-1,5-lactone under the catalytic effect of GOx. The H_2O_2 produced in the process is proportional to the initial glucose concentration. As shown in reaction in equation 7.3, the dissociation of H_2O_2 molecules is catalyzed by Pt and this induces electron transfer (Faradaic current) to the Pt gate electrode. This Faradaic contribution can be described by Nernst's equation. Since the device is under constant bias, the Faradaic current due to H_2O_2 decomposition changes the potential distribution across the gate electrolyte and channel interface which leads to an increase in the effective gate voltage (V_G^{eff}) and a decrease in the magnitude of the drain current ($|I_D|$) [72]. Therefore, a

decrease in $|I_D|$ is expected as the electrolyte glucose concentration increases, which can be used for glucose detection.

To evaluate and compare the performance of the four types of OECT based glucose sensors, the OECTs were biased under constant drain and gate voltage (V_G = 0.6 V and V_D = -0.2 V). The I_D was then measured as a function of time with an incremental concentration of the glucose solution added directly to the electrolyte. Figure 7.2 (d) shows that unfunctionalized OECT, without GOx in the electrolyte, exhibits negligible I_D change with an increase in glucose concentration up to 50 mM. Thus, unfunctionalized OECT cannot be directly used for the detection of glucose concentration.

Figure 7.3 shows the I_D response of the OECTs with four different functionalization configurations to the addition of glucose solution. Figure 7.3 (a) shows the real-time I_D response of the floating GOx case, in which an unfunctionalized OECT with 3 μL of GOx solution was added to the electrolyte before adding glucose and measured with a printed Pt gate. Figure 7.3 (b) shows the I_D response of a printed OECT with GOx physically adsorbed onto the PEDOT:PSS channel region and measured using a printed Pt gate. Figure 7.3 (c) - (d) shows the I_D response of an OECT with GOx functionalized printed Pt gate and the I_D response of an OECT with GOx functionalized sputtered Pt gate, respectively. For all the four different cases, a clear shift of I_D was observed after each glucose addition. As expected, the magnitude of I_D decreases as the glucose concentration increases. The corresponding gate current (I_G) response of the OECTs during glucose measurement for the four functionalization configurations offer additional evidence of the generation of Faradaic current as shown in the Supplementary Figure A.2. For the first few glucose concentrations, because there is less amount of glucose molecules, the current response is much lower as compared to the higher glucose concentration measurements. The real-time I_D response in Figure 7.3 was used to extract the normalized drain current response for the four different functionalization configurations to compare the device sensitivities. The normalized

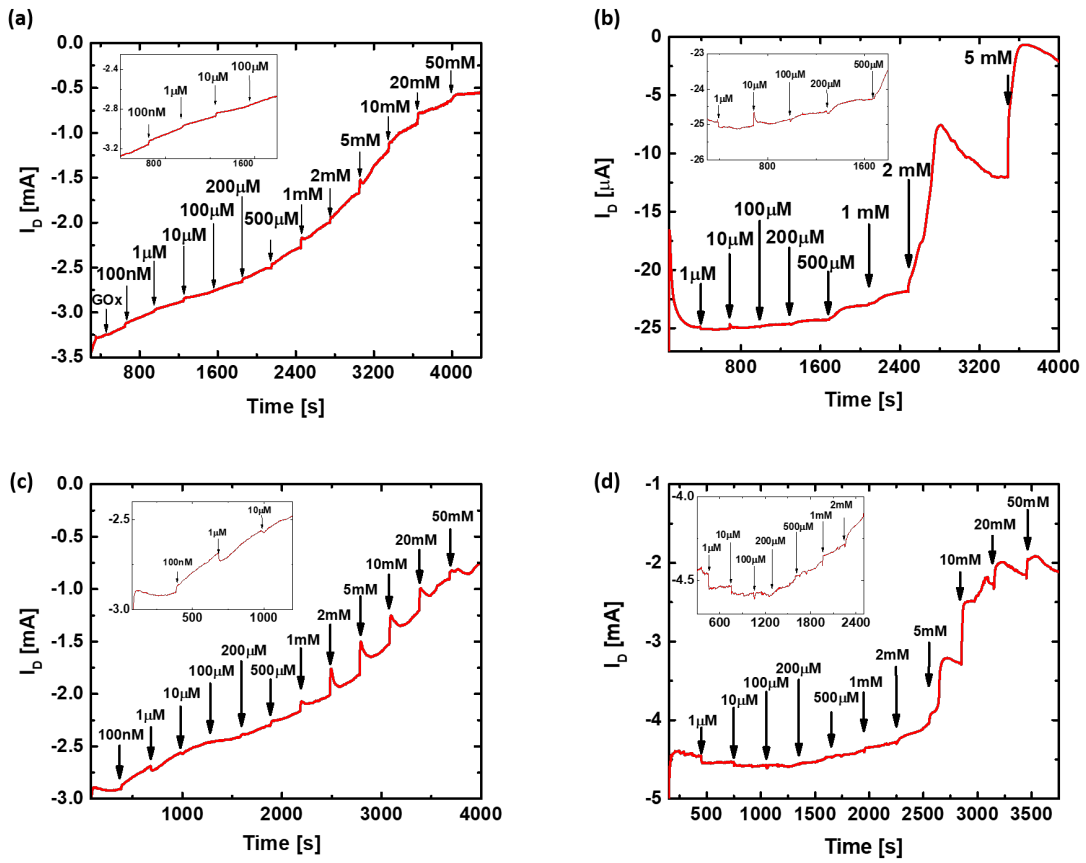

Figure 7.3: I_D response of printed OECTs to additions of glucose solution under constant biases (V_G = 0.6 V and V_D = -0.2 V). (a) I_D response of an unfunctionalized OECT measured with printed Pt gate and floating GOx. (Inset: I_D response to the addition of glucose concentration from 100 nM to 100 μM) (b) I_D response of an OECT with the channel functionalized with GOx and printed Pt gate. (Inset: I_D response to the addition of glucose concentration from 1 μM to 500 μM) (c) I_D response of an OECT with GOx functionalized printed Pt gate. (Inset: I_D response to the addition of glucose concentration from 100 nM to 10 μM) (d) I_D response of a printed OECT with functionalized sputtered Pt gate. (Inset: I_D response to the addition of glucose concentration from 1 μM to 2 mM)

I_D response (NR) was then plotted against the logarithmic glucose concentration as shown in Figure 7.4.

Figure 7.4 (a) shows the NR of the floating GOx case averaged over three different devices. In this case, two distinctive linear regions are observed; a correlation coefficient (R) of 0.993 and sensitivity of 0.020NR/dec is obtained for the glucose concentration range of 100 nM - 153 μM, and R = 0.991 and higher sensitivity of

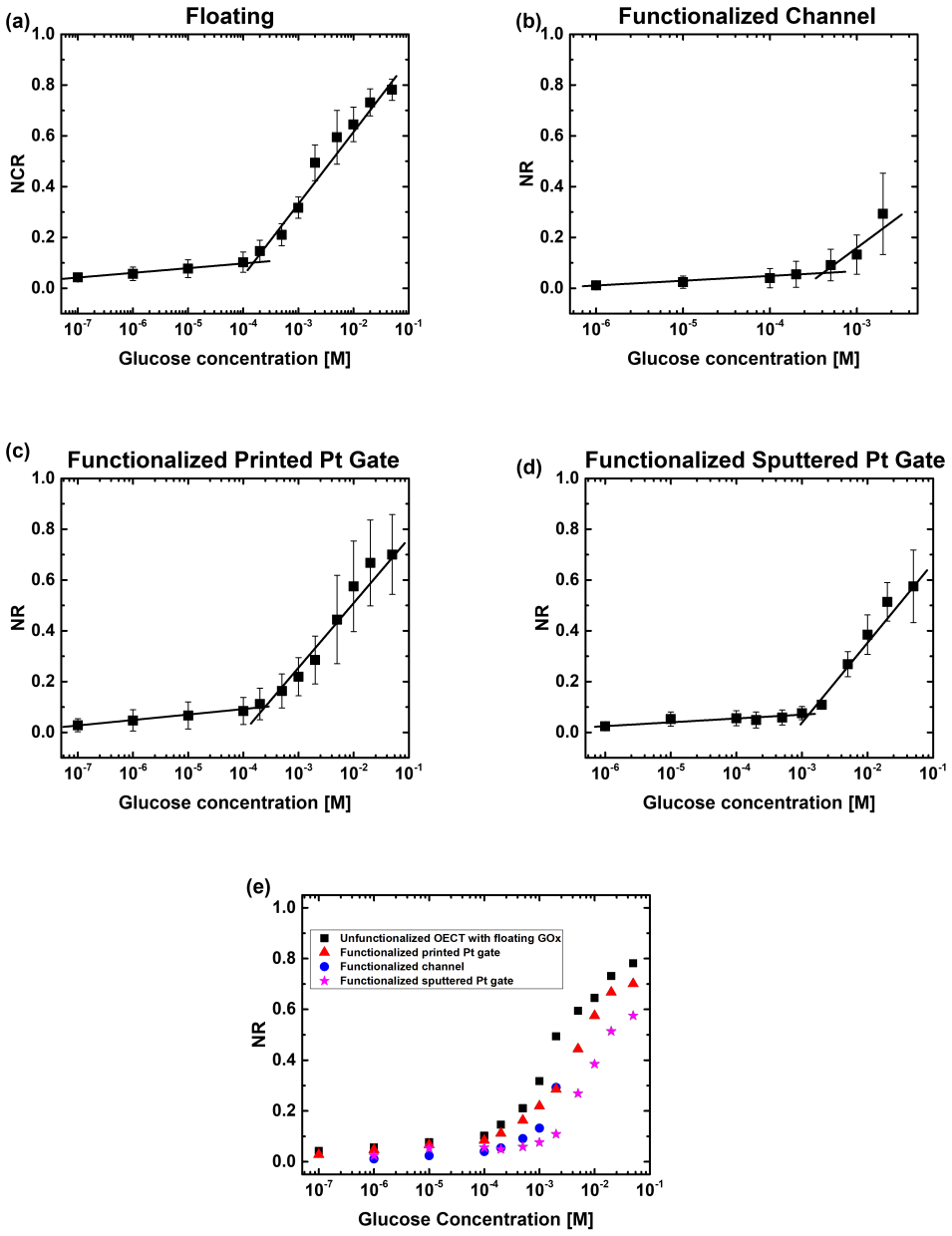

Figure 7.4: Normalized I_D response (NR) of OECT to the logarithmic glucose concentration. (a) The average NR of OECTs with floating GOx and printed Pt gate showing two linear regions with a slope of 0.020NR/dec for glucose concentration of 100 nM to 153 μM and a slope of 0.283NR/dec for glucose concentration of 153 μM to 50 mM. (b) The average NR of OECT with functionalized channel and printed Pt gate with two linear regions showing a slope of 0.019NR/dec for glucose concentration of 10 μM to 413 μM and a slope of 0.254 NR/dec for 413 μM to 2 mM. (c) The

average NR of OECTs with functionalized printed Pt gate showing two linear regions with a slope of 0.022NR/dec for glucose concentration of 100 nM to 250 μM and a slope of 0.255NR/dec for glucose concentration of 250 μM to 50 mM. (d) The average NR of OECTs with functionalized sputtered Pt gate showing two linear regions with a slope of 0.015NR/dec for glucose concentration of 1 μM to 1.3 mM and a slope of 0.314NR/dec for glucose concentration of 1.3 mM to 50 mM. (e) Average NR for all four functionalization methods plotted in the same graph. Error bar represents standard error for all the plots.

0.283NR/dec was obtained for the range of 150 μM - 50 mM. Figure 7.4 (b) demonstrates the NR of OECTs with functionalized channel averaged over three different devices. I_D scaled linearly with a slope of 0.019NR/dec for 1 μM – 413 μM and a second linear slope of 0.254NR/dec for 413 μM – 2 mM is observed in this case. Figure 7.4 (c) shows the average NR of three different OECTs with functionalized printed Pt gate, and two sensitivity regions are also observed here with 0.022NR/dec and R = 0.983 for lower glucose concentration range of 100 nM - 250 μM, and 0.255NR/dec and R = 0.976 for higher glucose concentration range of 250 μM – 50 mM. Figure 7.4 (d) demonstrates the average NR of three OECTs with functionalized sputtered Pt gate. There are also two sensitivity regions in this case. A sensitivity of 0.015NR/dec and R = 0.965 is obtained for 1 μM – 1 mM, and a sensitivity of 0.314NR/dec and R = 0.960 is obtained for glucose concentration range of 1 mM – 50 mM. Two linear slopes are observed for each OECT functionalization configuration. Since a fixed amount of GOx molecules were presented in each functionalization configuration, for the initial low glucose concentration sensing, there were enough free GOx molecules to convert all the added glucose molecules. Thus, as the glucose concentration kept increasing, all the GOx molecules had reacted which led to a reduction in the reaction rate. In addition, as the glucose concentration increased, the H_2O_2 molecules produced also increased. Since the Pt surface area was fixed for each functionalization configuration, the dissociation of H_2O_2 molecules was limited by the surface area at higher glucose concentrations instead of the H_2O_2 molecule diffusion rate for the lower glucose concentrations. The changes in the reaction rate may be the reason why we

observe the two sensitivity ranges for these OECT based glucose sensors.

Figure 7.4 (e) shows the average NR extracted for all four functionalization configurations plotted in the same graph. For the unfunctionalized OECT with floating GOx, since the device was unmodified and the GOx solution was directly added to the electrolyte, the device performance and the quantity and activity of the enzymes were fully preserved. Hence, the OECT responded to a large range of glucose concentration (100 nM to 50 mM). However, this configuration is not suitable for non-invasive glucose sensor development, as it requires an additional step to add the enzyme prior to the test, which could induce potential issues such as inconvenience in testing, additional requirements for the storage and transportation of the enzyme solution, and calibration and/or measurement error due to inconsistent enzyme amount. The printed OECTs with functionalized channel showed poor sensor performance, including a lower detection range of 10 μM to 5 mM and a lower I_D magnitude when compared to the other functionalization configurations. This is likely due to the degradation of the PEODT:PSS film conductivity after GOx adsorption, which leads to the decrease in the device transconductance, and hence lower sensitivity. In addition, it took longer for the H_2O_2 molecules produced at the channel to diffuse to the Pt gate surface and get oxidized, which also contributed to the poor sensor performance. Therefore, channel is not a favored functionalization site for immobilizing GOx by physisorption technique. The OECT with functionalized printed Pt gate exhibited similar sensitivities and detection range as compared to the unfunctionalized OECT with floating GOx, indicating that both the device sensitivity and enzyme bioactivity were not affected by the functionalization. This also indicated that the amount of GOx immobilized onto the gate surface is adequate for glucose detection in the desirable concentration range. Additionally, since GOx is immobilized on the gate, it is more convenient to be directly used as non-invasive glucose sensor. When compared with the channel functionalization, gate is a more appropriate functionalization site to maintain the device performance. Even though the printed OECT with function-

alized sputtered Pt gate had the highest average sensitivity for the higher glucose concentration range (1.3 mM to 50 mM) among the four types of sensors, it was also less sensitive for the lower glucose concentration range (1 μM to 1.3 mM), which is a more important range for developing sweat glucose sensors, as the glucose levels in sweat (0.277 - 1.11 mM) [15, 164] are lower than the levels in blood (3 - 20 mM) [176]. A higher surface roughness of the printed Pt nanoparticle-based film was observed in the scanning electron microscope (SEM) and atomic force microscopic (AFM) images in Figure A.3. The RMS roughness (R_q) of the printed Pt thin film was 13.8 nm, which is approximately 16 times of the value for the sputtered Pt thin film (R_q = 0.852 nm). The higher surface area of the printed Pt films facilitates more GOx adsorption per unit area and the electrochemical oxidation of H_2O_2, which results in higher sensitivity for low glucose concentration range. Hence, among the four types of OECT based glucose sensors we found that the printed Pt gate functionalization was the most suitable one for sweat glucose detection.

Our results along with some other OECT based glucose sensors reported in the literature are listed in Table 7.1. Several studies have utilized nanomaterials, such as nanoparticles and graphene, and demonstrated improvement in the limit of detection and sensor sensitivity due to their excellent electrical and chemical properties and, more importantly, higher surface area to volume ratio, which improves the electrocatalysis and enzyme immobilization [72, 166, 178]. In our case, we have utilized a nanoparticle-based ink for printing the gate electrode and demonstrated an improvement in the limit of detection and sensitivity for lower concentration range as compared with the sample prepared using magnetron sputtering. In addition, utilizing AJ printing technique is capable of achieving high particle density films by a one-step nanoparticle ink patterning and deposition and rapid film annealing by laser sintering. Another type of key material used by many groups is biopolymers, such as CHIT and Nafion, which improve enzyme immobilization due to their excellent biocompatibilities [72, 166, 178]. Similarly, in this study, the OECT with the en-

Table 7.1: Comparison of the detection range and sensitivity of different types of OECT based glucose sensors

Channel material	Gate material	Sensing technique	Detection range	Sensitivity	Ref.
PEDOT:PSS	AJ printed Pt	Floating GOx	100 nM – 153 μM	0.020NR/dec	This work
			153 μM – 50 mM	0.283NR/dec	
CHIT/GOx/ PEDOT:PSS	AJ printed Pt	Immobilized GOx	10 μM – 413 μM	0.019NR/dec	This work
			413 μM – 5 mM	0.254NR/dec	
PEDOT:PSS	CHIT/GOx/ AJ printed Pt/	Immobilized GOx	100 nM – 250 μM	0.022NR/dec	This work
			250 μM - 50 mM	0.255NR/dec	
PEDOT:PSS	CHIT/GOx/Pt	Immobilized GOx	1 μM – 1.3 mM	0.015NR/dec	This work
			1.3 mM – 50 mM	0.317NR/dec	
PEDOT:PSS	Pt	Floating GOx	1 μM – 10 mM	0.01NR/μM	[177]
PEDOT:PSS	Nafion/GOx/ Pt NPs TNTA	Immobilized GOx	100 nM – 5 mM	0.0082NR/dec	[72]
PPy/rGO	PPy/rGO/PA6/ GOx/Nafion	Immobilized GOx	1 nM - 5 μM	0.773NR/dec	[166]
PEDOT:PSS	CHIT/GOx/Pt NPs PEDOT:PSS/Au	Immobilized GOx	10 μM - 5 mM	0.4762NR/mM	[178]
NDI-T2 (P90)	GOx/Au	Immobilized GOx	10 nM – 20 mM	0.26NR/dec- 16.32NR/dec	[173]

PPy: polypyrrole
rGO: reduced graphene oxide
TNTA: TiO_2 nanotube array

zyme modified printed gate shows similar detection range and sensitivity with the unfunctionalized OECT tested with floating GOx, indicating that the bioactivity of the enzyme is well preserved after immobilization.

7.5.2 Glucose sensing in artificial sweat buffer

Glucose sensing in artificial sweat buffer was conducted using the OECT with functionalized printed Pt gate, as it exhibited the best performance among the four functionalization configurations. The measurements were carried out with biasing the OECT at constant voltages (V_G = 0.6 V and V_D = -0.2 V) and using artificial sweat buffer as the background electrolyte. Once I_D settled, 10 μL of glucose solutions dissolved in the artificial sweat buffer with concentrations of 100 μM, 500 μM, 1 mM, and 10 mM were consecutively added to the electrolyte, and the change in I_D and I_G were recorded as shown in Figure 7.5 (a). Distinctive decrease in I_D (black curve)

after each glucose addition can be observed, and the increase in I_G (blue curve) is a clear indication for the Faradaic current due to H_2O_2 oxidation. This detection range covers the glucose levels found in human sweat (0.227 - 1.11 mM). When compared to the measurements conducted using PBS solution, I_D took longer time to settle after each glucose solution addition. The slower response might be attributed to the composition and pH difference of the two types of buffer solutions, which leads to slower molecule diffusion rate and change in the enzymatic activity of GOx. Figure 7.5 (b) shows the corresponding normalized $I_D$response of printed OECT with printed Pt gate averaged over three different devices. Like the measurements conducted in PBS solution, there are two sensitivity regions with a slope of 0.068NR/dec and R = 1 for sweat glucose concentration range of 100 μM - 500 μM and a slope of 0.384NR/dec and R = 1 for sweat glucose concentration range of 500 μM - 10 mM.

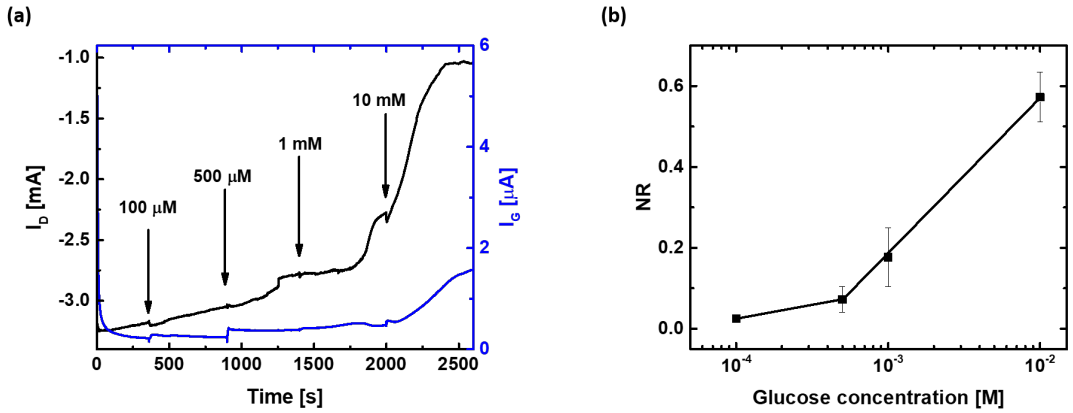

Figure 7.5: (a) I_D response of a printed OECT with GOx functionalized printed Pt gate to the additions of glucose solutions dissolved in artificial sweat buffer. (b) Average NR of printed OECTs with functionalized printed Pt gate to the logarithmic sweat glucose concentration. Two linear regions are observed with slopes of 0.068NR/dec and 0.384NR/dec for concentration ranges of 100 μM - 500 μM and 500 μM – 10 mM, respectively. Error bar represents the standard error.

Table 7.2 summarizes some previously reported transistor and electrode based sweat glucose biosensors along with our printed OECT based sweat glucose sensor. Most of these sweat glucose biosensors have utilized nanostructures or nanomaterials to increase the surface-to-volume ratio of the active area of the device for improving

the sensing performance for low concentration detection. It also has been demonstrated that pH value of the testing solution affects the sensitivity of the glucose sensors [19, 179, 180]. As human sweat has a pH ranging from 3 to 6.5 with average value of 4.8 [181], the pH value should be taken into consideration when developing sweat glucose sensors. Future improvement of these printed OECT based glucose sensors would include channel dimension optimized for specific concentration ranges to improve the sensitivity and pH calibration to improve the accuracy.

Table 7.2: Summary of glucose biosensors for artificial or human sweat glucose analysis.

Device	**Sample Solution**	**Detection Range**	**Ref.**
Printed OECT	Artificial sweat	0.1 -10 mM	This work
In_2O_3 nanoribbon transistor	Artifical Sweat	0.1 μM - 1 mM	[15]
Solution gated graphene transistor	Artificial sweat	0.01 – 31 mM	[182]
Fiber electrode	Artificial sweat	0 – 0.5 mM	[183]
rGO nanocomposite electrode	Human sweat	0 – 2.4 mM	[180]
Zinc Oxide (ZnO) based electrode	Human sweat	0.01 – 200 mg/dL (0.55 μM – 11 mM)	[184]

Here, we have demonstrated that different OECT functionalization configurations affect the sensing range and sensitivity using the example of a OECT based glucose sensor. The choice of functionalization technique and site depends on the materials used for the device fabrication and configuration, the bio-recognition element to be attached to the surface, and the analyte to be detected. Physisorption may not be a suitable technique for immobilizing all types of biomolecules. For instance, chemisorption techniques are more frequently used for antibody functionalization, as antibodies, which are often used in the development of immunosensor due to their

high binding specificity, experience conformational changes during the adsorption process and this leads to a decrease in their bioactivity [185]. Field-effect transistors (FETs) with different active channel materials benefit from various functionalization sites. An extended gate configuration is adopted by ion-sensitive field-effect transistors (ISFETs) that are based on metal-oxide semiconductor field-effect transistors (MOSFETs). In this sensor architecture, a functional extended gate can be integrated with a standard MOSFET, and gate functionalization improves their selectivity with high sensitivity [186–188]. Recent studies of SARS-CoV-2 antibody functionalized FET biosensors have used carbon-based nanomaterials as their active channel. Carbon based nanomaterials facilitates chemisorption with antibodies; hence, in these studies, the antibodies were directly functionalized onto the channel. These sensors were ultrasensitive to the targeted antibody-antigen binding [189, 190]. Another factor to consider for biosensor design is the type of analyte solution. The stability and activity of attached biomolecules in the analyte solution and any inhibitors or competing entities present in the analyte solution may all have an impact on the biosensor performance. Thus, based on the analyte to be detected and the type of sensor different approaches can be chosen for functionalization.

7.6 Conclusion

In this work, we demonstrated the use of aerosol jet printed OECTs with in-plane Pt gate for glucose detection with four different functionalization configurations: unfunctionalized OECT with floating GOx, functionalized channel, functionalized printed Pt gate, and functionalized sputtered Pt gate. The glucose detection range and sensitivity were extracted and compared for all four functionalization configurations. The printed OECT with the printed Pt gate exhibited the best sensing performance with a large glucose detection range of 100 nM–50 mM in PBS. By using the nanoparticle-based Pt ink for gate printing and biopolymer for enzyme immobilization, the functionalized device exhibited an improved limit of detection and a higher sensitivity to

a lower glucose concentration range. The printed OECT with functionalized printed Pt gate shows two different sensitivity of 0.022NR/dec for 100 nM to 250 μM and 0.255NR/dec for 250 μM to 50 mM and is the most suitable for application as sweat glucose sensor. Glucose sensing in artificial sweat buffer using OECT with functionalized printed Pt gate demonstrated a detection range of 0.1 to 10 mM, which covers the sweat glucose range, with two linear slopes of 0.068NR/dec for 100 - 500 μM and 0.384NR/dec for 500 μM - 10 mM. Thus, clearly the functionalization strategy is an extremely important parameter in designing a biosensor. For the glucose detection, we found the nanostructured gate electrode functionalization to be the best option. The sensor design will have to be modified for sweat collection [191] for use as a wearable glucose sensor. Both pH and temperature affect the GOx enzyme activity. Thus, integrating these would improve the glucose measurement. In addition, a sensor array and/or logic circuit may also be implemented to improve detection accuracy. Also, it would be beneficial to be able to transfer the data from the wearable sensor to the user's cell phone and healthcare professionals. This will enable remote monitoring of patients' conditions including people in remote locations. Thus, this is an enabling technology that can be utilized for wearable sensors.

Chapter 8

Aerosol Jet Printed OECT with N-heterocyclic Carbene (NHC) Functionalized Gate for Biosensing Applications

8.1 Introduction

Organic electrochemical transistors (OECTs) have attracted great research attention during the past few decades for developing the next-generation bioelectronics [192], as they are compatible with aqueous environments with low operating voltages and capable of converting the ionic signal to electrical signal with intrinsic amplification. Biological and chemical sensing has been achieved by altering the device materials and functionalizing the device surfaces. Surface functionalization is the key to improve selectivity and sensitivity of a biosensor. OECTs are three-terminal devices with source, drain, and gate contacts. As both the channel and the gate are immersed in an electrolyte and in direct contact with the analyte, the surface modification has been focused on the channel and gate electrode surfaces. Functionalizing the channel provides a direct indication of the interaction with the analyte, but it may lead to deterioration of the channel material and device performance, thus is less preferred. Gate functionalization offers the advantage of tailoring the interfacial properties without affecting the channel conductivity. By using an external gate electrode, the function-

alization process can be completely separated from the other part of the device to help retaining the device performance and achieving better sensitivity. In this work, gold was selected as the gate material as it is inert, biocompatible, and capable of withstanding harsh chemical cleaning processes.

As mentioned in chapter 2, even though physisorption is the simplest functionalization method, it suffers from poor stability and may not be suitable for all types of biomolecules. Chemisorption techniques are often used for immobilizing antibodies, as strong covalent bonds are formed between the biomolecules and the surface, and the orientation of attachment could also be controlled to obtain more homogenous surface. Self-assembled monolayers (SAMs) of organic molecules are widely used to activate the surface with functional groups to facilitate biomolecule attachment. Utilizing the interaction between sulfur and gold, thiol-based ligands are the most common molecule class for functionalizing gold surface. Thiol-based functional groups have been widely implemented in biomolecule sensing technologies [78, 88, 193–195]. However, the main challenges associated with the thiol-base SAMs are their rapid oxidation and degradation under ambient conditions [196–199]. The instability of thiol functionalized surfaces is one of the most serious problems for applications under ambient and aqueous environments which are often required for biosensing applications. In 2014, Crudden *et al.* have demonstrated ultra stable N-heterocyclic carbene (NHC) SAMs on gold surfaces. Once bound to the Au surface, NHC based SAMs have shown high thermal, hydrolytic, chemical, oxidative, and electrochemical stabilities [200] which are promising properties for biosensor development. There have been a few biosensors developed using NHC modified Au surface, and they are mainly optical sensors based on surface plasmon resonance [201, 202]. Mayall *et al.* were the first to demonstrate an electrochemical biosensor based on NHC modified Au for measles virus detection [193].

In this chapter, we developed a biosensor using an aerosol jet printed OECT in conjugation with an external planer printed Au gate functionalized with NHC.

The biosensor showed selectivity towards streptavidin protein, and the detection was achieved by functionalizing the external gate electrode with biotin which is linked to the surface by NHC based ligands. As the gate functionalization process was completely separated from the OECT, the device performance was not affected. This work has presented an alternative method to expand the sensing capability of OECT based biosensors and can be viewed as a generalized biosensor technology platform that is easy to be adapted to other biomolecule detection.

8.2 Experimental Details

8.2.1 Au Electrode and OECT Fabrication

The Au gate electrodes and OECTs were printed using Optomec Aerosol Jet 5X 3D printer on flexible polyimide (Kapton) substrates. The Au gate, source and drain electrodes of OECT were printed using gold nanoparticle (Au NP) ink (UT Dots, Inc.) which was deposited using the ultrasonic atomizer (UA). The printed Au traces were annealed at 280℃ for 1 hour on a hotplate. The channel of OECT was printed with UA using poly(3,4-ethylenedioxythiophene) polystyrene sulfonate (PEDOT:PSS) mixture consisted of 94% Heraeus Clevios™ PH-1000, 5% ethylene glycol (EG), 0.1% dodecylbenzenesulfonic acid solution (DBSA) (70 wt.% in isopropanol), and 1 wt.% (3-glycidyloxypropyl) trimethoxysilane (GOPS) ($\geq$ 98%) and annealed in an oven at 130℃ for 20 minutes. Finally, a layer of UV-curable polydimethylsiloxane (PDMS) (Shin-Etsu Chemical Co., Ltd.) diluted by hexanes with volume ratio of 3:1 was deposited by the pneumatic atomizer (PA) to protect the metal traces from shorting with the liquid electrolyte. The PDMS insulating layer was cured with UV on-the-fly while printing and then post annealed at 130℃ for 30 minutes.

8.2.2 Au Electrode Functionalization

Alkyne-NHC Au

Before functionalization, the printed Au gate electrodes were cleaned thoroughly with acetone, isopropanol, ethanol, and deionized water, dried under nitrogen, and kept under vacuum. The Au electrodes were fixed to the sidewall of a round bottom flask using double sided Kapton tapes to ensure they were in place during the reaction process. The functional groups were deposited by immersing the Au electrode in a heated solution of the NHC ligand and potassium *tert*-butoxide dissolved in anhydrous acetonitrile under nitrogen environment for 2 days. The functionalized electrodes were cleaned with acetonitrile and dimethyl sulfoxide (DMSO) and fully dried under vacuum for 4 hours. The deprotection of the terminal alkyne groups was carried out by placing the Au electrodes in a solution of K_2CO_3 in methanol/THF (1:1) for 30 minutes. The resulting alkyne-NHC Au electrodes were cleaned with methanol and dried under nitrogen.

Copper(I)-catalyzed alkyne-azide cycloaddition

Copper(I)-catalyzed alkyne-azide cycloaddition (CuAAC) was used to attach fluorescein and biotin to the alkyne-NHC functionalized Au electrodes. The click chemistry was performed under ambient condition following the references [203, 204].

To verify the click chemistry reaction, azide-fluorescein was used to modify the Au electrode, which can be then used to take fluorescence images after surface functionalization. The reaction was carried out by mixing azide-fluorescein (1 equiv.), copper(II) sulfate pentahydrate ($Cu_2SO_4{\cdot}5H_2O$) (2 equiv.), and L-ascorbic acid (L-AA) (10 equiv.) in 20 mL ultrapure water in dark for 24 hours. After reaction, the electrodes were rinsed multiple times and soaked in DI H_2O for 1 hour to remove the unreacted molecules. The functionalized electrodes were then dried using nitrogen and kept in dark under vacuum before taking fluorescence images.

The immobilization of biotin was carried out by immersing the NHC functionalized

Au electrodes in a solution of 1 equiv. azide-PEG_7-biotin, 2 equiv. $Cu_2SO_4 \cdot 5H_2O$, and 10 equiv. L-AA in 20 mL ultrapure H_2O for 24 hours. The electrodes were then rinsed and soaked in DI H_2O for 1 hour to remove the unreacted molecules and dried under nitrogen. The biotin functionalized electrodes were kept in a sample desiccator before the measurements.

8.2.3 X-ray Photoelectron Spectroscopy (XPS) Characterization

XPS measurements were performed using a Kratos Axis (Ultra) spectrometer with monochromatized Al Kα (hν = 1486.71 eV) and calibrated using the binding energy (84.0 eV) of Au $4f_{7/2}$ with respect to Fermi level. The measurements were carried out with an analysis chamber pressure lower than 5×10^{-10} Torr. A hemispherical electron-energy analyzer with pass energy of 20 eV was used to collect core-level spectra, while survey spectrum within binding energies ranging from 0 to 1100 eV was collected at analyzer pass energy of 160 eV. Charge effects were corrected by using C 1s peak at 284.8 eV. A Shirley background was applied to subtract the inelastic background of core-level peaks. Non-linear optimization using the Marquardt Algorithm (CasaXPS) was used to determine the peak model parameters such as peak positions, widths, and peak intensities. The peak fitting was based on a product of Gaussian and Lorentzian functions. CasaXPS was used for component analysis to fit the high-resolution spectra of C 1s and N 1s.

8.2.4 Fluorescence Imaging

The printed Au electrodes modified with fluorescein via click chemistry were imaged a ChemiDoc™ MP gel imaging system with the samples immersed in 1xPBS solution and the Alexa 488 filter.

8.2.5 Electrochemical Measurements

The electrochemical measurements were conducted using a Gamry Reference 600+ potentiostat. All the measurements were performed at room temperature using a standard three-electrode configuration where the modified printed Au electrode acting as the working electrode, a Pt counter electrode, and an Ag/AgCl (in saturated KCl) reference electrode were used. All the measurements were carried out in a 10 mL cell containing 5 mM $K_4Fe(CN)_6/K_3Fe(CN)_6$ aqueous solution with 100 mM KCl supporting electrolyte. The cyclic voltammetry measurements were collected by scanning between -0.2 and +0.7 V vs Ag/AgCl with a scan rate of 50 mV/s for three cycles, and the third cycle was used for analysis. The EIS measurements were obtained at the frequency range of 0.01 Hz to 100 kHz with 5 mV AC amplitude and a DC potential at 0.3 V vs Ag/AgCl. Echem Analyst software was used to analyze the data. The constant phase element (CPE) with diffusion equivalent circuit model (as shown in Appendix B) was used for analyzing the impedance results.

8.2.6 Electrical Characterization and Measurements

All the electrical measurements of OECT were performed using a Keithley 2412B sourcemeter and signatone micropositioner probes controlled by LabVIEW. 1xPBS was used as the electrolyte for all the measurements. The transfer characteristics were obtained by measuring the drain current (I_D) under a constant drain bias (V_D) of -0.2 V and sweeping the gate voltage (V_G) from -0.4 to 1.2 V.

Streptavidin (SA) and bovine serum albumin (BSA) proteins were dissolved in 1xPBS to 1 mg/mL solutions. For measuring the biotin-streptavidin binding, 50 μL of 1 mg/mL SA solution was placed onto the biotin-functionalized printed Au electrode for 1 hour, and the electrodes were thoroughly washed with PBS and DI water before any measurements. To test the selectivity of biotin-functionalized Au electrode, it was immersed in 50 μL of 1 mg/mL BSA solution, thoroughly washed with PBS and DI water, and used for electrochemical and OECT measurements.

8.3 Results and Discussions

8.3.1 Printed Au Electrode Functionalization

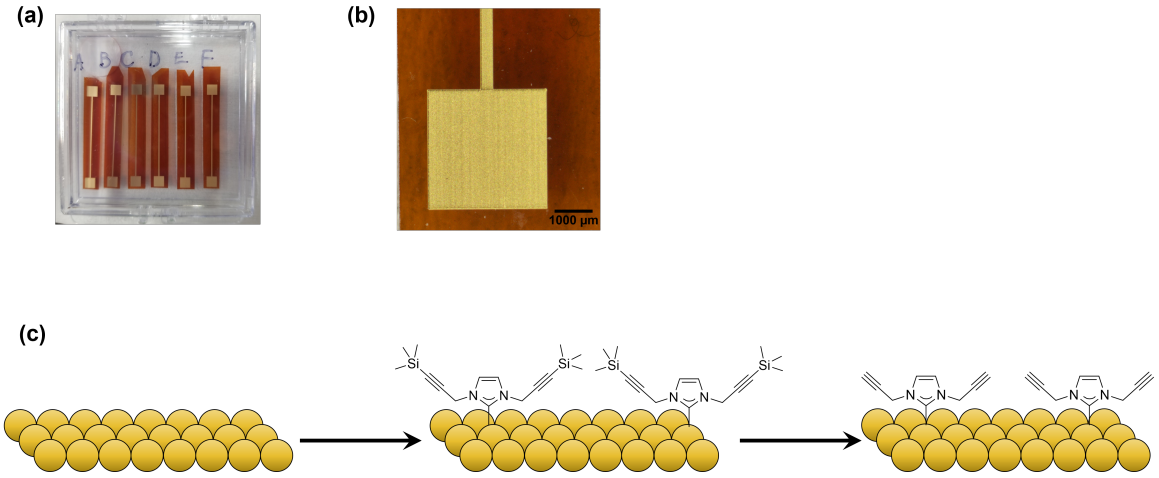

Figure 8.1: (a) Photo of printed Au electrodes on Kapton substrate. (b) Microscope image of a printed Au electrode. (c) Reaction schematic for depositing alkyne-NHC onto Au surface.

Figure 8.1 (a) shows a photo of the printed Au electrodes used for NHC functionalization in this work, and a close up view of the printed Au electrode is shown in Figure 8.1 (b). The electrodes were designed as two 3 x 3 mm^2 squares connected by a 300 μm wide Au trace and the overall length was 3 cm. Only one end of the electrode was immersed in the ligand solution to control the area of functionalization and the other Au pad was designed to ensure a good contact for electrochemical measurements. The alkyne-NHC deposition reaction schematic is shown in Figure 8.1 (c). The Au electrodes were immersed in the ligand solution to form tetramethylsilane (TMS) terminated alkyne functionalized NHC groups. Then the TMS protection groups were removed, and alkyne-NHC groups were left on the printed Au electrode surface. NHC ligands were engineered with alkyne functional groups to facilitate biomolecule immobilization through click chemistry. XPS and EIS measurements were performed on the modified Au electrodes to verify the alkyne-NHC deposition. Figure 8.2 (a)-(d) shows the XPS spectra for a blank Au film and an alkyne-NHC Au film. The central

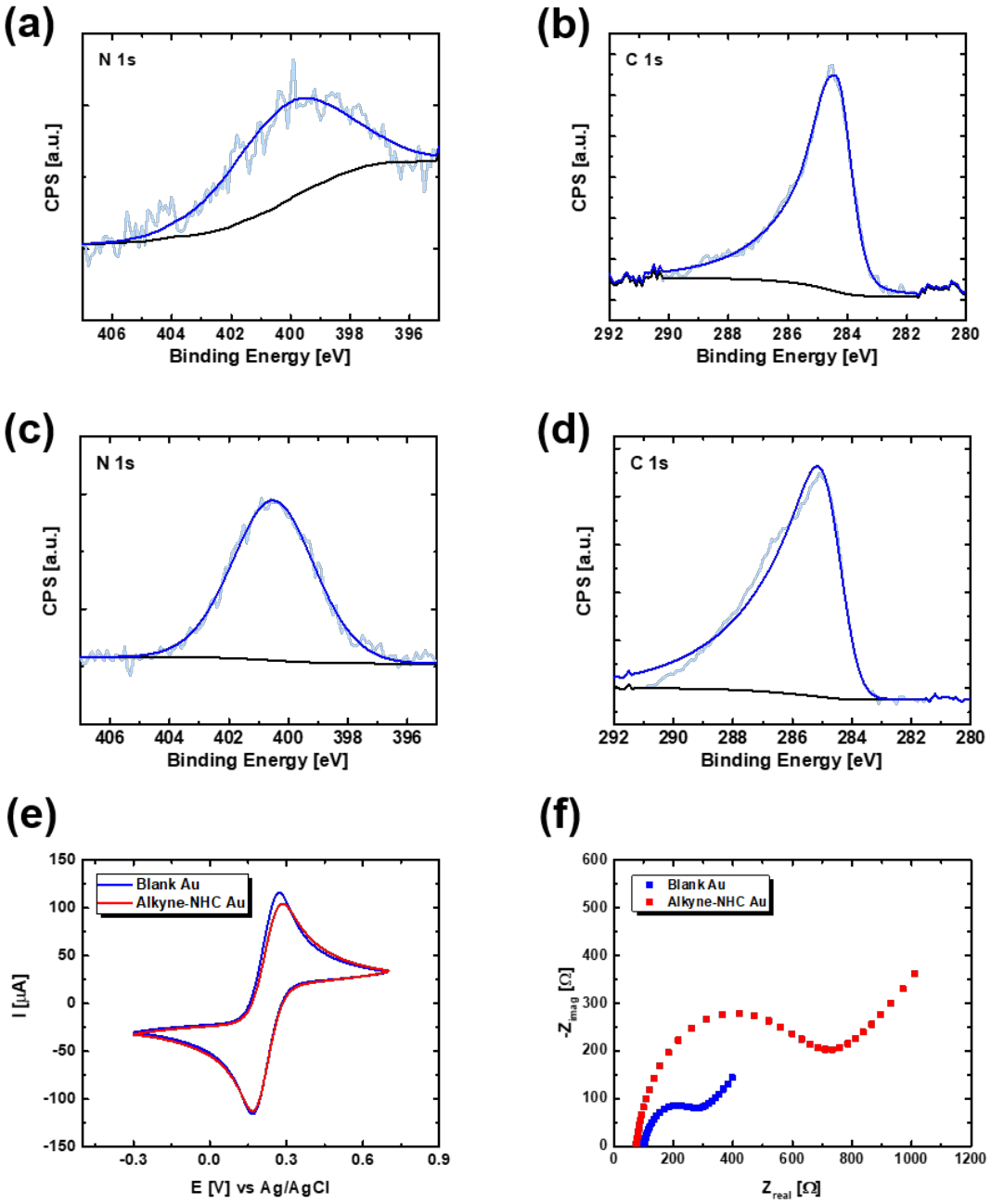

Figure 8.2: (a) XPS analysis showing N 1s and (b) C 1s regions for blank Au with peak at 400.0 eV and 284.4 eV, respectively. (c) XPS N 1s and (d) C 1s spectra for alkyne-NHC Au sample with peak at 400.5 eV and 284.7 eV, respectively. (e) CV and (f) EIS comparison of the blank Au sample and the alkyne-NHC functionalized Au.

peak of N 1s spectrum for the blank Au film was detected at 400.0 eV, which is 0.5 eV lower than the value measured for the alkyne-NHC modified Au film. Similarly, the

C 1s peak for blank Au was centered at 284.4 eV, which is 0.3 eV lower than the C 1s peak observed for the alkyne-NHC modified Au film. These values are comparable to the literature values of 400.45 eV for N 1s and 284.84 eV for C 1s [205]. The NHC deposition on the printed Au electrodes was further verified with electrochemical measurements. Both CV and EIS were performed on the same printed Au electrode before and after alkyne-NHC functionalization. As shown in the CV (Figure 8.2 (e)), the anodic current peak decreased from 115.7 μA to 104.3 μA, and the peak separation increased from 104.8 mV to 117.7 mV after the alkyne-NHC functionalization. From the Nyquist plot (Figure 8.2 (f)), the impedance of the Au electrode increased after functionalization. Therefore, both CV and impedance indicated that the NHC was successfully deposited onto the printed Au surface. Additional evidence of NHC deposition is present in appendix B.

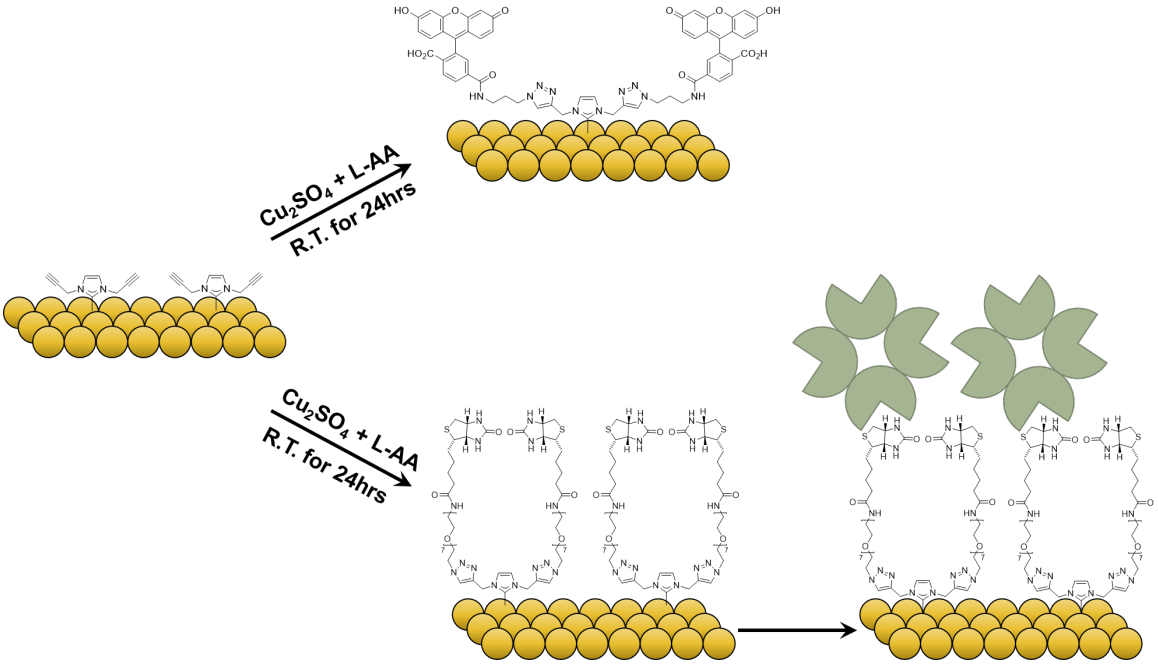

Figure 8.3: Reaction schematic of Copper (I)-catalyzed alkyne-azide cycloaddition (CuAAC).

Copper (I)-catalyzed alkyne-azide cycloaddition (CuAAC) was used for attaching the biomolecules in this work, and the reaction schematic is shown in Figure 8.3. The click chemistry reaction was first performed with azide-fluorescein. The reagents

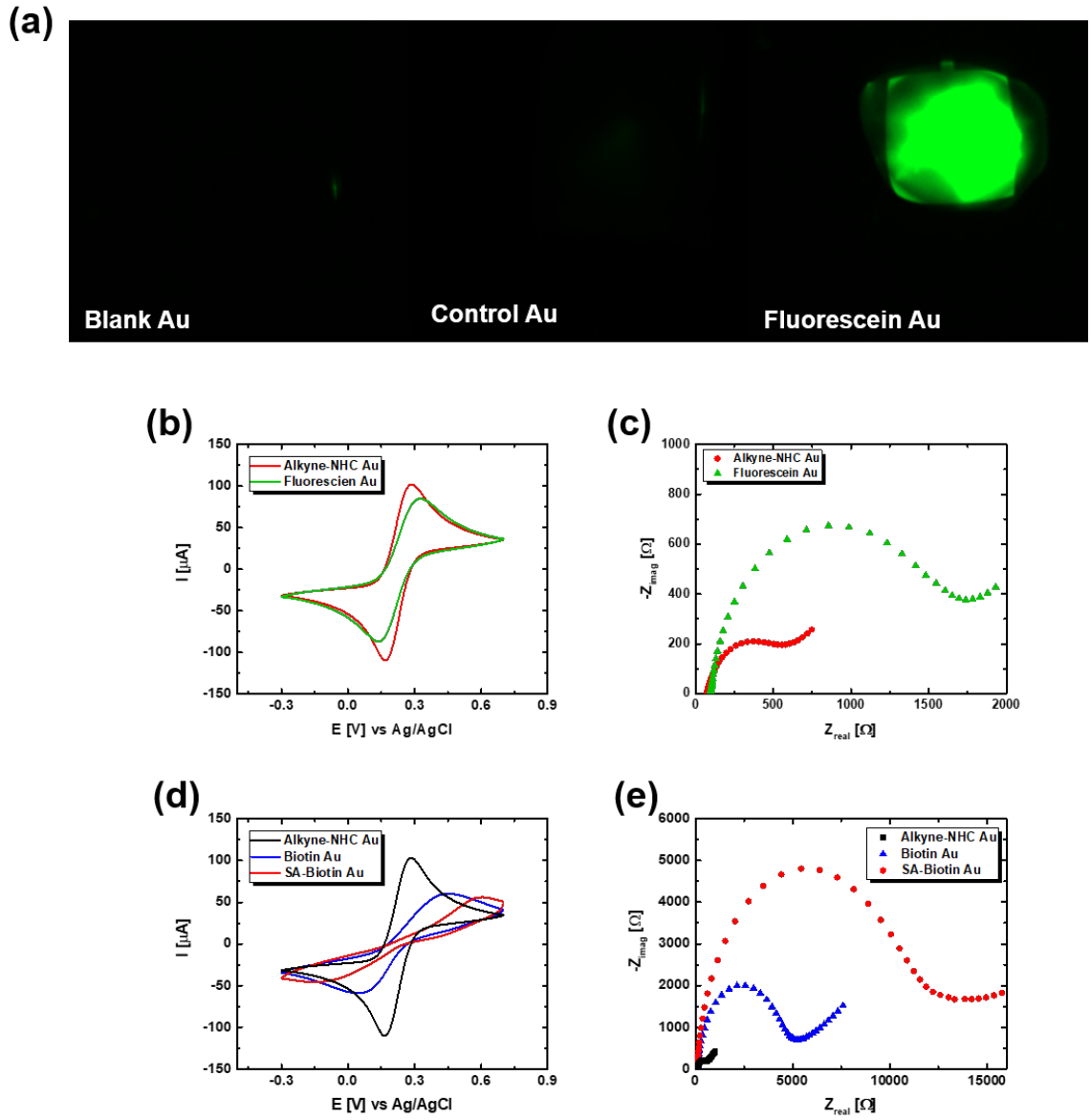

Figure 8.4: (a) Fluorescence images of blank Au, control Au, and fluorescein functionalized Au electrodes. (b) CV and (c) EIS measurements of an alkyne-NHC Au electrode before (red) and after(green) reacted with azide-fluorescein. (e) CV and (f) EIS measurements of an alkyne-NHC Au electrode before (black) and after (blue) biotin attachment and after streptavidin binding (red).

were added into a round bottom flask with 20 mL of ultrapure water and the Au electrodes were immersed in the solution for 24 hours in dark under ambient conditions. The control experiment was performed by immersing a blank Au electrode along with the alkyne-NHC functionalized Au electrodes in the same solution. From

the fluorescence images (Figure 8.4) taken for a blank Au electrode (left), a control Au electrode (middle), and an alkyne-NHC modified Au electrode (right) after the click reaction, it is observed that the azide-fluorescein molecules only attached to the alkyne-NHC modified Au electrode as expected, and no fluorescence was observed for the control or the blank Au electrode. The surface modification was further confirmed with CV and EIS. Figure 8.4 (b)-(c) shows the electrochemical measurements of an alkyne-NHC Au electrode and a fluorescein Au electrode. After functionalizing with fluorescein, the anodic peak current was reduced by 17.1 μA, the peak separation increased by 70.4 mV, and the impedance also increased. Therefore, these results are the evidence of fluorescein attaching to the Au electrode via the NHC linker and click chemistry. To demonstrate the potential of using the alkyne-NHC Au electrodes for biosensor development, azide-PEG_7-biotin molecules were attached via click chemistry. The same molarity ratio used for immobilizing fluorescein was used for the biotin attachment. Electrochemical measurements were conducted for the biotin modified Au electrode before and after streptavidin binding. As shown in Figure 8.4 (d)-(e), the reduction in CV anodic peak amplitude, increase in the CV peak separation, and a significant increase in the impedance indicated that the biotin molecules were bound to the alkyne-NHC Au surface.

8.3.2 Streptavidin Detection

The modified Au electrodes were implemented as external gate electrodes for OECT measurements. The OECTs used in this work were based on the optimized Au-OECTs from chapter 5. The channel dimensions were optimized to be L = 100 μm and W/L = 10. The measurement setup is shown in Figure 8.5 (a), the functionalized Au electrode was placed next to an unmodified OECT, and both the channel and the modified area of the gate electrode were fully covered by the electrolyte. The effects of functionalization were analyzed by comparing the transfer curves measured after each step of the modification using the same OECT device. 1xPBS was used as the

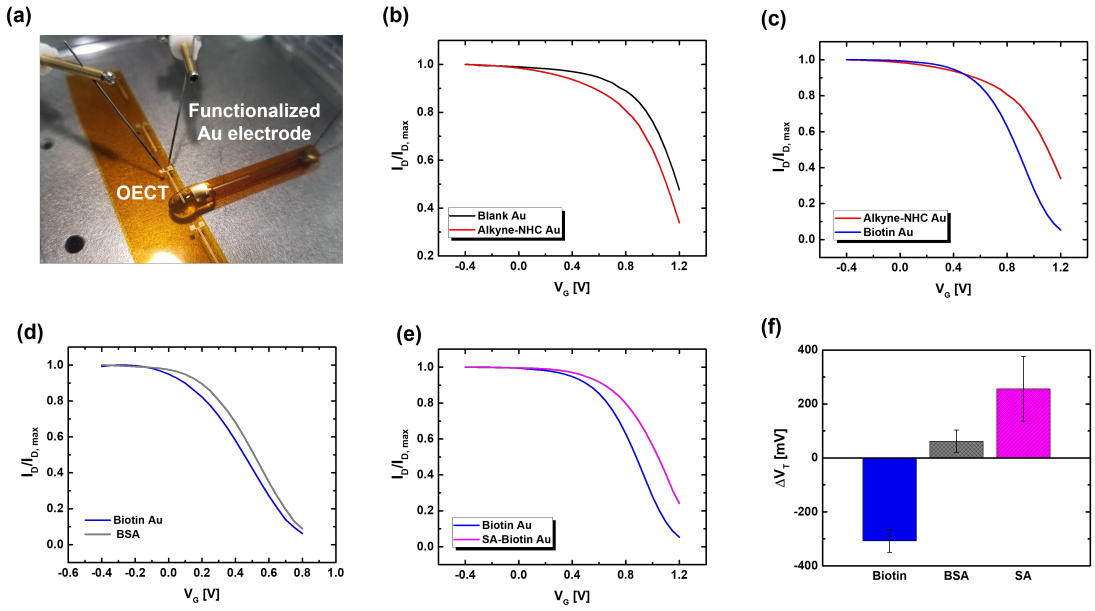

Figure 8.5: (a) Photo of the measurement setup using a printed OECT with an external functionalized Au gate electrode. (b) Transfer curves of an OECT measured with a blank electrode and after it being functionalized with alkyne-NHC. (c) Transfer curves of an OECT measured with an alkyne-NHC electrode and after biotin functionalization. (d) Transfer curves of an OECT measured using the biotin modified before and after incubated in 1 mg/mL BSA solution. (e) Transfer curves of an OECT measured with an biotin electrode before and after incubation in streptavidin solution. (f) The average changes in the threshold voltage (ΔV_T) extracted from transfer curves measured using Au electrodes after biotin functionalization, BSA incubation, and streptavidin binding.

electrolyte and a constant V_D of -0.2 V was applied for all measurements. As shown in Figure 8.5 (b), the transfer curve shifted to a lower V_G after functionalizing with alkyne-NHC. This shift in the transfer characteristic is because of the change in metal work function after NHC functionalization[206], which changes the interfacial potential profile at the gate/electrolyte interface for the OECT measurement. After biotin functionalization, a larger shift to the lower V_G was observed in 8.5 (c). After 1 hour incubation in BSA and SA solutions, the transfer curves shifted to higher V_G. The change after BSA incubation (Figure 8.5 (d)) is significantly lower than the change observed after SA incubation (Figure 8.5 (e)). The change after BSA incubation is likely due to non-specific adsorption of small amount of BSA molecules onto the Au

surface. Whereas the change after SA incubation is attributed to biotin-SA binding reaction. The change in the transfer characteristics is quantified by extracting the threshold voltage (V_T) from each measurement, and the difference of V_T (ΔV_T) was calculated. As shown in Figure 8.5 (f), the average ΔV_T after biotin functionalization, BSA incubation, and streptavidin binding are -307.7 ± 42.4 mV, 61.9 ± 41.1 mV, and 255.9 ± 120.0 mV, respectively. These results were extracted from measurements of four different Au electrodes and each Au electrode was measured with three different OECTs after each step of functionalization. There was a clear change due to SA binding, which confirms the functionalization of Au electrodes via NHC based functional groups.

8.4 Conclusion

In conclusion, we have demonstrated the modification of aerosol jet printed Au electrodes with alkyne functionalized NHC and the detection of streptavidin-biotin binding by integrating the functionalized Au electrode with a printed OECT. Despite the ubiquitous use of thiol-based functional groups for surface functionalization and biomolecule immobilization, their rapid degradation under ambient conditions remains a challenge. NHC forms strong and ultra-stable bond with transition metals and may potentially be a better alternative to thiol-based ligands for surface functionalization. Even though the alkyne-NHC ligand was synthesized for this work, there are commercially available NHC products that could be directly used for facile surface functionalization. Each step of the surface functionalization was observed as a shift in the OECT transfer curve due to interfacial potential profile change within the device. Since the gate functionalization process was completely isolated, the device performance was well-preserved and could be used for multiple measurements and for different electrodes to eliminate the effect of device variation. Hence, this work provides a technology platform for biosensor development via transducer surface engineering and is ready to be implemented for different biosensing applications.

Chapter 9

Rapid SARS-CoV-2 Detection Using Point-of-Care (POC) Biosensor Based on Aerosol Jet Printed OECT

9.1 Abstract

The continuous spread of COVID-19 poses a severe threat to public health. Rapid screening of large groups helps to identify outbreaks and make adaptive decisions. A convenient, accurate, and fast COVID-19 diagnosis tool is essential for containing the outbreaks. Here, we report a point-of-care (POC) rapid COVID-19 diagnostic tool that consists of a SARS-CoV-2 biosensor based on an organic electrochemical transistor (OECT) and a custom designed data acquisition and processing circuit. Our POC COVID-19 diagnostic tool detects SARS-CoV-2 antigens in less than 10 mins. The biosensor is produced by functionalizing the in-plane Au gate electrode of a fully aerosol jet printed OECT with anti-SARS-CoV-2 antibodies. The OECT based biosensor is capable of detecting various SARS-CoV-2 antigens in different test solutions. Selective sensing of SASR-CoV-2 spike protein is achieved in PBS with a detectable range of 1 fg/mL to 1 μg/mL. The OECT biosensor successfully detects SARS-CoV-2 virus-like particles (VLPs) in cell culture medium with a sensitivity of -45.7 $\pm$ 13.0 mV/dec. In addition, our POC COVID-19 diagnostic tool can be di-

rectly used for testing clinical nasopharyngeal samples in universal transport medium (UTM) and demonstrates an overall accuracy of 87.5% and correlation with sample viral load. Hence, this POC COVID-19 diagnostic tool show promise for on-site and at-home SARS-CoV-2 infection screening.

9.2 Introduction

The emergence of coronavirus disease 2019 (COVID-19), caused by severe acute respiratory syndrome coronavirus-2 (SARS-CoV-2), remains a threat to public health and the global economy. Efforts are being made to reduce the transmission through public health interventions including physical distancing, face mask ordinances, isolation of cases, and contact tracing [207, 208]. Rapid identification of SARS-CoV-2 infection and case isolation is crucial for controlling the spread and mortality of COVID-19. Currently, the real-time reverse transcription polymerase chain reaction (RT-PCR) test of nasopharyngeal swab samples is the primary diagnostic method of COVID-19 [209–212]. RT-PCR demonstrates excellent sensitivity for viral detection; however, it requires the use of sophisticated laboratory equipment and the testing process takes approximately 3 hours including sample preparation. Considering the time required for sample transportation, it may take several days and even a week for returning the results to the patients. Hence, developing a sensitive and accurate point-of-care (POC) diagnostic tool that directly targets the viral antigen and does not require sample preparation is necessary for rapid mass population screening.

There has been increased research on developing rapid COVID-19 diagnostic tools, such as graphene [213] and single-walled carbon nanotube [190] field-effect transistor (FET) based biosensor, cell-based biosensor [214], aptamer sensor based on silicon (Si) thin film transistor (TFT) [215], fluorescence immunochromatographic assay [216], and electrochemical biosensor developed using electrode based on screen printed carbon [217], graphene [218, 219], Cu_2O nanocubes modified screen printed carbon [220], and carbon nanofiber modified screen printed electrode coated with cotton padding

[221]. Among several potential approaches, biosensors based on nanomaterial FET attached with antibody demonstrated promising high sensitivity for both samples in buffer solution and clinical samples. However, due to fabrication limitations, mass production of these devices remains a challenge.

Organic electrochemical transistor (OECT) based biosensors are promising method for developing such POC devices for COVID-19 diagnosis. OECTs have excellent properties for chemical and biological sensing applications, such as intrinsic amplification, low operation voltages, and compatibility with aqueous media. Numerous studies have demonstrated that OECTs are capable of sensing various analytes such as ions [111, 120, 123], molecules [16, 63, 65], and biomolecules [66–68, 88, 222, 223]. An OECT consists of metal source and drain contacts, an ion permeable conducting polymer channel that is in direct contact with the electrolyte, and a gate electrode that is also immersed in the electrolyte. The drain current is modulated by the electrochemical doping/dedoping of the active channel material, which attributes to the ion injection from the electrolyte driven by the gate voltage. In order to use OECTs for COVID-19 diagnosis, either the gate or the channel surface could be modified with the antibodies that target SARS-CoV-2. It has been demonstrated in other studies that using functionalized OECTs, the antibody-antigen binding events could be detected [67, 69, 88, 224, 225]. Guo *et al.* have demonstrated the use of nanobody-functionalized OECT for rapid single molecule detection of COVID-19 and MERS antigens [226]. In addition, OECTs can be fabricated by conventional microfabrication techniques, and they are also compatible with low temperature processing techniques such as inkjet printing [101, 224, 227], screen-printing [40, 97], 3D printing [103, 104, 123], and aerosol jet printing [63, 105]. Printing techniques offer the benefits of easy design modification, reduced manufacturing cost, and the possibility of production using continuous large-scale roll-to-roll processing. Therefore, OECT is an excellent candidate for low-cost disposable biosensors for a POC diagnostic device.

Here, we present a POC COVID-19 diagnostic device that is based on aerosol jet

printed OECTs functionalized with SARS-CoV-2 spike S1 antibody and a custom-made data processing circuit. The OECTs were printed on flexible Kapton substrate using commercially available gold nanoparticle (AuNP) ink for the source, drain and gate contacts, poly(3,4-ethylenedioxythiophene) polystyrene sulfonate (PEDOT:PSS) as the channel, and polydimethylsiloxane (PDMS) as the insulator. SARS-CoV-2 spike S1 antibodies were immobilized onto the printed Au gate electrode via self-assembled monolayer (SAM) of 3,3'-Dithiodipropionic acid di(N-hydroxy succinimide ester) (DSP). Our OECT based SARS-CoV-2 sensor shows selectivity towards the target spike protein with a limit of detection (LOD) of 1 fg/mL. Moreover, our OECT based POC COVID-19 diagnostic device has demonstrated potentials for clinical application by direct detection of the nasopharyngeal swabs sample suspended in universal transport medium (UTM). This is a simple and cost-effective platform that opens new opportunities for the development of rapid SARS-CoV-2 detection and is also potentially applicable to a wide range of diagnoses.

9.3 Experimental Details

9.3.1 Materials and Reagents

10x Phosphate buffer saline (PBS) stock solution, bovine serum albumin (BSA), dimethyl sulfoxide (DMSO), Tris base, Dulbecco's Modified Eagle Medium (DMEM), Invitrogen™ Zip Alexa Fluor™ 647 rapid antibody labeling kit, and Molecular Probes™ Alexa Fluor™ 488 hydrazide was purchased from Fisher Scientific. 10x PBS was diluted to obtain 1xPBS solution (pH = 7.4) using ultrapure water. 1 M Tris-HCl solution was prepared by dissolving Tris base in ultrapure water and the pH was adjusted to 7.5 using concentrated HCl. 3,3'-Dithiodipropionic acid di(N-hydroxysuccinimide ester) (DSP) was purchased from Sigma Aldrich. Recombinant SARS-CoV-2 spike S1 antibody (1 mg/mL) and SARS-CoV-2 spike subunit 1 (S1) protein (His tag) were purchased from antibodies-online Inc. SARS-CoV-2 spike S1 antibody was diluted to

250 μg/mL with 1xPBS solution. SARS-CoV-2 spike S1 protein was first dissolved in ultrapure water and diluted to different concentrations (1 fg/mL to 1 μg/mL) in 1xPBS containing 0.1% BSA suggested by the datasheet. Human coronavirus HKU1 (HCoV-HKU1) spike S1 protein (S1 subunit, His tag) and middle east respiratory syndrome coronavirus (MERS-CoV) spike S1 Protein (S1 Subunit, aa 1-725, His tag) were purchased from SinoBiological and diluted to different concentrations in 1xPBS containing 0.1% BSA. SARS-CoV-2 virus like particles (VLPs) in DMEM were purchased from Virongy. The VLPs solution was diluted using PBS for the measurements.

9.3.2 OECT Fabrication

OECTs were fabricated using the Optomec Aerosol Jet 5X 3D printer with commercially available materials. Gold nanoparticle (Au NP) ink (UT Dots, Inc.) was deposited onto a Kapton HN film to form source, drain, and gate electrodes and all the metal interconnects and annealed at 280℃ for 1 hour. The printed Au traces have an average thickness of 584 nm and an average resistivity of 8.32 x $10^{-6}\Omega$-cm. The channel of OECT was printed using poly(3,4-ethylenedioxythiophene) polystyrene sulfonate (PEDOT:PSS) mixture composed of 94% Heraeus CleviosTM PH 1000, 5% ethylene glycol (EG), 0.1% dodecylbenzenesulfonic acid solution (DBSA) (70 wt. % in isopropanol), and 1wt. % (3-glycidyloxypropyl) trimethoxysilane (GOPS) ($\geq$98%) and annealed at 130℃ for 20 minutes. Finally, a 1.05 μm thick layer of UV-curable polydimethylsiloxane (PDMS) (Shin-Etsu Chemical Co., Ltd.) was printed to passivate the metal traces, acting as an insulating layer to prevent shorting from the liquid electrolyte. The PDMS insulating layer was cured with UV on-the-fly while printing and then annealed at 130℃ for 30 minutes. The PDMS reservoirs were made using a 3D printed plastic mold and the SYLGARD™ 184 Silicone Elastomer Kit with a mix ratio of 10:1 and cured at 80℃ in an oven overnight. Then the wells were removed from the mold and cleaned with IPA and dried. To attach the PDMS well, a thin

layer of the SYLGARD PDMS was applied on the bottom of the well. The well was then placed on top of the OECT and baked at 80℃ in an oven for 2 hours.

9.3.3 SARS-CoV-2 Antibody Immobilization

To attach the SARS-CoV-2 spike S1 antibody onto a printed gold gate electrode surface, chemisorption technique using a self-assembled monolayer (SAM) was adopted. First, the printed OECT was cleaned with acetone, isopropanol (IPA), ethanol, and deionized (DI) water thoroughly and dried under nitrogen. 10 mM DSP solution was prepared freshly before each reaction using DMSO. The DSP solution was added onto the gate electrode surface using a micropipette and left at room temperature for 30 minutes. Then, the device was rinsed thoroughly with DMSO and DI water and dried under nitrogen. The SARS-CoV-2 spike S1 antibody solution (250 μg/mL in PBS) was immediately added to the DSP modified gate electrode and left for 2 hours under ambient conditions. After the antibody immobilization, the device was rinsed several times with 1xPBS and DI water to remove the non-specific adsorption and the reaction by-products. Lastly, the device was immersed in 1 M Tris-HCl buffer (pH = 7.5) for 20 mins to quench the un-reacted DSP, and the device was washed again with DI water and 1xPBS. The functionalized OECTs were stored in 1xPBS solution at 4℃.

9.3.4 FTIR Characterization

Attenuated total reflection Fourier transform infrared (ATR-FTIR) spectra were collected using a Thermo Nicolet iS50 FTIR spectrometer. The absorbance was obtained for a wavenumber range of 4000 - 400 cm^{-1} with a scan resolution of 4 cm^{-1} and 128 scans for each measurement. FTIR samples were prepared using printed Au films with the same procedure described for OECT functionalization. The film modified with DSP SAM was measured immediately after the preparation.

9.3.5 Fluorescence Characterization

The fluorescence samples were prepared using the printed Au films (5 x 5 mm^2). Alexa Fluor 488 hydrazide was dissolved in 1xPBS to achieve a final concentration of 1 mM. 100 μL of SARS-CoV-2 antibody conjugated with Alexa 647 fluorophore was prepared following the quick reference provided by Thermo Fisher Scientific. The Au film functionalization procedure is similar to the OECT functionalization. Briefly, after modifying the films with DSP SAM, 30 μL of 1 mM Alexa 488 hydrazide and 30 μL of Alexa 647 labeled SARS-CoV-2 antibody solution was dispensed onto separate Au films for 2 hrs. Fluorescence images were taken using ChemiDoc™ MP Gel Imaging System with the samples covered with 1xPBS solution and the filters Alexa 488 and Alexa 647.

9.3.6 Cyclic Voltammetry

Cyclic voltammetry (CV) was performed using a standard three-electrode setup with 0.09 cm^2 printed Au electrode on Kapton substrate as the working electrode, a platinum counter electrode, and Ag/AgCl reference electrode (saturated with KCl). The measurements were carried out in an aqueous electrolyte containing 5 mM ferro/ferricyanide and 100 mM KCl. The CV was scanned between -0.2 to 0.5 V vs Ag/AgCl at a rate of 50 mV/s. For each sample, CV was collected for three cycles and the last cycle was used for analysis.

9.3.7 Electrical Measurements and Characterization

The electrical characteristics of the printed OECTs were measured using a dual channel Keithley 2612B sourcemeter controlled via a customized LabVIEW program. The output characteristics and transfer curves were obtained using 1xPBS solution as the electrolyte before the gate functionalization. The transfer curve measured in 1xPBS after antibody immobilization was used as the baseline before the addition of spike protein or VLP solution. The functionalized OECT was measured after incubating

with sample solutions for 3-5 minutes before the transfer characteristic measurement. The transfer curve was measured by biasing the drain voltage (V_D) at -0.4 V and sweeping the gate voltage (V_G) from -0.4 V to 1.1 V with a step size of 0.05 V.

The threshold voltage (V_T) was extracted based on the linear extrapolation method and calculated from the transfer curve by finding the maximum slope for the curve and adding $V_D/2$ to the extrapolated x-intercept ($I_D = 0$) [145].

Testing of clinical samples containing SARS-CoV-2 was conducted in Provincial Laboratory for Public Health (ProvLab) at the University of Alberta using the OECT based biosensors and the custom designed circuit board. The samples were nasopharyngeal swabs suspended in universal transport medium (UTM) and verified with real-time reverse transcription polymerase chain reaction (RT-PCR) with a cycle threshold (Ct) cutoff of 38.00 cycles for COVID-19 positive result.

9.4 Results and Discussions

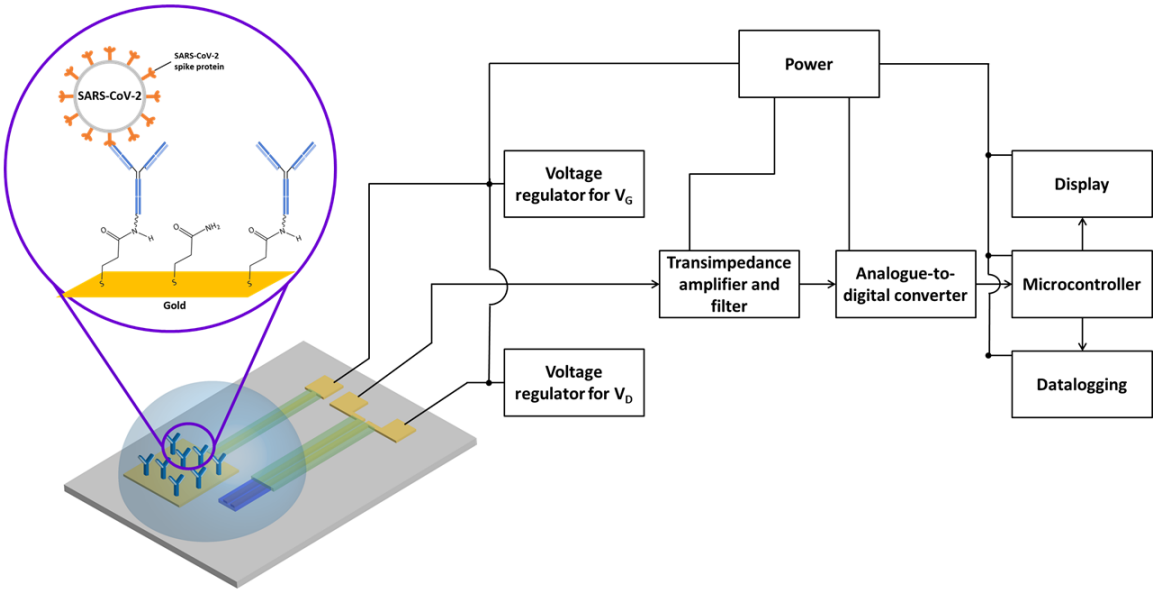

Figure 9.1: Schematic of the POC diagnostic device showing the printed OECT based SARS-CoV-2 biosensor and the block diagram for the circuit components.

Figure 9.1 shows an overall schematic of the OECT based POC COVID-19 diag-

nostic tool developed for this work. The detection of SARS-CoV-2 was achieved by sensing the antibody-antigen interaction using a functionalized OECT. The OECT consisted of Au source, drain and gate electrode and PEDOT:PSS channel. The gate electrode was functionalized with SARS-CoV-2 antibodies using a self-assembled monolayer of DSP. The chemical reaction involved in the surface functionalization and antibody immobilization is shown in Figure 9.2 (a). This reaction utilizes the functional group N-hydroxysuccinimde (NHS) ester that reacts with the primary amine groups on the target biomolecule to form a stable amide bond [228]. The Au surface was first immersed in DSP solution to form active ester groups on the surface via Au-S bonds and then immersed in buffer solution to attach the antibodies to the surface [195]. Several methods were used in this study to verify the chemisorption reactions. ATR-FTIR spectra were obtained for the printed Au films conjugated with DSP molecules only and anti SARS-CoV-2 antibodies via the DSP molecules. As shown in Figure 9.2 (b), for the sample with antibodies, two distinctive peaks are observed at $\sim$1658 cm^{-1} and $\sim$1548 cm^{-1} that are corresponding to amide I and amide II bond, respectively [69, 151, 229]. Fluorescence imaging also provides complementary evidence about the covalent coupling of antibodies to the gold surface. Figure 9.2 (c) shows the fluorescence images of an unmodified printed Au film, a printed Au film with Alexa 488 fluorophore attached via DSP linker, and a printed Au film conjugated with Alexa 647 fluorophore labeled SARS-CoV-2 antibodies by DSP SAM. CV of ferro/ferricyanide has been used as a conventional method to monitor the characteristics of a modified electrode [230]. Figure 9.2 (d) shows the CV plots of a printed Au film before functionalization, after antibody immobilization, and after binding with the antigen. The antibody conjugation was indicated by the peak current decrease and peak separation increase. These results confirmed that the antibodies were covalently bound to the printed Au surface by the DSP linker. By functionalizing the gate electrode of an OECT with SARS-CoV-2 antibody using this method, the SARS-CoV-2 antigens can be recognized, and the antibody-antigen

reaction changes the surface potential of the gate electrode, which results in a shift in the transfer characteristics of the OECT [68, 69].

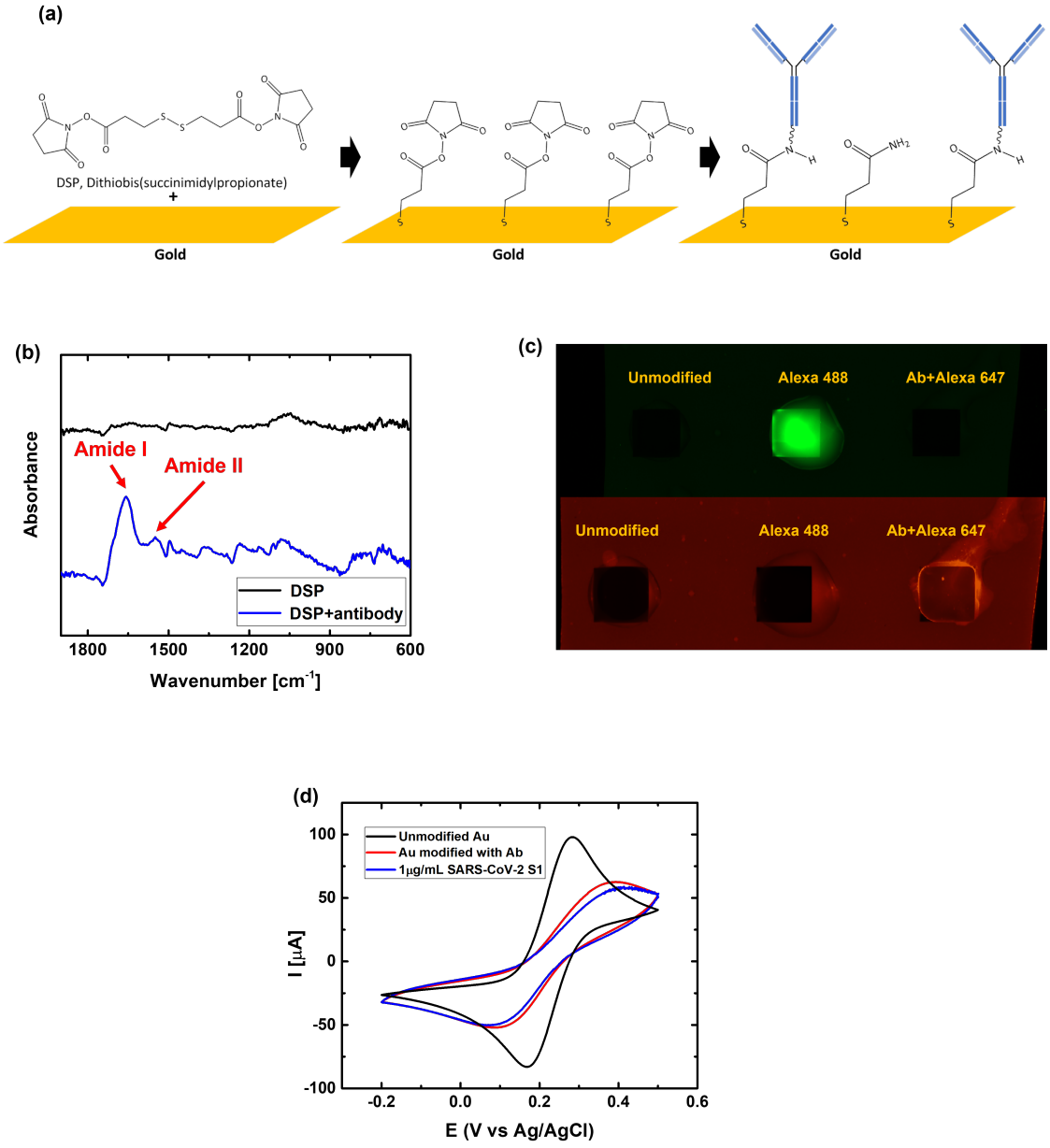

Figure 9.2: (a) Reaction schematic for antibody functionalization. (b) Infrared spectra of Au thin film modified with DSP SAM (black line) and Au thin film modified with SARS-CoV-2 antibody via DSP linker. (c) Fluorescence images of a unmodified printed Au film (left), a printed Au film linked with fluorophore Alexa 488 using DSP SAM (middle), and a printed Au film functionalized with SARS-CoV-2 antibodies labelled with Alexa 647. (d) CV of a printed Au electrode before functionalization (black) , after antibody (Ab) functionalization (red), and after immersed in 1 μg/mL Spike protein solution (blue).

The initial SARS-CoV-2 detection was carried out using OECT with channel dimensions of W/L = 10, L = 100 μm, and gate size = 1 mm^2 as shown in Figure 9.3 (a). The initial antigen sensing was conducted by measuring the I_D change under constant voltage bias and consecutive addition of SARS-CoV-2 spike protein solutions with increasing concentrations. As shown in Figure 9.3 (b), there is no significant change observed in I_D for spike protein concentration lower than 100 μg/mL. Hence, the standard measurement technique used for developing glucose sensor in chapter 7 could not be directly used, and OECT geometry optimized was first conducted to select the device with desired sensing performance.

Nine printed Au-OECTs with similar channel thickness of 780 nm and different channel widths-to-length ratios(W/L = 1, 2, and 5) and gate sizes (A_{gate} = 1, 4, and 9 mm^2) were functionalized with the SARS-CoV-2 antibody under the same conditions as mentioned in the experimental details. Then they were measured with SARS-CoV-2 spike S1 protein solutions with increasing concentrations. Figure 9.4 shows the transfer curves collected for each device after incubation with different

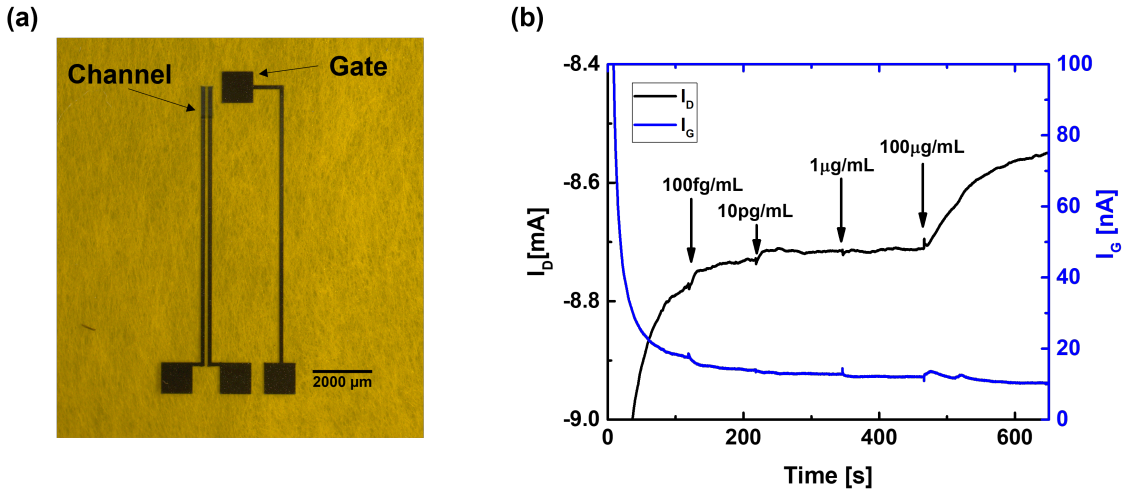

Figure 9.3: (a) Optical microscope image of an aerosol jet printed OECT with channel dimensions of L = 100 μm, W/L = 10, and gate size = 1 mm^2.(b) Real-time I_D response of an OECT with SARS-CoV-2 functionalized gate to the addition of SARS-CoV-2 spike protein solutions in PBS under constant biases (V_G = 0.6 V and V_D = -0.6 V).

concentrations of SARS-CoV-2 S1 protein solutions. It can be observed from Figure 9.4 (a)-(c) that the OECTs with a gate size of 1 mm^2 did not show consistent changes. This is likely due to the small gate size which did not have a sufficient amount of antibodies attached. For OECTs with a gate size of 4 mm^2, only the device with W/L = 2 showed consistent shifts in the transfer curve as the S1 protein concentration increases as shown in Figure 9.4 (d)-(f). Figure 9.4 (g)-(i) shows the transfer curves for OECTs with gate size of 9 mm^2. In this case, all three devices showed consistent

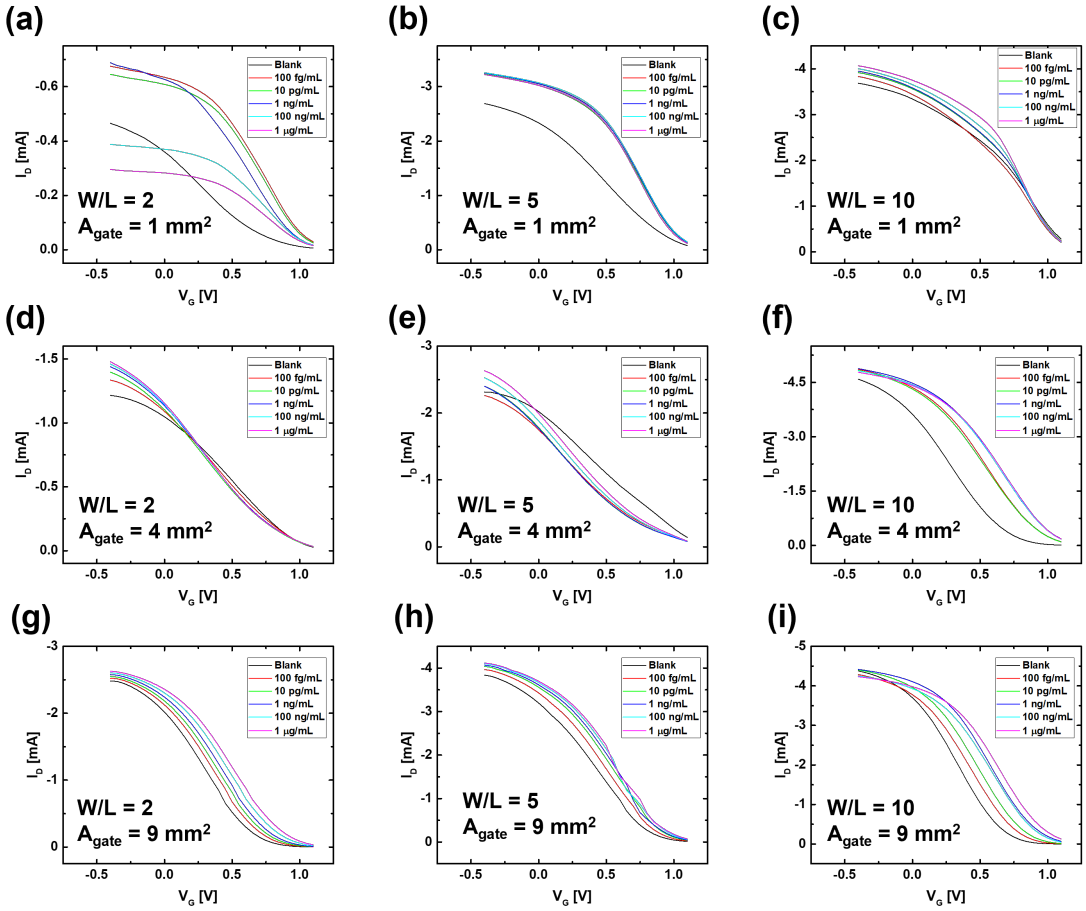

Figure 9.4: Transfer curves of OECTs with functionalized gate and different device dimensions (a) W/L = 2 and gate size = 1 mm^2, (b) W/L = 5 and gate size = 1 mm^2, (c) W/L = 10 and gate size = 1 mm^2, (d) W/L = 2 and gate size = 4 mm^2, (e) W/L = 5 and gate size = 4 mm^2, (f) W/L = 10 and gate size = 4 mm^2, (g) W/L = 2 and gate size = 9 mm^2, (h) W/L = 5 and gate size = 9 mm^2, and (i) W/L = 10 and gate size = 9 mm^2. The curves were collected after incubating with increase concentration of SARS-CoV-2 S1 protein solutions.

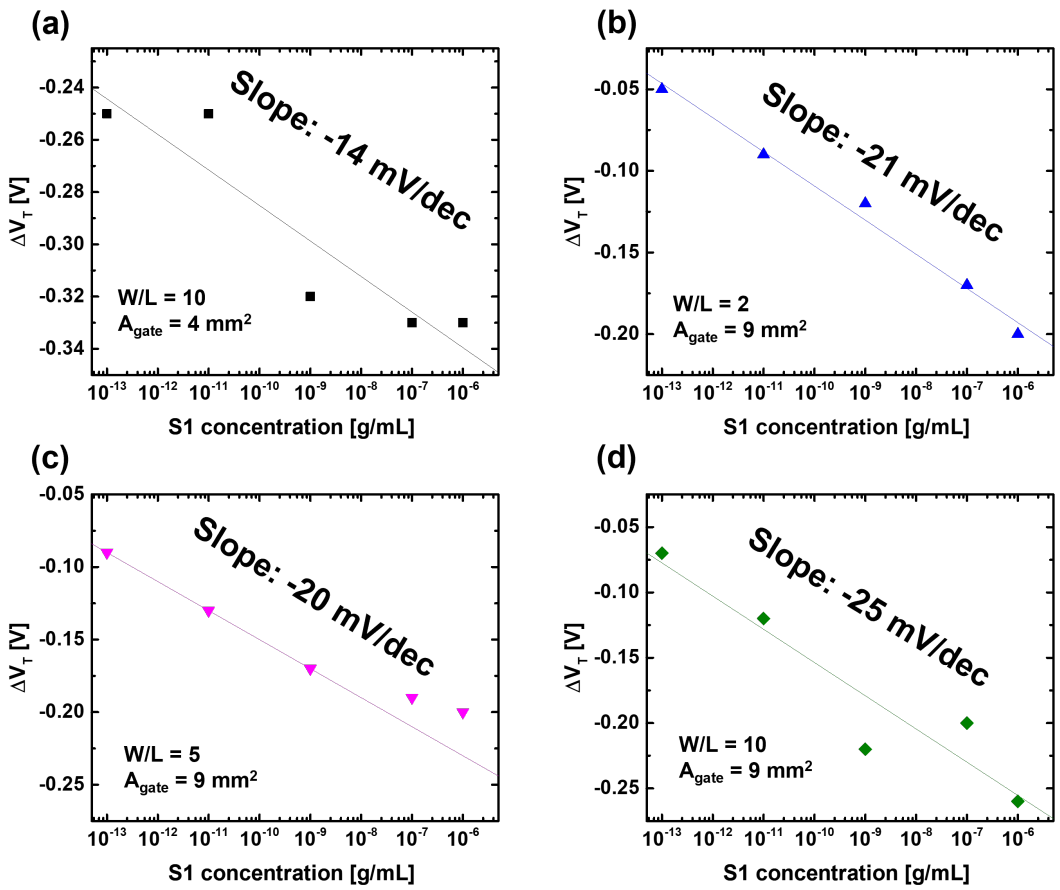

Figure 9.5: Semi-logarithmic plot of average shift in threshold voltage (ΔV_T) as a function of spike protein concentration for devices with dimensions of (a) W/L = 10 and gate size = 4 mm^2, (b) W/L = 2 and gate size = 9 mm^2, (c) W/L = 5 and gate size = 9 mm^2, and (d) W/L = 10 and gate size = 9 mm^2.

shifts towards higher V_G as the S1 protein concentration increased.

The shift in the transfer curves of the four working devices was then extracted as the change in the threshold voltage (ΔV_T) and plotted against the S1 protein concentration as shown in Figure 9.5. A logarithmic dependence of ΔV_T on the S1 protein concentration is observed and the slope was extracted for sensitivity analysis. Devices with a gate size of 9 mm^2 show higher sensitivities compared to the device with a gate size of 4 mm^2. For the OECTs with a gate size of 9 mm^2 and different W/L, it can be observed from Figure 9.5 (b)-(d) that the slope of the curve increases as the device W/L increase. Since transconductance is proportional with W/L as

Table 9.1: OECT geometry optimization for SARS-CoV-2 sensing

Gate size [mm²]	**W/L**	**$g_{m,max}$ (V_D = -0.4 V)**	**Sensitivity [mV/dec]**
1	2	0.99	N/A
1	5	3.26	N/A
1	10	5.58	N/A
4	2	1.42	N/A
4	5	3.60	N/A
4	10	6.59	-14
9	2	2.91	-21
9	5	4.85	-20
9	10	6.13	-25

observed in chapter 5, higher W/L results in higher sensitivity.

The device dimension and their sensitivity are listed in Table 9.1. Based on the device geometry optimization, a larger gate area is required to ensure an adequate amount of antibody is immobilized onto the gate, and a higher W/L is preferred to increase the sensitivity. Therefore, the OECTs with gate size of 9 mm^2 and W/L = 10 were selected for developing the SARS-CoV-2 biosensor.

Figure 9.6 (a) is an optical microscope image of the OECT with optimized dimension for developing the SARS-CoV-2 biosensor. The device dimensions were optimized to a channel length of 100 μm, a channel width-to-length ratio (W/L) of 10, and a gate size of 9 mm^2 in order to achieve desired device performance with an adequate amount of antibody immobilization. The output and transfer characteristics and the transconductance curves of an unfunctionalized OECT measured using PBS as the electrolyte are shown in Figure 9.6 (b)-(d). These devices demonstrated typical p-type depletion mode device behaviors that are expected for PEDOT:PSS based OECTs. As a small polarizable gate electrode was used, a higher gate voltage was needed to

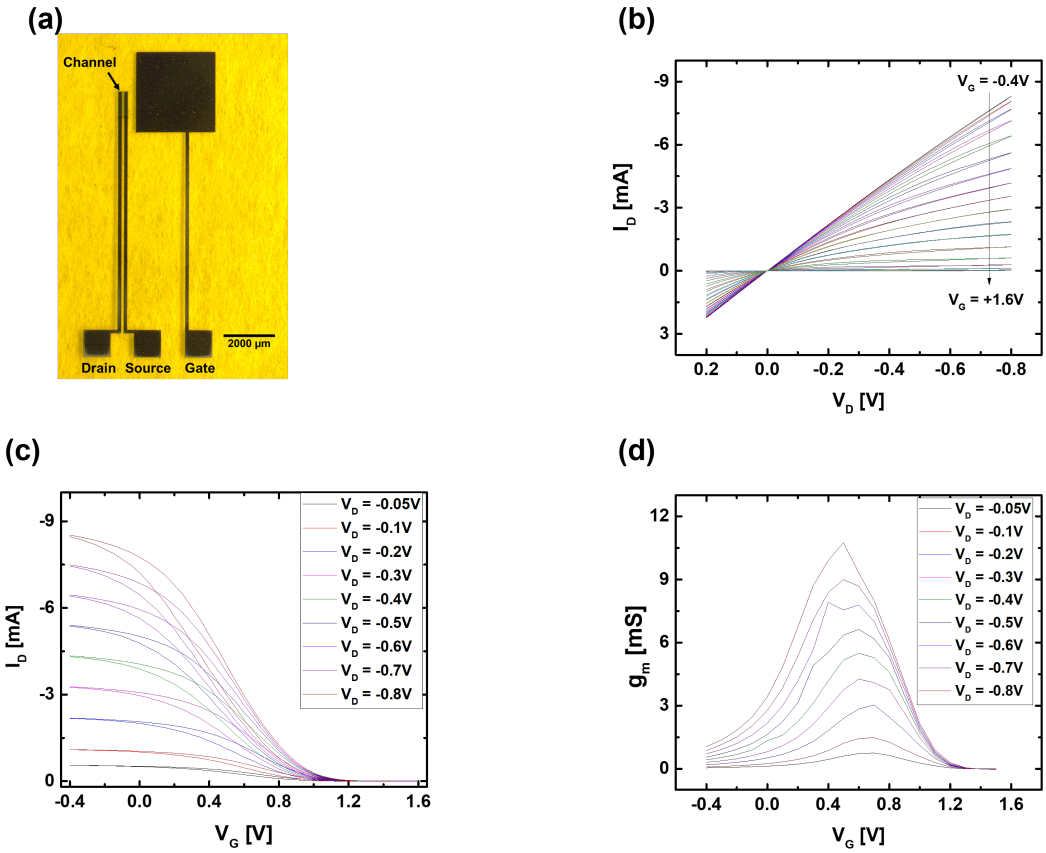

Figure 9.6: (a) Optical microscope image of an aerosol jet printed OECT with channel dimensions of L = 100 μm, W/L = 10, and gate size = 9 mm^2. (b) I-V characteristics of the OECT measured using 1xPBS as the electrolyte. (c) Transfer characteristics of the OECT measured under different drain biases. (d) The corresponding transconductance curves extracted from the transfer characteristics.

turn the device off fully. However, the maximum transconductance still occurred at a gate voltage smaller than 1 V, which is within the stability window of water.

The detection of antigen was performed by measuring the transfer curve of the functionalized OECT at a fixed drain bias of -0.4 V. Figure 9.7 (a) shows the transfer characteristics of an OECT measured before and after SARS-CoV-2 antibody functionalization in 1xPBS solution, demonstrating a clear shift to the lower V_G. The performance of the functionalized OECTs was first verified using the SARS-CoV-2 spike S1 protein antigen. The transfer characteristics were acquired after incubating the OECT in SARS-CoV-2 spike S1 protein solution with concentrations ranging

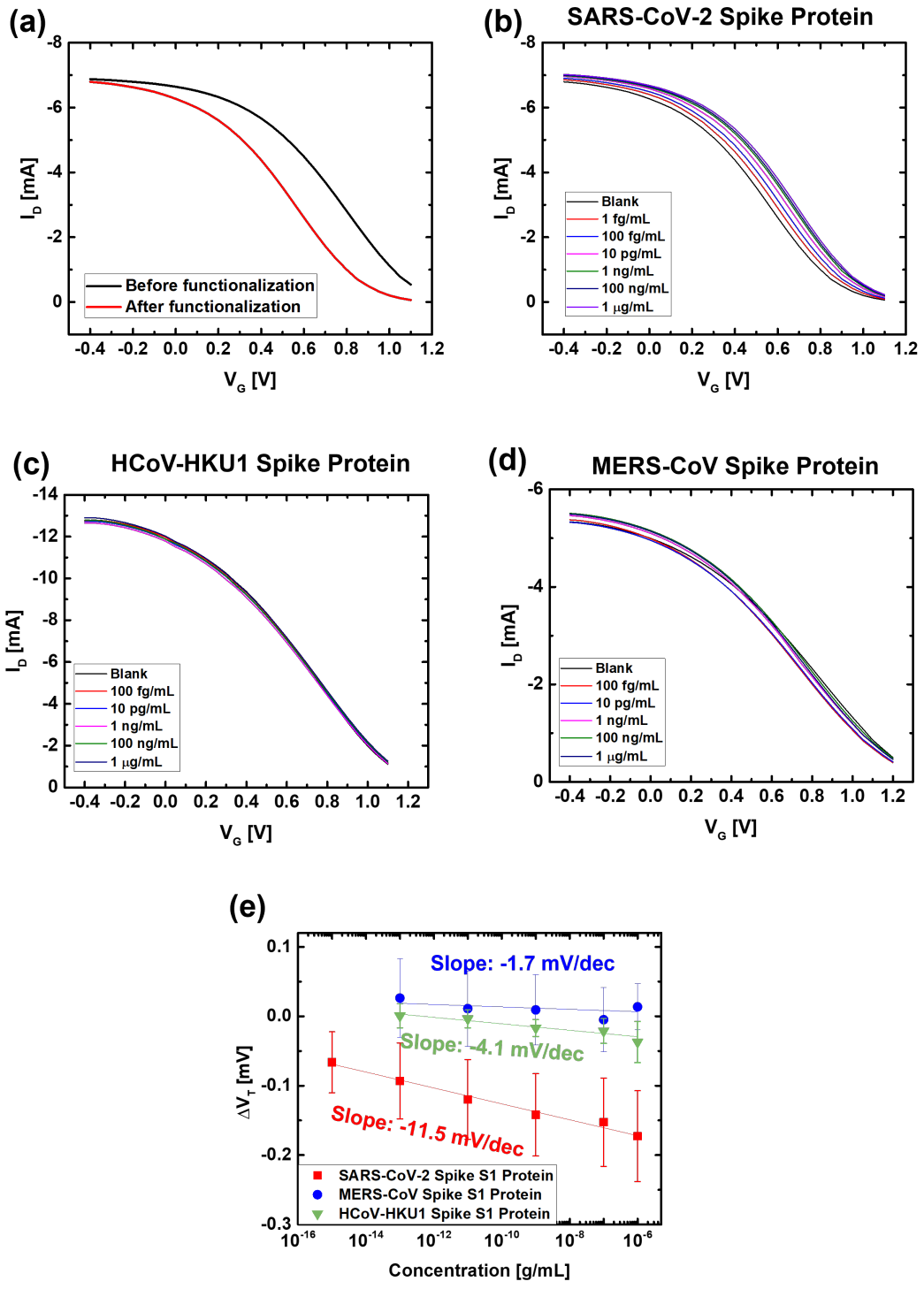

Figure 9.7: (a) Transfer characteristics (I_D vs V_G) of a printed OECT measured in 1xPBS before and after SARS-CoV-2 functionalization on gate electrode. The device was biased V_D = -0.4 V and V_G from -0.4 V to +1.1 V with a step size of 0.1 V. (Continued on the following page.)

(Continued from the previous page.) (b) Transfer characteristics of a functionalized OECT measured after being incubated in increasing concentration of SARS-CoV-2 spike S1 protein solution. (c) Transfer characteristics of a functionalized OECT measured after incubation in increasing concentration of HCoV-HKU1 spike S1 protein solution. (d) Transfer characteristics of a functionalized OECT measured after incubation in increasing concentration of MERS-CoV spike S1 protein solution. (e) Semi-logarithmic plot of average shift in threshold voltage (ΔV_T) as a function of spike protein concentrations. Functionalized OECTs showed negligible change to the increase of HCoV-HKU1 and MERS-CoV spike protein concentrations and logarithmic dependence to the increase SARS-CoV-2 spike protein concentrations with an average slope of -11.5 mV/dec. Error bar represents the standard deviation.

from 1 fg/mL to 1 μg/mL for a short period. It can be observed from Figure 9.7 (b) that the transfer curve shifted to higher V_G as the concentration of spike protein solution increases. The selectivity tests were carried out with HCoV-HKU1 and MERS-CoV spike S1 proteins in the same manner as the measurement for SARS-CoV-2 spike protein. Figure 9.7 (c)-(d) shows the transfer curves of the functionalized OECTs measured with HCoV-HKU1 and MERS-CoV spike S1 protein solutions, respectively. The functionalized OECTs showed negligible responses in both cases. To analyze the sensor performance, the average net shift in the transfer curves was extracted by extrapolating the threshold voltage shift (ΔV_T) and plotted against the logarithmic concentrations of spike S1 protein solution of SARS-CoV-2, MERS-CoV, and HCoV-HKU1 as shown in Figure 9.7 (e). A logarithmic correlation between ΔV_T and SARS-CoV-2 spike protein concentration is observed with a slope of -11.5 $\pm$ 2.4 mV per decade (mV/dec) (n = 5). Whereas for HCoV-HKU1 and MERS-CoV spike proteins, the slopes are -4.6 $\pm$ 0.8 mV/dec and -1.7 $\pm$ 1.0 mV/dec. These results indicated that the OECT based biosensor with the functionalized gate electrode is sensitive and selective to SARS-CoV-2 spike protein.

To further verify whether the OECT based sensors could detect the SARS-CoV-2 virus, we conducted measurements using SARS-CoV-2 virus like particles (VLPs). The VLPs were suspended in Dulbecco's modified eagle medium (DMEM), which contains various reagents that may cause competing reactions; therefore, we first

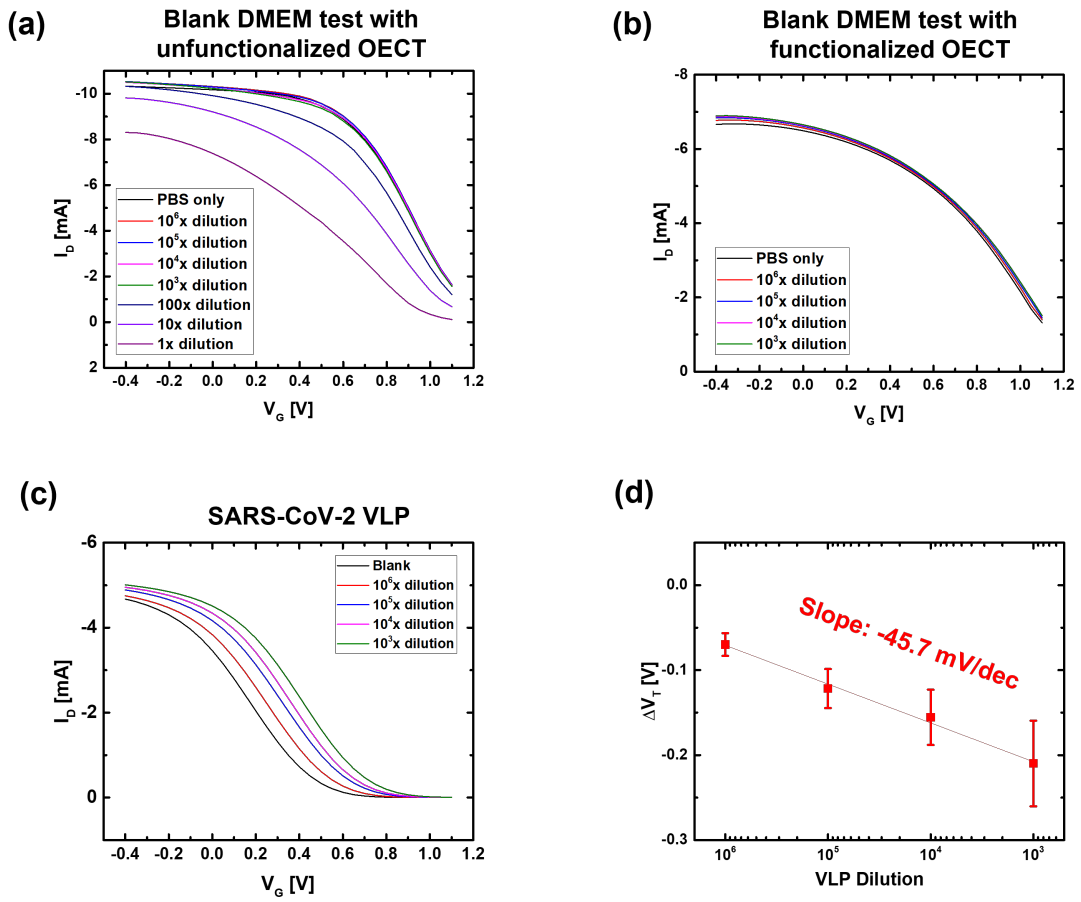

Figure 9.8: (a) Transfer curves of an unfunctionalized OECT measured with different dilutions (10^6x to 1x) of DMEM in PBS. No significant change in I_D was observed for the DMEM dilution range of 10^6 to 10^3. (b) Transfer curves of a functionalized OECT measured with different dilutions (10^6x to 10^3x) of DMEM in PBS showing negligible change in I_D. (c) Transfer curves of a functionalized OECT measured with different dilutions (10^6x to 10^3x) of VLP in PBS. (d) Semi-log plot of average ΔV_T plotted with respect to VLP dilutions. A slope of 45.7 ± 13.0 mV/dec (n = 5) is observed. Error bar represents the standard deviation.

measured the transfer curves of an unfunctionalized OECT using DMEM diluted using PBS into different concentrations (10^6x dilution to undiluted) as shown Figure 9.8 (a). There is nearly no change in the transfer characteristics measured with PBS and DMEM dilution of 10^6x to 10^3x, and more significant shifts to lower V_G were observed for DMEM dilution ranging from 100x to 1x. Hence, we selected the DMEM dilutions ranging from 10^6x to 10^3x and tested the effect on OECTs with functionalized gate electrode. As shown in the transfer characteristics in Figure 9.8

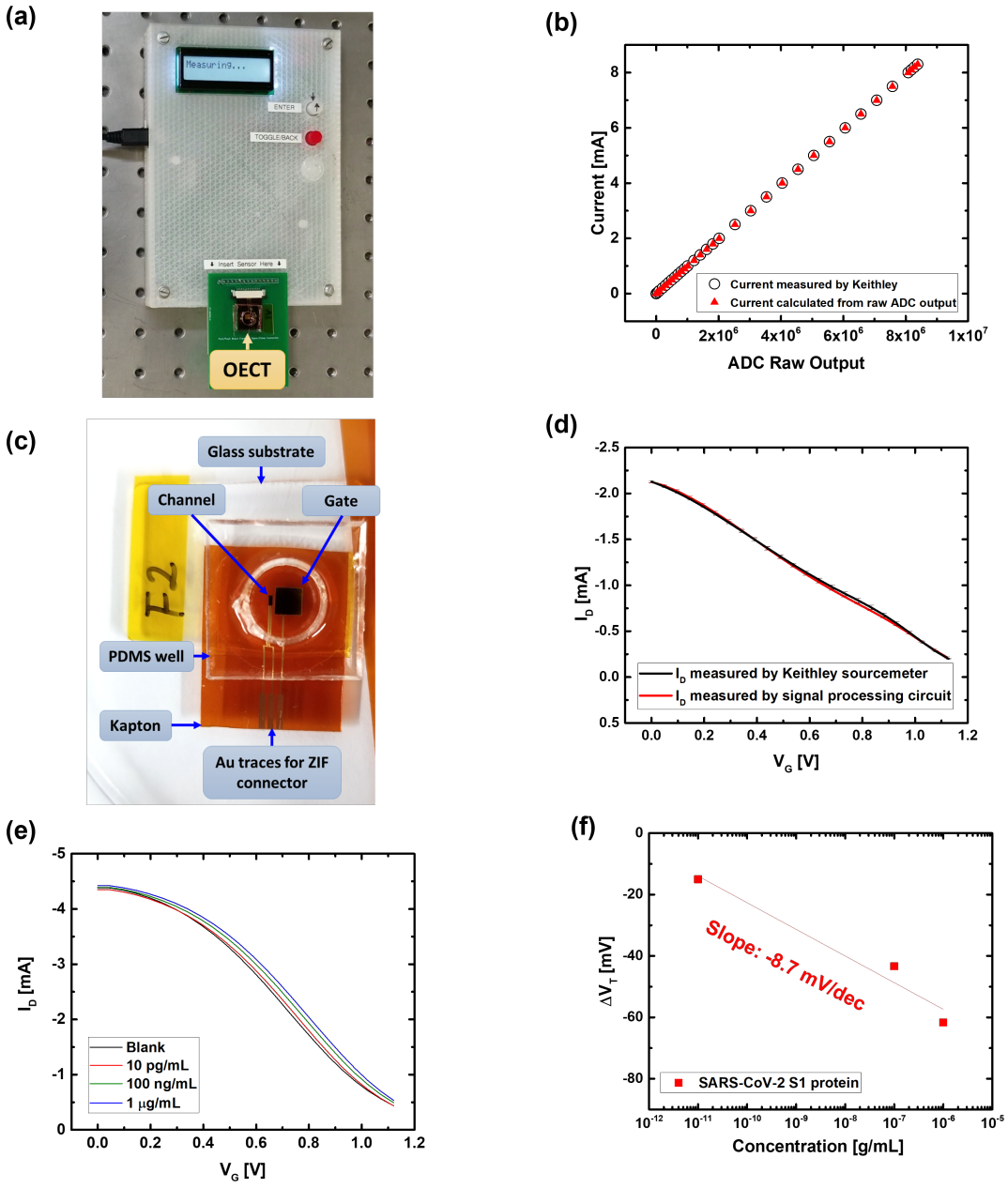

Figure 9.9: (a) Photograph of the POC COVID-19 diagnostic tool integrated with fully custom designed circuit and an OECT functionalized with SARS-CoV-2 Spike S1 antibody as the disposable biosensor. (b) Scattered plots showing the input current sourced by Keithley and the calculated current reading from the ADC results coincide with each other. (c) Photograph of an aerosol jet printed OECT based SARS-CoV-2 biosensor. (d) Comparison of the transfer curve obtained by the signal processing circuit to the one obtained by Keithley sourcemeter. (Continued on the following page.)

(Continued from the previous page.) The plots are the average of four measurements collected from each system, and the error bar represents the standard deviation. (e) Circuit collected transfer characteristics of a functionalized OECT measured after being incubated in increasing concentration of SARS-CoV-2 spike S1 protein solution. (f) Semi-logarithmic plot of ΔV_T as a function of spike protein concentration extracted from the transfer curves collected using the data processing circuit.

(b), as expected, the transfer characteristics remained nearly identical for 1xPBS and the selected DMEM dilution range. Therefore, the same dilution range from 10^6x to 10^3x of SARS-CoV-2 VLPs was used to eliminate the effect from DMEM. Similar to the spike protein test, the OECT was first incubated in VLP solution for 3 minutes, and the transfer curve was acquired for biasing V_D = -0.4 V and sweeping V_G from -0.4 V to 1.1 V. The transfer curve shifted to higher V_G as the concentration of VLP increased as shown in Figure 9.8 (c), and this was the same trend observed for the spike protein detection. A logarithmic dependence of ΔV_T to the VLP dilution was observed with an average slope of -45.7 $\pm$ 13.0 mV/dec (n = 5) as shown in Figure 9.8 (d). These results confirmed that the printed OECT with antibody functionalized gate can be used for SARS-CoV-2 virus detection.

Figure 9.9 (a) shows a photo of the OECT based POC COVID-19 diagnostic device. The schematic diagram of the custom designed data acquisition and processing circuit is shown in Appendix C. We utilized an Atmel ATmega328P microcontroller and a Texas Instruments ADS124S08 24-bit delta-sigma (Δ-Σ) analog-to-digital converter (ADC) as the core of our system. To integrate the OECT as the sensor, the V_D was biased at a constant voltage of -0.4 V using a voltage regulator, and the V_G was stepped through 0 – 1.121 V using an 8-bit digital to analog converter (DAC) with a step size of approximately 49 mV. As the OECT sensor relies on the change of I_D for SARS-CoV-2 detection, a transimpedance amplifier (TIA) was used to first convert the current signal into a voltage, V_{Id}. The feedback resistor (R_{gain}) was selected based on the OECT I_D magnitude measured using the Keithley sourcemeter to ensure that the converted voltage would be within the input voltage range of the 24-bit Δ-Σ

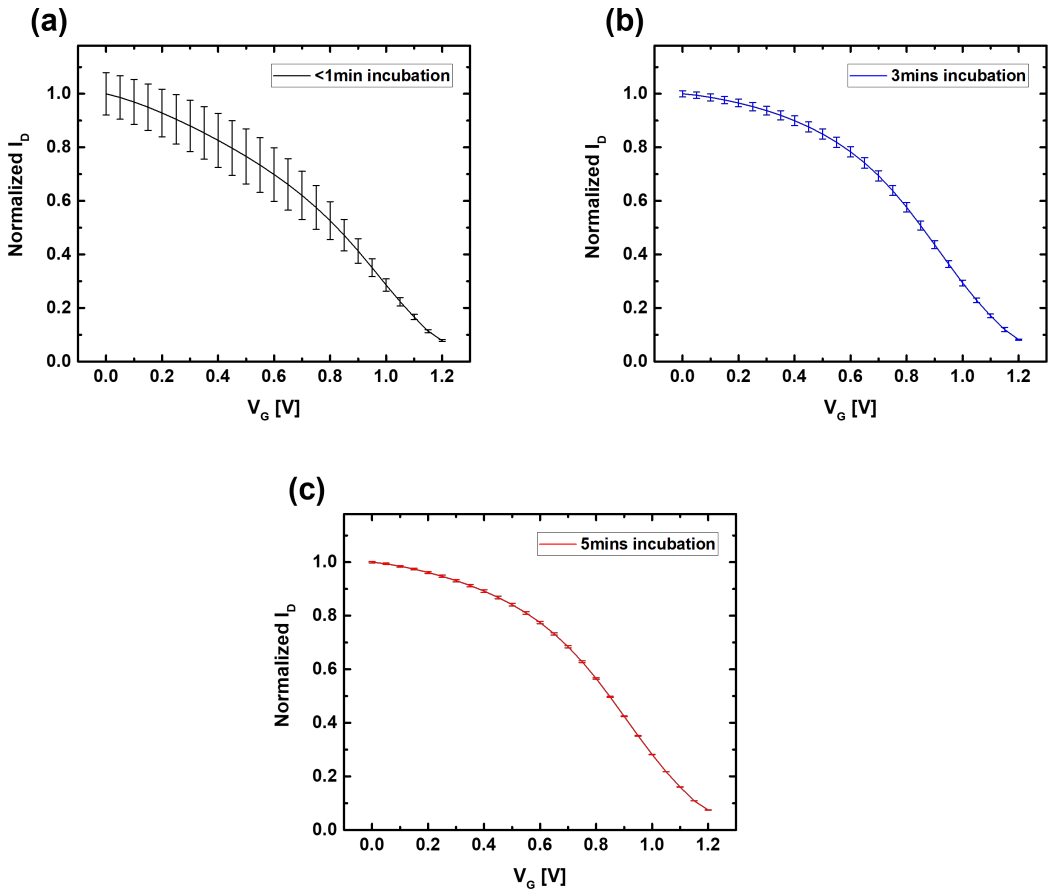

Figure 9.10: Blank UTM testing using aerosol jet printed OECT. Normalized I_D vs V_G curve averaged over three consecutive measurements with (a) less than 1 min waiting time, (b) 3 mins waiting time, and (c) 5 mins waiting time between each measurement. The error bar represents the standard deviation in this case.

ADC and finely resolved for the threshold voltage extraction. Both V_G and V_{Id} were measured by the ADC for each step of V_G, and the raw ADC data was then transferred by the central microcontroller to an Openlog datalogger and saved on a microSD card. The TIA and ADC were characterized in the lab using a Keithley sourcemeter to validate their output response. The calibration curves for the TIA and ADC demonstrated excellent linearity with a coefficient of determination $R^2 = 1$ as shown in Appendix C. As shown in Figure 9.9 (b), the current values calculated from the raw ADC data match with the input current values measured with Keithley. To connect the OECT to the circuit, an upper-contact zero insertion force (ZIF) flat flexible

Table 9.2: COVID-19 test results of clinical samples acquired by PCR and OECT based diagnostic tool.

Biosensor ID	**PCR Results**	**PCR Ct [cycles]**	ΔV_T **[mV]**	**Biosensor Results**
D1	Negative	-	-3.88	Negative
D3	Negative	-	-17.60	False Positive
C2	Negative	-	-4.55	Negative
E1	Negative	-	-8.15	Negative
E3	Negative	-	-27.24	Defective
D2	Positive	23.46	-15.50	Positive
C1	Positive	26.23	-1.11	Defective
B3	Positive	26.87	-16.09	Positive
E2	Positive	36.00	-14.26	Positive
C3	Positive	14.67	-20.76	Positive

connector (FFC) was used. Due to the limited mating cycles of ZIF connectors, we have designed the connector on a separate breakout board for easy replacement, and this also helps to isolate the sensor from the other circuit components to avoid contamination and damage. This breakout board is connected to the circuit through standard friction-fit push-pull female and male pin headers. We designed and 3D printed the enclosure for the circuit using a Markforged Mark Two 3D printer with nylon filaments. Figure 9.9 (c) shows an OECT biosensor designed for the circuit, the contact traces for the FFC were printed using the same Au NP ink, the Kapton substrate was cut to a smaller size and attached to a glass substrate for handling convenience, and a PDMS reservoir was attached to the OECT for containing the testing solution. To further verify the circuit performance, we measured the transfer curves of the same OECT using both the signal processing circuit and the Keithley sourcemeter. As illustrated in Figure 9.9 (d), the transfer curves collected using the two systems for the same OECT nearly coincide, demonstrating no change in the

sensor performance with the circuit. We also performed the SARS-CoV-2 spike S1 protein detection using a functionalized OECT with the circuit. The transfer curves and the corresponding ΔV_T extracted from these measurements are shown in Figure 9.9 (e)-(f). The shifts in the transfer curves and slope were within the range of the measurements obtained from the Keithley sourcemeter. Therefore, the circuit has sufficient precision for the desired purposes.

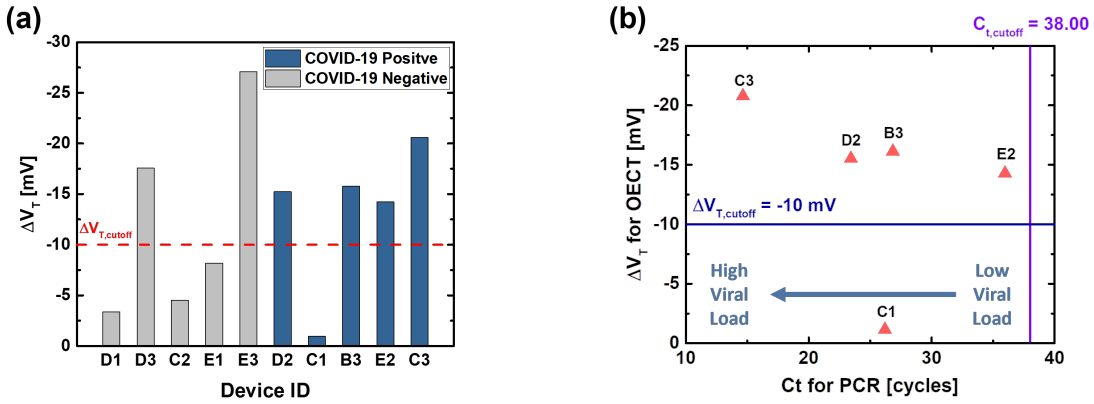

Figure 9.11: (a) ΔV_T of clinical samples collected using the OECT based SARS-CoV-2 sensor and the custom designed signal processing circuit board. The cut-off threshold voltage change, $\Delta V_{T,cutoff}$, was selected as -10 mV for SARS-CoV-2 positive samples. Device C1 and E3 were defective and their transfer curves before and after functionalization were shown in Appendix C. (b) ΔV_T collected by the OECT based biosensors plotted against the cycle threshold (Ct) measured by PCR for the 5 COVID-19 positive samples showing the correlation between ΔV_T and the sample viral load.

We then prepared to use the developed POC COVID-19 diagnostic tool for clinical sample testing. As the clinical collected nasopharyngeal samples are normally kept in UTM, before testing the clinical samples, we measured OECTs with blank UTM to check if there is any interference due to it. The transfer curves of OECTs were measured using blank undiluted UTM with different waiting intervals (<1 min, 3 mins, and 5 mins) in between consecutive measurements. The normalized I_D vs V_G averaged over three consecutive measurements for each case is shown in Figure 9.10 (a)-(c). It can be observed that with 3 and 5 minutes waiting time, the deviation between the measurements has greatly reduced indicating that with long enough waiting time

the OECT can be directly used with undiluted UTM. In order to use this platform for SARS-CoV-2 sensing, the system has been designed and programmed such that for the test cycle of each disposable biosensor, a blank test will first be performed to determine the baseline, and then the second transfer curve will be collected after incubating the sample for 5 mins. For each step, a message will prompt on the LCD screen to guide the user. One test cycle, including the baseline measurement and the sample incubation period, takes less than 10 mins. The sensor will be disposed after one test cycle. A total of 5 PCR COVID-19 positive samples and 5 PCR COVID-19 negative samples were tested using our COVID-19 diagnostic tool with 10 disposable SARS-CoV-2 biosensors. All clinical samples were nasopharyngeal swabs suspended in UTM without further dilution. The sample COVID-19 results collected by PCR and our OECT based biosensors are listed in Table 9.2. Figure 9.11 (a) shows the results of the measured clinical samples using a $\Delta V_{T,\ cutoff}$ of -10 mV. C1 and E3 were defective devices as observed from their transfer curves in Appendix C. For device C1, the transfer curve were almost identical before and after antibody immobilization, which indicated that the functionalization has not worked for this device. Whereas for device E3, the magnitude of drain current had decreased more than 3-fold, and this may be caused by accidental damage during device handling. Hence, the results of C1 and E3 were excluded in the accuracy analysis. 7 out of 8 samples were accurately detected using the selected cut-off voltage. Hence, for preliminary clinical sample testing, we obtained an overall testing accuracy of 87.5%. In PCR test, Ct is the parameter that correlates with sample viral load. A lower Ct value indicates that the sample initially contains more viruses than the sample with a higher Ct value. As shown in Figure 9.11 (b), ΔV_T extracted from OECT based biosensors are plotted with respect to the Ct values obtained from the PCR test for the 5 COVID-19 positive samples, and an increase in the ΔV_T value is observed as the sample viral load increases.With the limited numbers of COVID-19 patient samples being tested, our OECT based SARS-CoV-2 biosensors have demonstrated the capability of indi-

cating sample viral load. The preliminary clinical sample testing has demonstrated that there is a potential to use our POC COVID-19 diagnostic tool for determining SARS-CoV-2 infection and measuring viral load. As reported in other studies, SARS-CoV-2 viral load is associated with the infectivity and severity of the illness and can be used to evaluate the disease progression [231–234]. Recently, Merck and Ridgeback Biotherapeutics has released the clinical trial results of the experimental orally administrated antiviral drug – Molnupiravir for mild or moderate COVID-19 patients who had initial onset of COVID-19 symptoms for $\leq$ 5 days. The clinical data has shown that Molnupiravir reduced the risk of hospitalization or death by approximately 50% as compared to placebo. Our OECT based SARS-CoV-2 biosensors may be used to identify the stage of infection and aid to identify suitable treatments for patients [235, 236]. However, a more extensive study of testing various clinical samples is required to confirm our OECT SARS-CoV-2 biosensor performance and the association with the sample viral load.

9.5 Conclusion

In conclusion, a rapid POC COVID-19 diagnostic device was developed. The biosensor was based on aerosol jet printed OECTs with SARS-CoV-2 antibody conjugated to the gate surface. These biosensors demonstrated selectivity towards SARS-CoV-2 spike protein with a low concentration of 1 fg/mL in PBS. They were also capable of detecting VLPs with a sensitivity of -45.7 $\pm$ 13.0 mV/dec. Moreover, the rapid POC COVID-19 diagnostic device was used to test undiluted clinical nasopharyngeal swab samples suspended in UTM and the preliminary results demonstrated an overall accuracy of 87.5%. The testing takes less than 10 mins and does not require sample preparation or labeling steps. Rapid biosensing devices with high sensitivity and accuracy are important tools for controlling the spread of the SARS-CoV-2 and are in high demand during the pandemic. The rapid POC diagnostic system developed in this study is portable and user-friendly. It could be easily translated to real-world on-

site or at home detection. Such system is a facile technology platform for developing sensors for detecting other target biomolecules in the future.

Chapter 10

Summary and Future Works

In this thesis, various biosensors were developed based on OECTs fabricated by printing techniques. I started with optimizing the material printing and annealing conditions, sequentially geometry optimization of printed OECTs, towards ion and molecule sensing using unfunctionalized OECTs, and then device modifications and optimization for specific biosensing applications. This work has demonstrated the versatility of OECT for biosensing applications. We have shown that OECTs are compatible with different fabrication techniques and can be modified using various approaches to achieve selective sensing for the target analytes. Therefore, OECTs are a promising candidate for next-generation wearable biosensing platforms.

In chapter 3, I optimized the printing and post-processing conditions for substrate, contact, channel, and insulator materials using the nScrypt 3D printing system and the Optomec aerosol jet printing system. The printing and annealing conditions were optimized to achieve continuous films with high conductivities for the metal contact and the channel material to ensure OECT performance. By utilizing the nScrypt 3D printing system, the printed Ag film showed an average thickness of 9 μm and resistivity of 13.0 $\mu\Omega$-cm, which is about 8 times of bulk Ag. The nScrypt printed PEDOT:PSS film had an average thickness of 2.5 μm and resistivity of 50.9 mΩ-cm, equivalent to 19.6 S/cm. Several metal nanoparticle inks were optimized using the Optomec AJ5X printing system. The AJ printed Ag film had an average thickness

of 2.44 μm and resistivity of 4.74 $\mu\Omega$-cm about 3 times bulk Ag. The AJ printed Au film showed an average thickness of 580 nm and resistivity of 14.23 $\mu\Omega$-cm about 6 times bulk Au. With the optimized recipe, we obtained AJ printed PEDOT:PSS films with an average thickness of 790 nm and conductivity of 40.40 S/cm. These optimized printing and annealing parameters were used to fabricate OECT devices for biosensor development. Moreover, to fabricate flexible biosensors for wearables, the substrate should be carefully selected with suitable properties such as mechanical flexibility, conformability, bendability, and wear resistance. The material printing should be further optimized to achieve thinner films to improve the mechanical flexibility of wearable devices.

In chapter 4, OECTs were fabricated on flexible substrates using the nScrypt 3D printing system. The OECT was assembled on fully 3D printed soft PLA substrate and commercially available PET substrate. This was the first work demonstrating functional OECTs completely fabricated by 3D printing, including the 3D printed substrate. Compared to other literature, the fully 3D printed OECTs had a considerably high transconductance of 38.9 $\pm$ 2.4 mS, likely due to the thick printed channel film. The preliminary tests of K^+ ion concentration and pH were achieved using the 3D printed OECTs without functionalization due to the intrinsic ion sensitivity of PEDOT:PSS. High sensitivity of 240 mV/dec was observed for K^+ detection, which is correlated to the high transconductance.

In chapter 5, OECTs were fabricated on commercially available substrates using the Optomec AJ5X printing system. The influences of device geometry on the OECT performance were studied for OECTs with Ag and Au contacts. We observed that the magnitude of I_D, transconductance, ON/OFF ratio of both Ag-OECTs and Au-OECTs scale with the channel thickness and W/L. The channel thickness should be further optimized to improve the drain current ON/OFF ratio and the device response time. The effect of contact resistance of the channel and the source and drain electrode should be studies and optimized for device performance optimization.

In chapter 6, we utilized unfunctionalized AJ printed OECTs with an external Pt wire as the gate electrode to detect the concentration of Δ^9-THC molecules in synthetic saliva buffer. The THC detection was achieved by sensing the Faradaic current generated from the oxidation of phenol groups on the THC molecules at the Pt gate surface. This method is a label-free technique with an overall testing time of fewer than 10 minutes. Further improvements are needed to use the OECT as a disposable salivary THC sensor for roadside testing. One aspect of improvement is to substitute the external Pt wire with a printed in-plane gate electrode, such that there is more control over the gate surface area and the distance between the gate and channel. The in-plane gate is also easier to be integrated with the data processing circuit. Since the OECT was unfunctionalized, the Δ^9-THC sensor had poor reproducibility when testing with synthetic saliva buffer. Moreover, the change in ion concentration and other electroactive species in the testing solution could lead to errors in reading. To address this issue, biorecognition elements, such as anti-THC antibodies or aptamers, need to be incorporated onto OECT to improve selectivity.

In chapter 7, a systematic functionalization study was conducted using aerosol jet printed OECT based glucose biosensors. Glucose sensing was achieved by incorporating GOx enzyme to the electrolyte, channel, and gate of the printed OECTs. Glucose sensing in PBS was repeated with three devices for each functionalization configuration, and sensing sensitivity was extracted from these measurements. Two linear slopes were observed for each case, likely due to limited GOx amount and fixed Pt gate size. The OECT with GOx functionalized printed Pt gate exhibited the best performance among different functionalization configurations and could detect glucose concentration in artificial sweat buffer a detection range of 0.1 to 10 mM covering the human sweat glucose range with two linear slopes of 0.068NR/dec for 100 - 500 μM and 0.384NR/dec for 500 μM - 10 mM. These results confirm that the AJ printed OECT with functionalized gate is highly promising for non-invasive glucose sensing. Using glucose sensors as an example, this work also demonstrates that the

choice of functionalization site and functional materials are critical to the biosensor design. Further testing with real human sweat samples should be performed to verify the sensor performance. Moreover, a compact circuit for power supply and data transmission is required to use the OECT based biosensor as wearables for continuous glucose monitoring.

Chapter 8 demonstrated the detection of streptavidin protein using printed OECT with external printed Au gate electrodes that were functionalized with biotin via NHC functional groups. We selected the NHC ligand due to its high binding affinity to gold. The alkyl groups could be chemically modified based on application needs. In this work, the alkyne-NHC ligands were synthesized to facilitate biomolecule attachment through click chemistry. The surface modification was verified by optical, electrochemical, and electrical methods. The biotin functionalized electrode showed selectivity towards streptavidin with an Δ V_T of 255.9 $\pm$ 120.0 mV extracted from four functionalized Au electrodes, each measured with three OECTs. The high standard deviation of the Δ V_T value is likely due to variation in the amount of bound streptavidin. Since each streptavidin has four identical subunits, each streptavidin molecule could interact with several biotin molecules leading to the deviation between measurements. The next step is to conduct the stability study of the gate electrode functionalized by the NHC SAM and compare the results with the one modified by the thiol-based SAM. This approach could be potentially used for improving the selectivity of OECT based Δ^9-THC biosensor by functionalizing an external gate with suitable biorecognition elements.

In chapter 9, we have developed a POC rapid COVID-19 diagnostic device consisting of a disposable AJ printed OECT based biosensor and a custom-designed signal processing circuit. The OECT biosensors were modified with the anti-SARS-CoV-2 antibody on the Au gate electrode for selectivity. Device geometry optimization was first conducted to achieve better sensitivity. The function of OECT based SARS-CoV-2 biosensor was validated with SARS-CoV-2 spike protein with a detection range of 1

fg/mL to 1μg/mL and virus-like particles with a detection range of approximately 10^3 copies/mL to 10^6 copies/mL and average sensitivity of -45.7 mV/dec. Our COVID-19 diagnostic tool was tested with clinical nasopharyngeal swab samples suspended in UTM and demonstrated an overall accuracy of 87.5%. This label-free technique does not require extra sample preparation steps, and the overall testing time is less than 10 minutes. With the limited number of COVID-19 positive clinical samples, the change in ΔV_T of our OECT based SARS-CoV-2 demonstrated correlation with the sample viral load. Along with the potable signal processing circuit, this tool can be used on-site and even at home. There is still room for improvement to meet the requirements for practical applications. The OECTs based SARS-CoV-2 sensors were tested within three days after being functionalized, and we have not conducted any tests for the stability of the sensors after a long time of storage. This is an important factor for actual implementation as a diagnostic tool to prevent error reading due to material degradation. Moreover, the functionalized gate is unprotected and potentially exposed to contaminants in the environment that may lead to the degradation of antibodies. Incorporating a microfluidic device would help enclose the functionalized gate and also minimize the stock buffer solution evaporation. In the current circuit design, the data is only saved locally on a microSD card, and the data analysis was performed using MATLAB. Both of these need to be further improved to provide real-time feedback on the results.

Despite the aspects discussed above for each chapter, some other factors should also be taken into consideration for future improvement of OECT based biosensors. Since the Optomec AJ5X system has 5-axis printing capability, there is a potential for conformal printing onto non-planar substrate to improve the wearability of the printed biosensors. The device functionalization could be further optimized by using printing techniques to deposit the functional materials and biomaterials to the designated areas. By using printing techniques, the functionalization process is carried out in a more controlled manner to improve accuracy and efficiency. Another important

aspect is to improve sensing accuracy using multiple sensor arrays to target specific concentration ranges and for data validation. Temperature and pH sensors should always be integrated, as they are the factors that affect the bioactivity of enzymes and other biomolecules for recognizing the analyte. The power and data synchronizing issues were not addressed in this thesis, but they are critical aspects that need to be optimized to make the OECT based biosensors truly portable and wearable. A smartphone application could be implemented to improve the accessibility of data to the device users and healthcare professionals.

Bibliography

[1] Grand View Research. (2021). "Biosensors market size, share & trends analysis report by application (medical, agriculture, environment) by technology (thermal, electrochemical, optical), by end-use, by region, and segment forecasts, 2021 - 2028," [Online]. Available: https://www.grandviewresearch.com/industry-analysis/biosensors-market (visited on 07/26/2021).

[2] I. J. Miller, S. R. Peters, K. A. Overmyer, B. R. Paulson, M. S. Westphall, and J. J. Coon, "Real-time health monitoring through urine metabolomics," *NPJ digital medicine*, vol. 2, no. 1, pp. 1–9, 2019, ISSN: 2398-6352.

[3] M. Bariya, H. Y. Y. Nyein, and A. Javey, "Wearable sweat sensors," *Nature Electronics*, vol. 1, no. 3, pp. 160–171, 2018, ISSN: 2520-1131.

[4] X. Li, J. Dunn, D. Salins, G. Zhou, W. Zhou, S. M. Schüssler-Fiorenza Rose, D. Perelman, E. Colbert, R. Runge, and S. Rego, "Digital health: Tracking physiomes and activity using wearable biosensors reveals useful health-related information," *PLoS biology*, vol. 15, no. 1, e2001402, 2017, ISSN: 1544-9173.

[5] E. Bakker and Y. Qin, "Electrochemical sensors," *Anal Chem*, vol. 78, no. 12, pp. 3965–84, 2006, ISSN: 0003-2700 (Print) 0003-2700 (Linking). DOI: 10.1021/ac060637m. [Online]. Available: https://www.ncbi.nlm.nih.gov/pubmed/16771535.

[6] S. Imran, S. Ahmadi, and K. Kerman, "Electrochemical biosensors for the detection of sars-cov-2 and other viruses," *Micromachines (Basel)*, vol. 12, no. 2, 2021, ISSN: 2072-666X (Print) 2072-666X (Linking). DOI: 10.3390/mi12020174. [Online]. Available: https://www.ncbi.nlm.nih.gov/pubmed/33578979.

[7] D. Khodagholy, J. Rivnay, M. Sessolo, M. Gurfinkel, P. Leleux, L. H. Jimison, E. Stavrinidou, T. Herve, S. Sanaur, R. M. Owens, and G. G. Malliaras, "High transconductance organic electrochemical transistors," *Nat Commun*, vol. 4, p. 2133, 2013, ISSN: 2041-1723 (Electronic) 2041-1723 (Linking). DOI: 10.1038/ncomms3133. [Online]. Available: https://www.ncbi.nlm.nih.gov/pubmed/23851620.

[8] N. Wang, A. Yang, Y. Fu, Y. Li, and F. Yan, "Functionalized organic thin film transistors for biosensing," *Acc Chem Res*, vol. 52, no. 2, pp. 277–287, 2019, ISSN: 1520-4898 (Electronic) 0001-4842 (Linking). DOI: 10.1021/acs.accounts.8b00448. [Online]. Available: https://www.ncbi.nlm.nih.gov/pubmed/30620566.

[9] L. Torsi, M. Magliulo, K. Manoli, and G. Palazzo, "Organic field-effect transistor sensors: A tutorial review," *Chemical Society Reviews*, vol. 42, no. 22, pp. 8612–8628, 2013.

[10] D. Sadighbayan, M. Hasanzadeh, and E. Ghafar-Zadeh, "Biosensing based on field-effect transistors (fet): Recent progress and challenges," *Trends Analyt Chem*, vol. 133, p. 116 067, 2020, ISSN: 0165-9936 (Print) 0165-9936 (Linking). DOI: 10.1016/j.trac.2020.116067. [Online]. Available: https://www.ncbi.nlm.nih.gov/pubmed/33052154.

[11] D. R. Thévenot, K. Toth, R. A. Durst, and G. S. Wilson, "Electrochemical biosensors: Recommended definitions and classification," *Biosensors and bioelectronics*, vol. 16, no. 1-2, pp. 121–131, 2001, ISSN: 0956-5663.

[12] P. Mehrotra, "Biosensors and their applications–a review," *Journal of oral biology and craniofacial research*, vol. 6, no. 2, pp. 153–159, 2016, ISSN: 2212-4268.

[13] P. Li, G. H. Lee, S. Y. Kim, S. Y. Kwon, H. R. Kim, and S. Park, "From diagnosis to treatment: Recent advances in patient-friendly biosensors and implantable devices," *ACS Nano*, vol. 15, no. 2, pp. 1960–2004, 2021, ISSN: 1936-086X (Electronic) 1936-0851 (Linking). DOI: 10.1021/acsnano.0c06688. [Online]. Available: https://www.ncbi.nlm.nih.gov/pubmed/33534541.

[14] H. C. Ates, A. K. Yetisen, F. Güder, and C. Dincer, "Wearable devices for the detection of covid-19," *Nature Electronics*, vol. 4, no. 1, pp. 13–14, 2021, ISSN: 2520-1131. DOI: 10.1038/s41928-020-00533-1.

[15] Q. Liu, Y. Liu, F. Wu, X. Cao, Z. Li, M. Alharbi, A. N. Abbas, M. R. Amer, and C. Zhou, "Highly sensitive and wearable in2o3 nanoribbon transistor biosensors with integrated on-chip gate for glucose monitoring in body fluids," *ACS Nano*, vol. 12, no. 2, pp. 1170–1178, 2018, ISSN: 1936-086X (Electronic) 1936-0851 (Linking). DOI: 10.1021/acsnano.7b06823. [Online]. Available: https://www.ncbi.nlm.nih.gov/pubmed/29338249.

[16] L. J. Currano, F. C. Sage, M. Hagedon, L. Hamilton, J. Patrone, and K. Gerasopoulos, "Wearable sensor system for detection of lactate in sweat," *Sci Rep*, vol. 8, no. 1, p. 15 890, 2018, ISSN: 2045-2322 (Electronic) 2045-2322 (Linking). DOI: 10.1038/s41598-018-33565-x. [Online]. Available: https://www.ncbi.nlm.nih.gov/pubmed/30367078.

[17] H. Teymourian, A. Barfidokht, and J. Wang, "Electrochemical glucose sensors in diabetes management: An updated review (2010-2020)," *Chem Soc Rev*, vol. 49, no. 21, pp. 7671–7709, 2020, ISSN: 1460-4744 (Electronic) 0306-0012 (Linking). DOI: 10.1039/d0cs00304b. [Online]. Available: https://www.ncbi.nlm.nih.gov/pubmed/33020790.

[18] J. Kim, A. S. Campbell, and J. Wang, "Wearable non-invasive epidermal glucose sensors: A review," *Talanta*, vol. 177, pp. 163–170, 2018, ISSN: 1873-3573 (Electronic) 0039-9140 (Linking). DOI: 10.1016/j.talanta.2017.08.077. [Online]. Available: https://www.ncbi.nlm.nih.gov/pubmed/29108571.

[19] H. Lee, C. Song, Y. S. Hong, M. S. Kim, H. R. Cho, T. Kang, K. Shin, S. H. Choi, T. Hyeon, and D. H. Kim, "Wearable/disposable sweat-based glucose monitoring device with multistage transdermal drug delivery module," *Sci Adv*, vol. 3, no. 3, e1601314, 2017, ISSN: 2375-2548 (Electronic) 2375-2548 (Linking). DOI: 10.1126/sciadv.1601314. [Online]. Available: https://www.ncbi.nlm.nih.gov/pubmed/28345030.

[20] H. Teymourian, M. Parrilla, J. R. Sempionatto, N. F. Montiel, A. Barfidokht, R. Van Echelpoel, K. De Wael, and J. Wang, "Wearable electrochemical sensors for the monitoring and screening of drugs," *ACS Sens*, vol. 5, no. 9, pp. 2679–2700, 2020, ISSN: 2379-3694 (Electronic) 2379-3694 (Linking). DOI: 10.1021/acssensors.0c01318. [Online]. Available: https://www.ncbi.nlm.nih.gov/pubmed/32822166.

[21] X. Wang, Z. Liu, and T. Zhang, "Flexible sensing electronics for wearable/attachable health monitoring," *Small*, vol. 13, no. 25, p. 1 602 790, 2017, ISSN: 1613-6829 (Electronic) 1613-6810 (Linking). DOI: 10.1002/smll.201602790. [Online]. Available: https://www.ncbi.nlm.nih.gov/pubmed/28306196.

[22] S. Li, Z. Ma, Z. Cao, L. Pan, and Y. Shi, "Advanced wearable microfluidic sensors for healthcare monitoring," *Small*, vol. 16, no. 9, e1903822, 2020, ISSN: 1613-6829 (Electronic) 1613-6810 (Linking). DOI: 10.1002/smll.201903822. [Online]. Available: https://www.ncbi.nlm.nih.gov/pubmed/31617311.

[23] A. Nag, S. C. Mukhopadhyay, and J. Kosel, "Wearable flexible sensors: A review," *IEEE Sensors Journal*, vol. 17, no. 13, pp. 3949–3960, 2017, ISSN: 1530-437X 1558-1748 2379-9153. DOI: 10.1109/jsen.2017.2705700. [Online]. Available: https://ieeexplore.ieee.org/document/7931559/.

[24] Y. Yang and W. Gao, "Wearable and flexible electronics for continuous molecular monitoring," *Chem Soc Rev*, vol. 48, no. 6, pp. 1465–1491, 2019, ISSN: 1460-4744 (Electronic) 0306-0012 (Linking). DOI: 10.1039/c7cs00730b. [Online]. Available: https://www.ncbi.nlm.nih.gov/pubmed/29611861.

[25] M. Xu, D. Obodo, and V. K. Yadavalli, "The design, fabrication, and applications of flexible biosensing devices," *Biosensors and Bioelectronics*, vol. 124, pp. 96–114, 2019, ISSN: 0956-5663.

[26] J. Rivnay, R. M. Owens, and G. G. Malliaras, "The rise of organic bioelectronics," *Chemistry of Materials*, vol. 26, no. 1, pp. 679–685, 2013, ISSN: 0897-4756 1520-5002. DOI: 10.1021/cm4022003.

[27] X. Strakosas, M. Bongo, and R. M. Owens, "The organic electrochemical transistor for biological applications," *Journal of Applied Polymer Science*, vol. 132, no. 15, 2015, ISSN: 0021-8995.

[28] S. H. Kim, K. Hong, W. Xie, K. H. Lee, S. Zhang, T. P. Lodge, and C. D. Frisbie, "Electrolyte-gated transistors for organic and printed electronics," *Advanced Materials*, vol. 25, no. 13, pp. 1822–1846, 2013, ISSN: 0935-9648.

[29] J. Wang, D. Ye, Q. Meng, C. Di, and D. Zhu, "Advances in organic transistor-based biosensors," *Advanced Materials Technologies*, vol. 5, no. 7, 2020, ISSN: 2365-709X 2365-709X. DOI: 10.1002/admt.202000218.

[30] S. Inal, G. G. Malliaras, and J. Rivnay, "Benchmarking organic mixed conductors for transistors," *Nat Commun*, vol. 8, no. 1, p. 1767, 2017, ISSN: 2041-1723 (Electronic) 2041-1723 (Linking). DOI: 10.1038/s41467-017-01812-w. [Online]. Available: https://www.ncbi.nlm.nih.gov/pubmed/29176599.

[31] D. A Bernards and G. G Malliaras, "Steady-state and transient behavior of organic electrochemical transistors," *Advanced Functional Materials*, vol. 17, no. 17, pp. 3538–3544, 2007, ISSN: 1616301X. DOI: 10.1002/adfm.200601239.

[32] J. T. Friedlein, R. R. McLeod, and J. Rivnay, "Device physics of organic electrochemical transistors," *Organic Electronics*, vol. 63, pp. 398–414, 2018, ISSN: 15661199. DOI: 10.1016/j.orgel.2018.09.010.

[33] J. Rivnay, P. Leleux, M. Ferro, M. Sessolo, A. Williamson, D. A. Koutsouras, D. Khodagholy, M. Ramuz, X. Strakosas, R. M. Owens, C. Benar, J. M. Badier, C. Bernard, and G. G. Malliaras, "High-performance transistors for bioelectronics through tuning of channel thickness," *Sci Adv*, vol. 1, no. 4, e1400251, 2015, ISSN: 2375-2548 (Print) 2375-2548 (Linking). DOI: 10.1126/sciadv.1400251. [Online]. Available: https://www.ncbi.nlm.nih.gov/pubmed/26601178.

[34] C. Liao, M. Zhang, M. Y. Yao, T. Hua, L. Li, and F. Yan, "Flexible organic electronics in biology: Materials and devices," *Advanced materials*, vol. 27, no. 46, pp. 7493–7527, 2015, ISSN: 0935-9648.

[35] W. Lee, D. Kim, N. Matsuhisa, M. Nagase, M. Sekino, G. G. Malliaras, T. Yokota, and T. Someya, "Transparent, conformable, active multielectrode array using organic electrochemical transistors," *Proc Natl Acad Sci U S A*, vol. 114, no. 40, pp. 10 554–10 559, 2017, ISSN: 1091-6490 (Electronic) 0027-8424 (Linking). DOI: 10.1073/pnas.1703886114. [Online]. Available: https://www.ncbi.nlm.nih.gov/pubmed/28923928.

[36] P. A. Ersman, D. Nilsson, J. Kawahara, G. Gustafsson, and M. Berggren, "Fast-switching all-printed organic electrochemical transistors," *Organic Electronics*, vol. 14, no. 5, pp. 1276–1280, 2013, ISSN: 15661199. DOI: 10.1016/j.orgel.2013.02.027.

[37] J. Peng, T. He, Y. Sun, Y. Liu, Q. Cao, Q. Wang, and H. Tang, "An organic electrochemical transistor for determination of microrna21 using gold nanoparticles and a capture dna probe," *Mikrochim Acta*, vol. 185, no. 9, p. 408, 2018, ISSN: 1436-5073 (Electronic) 0026-3672 (Linking). DOI: 10.1007/s00604-018-2944-x. [Online]. Available: https://www.ncbi.nlm.nih.gov/pubmed/30097715.

[38] Y. Liang, M. Ernst, F. Brings, D. Kireev, V. Maybeck, A. Offenhausser, and D. Mayer, "High performance flexible organic electrochemical transistors for monitoring cardiac action potential," *Adv Healthc Mater*, vol. 7, no. 19, e1800304, 2018, ISSN: 2192-2659 (Electronic) 2192-2640 (Linking). DOI: 10.1002/adhm.201800304. [Online]. Available: https://www.ncbi.nlm.nih.gov/pubmed/30109770.

[39] W. Ji, D. Wu, W. Tang, X. Xi, Y. Su, X. Guo, and R. Liu, "Carbonized silk fabric-based flexible organic electrochemical transistors for highly sensitive and selective dopamine detection," *Sensors and Actuators B: Chemical*, vol. 304, 2020, ISSN: 09254005. DOI: 10.1016/j.snb.2019.127414.

[40] I. Gualandi, M. Marzocchi, A. Achilli, D. Cavedale, A. Bonfiglio, and B. Fraboni, "Textile organic electrochemical transistors as a platform for wearable biosensors," *Sci Rep*, vol. 6, p. 33 637, 2016, ISSN: 2045-2322 (Electronic) 2045-2322 (Linking). DOI: 10.1038/srep33637. [Online]. Available: https://www.ncbi.nlm.nih.gov/pubmed/27667396.

[41] E. Bihar, Y. Deng, T. Miyake, M. Saadaoui, G. G. Malliaras, and M. Rolandi, "A disposable paper breathalyzer with an alcohol sensing organic electrochemical transistor," *Sci Rep*, vol. 6, p. 27 582, 2016, ISSN: 2045-2322 (Electronic) 2045-2322 (Linking). DOI: 10.1038/srep27582. [Online]. Available: https://www.ncbi.nlm.nih.gov/pubmed/27291059.

[42] T. Ito, H. Shirakawa, and S. Ikeda, "Simultaneous polymerization and formation of polyacetylene film on the surface of concentrated soluble ziegler-type catalyst solution," *Journal of polymer science: polymer chemistry edition*, vol. 12, no. 1, pp. 11–20, 1974, ISSN: 0360-6376.

[43] H. S. White, G. P. Kittlesen, and M. S. Wrighton, "Chemical derivatization of an array of three gold microelectrodes with polypyrrole: Fabrication of a molecule-based transistor," *Journal of the American Chemical Society*, vol. 106, no. 18, pp. 5375–5377, 1984. DOI: 10.1021/ja00330a070.

[44] E. Zeglio and O. Inganas, "Active materials for organic electrochemical transistors," *Adv Mater*, vol. 30, no. 44, e1800941, 2018, ISSN: 1521-4095 (Electronic) 0935-9648 (Linking). DOI: 10.1002/adma.201800941. [Online]. Available: https://www.ncbi.nlm.nih.gov/pubmed/30022545.

[45] M. Nishizawa, T. Matsue, and I. Uchida, "Fabrication of a ph-sensitive microarray electrode and applicability to biosensors," *Sensors and Actuators B: Chemical*, vol. 13, no. 1-3, pp. 53–56, 1993, ISSN: 0925-4005.

[46] M. Moser, J. F. Ponder Jr, A. Wadsworth, A. Giovannitti, and I. McCulloch, "Materials in organic electrochemical transistors for bioelectronic applications: Past, present, and future," *Advanced Functional Materials*, vol. 29, no. 21, p. 1 807 033, 2019, ISSN: 1616-301X.

[47] B. Piro, G. Mattana, S. Zrig, G. Anquetin, N. Battaglini, D. Capitao, A. Maurin, and S. Reisberg, "Fabrication and use of organic electrochemical transistors for sensing of metabolites in aqueous media," *Applied Sciences*, vol. 8, no. 6, 2018, ISSN: 2076-3417. DOI: 10.3390/app8060928.

[48] A. Epstein, J. Ginder, F Zuo, H.-S. Woo, D. Tanner, A. Richter, M Angelopoulos, W.-S. Huang, and A. MacDiarmid, "Insulator-to-metal transition in polyaniline: Effect of protonation in emeraldine," *Synthetic Metals*, vol. 21, no. 1-3, pp. 63–70, 1987, ISSN: 0379-6779.

[49] D. Orata and D. A. Buttry, "Determination of ion populations and solvent content as functions of redox state and ph in polyaniline," *Journal of the American Chemical Society*, vol. 109, no. 12, pp. 3574–3581, 1987, ISSN: 0002-7863.

[50] P. Bartlett and J. Wang, "Electroactivity, stability and application in an enzyme switch at ph 7 of poly (aniline)–poly (styrenesulfonate) composite films," *Journal of the Chemical Society, Faraday Transactions*, vol. 92, no. 20, pp. 4137–4143, 1996.

[51] D. Raffa, K. Leung, and F. Battaglini, "A microelectrochemical enzyme transistor based on an n-alkylated poly (aniline) and its application to determine hydrogen peroxide at neutral ph," *Analytical Chemistry*, vol. 75, no. 19, pp. 4983–4987, 2003, ISSN: 0003-2700.

[52] J. Rivnay, S. Inal, A. Salleo, R. M. Owens, M. Berggren, and G. G. Malliaras, "Organic electrochemical transistors," *Nature Reviews Materials*, vol. 3, no. 2, 2018, ISSN: 2058-8437. DOI: 10.1038/natrevmats.2017.86.

[53] A. Elschner, S. Kirchmeyer, W. Lovenich, U. Merker, and K. Reuter, *PEDOT: principles and applications of an intrinsically conductive polymer*. CRC press, 2010, ISBN: 1420069128.

[54] A. Giovannitti, C. B. Nielsen, D. T. Sbircea, S. Inal, M. Donahue, M. R. Niazi, D. A. Hanifi, A. Amassian, G. G. Malliaras, J. Rivnay, and I. McCulloch, "N-type organic electrochemical transistors with stability in water," *Nat Commun*, vol. 7, p. 13 066, 2016, ISSN: 2041-1723 (Electronic) 2041-1723 (Linking). DOI: 10.1038/ncomms13066. [Online]. Available: https://www.ncbi.nlm.nih.gov/pubmed/27713414.

[55] H. Sun, M. Vagin, S. Wang, X. Crispin, R. Forchheimer, M. Berggren, and S. Fabiano, "Complementary logic circuits based on high-performance n-type organic electrochemical transistors," *Adv Mater*, vol. 30, no. 9, 2018, ISSN: 1521-4095 (Electronic) 0935-9648 (Linking). DOI: 10.1002/adma.201704916. [Online]. Available: https://www.ncbi.nlm.nih.gov/pubmed/29318706.

[56] K. Wilbourn and R. W. Murray, "The electrochemical doping reactions of the conducting ladder polymer benzimidazobenzophenanthroline (bbl)," *Macromolecules*, vol. 21, no. 1, pp. 89–96, 1988, ISSN: 0024-9297 1520-5835. DOI: 10.1021/ma00179a019.

[57] H. Sun, J. Gerasimov, M. Berggren, and S. Fabiano, "N-type organic electrochemical transistors: Materials and challenges," *Journal of Materials Chemistry C*, vol. 6, no. 44, pp. 11 778–11 784, 2018, ISSN: 2050-7526 2050-7534. DOI: 10.1039/c8tc03185a.

[58] F. Lin and M. C. Lonergan, "Gate electrode processes in an electrolyte-gated transistor: Non-faradaically versus faradaically coupled conductivity modulation of a polyacetylene ionomer," *Applied physics letters*, vol. 88, no. 13, p. 133 507, 2006, ISSN: 0003-6951.

[59] G. Tarabella, C. Santato, S. Y. Yang, S. Iannotta, G. G. Malliaras, and F. Cicoira, "Effect of the gate electrode on the response of organic electrochemical transistors," *Applied Physics Letters*, vol. 97, no. 12, 2010, ISSN: 0003-6951 1077-3118. DOI: 10.1063/1.3491216.

[60] F. Cicoira, M. Sessolo, O. Yaghmazadeh, J. A. DeFranco, S. Y. Yang, and G. G. Malliaras, "Influence of device geometry on sensor characteristics of planar organic electrochemical transistors," *Adv Mater*, vol. 22, no. 9, pp. 1012–6, 2010, ISSN: 0935-9648 (Print) 0935-9648 (Linking). DOI: 10.1002/adma.200902329. [Online]. Available: https://www.ncbi.nlm.nih.gov/pubmed/20217831.

[61] H. Tang, P. Kumar, S. Zhang, Z. Yi, G. D. Crescenzo, C. Santato, F. Soavi, and F. Cicoira, "Conducting polymer transistors making use of activated carbon gate electrodes," *ACS applied materials & interfaces*, vol. 7, no. 1, pp. 969–973, 2015, ISSN: 1944-8244.

[62] H. Tang, P. Lin, H. L. Chan, and F. Yan, "Highly sensitive dopamine biosensors based on organic electrochemical transistors," *Biosens Bioelectron*, vol. 26, no. 11, pp. 4559–63, 2011, ISSN: 1873-4235 (Electronic) 0956-5663 (Linking). DOI: 10.1016/j.bios.2011.05.025. [Online]. Available: https://www.ncbi.nlm.nih.gov/pubmed/21652201.

[63] D. Majak, J. Fan, S. Kang, and M. Gupta, "Delta-9-tetrahydrocannabinol (Δ 9-thc) sensing using an aerosol jet printed organic electrochemical transistor (oect)," *J Mater Chem B*, vol. 9, no. 8, pp. 2107–2117, 2021, ISSN: 2050-7518 (Electronic) 2050-750X (Linking). DOI: 10.1039/d0tb02951c. [Online]. Available: https://www.ncbi.nlm.nih.gov/pubmed/33596277.

[64] D. J. Macaya, M. Nikolou, S. Takamatsu, J. T. Mabeck, R. M. Owens, and G. G. Malliaras, "Simple glucose sensors with micromolar sensitivity based on organic electrochemical transistors," *Sensors and Actuators B: Chemical*, vol. 123, no. 1, pp. 374–378, 2007, ISSN: 09254005. DOI: 10.1016/j.snb.2006.08.038.

[65] H. Tang, F. Yan, P. Lin, J. Xu, and H. L. W. Chan, "Highly sensitive glucose biosensors based on organic electrochemical transistors using platinum gate electrodes modified with enzyme and nanomaterials," *Advanced Functional Materials*, vol. 21, no. 12, pp. 2264–2272, 2011, ISSN: 1616301X. DOI: 10.1002/adfm.201002117.

[66] L. Chen, Y. Fu, N. Wang, A. Yang, Y. Li, J. Wu, H. Ju, and F. Yan, "Organic electrochemical transistors for the detection of cell surface glycans," *ACS Appl Mater Interfaces*, vol. 10, no. 22, pp. 18 470–18 477, 2018, ISSN: 1944-8252 (Electronic) 1944-8244 (Linking). DOI: 10.1021/acsami.8b01987. [Online]. Available: https://www.ncbi.nlm.nih.gov/pubmed/29749223.

[67] E. Macchia, P. Romele, K. Manoli, M. Ghittorelli, M. Magliulo, Z. M. Kovács-Vajna, F. Torricelli, and L. Torsi, "Ultra-sensitive protein detection with organic electrochemical transistors printed on plastic substrates," *Flexible and Printed Electronics*, vol. 3, no. 3, 2018, ISSN: 2058-8585. DOI: 10.1088/2058-8585/aad0cb.

[68] W. Tao, P. Lin, J. Hu, S. Ke, J. Song, and X. Zeng, "A sensitive dna sensor based on an organic electrochemical transistor using a peptide nucleic acid-modified nanoporous gold gate electrode," *RSC Advances*, vol. 7, no. 82, pp. 52 118–52 124, 2017, ISSN: 2046-2069. DOI: 10.1039/c7ra09832d.

[69] J. Yu, A. Yang, N. Wang, H. Ling, J. Song, X. Chen, Y. Lian, Z. Zhang, F. Yan, and M. Gu, "Highly sensitive detection of caspase-3 activity based on peptide-modified organic electrochemical transistor biosensors," *Nanoscale*, vol. 13, no. 5, pp. 2868–2874, 2021, ISSN: 2040-3372 (Electronic) 2040-3364 (Linking). DOI: 10.1039/d0nr08453k. [Online]. Available: https://www.ncbi.nlm.nih.gov/pubmed/33464252.

[70] L. Zhang, G. Wang, D. Wu, C. Xiong, L. Zheng, Y. Ding, H. Lu, G. Zhang, and L. Qiu, "Highly selective and sensitive sensor based on an organic electrochemical transistor for the detection of ascorbic acid," *Biosens Bioelectron*, vol. 100, pp. 235–241, 2018, ISSN: 1873-4235 (Electronic) 0956-5663 (Linking). DOI: 10.1016/j.bios.2017.09.006. [Online]. Available: https://www.ncbi.nlm.nih.gov/pubmed/28923558.

[71] D. J. Kim, N. E. Lee, J. S. Park, I. J. Park, J. G. Kim, and H. J. Cho, "Organic electrochemical transistor based immunosensor for prostate specific antigen (psa) detection using gold nanoparticles for signal amplification," *Biosens Bioelectron*, vol. 25, no. 11, pp. 2477–82, 2010, ISSN: 1873-4235 (Electronic) 0956-5663 (Linking). DOI: 10.1016/j.bios.2010.04.013. [Online]. Available: https://www.ncbi.nlm.nih.gov/pubmed/20435461.

[72] J. Liao, S. Lin, Y. Yang, K. Liu, and W. Du, "Highly selective and sensitive glucose sensors based on organic electrochemical transistors using tio2 nanotube arrays-based gate electrodes," *Sensors and Actuators B: Chemical*, vol. 208, pp. 457–463, 2015, ISSN: 09254005. DOI: 10.1016/j.snb.2014.11.038.

[73] C. Liao, M. Zhang, L. Niu, Z. Zheng, and F. Yan, "Highly selective and sensitive glucose sensors based on organic electrochemical transistors with graphene-modified gate electrodes," *J Mater Chem B*, vol. 1, no. 31, pp. 3820–3829, 2013, ISSN: 2050-7518 (Electronic) 2050-750X (Linking). DOI: 10.1039/c3tb20451k. [Online]. Available: https://www.ncbi.nlm.nih.gov/pubmed/32261135.

[74] C. Xiong, Y. Wang, H. Qu, L. Zhang, L. Qiu, W. Chen, F. Yan, and L. Zheng, "Highly sensitive detection of gallic acid based on organic electrochemical transistors with poly(diallyldimethylammonium chloride) and carbon nanomaterials nanocomposites functionalized gate electrodes," *Sensors and Actuators B: Chemical*, vol. 246, pp. 235–242, 2017, ISSN: 09254005. DOI: 10.1016/j.snb.2017.02.025.

[75] N. R. Mohamad, N. H. C. Marzuki, N. A. Buang, F. Huyop, and R. A. Wahab, "An overview of technologies for immobilization of enzymes and surface analysis techniques for immobilized enzymes," *Biotechnology & Biotechnological Equipment*, vol. 29, no. 2, pp. 205–220, 2015, ISSN: 1310-2818.

[76] S. Liebana and G. A. Drago, "Bioconjugation and stabilisation of biomolecules in biosensors," *Essays in biochemistry*, vol. 60, no. 1, pp. 59–68, 2016, ISSN: 0071-1365.

[77] M. A. Morales and J. M. Halpern, "Guide to selecting a biorecognition element for biosensors," *Bioconjugate chemistry*, vol. 29, no. 10, pp. 3231–3239, 2018, ISSN: 1043-1802.

[78] N. G. Welch, J. A. Scoble, B. W. Muir, and P. J. Pigram, "Orientation and characterization of immobilized antibodies for improved immunoassays," *Biointerphases*, vol. 12, no. 2, p. 02D301, 2017.

[79] A. Sassolas, B. D. Leca-Bouvier, and L. J. Blum, "Dna biosensors and microarrays," *Chemical reviews*, vol. 108, no. 1, pp. 109–139, 2008, ISSN: 0009-2665.

[80] S. M. Shadman, M. Daneshi, F. Shafiei, M. Azimimehr, M. R. Khorasgani, M. Sadeghian, H. Motaghi, and M. A. Mehrgardi, "Aptamer-based electrochemical biosensors," in *Electrochemical Biosensors*. 2019, pp. 213–251, ISBN: 9780128164914. DOI: 10.1016/b978-0-12-816491-4.00008-5.

[81] W. Tan, M. J. Donovan, and J. Jiang, "Aptamers from cell-based selection for bioanalytical applications," *Chemical reviews*, vol. 113, no. 4, pp. 2842–2862, 2013, ISSN: 0009-2665.

[82] G. Vasapollo, R. D. Sole, L. Mergola, M. R. Lazzoi, A. Scardino, S. Scorrano, and G. Mele, "Molecularly imprinted polymers: Present and future prospective," *International journal of molecular sciences*, vol. 12, no. 9, pp. 5908–5945, 2011.

[83] X. Strakosas, M. Sessolo, A. Hama, J. Rivnay, E. Stavrinidou, G. G. Malliaras, and R. M. Owens, "A facile biofunctionalisation route for solution processable conducting polymer devices," *J Mater Chem B*, vol. 2, no. 17, pp. 2537–2545, 2014, ISSN: 2050-7518 (Electronic) 2050-750X (Linking). DOI: 10.1039/c3tb21491e. [Online]. Available: https://www.ncbi.nlm.nih.gov/pubmed/32261421.

[84] W. Hai, T. Goda, H. Takeuchi, S. Yamaoka, Y. Horiguchi, A. Matsumoto, and Y. Miyahara, "Human influenza virus detection using sialyllactose - functionalized organic electrochemical transistors," *Sensors and Actuators B: Chemical*, vol. 260, pp. 635–641, 2018, ISSN: 09254005. DOI: 10.1016/j.snb.2018.01.081.

[85] M. Sessolo, J. Rivnay, E. Bandiello, G. G. Malliaras, and H. J. Bolink, "Ion-selective organic electrochemical transistors," *Advanced Materials*, vol. 26, no. 28, pp. 4803–4807, 2014, ISSN: 1521-4095 (Electronic) 0935-9648 (Linking). DOI: 10.1002/adma.201400731. [Online]. Available: https://www.ncbi.nlm.nih.gov/pubmed/24862110.

[86] R.-X. He, M. Zhang, F. Tan, P. H. M. Leung, X.-Z. Zhao, H. L. W. Chan, M. Yang, and F. Yan, "Detection of bacteria with organic electrochemical transistors," *Journal of Materials Chemistry*, vol. 22, no. 41, p. 22 072, 2012, ISSN: 0959-9428 1364-5501. DOI: 10.1039/c2jm33667g.

[87] J. Liao, H. Si, X. Zhang, and S. Lin, "Functional sensing interfaces of pedot:pss organic electrochemical transistors for chemical and biological sensors: A mini review," *Sensors (Basel)*, vol. 19, no. 2, 2019, ISSN: 1424-8220 (Electronic) 1424-8220 (Linking). DOI: 10.3390/s19020218. [Online]. Available: https://www.ncbi.nlm.nih.gov/pubmed/30634408.

[88] D. Gentili, P. D'Angelo, F. Militano, R. Mazzei, T. Poerio, M. Brucale, G. Tarabella, S. Bonetti, S. L. Marasso, M. Cocuzza, *et al.*, "Integration of organic electrochemical transistors and immuno-affinity membranes for label-free detection of interleukin-6 in the physiological concentration range through antibody-antigen recognition," *J Mater Chem B*, vol. 6, no. 33, pp. 5400–5406, 2018, ISSN: 2050-7518 (Electronic) 2050-750X (Linking). DOI: 10.1039/c8tb01697f. [Online]. Available: https://www.ncbi.nlm.nih.gov/pubmed/32254503.

[89] I. Gualandi, M. Tessarolo, F. Mariani, D. Arcangeli, L. Possanzini, D. Tonelli, B. Fraboni, and E. Scavetta, "Layered double hydroxide-modified organic electrochemical transistor for glucose and lactate biosensing," *Sensors (Basel)*, vol. 20, no. 12, 2020, ISSN: 1424-8220 (Electronic) 1424-8220 (Linking). DOI: 10.3390/s20123453. [Online]. Available: https://www.ncbi.nlm.nih.gov/pubmed/32570942.

[90] C. Liao, C. Mak, M. Zhang, H. L. Chan, and F. Yan, "Flexible organic electrochemical transistors for highly selective enzyme biosensors and used for saliva testing," *Adv Mater*, vol. 27, no. 4, pp. 676–81, 2015, ISSN: 1521-4095 (Electronic) 0935-9648 (Linking). DOI: 10.1002/adma.201404378. [Online]. Available: https://www.ncbi.nlm.nih.gov/pubmed/25469658.

[91] L. Chen, J. Wu, F. Yan, and H. Ju, "A facile strategy for quantitative sensing of glycans on cell surface using organic electrochemical transistors," *Biosens Bioelectron*, vol. 175, p. 112 878, 2021, ISSN: 1873-4235 (Electronic) 0956-5663 (Linking). DOI: 10.1016/j.bios.2020.112878. [Online]. Available: https://www.ncbi.nlm.nih.gov/pubmed/33298337.

[92] Y. Liang, C. Wu, G. Figueroa-Miranda, A. Offenhausser, and D. Mayer, "Amplification of aptamer sensor signals by four orders of magnitude via interdigitated organic electrochemical transistors," *Biosens Bioelectron*, vol. 144, p. 111 668, 2019, ISSN: 1873-4235 (Electronic) 0956-5663 (Linking). DOI: 10.

1016/j.bios.2019.111668. [Online]. Available: https://www.ncbi.nlm.nih.gov/pubmed/31522101.

[93] N. Saraf, E. R. Woods, M. Peppler, and S. Seal, "Highly selective aptamer based organic electrochemical biosensor with pico-level detection," *Biosens Bioelectron*, vol. 117, pp. 40–46, 2018, ISSN: 1873-4235 (Electronic) 0956-5663 (Linking). DOI: 10.1016/j.bios.2018.05.031. [Online]. Available: https://www.ncbi.nlm.nih.gov/pubmed/29885578.

[94] L. Zhang, Z. Liu, C. Xiong, L. Zheng, Y. Ding, H. Lu, G. Zhang, and L. Qiu, "Selective recognition of histidine enantiomers using novel molecularly imprinted organic transistor sensor," *Organic Electronics*, vol. 61, pp. 254–260, 2018, ISSN: 1566-1199.

[95] A. Hierlemann, O. Brand, C. Hagleitner, and H. Baltes, "Microfabrication techniques for chemical/biosensors," *Proceedings of the IEEE*, vol. 91, no. 6, pp. 839–863, 2003, ISSN: 0018-9219.

[96] A. M. Baracu and L. A. D. Gugoasa, "Recent advances in microfabrication, design and applications of amperometric sensors and biosensors," *Journal of The Electrochemical Society*, 2021, ISSN: 1945-7111.

[97] P. C. H"utter, A. Fian, K. Gatterer, and B. Stadlober, "Efficiency of the switching process in organic electrochemical transistors," *ACS Appl Mater Interfaces*, vol. 8, no. 22, pp. 14 071–6, 2016, ISSN: 1944-8252 (Electronic) 1944-8244 (Linking). DOI: 10.1021/acsami.6b02698. [Online]. Available: https://www.ncbi.nlm.nih.gov/pubmed/27191825.

[98] L. Contat-Rodrigo, C. Pérez-Fuster, J. V. Lidón-Roger, A. Bonfiglio, and E. García-Breijo, "Screen-printed organic electrochemical transistors for the detection of ascorbic acid in food," *Organic Electronics*, vol. 45, pp. 89–96, 2017, ISSN: 15661199. DOI: 10.1016/j.orgel.2017.02.037.

[99] L. Contat-Rodrigo, C. Pérez-Fuster, J. V. Lidón-Roger, A. Bonfiglio, and E. García-Breijo, "Characterization of screen-printed organic electrochemical transistors to detect cations of different sizes," *Sensors*, vol. 16, no. 10, p. 1599, 2016.

[100] R. Faddoul, R. Coppard, and T. Berthelot, "Inkjet printing of organic electrochemical immunosensors," in *SENSORS, 2014 IEEE*, IEEE, pp. 1088–1091, ISBN: 1479901628.

[101] M. Afonso, J. Morgado, and L. Alcácer, "Inkjet printed organic electrochemical transistors with highly conducting polymer electrolytes," *Journal of Applied Physics*, vol. 120, no. 16, 2016, ISSN: 0021-8979 1089-7550. DOI: 10.1063/1.4966651.

[102] R. Mannerbro, M. Ranlöf, N. Robinson, and R. Forchheimer, "Inkjet printed electrochemical organic electronics," *Synthetic Metals*, vol. 158, no. 13, pp. 556–560, 2008. DOI: 10.1016/j.synthmet.2008.03.030.

[103] V. Bertana, G. Scordo, M. Parmeggiani, L. Scaltrito, S. Ferrero, M. G. Gomez, M. Cocuzza, D. Vurro, P. D'Angelo, S. Iannotta, C. F. Pirri, and S. L. Marasso, "Rapid prototyping of 3d organic electrochemical transistors by composite photocurable resin," *Sci Rep*, vol. 10, no. 1, p. 13 335, 2020, ISSN: 2045-2322 (Electronic) 2045-2322 (Linking). DOI: 10.1038/s41598-020-70365-8. [Online]. Available: https://www.ncbi.nlm.nih.gov/pubmed/32770035.

[104] J. Fan, C. Montemagno, and M. Gupta, "3d printed high transconductance organic electrochemical transistors on flexible substrates," *Organic Electronics*, vol. 73, pp. 122–129, 2019, ISSN: 15661199. DOI: 10.1016/j.orgel.2019.06.012.

[105] G. Tarabella, D. Vurro, S. Lai, P. D'Angelo, L. Ascari, and S. Iannotta, "Aerosol jet printing of pedot:pss for large area flexible electronics," *Flexible and Printed Electronics*, vol. 5, no. 1, 2020, ISSN: 2058-8585. DOI: 10.1088/2058-8585/ab61c4.

[106] E. B. Secor, "Principles of aerosol jet printing," *Flexible and Printed Electronics*, vol. 3, no. 3, 2018, ISSN: 2058-8585. DOI: 10.1088/2058-8585/aace28.

[107] A. Mahajan, C. D. Frisbie, and L. F. Francis, "Optimization of aerosol jet printing for high-resolution, high-aspect ratio silver lines," *ACS Appl Mater Interfaces*, vol. 5, no. 11, pp. 4856–64, 2013, ISSN: 1944-8252 (Electronic) 1944-8244 (Linking). DOI: 10.1021/am400606y. [Online]. Available: https://www.ncbi.nlm.nih.gov/pubmed/23659570.

[108] N. Wilkinson, M. Smith, R. Kay, and R. Harris, "A review of aerosol jet printing—a non-traditional hybrid process for micro-manufacturing," *The International Journal of Advanced Manufacturing Technology*, vol. 105, no. 11, pp. 4599–4619, 2019, ISSN: 1433-3015.

[109] S. Binder, M. Glatthaar, and E. Rädlein, "Analytical investigation of aerosol jet printing," *Aerosol Science and Technology*, vol. 48, no. 9, pp. 924–929, 2014, ISSN: 0278-6826.

[110] R. A. Serway and J. W. Jewett, *Principles of physics*. Saunders College Pub. Fort Worth, TX, 1998, vol. 1.

[111] P. Lin, F. Yan, and H. L. Chan, "Ion-sensitive properties of organic electrochemical transistors," *ACS Appl Mater Interfaces*, vol. 2, no. 6, pp. 1637–41, 2010, ISSN: 1944-8244 (Print) 1944-8244 (Linking). DOI: 10.1021/am100154e. [Online]. Available: https://www.ncbi.nlm.nih.gov/pubmed/20499881.

[112] M. Ghittorelli, L. Lingstedt, P. Romele, N. I. Craciun, Z. M. Kovacs-Vajna, P. W. M. Blom, and F. Torricelli, "High-sensitivity ion detection at low voltages with current-driven organic electrochemical transistors," *Nat Commun*, vol. 9, no. 1, p. 1441, 2018, ISSN: 2041-1723 (Electronic) 2041-1723 (Linking). DOI: 10.1038/s41467-018-03932-3. [Online]. Available: https://www.ncbi.nlm.nih.gov/pubmed/29650956.

[113] G. Scheiblin, R. Coppard, R. M. Owens, P. Mailley, and G. G. Malliaras, "Referenceless ph sensor using organic electrochemical transistors," *Advanced Materials Technologies*, vol. 2, no. 2, 2017, ISSN: 2365709X. DOI: 10.1002/admt.201600141.

[114] A. E. Kirchan, K.-T. Kim, M. K. Steward, and S. Choi, "A pedot: Pss-based organic electrochemical transistor with a novel double-in-plane gate electrode for ph sensing application," in *2017 19th International Conference on Solid-State Sensors, Actuators and Microsystems (TRANSDUCERS)*, IEEE, pp. 214–217, ISBN: 1538627329.

[115] Y. Fu, N. Wang, A. Yang, H. K. Law, L. Li, and F. Yan, "Highly sensitive detection of protein biomarkers with organic electrochemical transistors," *Adv Mater*, vol. 29, no. 41, p. 1703787, 2017, ISSN: 1521-4095 (Electronic) 0935-9648 (Linking). DOI: 10.1002/adma.201703787. [Online]. Available: https://www.ncbi.nlm.nih.gov/pubmed/28922492.

[116] P. Lin, X. Luo, I. M. Hsing, and F. Yan, "Organic electrochemical transistors integrated in flexible microfluidic systems and used for label-free dna sensing," *Adv Mater*, vol. 23, no. 35, pp. 4035–40, 2011, ISSN: 1521-4095 (Electronic) 0935-9648 (Linking). DOI: 10.1002/adma.201102017. [Online]. Available: https://www.ncbi.nlm.nih.gov/pubmed/21793055.

[117] D. A. Bernards, D. J. Macaya, M. Nikolou, J. A. DeFranco, S. Takamatsu, and G. G. Malliaras, "Enzymatic sensing with organic electrochemical transistors," *J. Mater. Chem.*, vol. 18, no. 1, pp. 116–120, 2008, ISSN: 0959-9428 1364-5501. DOI: 10.1039/b713122d.

[118] M. Zhang, C. Liao, C. H. Mak, P. You, C. L. Mak, and F. Yan, "Highly sensitive glucose sensors based on enzyme-modified whole-graphene solution-gated transistors," *Sci Rep*, vol. 5, p. 8311, 2015, ISSN: 2045-2322 (Electronic) 2045-2322 (Linking). DOI: 10.1038/srep08311. [Online]. Available: https://www.ncbi.nlm.nih.gov/pubmed/25655666.

[119] M. Braendlein, A. Pappa, M. Ferro, A. Lopresti, C. Acquaviva, E. Mamessier, G. G. Malliaras, and R. M. Owens, "Lactate detection in tumor cell cultures using organic transistor circuits," *Adv Mater*, vol. 29, no. 13, p. 1605744, 2017, ISSN: 1521-4095 (Electronic) 0935-9648 (Linking). DOI: 10.1002/adma.201605744. [Online]. Available: https://www.ncbi.nlm.nih.gov/pubmed/28134450.

[120] N. Wang, Y. Liu, Y. Fu, and F. Yan, "Ac measurements using organic electrochemical transistors for accurate sensing," *ACS Appl Mater Interfaces*, vol. 10, no. 31, pp. 25834–25840, 2018, ISSN: 1944-8252 (Electronic) 1944-8244 (Linking). DOI: 10.1021/acsami.7b07668. [Online]. Available: https://www.ncbi.nlm.nih.gov/pubmed/28846372.

[121] I. Gualandi, D. Tonelli, F. Mariani, E. Scavetta, M. Marzocchi, and B. Fraboni, "Selective detection of dopamine with an all pedot:pss organic electrochemical transistor," *Sci Rep*, vol. 6, p. 35 419, 2016, ISSN: 2045-2322 (Electronic) 2045-2322 (Linking). DOI: 10.1038/srep35419. [Online]. Available: https://www.ncbi.nlm.nih.gov/pubmed/27739467.

[122] D. Nilsson, N. Robinson, M. Berggren, and R. Forchheimer, "Electrochemical logic circuits," *Advanced Materials*, vol. 17, no. 3, pp. 353–358, 2005, ISSN: 0935-9648 1521-4095. DOI: 10.1002/adma.200401273.

[123] D. Majak, J. Fan, and M. Gupta, "Fully 3d printed oect based logic gate for detection of cation type and concentration," *Sensors and Actuators B: Chemical*, vol. 286, pp. 111–118, 2019, ISSN: 09254005. DOI: 10.1016/j.snb.2019.01.120.

[124] S. Zhang, E. Hubis, G. Tomasello, G. Soliveri, P. Kumar, and F. Cicoira, "Patterning of stretchable organic electrochemical transistors," *Chemistry of Materials*, vol. 29, no. 7, pp. 3126–3132, 2017, ISSN: 0897-4756 1520-5002. DOI: 10.1021/acs.chemmater.7b00181.

[125] O. Yaghmazadeh, F. Cicoira, D. A. Bernards, S. Y. Yang, Y. Bonnassieux, and G. G. Malliaras, "Optimization of organic electrochemical transistors for sensor applications," *Journal of Polymer Science Part B: Polymer Physics*, vol. 49, no. 1, pp. 34–39, 2011, ISSN: 08876266. DOI: 10.1002/polb.22129.

[126] A. Yang, Y. Li, C. Yang, Y. Fu, N. Wang, L. Li, and F. Yan, "Fabric organic electrochemical transistors for biosensors," *Adv Mater*, vol. 30, no. 23, e1800051, 2018, ISSN: 1521-4095 (Electronic) 0935-9648 (Linking). DOI: 10.1002/adma.201800051. [Online]. Available: https://www.ncbi.nlm.nih.gov/pubmed/29707839.

[127] A. Hayat and J. L. Marty, "Disposable screen printed electrochemical sensors: Tools for environmental monitoring," *Sensors (Basel)*, vol. 14, no. 6, pp. 10 432–53, 2014, ISSN: 1424-8220 (Electronic) 1424-8220 (Linking). DOI: 10.3390/s140610432. [Online]. Available: https://www.ncbi.nlm.nih.gov/pubmed/24932865.

[128] A. J. Bandodkar, R. Nunez-Flores, W. Jia, and J. Wang, "All-printed stretchable electrochemical devices," *Adv Mater*, vol. 27, no. 19, pp. 3060–5, 2015. DOI: 10.1002/adma.201500768. [Online]. Available: https://www.ncbi.nlm.nih.gov/pubmed/25856153.

[129] W. Su, B. S. Cook, Y. Fang, and M. M. Tentzeris, "Fully inkjet-printed microfluidics: A solution to low-cost rapid three-dimensional microfluidics fabrication with numerous electrical and sensing applications," *Sci Rep*, vol. 6, p. 35 111, 2016, ISSN: 2045-2322 (Electronic) 2045-2322 (Linking). DOI: 10.1038/srep35111. [Online]. Available: https://www.ncbi.nlm.nih.gov/pubmed/27713545.

[130] L. Basiricò, P. Cosseddu, B. Fraboni, and A. Bonfiglio, "Inkjet printing of transparent, flexible, organic transistors," *Thin Solid Films*, vol. 520, no. 4, pp. 1291–1294, 2011, ISSN: 00406090. DOI: 10.1016/j.tsf.2011.04.188.

[131] K. E. Paul, W. S. Wong, S. E. Ready, and R. A. Street, "Additive jet printing of polymer thin-film transistors," *Applied Physics Letters*, vol. 83, no. 10, pp. 2070–2072, 2003, ISSN: 0003-6951.

[132] K. V. Wong and A. Hernandez, "A review of additive manufacturing," *ISRN Mechanical Engineering*, vol. 2012, pp. 1–10, 2012, ISSN: 2090-5130. DOI: 10.5402/2012/208760.

[133] K. Hon, L Li, and I. Hutchings, "Direct writing technology—advances and developments," *CIRP Annals*, vol. 57, no. 2, pp. 601–620, 2008, ISSN: 00078506. DOI: 10.1016/j.cirp.2008.09.006.

[134] P. Tehrani, A. Kanciurzewska, X. Crispin, N. Robinson, M. Fahlman, and M. Berggren, "The effect of ph on the electrochemical over-oxidation in pedot:pss films," *Solid State Ionics*, vol. 177, no. 39-40, pp. 3521–3527, 2007, ISSN: 01672738. DOI: 10.1016/j.ssi.2006.10.008.

[135] E. Vitoratos, S. Sakkopoulos, E. Dalas, N. Paliatsas, D. Karageorgopoulos, F. Petraki, S. Kennou, and S. Choulis, "Thermal degradation mechanisms of pedot:pss," *Organic Electronics*, vol. 10, no. 1, pp. 61–66, 2009, ISSN: 15661199. DOI: 10.1016/j.orgel.2008.10.008.

[136] M. Berggren and A. Richter-Dahlfors, "Organic bioelectronics," *Advanced Materials*, vol. 19, no. 20, pp. 3201–3213, 2007, ISSN: 09359648. DOI: 10.1002/adma.200700419.

[137] C. M. Proctor, J. Rivnay, and G. G. Malliaras, "Understanding volumetric capacitance in conducting polymers," *Journal of Polymer Science Part B: Polymer Physics*, vol. 54, no. 15, pp. 1433–1436, 2016, ISSN: 0887-6266 1099-0488. DOI: 10.1002/polb.24038.

[138] J. Rivnay, P. Leleux, M. Sessolo, D. Khodagholy, T. Herve, M. Fiocchi, and G. G. Malliaras, "Organic electrochemical transistors with maximum transconductance at zero gate bias," *Adv Mater*, vol. 25, no. 48, pp. 7010–4, 2013, ISSN: 1521-4095 (Electronic) 0935-9648 (Linking). DOI: 10.1002/adma.201303080. [Online]. Available: https://www.ncbi.nlm.nih.gov/pubmed/24123258.

[139] J. Fan, S. S. Rezaie, M. Facchini-Rakovich, D. Gudi, C. Montemagno, and M. Gupta, "Tuning pedot:pss conductivity to obtain complementary organic electrochemical transistor," *Organic Electronics*, vol. 66, pp. 148–155, 2019, ISSN: 15661199. DOI: 10.1016/j.orgel.2018.12.013.

[140] P. C. Hütter, T. Rothländer, A. Haase, G. Trimmel, and B. Stadlober, "Influence of geometry variations on the response of organic electrochemical transistors," *Applied Physics Letters*, vol. 103, no. 4, 2013, ISSN: 0003-6951 1077-3118. DOI: 10.1063/1.4816781.

[141] P. Kumar, Z. Yi, S. Zhang, A. Sekar, F. Soavi, and F. Cicoira, "Effect of channel thickness, electrolyte ions, and dissolved oxygen on the performance of organic electrochemical transistors," *Applied Physics Letters*, vol. 107, no. 5, p. 053 303, 2015, ISSN: 0003-6951 1077-3118. DOI: 10.1063/1.4927595.

[142] S. S. Rezaie, D. Gudi, J. Fan, and M. Gupta, "Geometrical optimization of organic electrochemical transistor for high transconductance," *ECS Journal of Solid State Science and Technology*, vol. 9, no. 8, p. 081 003, 2020, ISSN: 2162-8777. DOI: 10.1149/2162-8777/abb796.

[143] A. Ortiz-Conde, F. J. García-Sánchez, J. Muci, A. Terán Barrios, J. J. Liou, and C.-S. Ho, "Revisiting mosfet threshold voltage extraction methods," *Microelectronics Reliability*, vol. 53, no. 1, pp. 90–104, 2013, ISSN: 00262714. DOI: 10.1016/j.microrel.2012.09.015.

[144] G. Lucovsky and V. Misra, "Gate oxides: Properties and characterization," in *Encyclopedia of Materials: Science and Technology*, K. H. J. Buschow, R. W. Cahn, M. C. Flemings, B. Ilschner, E. J. Kramer, S. Mahajan, and P. Veyssière, Eds. Oxford: Elsevier, 2001, pp. 3478–3486, ISBN: 978-0-08-043152-9. DOI: https://doi.org/10.1016/B0-08-043152-6/00619-7. [Online]. Available: https://www.sciencedirect.com/science/article/pii/B0080431526006197.

[145] S. E. Doris, A. Pierre, and R. A. Street, "Dynamic and tunable threshold voltage in organic electrochemical transistors," *Adv Mater*, vol. 30, no. 15, e1706757, 2018, ISSN: 1521-4095 (Electronic) 0935-9648 (Linking). DOI: 10.1002/adma.201706757. [Online]. Available: https://www.ncbi.nlm.nih.gov/pubmed/29498110.

[146] J. Rivnay, S. Inal, B. A. Collins, M. Sessolo, E. Stavrinidou, X. Strakosas, C. Tassone, D. M. Delongchamp, and G. G. Malliaras, "Structural control of mixed ionic and electronic transport in conducting polymers," *Nat Commun*, vol. 7, p. 11 287, 2016, ISSN: 2041-1723 (Electronic) 2041-1723 (Linking). DOI: 10.1038/ncomms11287. [Online]. Available: https://www.ncbi.nlm.nih.gov/pubmed/27090156.

[147] R. L. Stoop, K. Thodkar, M. Sessolo, H. J. Bolink, C. Schönenberger, and M. Calame, "Charge noise in organic electrochemical transistors," *Physical Review Applied*, vol. 7, no. 1, 2017, ISSN: 2331-7019. DOI: 10.1103/PhysRevApplied.7.014009.

[148] V. Kaphle, S. Liu, A. Al-Shadeedi, C. Keum, and B. Lüssem, "Contact resistance effects in highly doped organic electrochemical transistors," *Advanced Materials*, vol. 28, no. 39, pp. 8766–8770, 2016, ISSN: 0935-9648.

[149] R. S. Niedbala, K. W. Kardos, D. F. Fritch, S. Kardos, T. Fries, J. Waga, J. Robb, and E. J. Cone, "Detection of marijuana use by oral fluid and urine analysis following single-dose administration of smoked and oral marijuana," *J Anal Toxicol*, vol. 25, no. 5, pp. 289–303, 2001, ISSN: 0146-4760 (Print) 0146-4760 (Linking). DOI: 10.1093/jat/25.5.289. [Online]. Available: https://www.ncbi.nlm.nih.gov/pubmed/11499881.

[150] R. K. Mishra, J. R. Sempionatto, Z. Li, C. Brown, N. M. Galdino, R. Shah, S. Liu, L. J. Hubble, K. Bagot, S. Tapert, and J. Wang, "Simultaneous detection of salivary delta(9)-tetrahydrocannabinol and alcohol using a wearable electrochemical ring sensor," *Talanta*, vol. 211, p. 120 757, 2020, ISSN: 1873-3573 (Electronic) 0039-9140 (Linking). DOI: 10.1016/j.talanta.2020.120757. [Online]. Available: https://www.ncbi.nlm.nih.gov/pubmed/32070607.

[151] H. Stevenson, A. Bacon, K. M. Joseph, W. R. W. Gwandaru, A. Bhide, D. Sankhala, V. N. Dhamu, and S. Prasad, "A rapid response electrochemical biosensor for detecting thc in saliva," *Sci Rep*, vol. 9, no. 1, p. 12 701, 2019, ISSN: 2045-2322 (Electronic) 2045-2322 (Linking). DOI: 10.1038/s41598-019-49185-y. [Online]. Available: https://www.ncbi.nlm.nih.gov/pubmed/31481686.

[152] C. Wanklyn, D. Burton, E. Enston, C. A. Bartlett, S. Taylor, A. Raniczkowska, M. Black, and L. Murphy, "Disposable screen printed sensor for the electrochemical detection of delta-9-tetrahydrocannabinol in undiluted saliva," *Chem Cent J*, vol. 10, p. 1, 2016, ISSN: 1752-153X (Print) 1752-153X (Linking). DOI: 10.1186/s13065-016-0148-1. [Online]. Available: https://www.ncbi.nlm.nih.gov/pubmed/26807144.

[153] J.-R. Lee, J. Choi, T. O. Shultz, and S. X. Wang, "Small molecule detection in saliva facilitates portable tests of marijuana abuse," *Analytical chemistry*, vol. 88, no. 15, pp. 7457–7461, 2016, ISSN: 0003-2700.

[154] M. Klimuntowski, M. M. Alam, G. Singh, and M. M. R. Howlader, "Electrochemical sensing of cannabinoids in biofluids: A noninvasive tool for drug detection," *ACS Sens*, vol. 5, no. 3, pp. 620–636, 2020, ISSN: 2379-3694 (Electronic) 2379-3694 (Linking). DOI: 10.1021/acssensors.9b02390. [Online]. Available: https://www.ncbi.nlm.nih.gov/pubmed/32102542.

[155] M. Renaud-Young, R. M. Mayall, V. Salehi, M. Goledzinowski, F. J. Comeau, J. L. MacCallum, and V. I. Birss, "Development of an ultra-sensitive electrochemical sensor for Δ 9-tetrahydrocannabinol (THC) and its metabolites using carbon paper electrodes," *Electrochimica Acta*, vol. 307, pp. 351–359, 2019, ISSN: 00134686. DOI: 10.1016/j.electacta.2019.02.117.

[156] M. A. Balbino, É. N. Oiye, M. F. M. Ribeiro, J. W. C. Júnior, I. C. Eleotério, A. J. Ipólito, and M. F. de Oliveira, "Use of screen-printed electrodes for quantification of cocaine and Δ 9-thc: Adaptions to portable systems for forensic purposes," *Journal of Solid State Electrochemistry*, vol. 20, no. 9, pp. 2435–2443, 2016, ISSN: 1433-0768.

[157] M. Balbino, I. C. Eleotério, B. Mccord, M. A. Balbino, and I. C. Eleoterio, "Electrochemical study of delta-9-tetrahydrocannabinol by cyclic voltammetry using screen printed electrode, improvements in forensic analysis," *Sensors and transducers*, vol. 207, pp. 73–78, 2016.

[158] International Diabetes Federation, "IDF DIABETES ATLAS," International Diabetes Federation, Report 9782930229874, 2019.

[159] American Diabetes Association, "1. improving care and promoting health in populations: Standards of medical care in diabetes-2019," *Diabetes Care*, vol. 42, no. Supplement 1, S7–S12, 2019, ISSN: 1935-5548 (Electronic) 0149-5992 (Linking). DOI: 10.2337/dc19-S001. [Online]. Available: https://www.ncbi.nlm.nih.gov/pubmed/30559227.

[160] Grand View Research. (2016). "Glucose biosensor market size, share & trends analysis report by end-use (hospitals, homecare diagnostics, research institutes, diagnostic centers, clinics), by region (u.s., uk, germany, china, india, brazil, saudi arabia, south africa), and segment forecasts, 2012 - 2022," [Online]. Available: https://www.grandviewresearch.com/industry-analysis/glucose-biosensors-market (visited on 05/18/2021).

[161] D. Rodbard, "Continuous glucose monitoring: A review of successes, challenges, and opportunities," *Diabetes Technol Ther*, vol. 18 Suppl 2, S3–S13, 2016, ISSN: 1557-8593 (Electronic) 1520-9156 (Linking). DOI: 10.1089/dia.2015.0417. [Online]. Available: https://www.ncbi.nlm.nih.gov/pubmed/26784127.

[162] M. Christiansen, T. Bailey, E. Watkins, D. Liljenquist, D. Price, K. Nakamura, R. Boock, and T. Peyser, "A new-generation continuous glucose monitoring system: Improved accuracy and reliability compared with a previous-generation system," *Diabetes Technol Ther*, vol. 15, no. 10, pp. 881–8, 2013, ISSN: 1557-8593 (Electronic) 1520-9156 (Linking). DOI: 10.1089/dia.2013.0077. [Online]. Available: https://www.ncbi.nlm.nih.gov/pubmed/23777402.

[163] B. J. Patel, B. Dave, D. Dave, P. Karmakar, M. Shah, and B. Sarvaiya, "Comparison and correlation of glucose levels in serum and saliva of both diabetic and non-diabetic patients," *J Int Oral Health*, vol. 7, no. 8, pp. 70–6, 2015, ISSN: 0976-7428 (Print) 0976-1799 (Linking). [Online]. Available: https://www.ncbi.nlm.nih.gov/pubmed/26464543.

[164] J. Moyer, D. Wilson, I. Finkelshtein, B. Wong, and R. Potts, "Correlation between sweat glucose and blood glucose in subjects with diabetes," *Diabetes Technology & Therapeutics*, vol. 14, pp. 398–402, 2012.

[165] S. Y. Yang, F. Cicoira, R. Byrne, F. Benito-Lopez, D. Diamond, R. M. Owens, and G. G. Malliaras, "Electrochemical transistors with ionic liquids for enzymatic sensing," *Chem Commun (Camb)*, vol. 46, no. 42, pp. 7972–4, 2010, ISSN: 1364-548X (Electronic) 1359-7345 (Linking). DOI: 10.1039/c0cc02064h. [Online]. Available: https://www.ncbi.nlm.nih.gov/pubmed/20871879.

[166] Y. Wang, X. Qing, Q. Zhou, Y. Zhang, Q. Liu, K. Liu, W. Wang, M. Li, Z. Lu, Y. Chen, and D. Wang, "The woven fiber organic electrochemical transistors based on polypyrrole nanowires/reduced graphene oxide composites for glucose sensing," *Biosens Bioelectron*, vol. 95, pp. 138–145, 2017, ISSN: 1873-4235 (Electronic) 0956-5663 (Linking). DOI: 10.1016/j.bios.2017.04.018. [Online]. Available: https://www.ncbi.nlm.nih.gov/pubmed/28437640.

[167] J. Liao, S. Lin, K. Liu, Y. Yang, R. Zhang, W. Du, and X. Li, "Organic electrochemical transistor based biosensor for detecting marine diatoms in seawater medium," *Sensors and Actuators B: Chemical*, vol. 203, pp. 677–682, 2014, ISSN: 09254005. DOI: 10.1016/j.snb.2014.07.052.

[168] L. Bai, C. G. Elosegui, W. Li, P. Yu, J. Fei, and L. Mao, "Biological applications of organic electrochemical transistors: Electrochemical biosensors and electrophysiology recording," *Front Chem*, vol. 7, p. 313, 2019, ISSN: 2296-2646 (Print) 2296-2646 (Linking). DOI: 10.3389/fchem.2019.00313. [Online]. Available: https://www.ncbi.nlm.nih.gov/pubmed/31134185.

[169] N Sandhyarani, "Surface modification methods for electrochemical biosensors," in *Electrochemical Biosensors*. Elsevier, 2019, pp. 45–75.

[170] B. D. Malhotra and M. A. Ali, "Nanomaterials in biosensors," in *Nanomaterials for Biosensors*. 2018, pp. 1–74, ISBN: 9780323449236. DOI: 10.1016/b978-0-323-44923-6.00001-7.

[171] R. Batool, A. Rhouati, M. H. Nawaz, A. Hayat, and J. L. Marty, "A review of the construction of nano-hybrids for electrochemical biosensing of glucose," *Biosensors (Basel)*, vol. 9, no. 1, 2019, ISSN: 2079-6374 (Electronic) 2079-6374 (Linking). DOI: 10.3390/bios9010046. [Online]. Available: https://www.ncbi.nlm.nih.gov/pubmed/30934645.

[172] G. Scheiblin, A. Aliane, R. Coppard, R. M. Owens, P. Mailley, and G. G. Malliaras, "Fully printed metabolite sensor using organic electrochemical transistor," *SPIE Organic Photonics + Electronics*, vol. 9568, 95681E, 2015, ISSN: 9781628417340. DOI: 10.1117/12.2186385.

[173] D. Ohayon, G. Nikiforidis, A. Savva, A. Giugni, S. Wustoni, T. Palanisamy, X. Chen, I. P. Maria, E. Di Fabrizio, P. Costa, I. McCulloch, and S. Inal, "Biofuel powered glucose detection in bodily fluids with an n-type conjugated polymer," *Nat Mater*, vol. 19, no. 4, pp. 456–463, 2020, ISSN: 1476-1122 (Print) 1476-1122 (Linking). DOI: 10.1038/s41563-019-0556-4. [Online]. Available: https://www.ncbi.nlm.nih.gov/pubmed/31844278.

[174] J. T. Friedlein, M. J. Donahue, S. E. Shaheen, G. G. Malliaras, and R. R. McLeod, "Microsecond response in organic electrochemical transistors: Exceeding the ionic speed limit," *Adv Mater*, vol. 28, no. 38, pp. 8398–8404, 2016, ISSN: 1521-4095 (Electronic) 0935-9648 (Linking). DOI: 10.1002/adma.201602684. [Online]. Available: https://www.ncbi.nlm.nih.gov/pubmed/27457055.

[175] Y. Kim, J. Do, J. Kim, S. Y. Yang, G. G. Malliaras, C. K. Ober, and E. Kim, "A glucose sensor based on an organic electrochemical transistor structure using a vapor polymerized poly(3,4-ethylenedioxythiophene) layer," *Japanese Journal of Applied Physics*, vol. 49, no. 1, 2010, ISSN: 0021-4922 1347-4065. DOI: 10.1143/jjap.49.01ae10.

[176] A. Heller and B. Feldman, "Electrochemical glucose sensors and their applications in diabetes management," *Chem Rev*, vol. 108, no. 7, pp. 2482–505, 2008, ISSN: 1520-6890 (Electronic) 0009-2665 (Linking). DOI: 10.1021/cr068069y. [Online]. Available: https://www.ncbi.nlm.nih.gov/pubmed/18465900.

[177] S. K. Kanakamedala, H. T. Alshakhouri, M. Agarwal, and M. A. DeCoster, "A simple polymer based electrochemical transistor for micromolar glucose sensing," *Sensors and Actuators B: Chemical*, vol. 157, no. 1, pp. 92–97, 2011, ISSN: 09254005. DOI: 10.1016/j.snb.2011.03.030.

[178] C. Diacci, J. W. Lee, P. Janson, G. Dufil, G. Méhes, M. Berggren, D. T. Simon, and E. Stavrinidou, "Real-time monitoring of glucose export from isolated chloroplasts using an organic electrochemical transistor," *Advanced Materials Technologies*, vol. 5, no. 3, 2019, ISSN: 2365-709X 2365-709X. DOI: 10.1002/admt.201900262.

[179] A. Bhide, S. Muthukumar, and S. Prasad, "Clasp (continuous lifestyle awareness through sweat platform): A novel sensor for simultaneous detection of alcohol and glucose from passive perspired sweat," *Biosens Bioelectron*, vol. 117, pp. 537–545, 2018, ISSN: 1873-4235 (Electronic) 0956-5663 (Linking). DOI: 10.1016/j.bios.2018.06.065. [Online]. Available: https://www.ncbi.nlm.nih.gov/pubmed/29982125.

[180] X. Xuan, H. S. Yoon, and J. Y. Park, "A wearable electrochemical glucose sensor based on simple and low-cost fabrication supported micro-patterned reduced graphene oxide nanocomposite electrode on flexible substrate," *Biosens Bioelectron*, vol. 109, pp. 75–82, 2018, ISSN: 1873-4235 (Electronic) 0956-5663 (Linking). DOI: 10.1016/j.bios.2018.02.054. [Online]. Available: https://www.ncbi.nlm.nih.gov/pubmed/29529511.

[181] J. L. Matousek and K. L. Campbell, "A comparative review of cutaneous ph," *Vet Dermatol*, vol. 13, no. 6, pp. 293–300, 2002, ISSN: 0959-4493 (Print) 0959-4493 (Linking). DOI: 10.1046/j.1365-3164.2002.00312.x. [Online]. Available: https://www.ncbi.nlm.nih.gov/pubmed/12464061.

[182] M. Ma, Y. Zhou, J. Li, Z. Ge, H. He, T. Tao, Z. Cai, X. Wang, G. Chang, and Y. He, "Non-invasive detection of glucose via a solution-gated graphene transistor," *Analyst*, vol. 145, no. 3, pp. 887–896, 2020, ISSN: 1364-5528 (Electronic) 0003-2654 (Linking). DOI: 10.1039/c9an01754b. [Online]. Available: https://www.ncbi.nlm.nih.gov/pubmed/31820746.

[183] Y. Zhao, Q. Zhai, D. Dong, T. An, S. Gong, Q. Shi, and W. Cheng, "Highly stretchable and strain-insensitive fiber-based wearable electrochemical biosensor to monitor glucose in the sweat," *Anal Chem*, vol. 91, no. 10, pp. 6569–6576, 2019, ISSN: 1520-6882 (Electronic) 0003-2700 (Linking). DOI: 10.1021/acs.analchem.9b00152. [Online]. Available: https://www.ncbi.nlm.nih.gov/pubmed/31006229.

[184] R. D. Munje, S. Muthukumar, and S. Prasad, "Lancet-free and label-free diagnostics of glucose in sweat using zinc oxide based flexible bioelectronics," *Sensors and Actuators B: Chemical*, vol. 238, pp. 482–490, 2017, ISSN: 09254005. DOI: 10.1016/j.snb.2016.07.088.

[185] S. K. Vashist and J. H. Luong, "Antibody immobilization and surface functionalization chemistries for immunodiagnostics," in *Handbook of Immunoassay Technologies*. Elsevier, 2018, pp. 19–46.

[186] J. Kwon, B.-H. Lee, S.-Y. Kim, J.-Y. Park, H. Bae, Y.-K. Choi, and J.-H. Ahn, "Nanoscale fet-based transduction toward sensitive extended-gate biosensors," *ACS sensors*, vol. 4, no. 6, pp. 1724–1729, 2019, ISSN: 2379-3694.

[187] T. Minamiki, T. Minami, R. Kurita, O. Niwa, S. I. Wakida, K. Fukuda, D. Kumaki, and S. Tokito, "A label-free immunosensor for igg based on an extended-gate type organic field effect transistor," *Materials (Basel)*, vol. 7, no. 9, pp. 6843–6852, 2014, ISSN: 1996-1944 (Print) 1996-1944 (Linking). DOI: 10.3390/ma7096843. [Online]. Available: https://www.ncbi.nlm.nih.gov/pubmed/28788216.

[188] S. Sheibani, L. Capua, S. Kamaei, S. S. A. Akbari, J. Zhang, H. Guerin, and A. M. Ionescu, "Extended gate field-effect-transistor for sensing cortisol stress hormone," *Communications materials*, vol. 2, no. 1, pp. 1–10, 2021, ISSN: 2662-4443.

[189] C. Beltrán-Pavez, C. L. Márquez, G. Muñoz, F. Valiente-Echeverría, A. Gaggero, R. Soto-Rifo, and G. P. Barriga, "Sars-cov-2 detection from nasopharyngeal swab samples without rna extraction," *bioRxiv*, 2020. DOI: 10.1101/2020.03.28.013508.

[190] W. Shao, M. R. Shurin, S. E. Wheeler, X. He, and A. Star, "Rapid detection of sars-cov-2 antigens using high-purity semiconducting single-walled carbon nanotube-based field-effect transistors," *ACS Appl Mater Interfaces*, vol. 13, no. 8, pp. 10 321–10 327, 2021, ISSN: 1944-8252 (Electronic) 1944-8244 (Linking). DOI: 10.1021/acsami.0c22589. [Online]. Available: https://www.ncbi.nlm.nih.gov/pubmed/33596036.

[191] P. Makaram, D. Owens, and J. Aceros, "Trends in nanomaterial-based non-invasive diabetes sensing technologies," *Diagnostics*, vol. 4, no. 2, pp. 27–46, 2014.

[192] H. Shen, A. Abtahi, B. Lussem, B. W. Boudouris, and J. Mei, "Device engineering in organic electrochemical transistors toward multifunctional applications," *ACS Applied Electronic Materials*, 2021, ISSN: 2637-6113.

[193] R. M. Mayall, C. A. Smith, A. S. Hyla, D. S. Lee, C. M. Crudden, and V. I. Birss, "Ultrasensitive and label-free detection of the measles virus using an n-heterocyclic carbene-based electrochemical biosensor," *ACS Sens*, vol. 5, no. 9, pp. 2747–2752, 2020. DOI: 10.1021/acssensors.0c01250. [Online]. Available: https://www.ncbi.nlm.nih.gov/pubmed/32820626.

[194] D. Ataman Sadık, H. Eksi-Kocak, G. Ertaş,
bibinitperiodI. H. Boyacı, and M. Mutlu, "Mixed-monolayer of n-hydroxysuccinimide-terminated cross-linker and short alkanethiol to improve the efficiency of biomolecule binding for biosensing," *Surface and Interface Analysis*, vol. 50, no. 9, pp. 866–878, 2018, ISSN: 01422421. DOI: 10.1002/sia.6489.

[195] C. Y. Lim, N. A. Owens, R. D. Wampler, Y. Ying, J. H. Granger, M. D. Porter, M. Takahashi, and K. Shimazu, "Succinimidyl ester surface chemistry: Implications of the competition between aminolysis and hydrolysis on covalent protein immobilization," *Langmuir*, vol. 30, no. 43, pp. 12 868–78, 2014, ISSN: 1520-5827 (Electronic) 0743-7463 (Linking). DOI: 10.1021/la503439g. [Online]. Available: https://www.ncbi.nlm.nih.gov/pubmed/25317495.

[196] M.-T. Lee, C.-C. Hsueh, M. S. Freund, and G. S. Ferguson, "Air oxidation of self-assembled monolayers on polycrystalline gold: The role of the gold substrate," *Langmuir*, vol. 14, no. 22, pp. 6419–6423, 1998, ISSN: 0743-7463.

[197] M. H. Schoenfisch and J. E. Pemberton, "Air stability of alkanethiol self-assembled monolayers on silver and gold surfaces," *Journal of the American Chemical Society*, vol. 120, no. 18, pp. 4502–4513, 1998, ISSN: 0002-7863.

[198] T. M. Willey, A. L. Vance, T Van Buuren, C Bostedt, L. Terminello, and C. Fadley, "Rapid degradation of alkanethiol-based self-assembled monolayers on gold in ambient laboratory conditions," *Surface Science*, vol. 576, no. 1-3, pp. 188–196, 2005, ISSN: 0039-6028.

[199] L. Srisombat, A. C. Jamison, and T. R. Lee, "Stability: A key issue for self-assembled monolayers on gold as thin-film coatings and nanoparticle protectants," *Colloids and Surfaces A: Physicochemical and Engineering Aspects*, vol. 390, no. 1-3, pp. 1–19, 2011, ISSN: 0927-7757.

[200] C. M. Crudden, J. H. Horton, I. Ebralidze, O. V. Zenkina, A. B. McLean, B. Drevniok, Z. She, H. B. Kraatz, N. J. Mosey, T. Seki, E. C. Keske, J. D. Leake, A. Rousina-Webb, and G. Wu, "Ultra stable self-assembled monolayers of n-heterocyclic carbenes on gold," *Nat Chem*, vol. 6, no. 5, pp. 409–14, 2014, ISSN: 1755-4349 (Electronic) 1755-4330 (Linking). DOI: 10.1038/nchem.1891. [Online]. Available: https://www.ncbi.nlm.nih.gov/pubmed/24755592.

[201] Z. Li, K. Munro, I. I. Ebralize, M. R. Narouz, J. D. Padmos, H. Hao, C. M. Crudden, and J. H. Horton, "N-heterocyclic carbene self-assembled monolayers on gold as surface plasmon resonance biosensors," *Langmuir*, vol. 33, no. 49, pp. 13 936–13 944, 2017, ISSN: 0743-7463.

[202] Z. Li, K. Munro, M. R. Narouz, A. Lau, H. Hao, C. M. Crudden, and J. H. Horton, "Self-assembled n-heterocyclic carbene-based carboxymethylated dextran monolayers on gold as a tunable platform for designing affinity-capture biosensor surfaces," *ACS applied materials & interfaces*, vol. 10, no. 21, pp. 17 560–17 570, 2018, ISSN: 1944-8244.

[203] K. Goodge and M. Frey, "Biotin-conjugated cellulose nanofibers prepared via copper-catalyzed alkyne-azide cycloaddition (cuaac) "click" chemistry," *Nanomaterials (Basel)*, vol. 10, no. 6, 2020, ISSN: 2079-4991 (Print) 2079-4991 (Linking). DOI: 10.3390/nano10061172. [Online]. Available: https://www.ncbi.nlm.nih.gov/pubmed/32560117.

[204] S. I. Presolski, V. P. Hong, and M. G. Finn, "Copper-catalyzed azide-alkyne click chemistry for bioconjugation," *Curr Protoc Chem Biol*, vol. 3, no. 4, pp. 153–162, 2011, ISSN: 2160-4762 (Electronic) 2160-4762 (Linking). DOI: 10.1002/9780470559277.ch110148. [Online]. Available: https://www.ncbi.nlm.nih.gov/pubmed/22844652.

[205] L. M. Sherman, S. L. Strausser, R. K. Borsari, D. M. Jenkins, and J. P. Camden, "Imidazolinium n-heterocyclic carbene ligands for enhanced stability on gold surfaces," *Langmuir*, 2021, ISSN: 0743-7463.

[206] H. K. Kim, A. S. Hyla, P. Winget, H. Li, C. M. Wyss, A. J. Jordan, F. A. Larrain, J. P. Sadighi, C. Fuentes-Hernandez, and B. Kippelen, "Reduction of the work function of gold by n-heterocyclic carbenes," *Chemistry of Materials*, vol. 29, no. 8, pp. 3403–3411, 2017, ISSN: 0897-4756.

[207] D. M. Hartley and E. N. Perencevich, "Public health interventions for COVID-19: Emerging evidence and implications for an evolving public health crisis," *Jama*, vol. 323, no. 19, pp. 1908–1909, 2020, ISSN: 0098-7484.

[208] P. Nouvellet, S. Bhatia, A. Cori, K. E. C. Ainslie, M. Baguelin, S. Bhatt, A. Boonyasiri, N. F. Brazeau, L. Cattarino, L. V. Cooper, H. Coupland, Z. M. Cucunuba, G. Cuomo-Dannenburg, A. Dighe, B. A. Djaafara, I. Dorigatti, O. D. Eales, S. L. van Elsland, F. F. Nascimento, R. G. FitzJohn, K. A. M. Gaythorpe, L. Geidelberg, W. D. Green, A. Hamlet, K. Hauck, W. Hinsley, N. Imai, B. Jeffrey, E. Knock, D. J. Laydon, J. A. Lees, T. Mangal, T. A. Mellan, G. Nedjati-Gilani, K. V. Parag, M. Pons-Salort, M. Ragonnet-Cronin, S. Riley, H. J. T. Unwin, R. Verity, M. A. C. Vollmer, E. Volz, P. G. T. Walker, C. E. Walters, H. Wang, O. J. Watson, C. Whittaker, L. K. Whittles, X. Xi, N. M. Ferguson, and C. A. Donnelly, "Reduction in mobility and covid-19 transmission," *Nat Commun*, vol. 12, no. 1, p. 1090, 2021, ISSN: 2041-1723 (Electronic) 2041-1723 (Linking). DOI: 10.1038/s41467-021-21358-2. [Online]. Available: https://www.ncbi.nlm.nih.gov/pubmed/33597546.

[209] T. Ji, Z. Liu, G. Wang, X. Guo, S. Akbar Khan, C. Lai, H. Chen, S. Huang, S. Xia, B. Chen, H. Jia, Y. Chen, and Q. Zhou, "Detection of covid-19: A review of the current literature and future perspectives," *Biosens Bioelectron*, vol. 166, p. 112 455, 2020, ISSN: 1873-4235 (Electronic) 0956-5663 (Linking). DOI: 10.1016/j.bios.2020.112455. [Online]. Available: https://www.ncbi.nlm.nih.gov/pubmed/32739797.

[210] W. Wang, Y. Xu, R. Gao, R. Lu, K. Han, G. Wu, and W. Tan, "Detection of sars-cov-2 in different types of clinical specimens," *JAMA*, vol. 323, no. 18, pp. 1843–1844, 2020, ISSN: 1538-3598 (Electronic) 0098-7484 (Linking). DOI:

10.1001/jama.2020.3786. [Online]. Available: https://www.ncbi.nlm.nih.gov/pubmed/32159775.

[211] Y. W. Tang, J. E. Schmitz, D. H. Persing, and C. W. Stratton, "Laboratory diagnosis of covid-19: Current issues and challenges," *J Clin Microbiol*, vol. 58, no. 6, 2020, ISSN: 1098-660X (Electronic) 0095-1137 (Linking). DOI: 10.1128/JCM.00512-20. [Online]. Available: https://www.ncbi.nlm.nih.gov/pubmed/32245835.

[212] N. Ravi, D. L. Cortade, E. Ng, and S. X. Wang, "Diagnostics for sars-cov-2 detection: A comprehensive review of the fda-eua covid-19 testing landscape," *Biosens Bioelectron*, vol. 165, p. 112 454, 2020, ISSN: 1873-4235 (Electronic) 0956-5663 (Linking). DOI: 10.1016/j.bios.2020.112454. [Online]. Available: https://www.ncbi.nlm.nih.gov/pubmed/32729549.

[213] G. Seo, G. Lee, M. J. Kim, S. H. Baek, M. Choi, K. B. Ku, C. S. Lee, S. Jun, D. Park, H. G. Kim, S. J. Kim, J. O. Lee, B. T. Kim, E. C. Park, and S. I. Kim, "Rapid detection of covid-19 causative virus (sars-cov-2) in human nasopharyngeal swab specimens using field-effect transistor-based biosensor," *ACS Nano*, vol. 14, no. 4, pp. 5135–5142, 2020, ISSN: 1936-086X (Electronic) 1936-0851 (Linking). DOI: 10.1021/acsnano.0c02823. [Online]. Available: https://www.ncbi.nlm.nih.gov/pubmed/32293168.

[214] S. Mavrikou, G. Moschopoulou, V. Tsekouras, and S. Kintzios, "Development of a portable, ultra-rapid and ultra-sensitive cell-based biosensor for the direct detection of the sars-cov-2 s1 spike protein antigen," *Sensors (Basel)*, vol. 20, no. 11, 2020, ISSN: 1424-8220 (Electronic) 1424-8220 (Linking). DOI: 10.3390/s20113121. [Online]. Available: https://www.ncbi.nlm.nih.gov/pubmed/32486477.

[215] T. Farrow, S. Laumier, I. Sandall, and H. v. Zalinge, "Silicon thin film transistor based aptamer sensor for covid-19 detection," 2020. DOI: 10.21203/rs.3.rs-74726/v1.

[216] L. Porte, P. Legarraga, V. Vollrath, X. Aguilera, J. M. Munita, R. Araos, G. Pizarro, P. Vial, M. Iruretagoyena, S. Dittrich, and T. Weitzel, "Evaluation of a novel antigen-based rapid detection test for the diagnosis of sars-cov-2 in respiratory samples," *Int J Infect Dis*, vol. 99, pp. 328–333, 2020, ISSN: 1878-3511 (Electronic) 1201-9712 (Linking). DOI: 10.1016/j.ijid.2020.05.098. [Online]. Available: https://www.ncbi.nlm.nih.gov/pubmed/32497809.

[217] S. Mahari, A. Roberts, D. Shahdeo, and S. Gandhi, "Ecovsens-ultrasensitive novel in-house built printed circuit board based electrochemical device for rapid detection of ncovid-19 antigen, a spike protein domain 1 of sars-cov-2," *bioRxiv*, 2020. DOI: 10.1101/2020.04.24.059204.

[218] B. Mojsoska, S. Larsen, D. A. Olsen, J. S. Madsen, I. Brandslund, and F. A. Alatraktchi, "Rapid sars-cov-2 detection using electrochemical immunosensor," *Sensors (Basel)*, vol. 21, no. 2, 2021, ISSN: 1424-8220 (Electronic) 1424-

8220 (Linking). DOI: 10.3390/s21020390. [Online]. Available: https://www.ncbi.nlm.nih.gov/pubmed/33429915.

[219] R. M. Torrente-Rodriguez, H. Lukas, J. Tu, J. Min, Y. Yang, C. Xu, H. B. Rossiter, and W. Gao, "Sars-cov-2 rapidplex: A graphene-based multiplexed telemedicine platform for rapid and low-cost covid-19 diagnosis and monitoring," *Matter*, vol. 3, no. 6, pp. 1981–1998, 2020, ISSN: 2590-2385 (Electronic) 2590-2385 (Linking). DOI: 10.1016/j.matt.2020.09.027. [Online]. Available: https://www.ncbi.nlm.nih.gov/pubmed/33043291.

[220] Z. Rahmati, M. Roushani, H. Hosseini, and H. Choobin, "Electrochemical immunosensor with cu2o nanocube coating for detection of sars-cov-2 spike protein," *Mikrochim Acta*, vol. 188, no. 3, p. 105, 2021, ISSN: 1436-5073 (Electronic) 0026-3672 (Linking). DOI: 10.1007/s00604-021-04762-9. [Online]. Available: https://www.ncbi.nlm.nih.gov/pubmed/33651173.

[221] S. Eissa and M. Zourob, "Development of a low-cost cotton-tipped electrochemical immunosensor for the detection of sars-cov-2," *Anal Chem*, vol. 93, no. 3, pp. 1826–1833, 2021, ISSN: 1520-6882 (Electronic) 0003-2700 (Linking). DOI: 10.1021/acs.analchem.0c04719. [Online]. Available: https://www.ncbi.nlm.nih.gov/pubmed/33370087.

[222] B. Kavosi, A. Salimi, R. Hallaj, and F. Moradi, "Ultrasensitive electrochemical immunosensor for psa biomarker detection in prostate cancer cells using gold nanoparticles/pamam dendrimer loaded with enzyme linked aptamer as integrated triple signal amplification strategy," *Biosens Bioelectron*, vol. 74, pp. 915–23, 2015, ISSN: 1873-4235 (Electronic) 0956-5663 (Linking). DOI: 10.1016/j.bios.2015.07.064. [Online]. Available: https://www.ncbi.nlm.nih.gov/pubmed/26257183.

[223] S. Wustoni, S. Wang, J. R. Alvarez, T. C. Hidalgo, S. P. Nunes, and S. Inal, "An organic electrochemical transistor integrated with a molecularly selective isoporous membrane for amyloid-beta detection," *Biosens Bioelectron*, vol. 143, p. 111 561, 2019, ISSN: 1873-4235 (Electronic) 0956-5663 (Linking). DOI: 10.1016/j.bios.2019.111561. [Online]. Available: https://www.ncbi.nlm.nih.gov/pubmed/31446202.

[224] S. Demuru, A. Marette, W. Kooli, P. Junier, and D. Briand, "Flexible organic electrochemical transistor with functionalized inkjet-printed gold gate for bacteria sensing," in *2019 20th International Conference on Solid-State Sensors, Actuators and Microsystems & Eurosensors XXXIII (TRANSDUCERS & EUROSENSORS XXXIII)*, IEEE, 2019, pp. 2519–2522. DOI: 10.1109/transducers.2019.8808309.

[225] E. Macchia, M. Ghittorelli, F. Torricelli, and L. Torsi, "Organic electrochemical transistor immuno-sensor operating at the femto-molar limit of detection," in *2017 7th IEEE International Workshop on Advances in Sensors and Interfaces (IWASI)*, IEEE, pp. 68–72, ISBN: 1509067078.

[226] K. Guo, S. Wustoni, A. Koklu, E. Díaz-Galicia, M. Moser, A. Hama, A. A. Alqahtani, A. N. Ahmad, F. S. Alhamlan, M. Shuaib, *et al.*, "Rapid single-molecule detection of covid-19 and mers antigens via nanobody-functionalized organic electrochemical transistors," *Nature Biomedical Engineering*, pp. 1–12, 2021, ISSN: 2157-846X.

[227] L. Basiricò, P. Cosseddu, A. Scidà, B. Fraboni, G. G. Malliaras, and A. Bonfiglio, "Electrical characteristics of ink-jet printed, all-polymer electrochemical transistors," *Organic Electronics*, vol. 13, no. 2, pp. 244–248, 2012, ISSN: 15661199. DOI: 10.1016/j.orgel.2011.11.010.

[228] G. T. Hermanson, *Bioconjugate techniques*. Academic press, 2013.

[229] J. Kong and S. Yu, "Fourier transform infrared spectroscopic analysis of protein secondary structures," *Acta biochimica et biophysica Sinica*, vol. 39, no. 8, pp. 549–559, 2007, ISSN: 1672-9145.

[230] X. Kang, Z. Mai, X. Zou, P. Cai, and J. Mo, "A novel glucose biosensor based on immobilization of glucose oxidase in chitosan on a glassy carbon electrode modified with gold-platinum alloy nanoparticles/multiwall carbon nanotubes," *Anal Biochem*, vol. 369, no. 1, pp. 71–9, 2007, ISSN: 0003-2697 (Print) 0003-2697 (Linking). DOI: 10.1016/j.ab.2007.07.005. [Online]. Available: https://www.ncbi.nlm.nih.gov/pubmed/17678866.

[231] K. A. Walsh, K. Jordan, B. Clyne, D. Rohde, L. Drummond, P. Byrne, S. Ahern, P. G. Carty, K. K. O'Brien, and E. O'Murchu, "Sars-cov-2 detection, viral load and infectivity over the course of an infection: Sars-cov-2 detection, viral load and infectivity," *Journal of Infection*, 2020, ISSN: 0163-4453.

[232] F. Yu, L. Yan, N. Wang, S. Yang, L. Wang, Y. Tang, G. Gao, S. Wang, C. Ma, and R. Xie, "Quantitative detection and viral load analysis of sars-cov-2 in infected patients," *Clinical Infectious Diseases*, vol. 71, no. 15, pp. 793–798, 2020, ISSN: 1058-4838.

[233] J. Fajnzylber, J. Regan, K. Coxen, H. Corry, C. Wong, A. Rosenthal, D. Worrall, F. Giguel, A. Piechocka-Trocha, and C. Atyeo, "Sars-cov-2 viral load is associated with increased disease severity and mortality," *Nature communications*, vol. 11, no. 1, pp. 1–9, 2020, ISSN: 2041-1723.

[234] Y. Pan, D. Zhang, P. Yang, L. L. Poon, and Q. Wang, "Viral load of sars-cov-2 in clinical samples," *The Lancet infectious diseases*, vol. 20, no. 4, pp. 411–412, 2020, ISSN: 1473-3099.

[235] Web Page, 2021. [Online]. Available: https://www.businesswire.com/news/home/20211001005189/en/.

[236] Web Page, 2021. [Online]. Available: https://clinicaltrials.gov/ct2/show/NCT04575597.

Appendix A: Supplementary Information for Chapter 7

A.1 SEM and AFM Characterization of Pt Thin Films

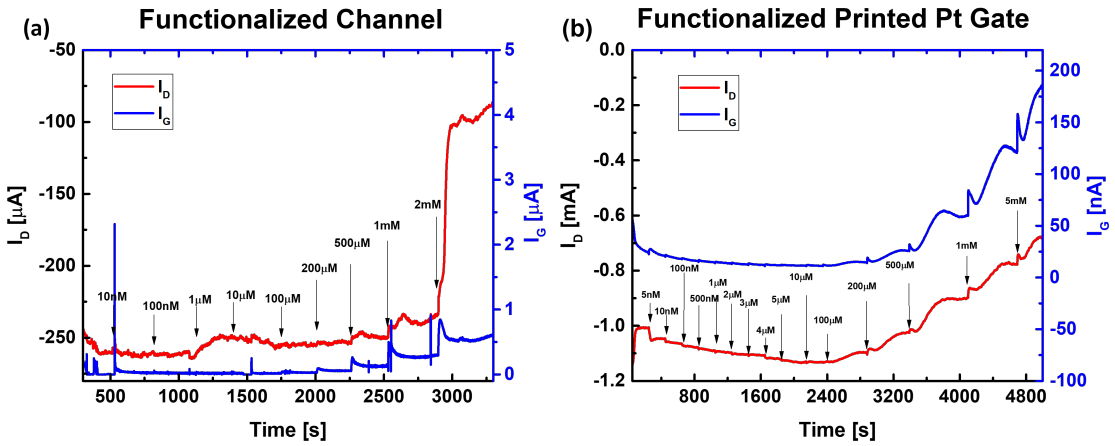

Figure A.1: Real time I_D measured for OECTs with functionalized (a) channel and (b) functionalized printed Pt gate. 3 μL of 8 mg/mL GOx stock solution was added to the designated functionalization site. PBS was used as the background electrolyte. The functionalized devices were biased with constant voltages (V_D = -0.2 V and V_G = 0.6 V). The change in I_D was monitored after the addition of glucose solutions with different concentrations. Lower current responses were observed for both cases.

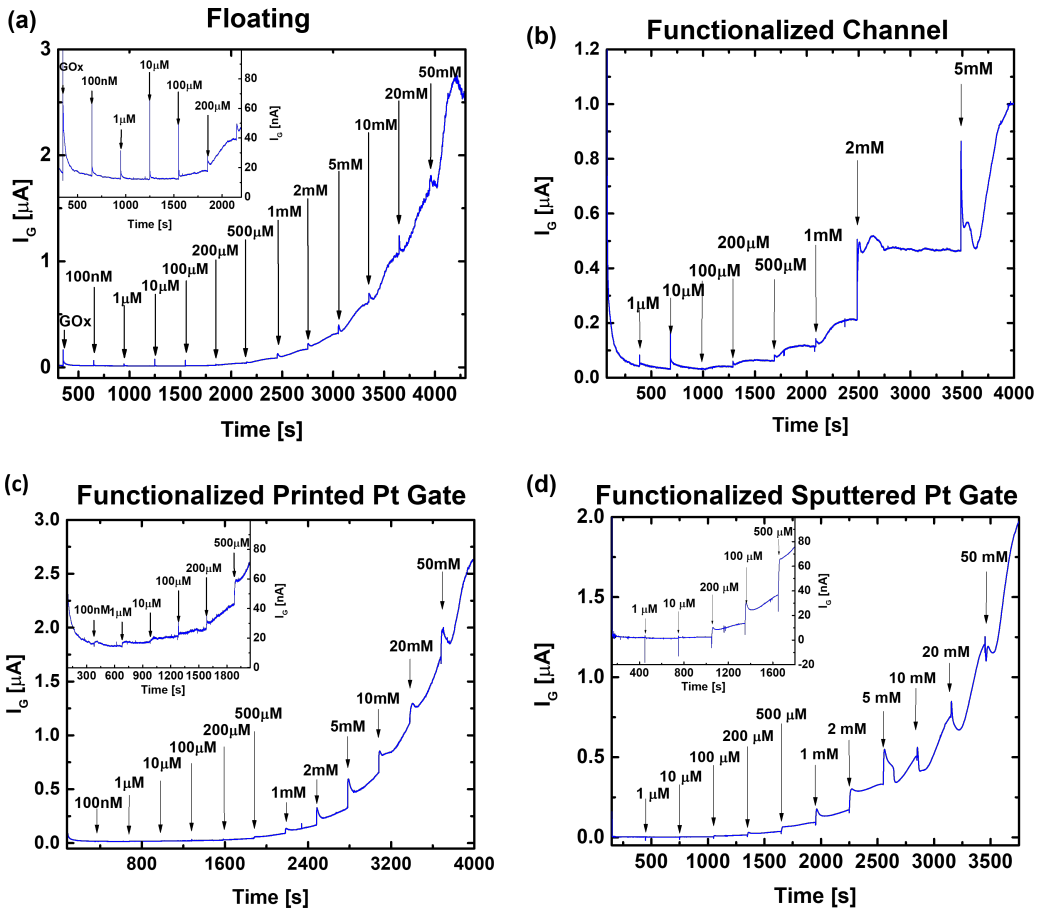

Figure A.2: The corresponding I_G response of the four OECT functionalization configurations as shown in Figure 7.3. (a) Unfunctionalized OECT with floating GOx. (b) OECT with functionalized channel. (c) OECT with functionalized printed Pt gate. (d) OECT with functionalized sputtered Pt gate. At higher glucose concentrations, I_G keeps increasing due to the limited GOx amount for glucose molecule oxidation and limited Pt surface area for H_2O_2 decomposition.

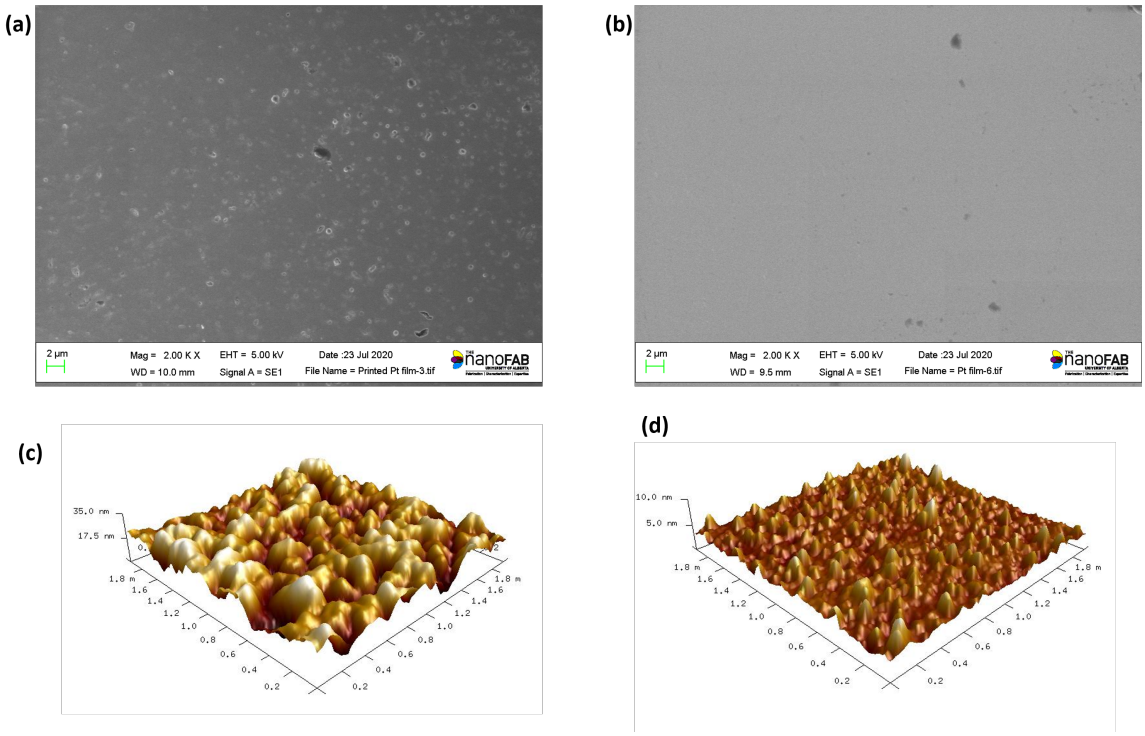

Figure A.3: Surface roughness comparison of printed and sputtered Pt films. (a) SEM image of printed Pt film. (b) SEM image of Pt thin film deposited by magnetron sputter system. (c) AFM image of printed Pt film. (d) AFM image of sputtered Pt film. The printed nanoparticle-based Pt film has higher surface RMS roughness (R_q) of 13.8 nm as compared to $R_q = 0.852$ nm for the sputtered Pt film.

Appendix B: Additional Data for NHC Modified Au

B.1 Additional Evidence of NHC Deposition

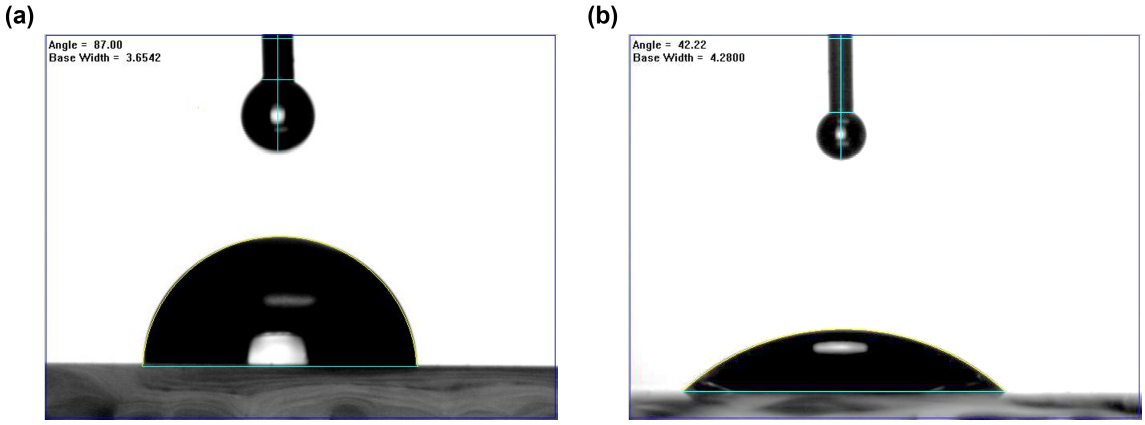

Figure B.1: Contact angles for (a) blank Au and (b) alkyne-NHC Au sample.

Due to the limited size of printed Au electrode, the contact angles were measured on glass slides coated with 10/100 nm Ti/Au film. As shown in Figure B.1, the contact angle decreased from 88 degree to 42.22 degree, indicating that the film hydrophilicity increased after alkyne-NHC deposition.

Figure B.2 shows the absorption spectrum collected for a TMS terminated alkyne-NHC modified printed Au electrode. The characteristic peaks were found at 2958.3, 2925.5, and 2854.2 cm^{-1} for aliphatic hydrocarbons (C-H_{aliph}), 848 and 808 cm^{-1} attributed to C=C bending, and 1262.2 cm^{-1} due to the methyl groups on TMS. Both results confirmed the formation of NHC based functional groups on Au surface.

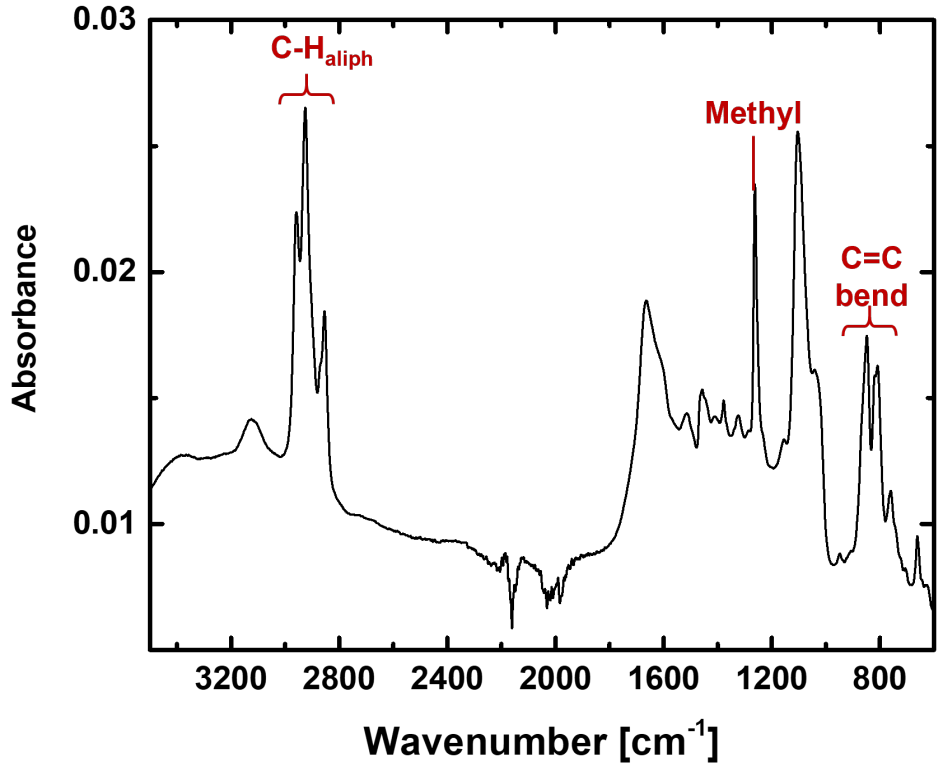

Figure B.2: IR spectrum of TMS protected alkyne-NHC Au electrode.

B.2 EIS Equivalent Circuit Model

Figure B.3 shows the equivalent circuit model used in this thesis to analyze the impedance. This model should be further improved to acquire a better fit for the data.

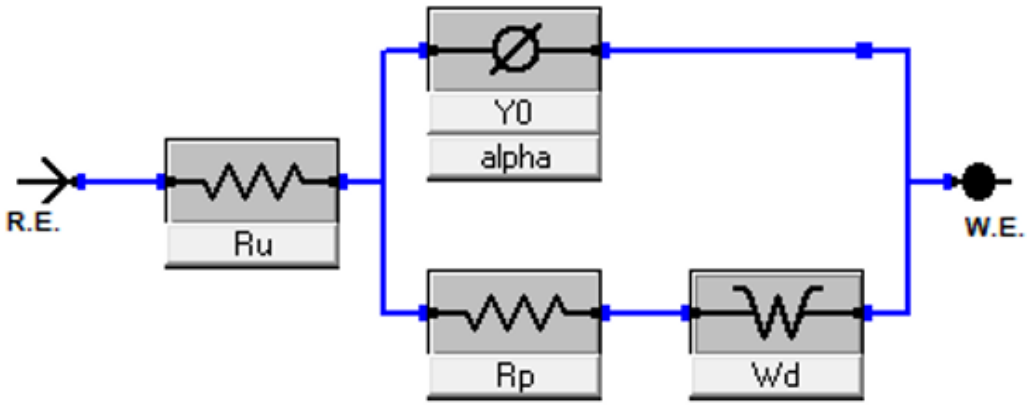

Figure B.3: The equivalent circuit model (CPE with diffusion) used for impedance analysis of EIS data. R_u is the series resistance, R_p is the parallel resistance component, W_d is the Warburg element accounting for the diffusion process, and Y_0 and alpha describes the CPE element.

Appendix C: The Signal Processing Circuit Schematic and Calibration for SARS-CoV-2 Diagnostic Tool

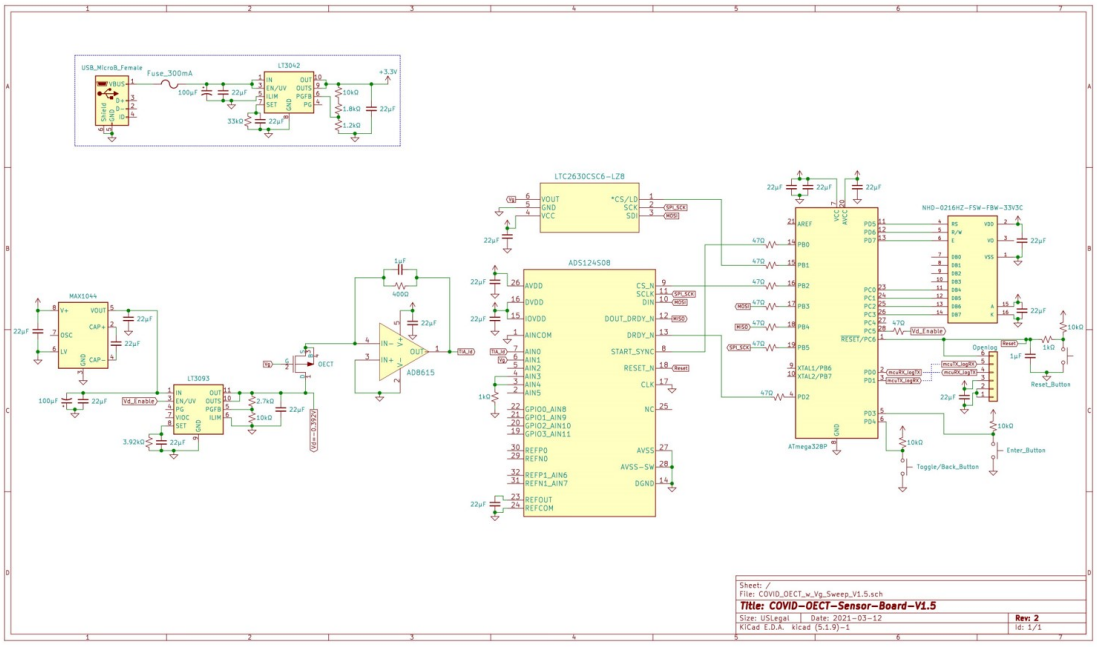

Figure C.1: Schematic of the circuit board designed for measuring the OECT based SARS-CoV-2 biosensor with a two-button user-interface.

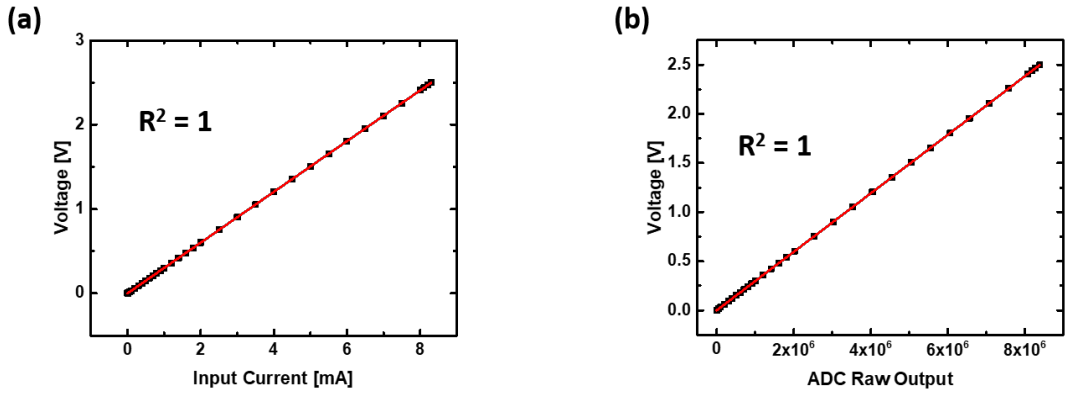

Figure C.2: (a) Calibration curve of the TIA obtained by sourcing the input current and measuring the output voltage using a Keithley sourcemeter. The linear fit has a slope of 301 Ω that matches the value of the feedback resistor, $R^2 = 1$, and a small offset voltage of -31.6 μV. (b) Calibration curve of the 24-bit Δ-Σ ADC collected by using a Keithley sourcemeter to source the input current and comparing the output of ADC raw data and the ADC pin voltage measured by Keithley. A linear correlation between the two sets of values with $R^2 = 1$ and a small ADC offset voltage of -115 μV is observed.

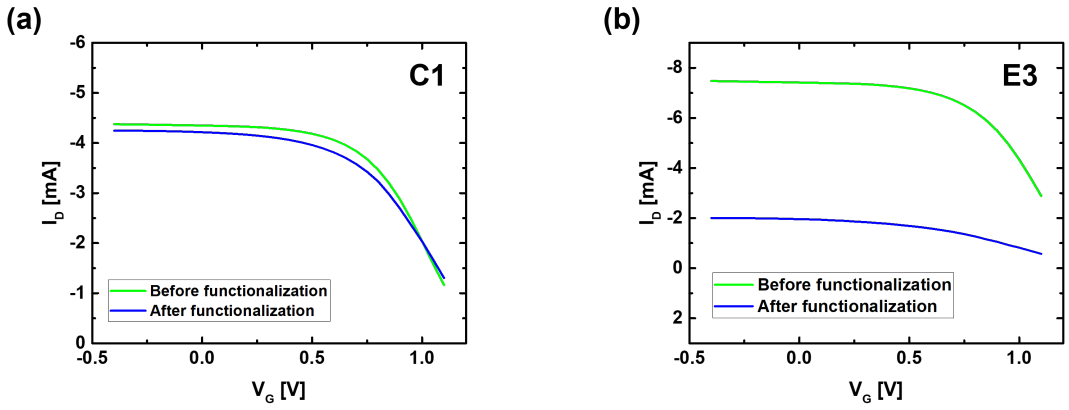

Figure C.3: Transfer curves measured in 1xPBS before and after functionalizing the in-plane gate with SARS-CoV-2 antibody for device (a) C1 and (b) E3.